Floor Response Spectra in Hybrid Base-Rocking and Reinforced Concrete Wall Buildings

Leikune F Aragaw

A thesis

submitted in partial fulfillment of the

requirements for the degree of

Master of Science in Civil Engineering

University of Washington

2017

Committee:

Paolo M. Calvi

John F. Stanton

Jeffrey W. Berman

Program Authorized to Offer Degree:

Civil and Environmental Engineering

University of Washington

Abstract

Floor Response Spectra in Hybrid Base-Rocking and Reinforced Concrete Wall Buildings

Leikune F Aragaw

Chair of the Supervisory Committee:
Assistant Professor Paolo M. Calvi
Civil and Environmental Engineering

Seismic events such as the Northridge (1994) and Nisqually (2001) earthquakes, amongst many others, have caused significant damage and financial losses to both structural and non-structural components of buildings. In response to this, significant research is being conducted with the aim of achieving higher performance objectives, which include: (i) the reduction and even elimination of structural damage during earthquakes, and (ii) the improvement of seismic risk mitigation for non-structural elements.

To address point (i), several innovative technologies have been proposed that could limit structural damage compared to traditional structural systems in which structural damage serves as a means of energy dissipation. Among these, hybrid base-rocking walls effectively combine unbonded post-tensioning and mild-steel reinforcement to eliminate damage and residual displacements while providing good energy dissipation. In this study, the seismic response of hybrid base-rocking walls is compared to the more “traditional” reinforced concrete (RC) walls, through non-linear time-history analysis of 4, 8 and 12-story case-study buildings. Special

attention is given to the floor acceleration response of both structural systems as it pertains to the performance of non-structural elements.

To address point (ii), this study proposes three simple methodologies for estimating acceleration demands on non-structural elements in hybrid base-rocking and RC wall buildings, through a floor response spectrum (FRS) method. In all three procedures, individual modal floor spectra are first generated and then combined through a simplified modal combination approach to generate floor spectra that account for the effects of multiple modes. In order to account for non-linear structural response, the first procedure utilizes the concept of transitory inelastic modes of vibration to generate inelastic modal floor spectra, while the second procedure utilizes empirical modal reduction factors that are used to reduce elastic modal floor spectra based on the expected ductility of the building. The third procedure focuses on how to estimate floor spectra in the early design phases of a building, when the modal characteristics of a building are not known. To this end, the procedure idealizes RC and hybrid base-rocking walls as continuous distributed-mass systems to estimate their modal characteristics, which are in turn used to estimate floor spectra. Each proposed procedure is then tested by comparison to floor spectra obtained from non-linear time-history analysis of 4, 8 and 12-story case-study buildings.

TABLE OF CONTENTS

LIST OF FIGURES

LIST OF TABLES

ACKNOWLEDGMENTS

I would like to express my deepest gratitude to my advisor Prof. Paolo Calvi for his constant support and guidance throughout the duration of this project. I am grateful for his insight and expertise, which were instrumental in helping me conduct a thorough research project.

I would also like to thank Prof. John Stanton and Prof. Jeffrey Berman for serving on my committee and for their advice and recommendations to improve the quality of this document.

Thank you to Nasser Marafi for constantly taking the time to help and give me advice, especially regarding time-history analyses of structures.

Thank you to my “good, but not the best,” ;) friends, Tom and Clare, for making More Hall an enjoyable place to work. I will not forget all their distractions that made the long days and nights there feel like a breeze.

Lastly, I would like to thank my family for their unconditional love and support throughout my time at the University of Washington. I am comforted by that fact that they will always have my back.

1 INTRODUCTION

1.1 Motivation

For many years, the seismic design of buildings has focused on life-safety with the main concern being the prevention of loss of life during strong earthquakes. In the context of past design philosophies, the damage caused to buildings during a seismic event (which can be both structural and non-structural), though undesirable, has been treated as a secondary problem. Consequently, past earthquakes have often caused significant damage and financial losses to both structural and non-structural components. Such was the case, for example, of the 1994 Northridge earthquake (Los Angeles) (Todd *et al.*, 1994; Villaverde, 1997). A recent study conducted by Charleson (2008) suggests that of the 66,000 buildings that were damaged during the earthquake, about 75% of the buildings suffered damage to non-structural elements alone (Ferner et al., 2014; Welch, 2016). Even relatively moderate earthquakes, without causing much structural damage and loss of life, have been responsible for substantial damage to non-structural elements. For instance, the 2001 Nisqually earthquake (Seattle-Olympia) is estimated to have caused two billion dollars' worth of damages, which was mostly associated with non-structural damage (Filiatrault *et al.*, 2001). This is not surprising considering that non-structural components and building contents can account for upwards of 80% of the total investment in a typical building (Taghavi and Miranda, 2003).

In response to this, current design philosophies are moving toward performance-based earthquake engineering (PBEE) approaches. In this approach, seismic risk is not only quantified in terms of life-safety but also in terms of financial losses, and more generally in terms of overall performance, looking at both structural and non-structural components of buildings. To this end, there is increasing research focusing on: (i) the reduction and even elimination of structural damage during earthquakes, and (ii) improvement of seismic risk mitigation for non-structural elements.

To address point (i), several innovative technologies have been proposed that could limit and even eliminate structural damage compared to traditional structural systems in which structural damage

serves as a means of energy dissipation. There are many "traditional" lateral load resisting systems that are currently in use. Amongst these, reinforced concrete (RC) structural walls have long been used as lateral load resisting systems for their excellent energy dissipation capacity and their overall performance observed in past earthquakes (Wood *et al.,* 1987; Fintel, 1995; Mitchell *et al.,* 1995). RC walls are typically designed such that an inelastic fuse (i.e. plastic hinge) forms at the base of the wall, so that the inelastic deformation is concentrated at one location, limiting the forces experienced by the wall. This design approach, however, causes significant damage to the wall (mostly in the plastic hinge region) and residual displacements in the structure, which can be difficult and costly to repair. An emerging technology that improves upon such a system is the hybrid base-rocking structural wall, which has good energy dissipation capabilities (albeit less compared to RC walls) but does not tolerate damage.

Hybrid base-rocking walls are not monolithically cast with the foundation of a building and thus do not form a plastic hinge at the base of the wall or experience structural damage. Instead, wall panels are post-tensioned to the foundation such that controlled rocking occurs during lateral loading. Energy dissipation, in the form of hysteretic dampers, is commonly provided through unbonded mild steel reinforcement that crosses the wall/foundation interface. It is important to note that friction (Kurama, 2001), viscous (Kurama, 2000) and other types of hysteretic dampers (Nakaki *et al.*, 1999; Perez *et al.*, 2004) have also been considered in the literature (Wiebe, 2008). Once lateral loading is removed, the post-tensioning force re-centers the wall eliminating any residual displacements that would otherwise be present in a traditional RC wall. Despite these benefits, higher floor accelerations have been observed in hybrid base-rocking walls relative to RC walls (Rodriguez et al., 2002; Wiebe, 2008), which can be concerning for the performance of acceleration-sensitive non-structural elements.

Regarding point (ii), there are ongoing studies looking into both the seismic behavior of non-structural elements as well as into the quantification of seismic loads on non-structural elements (Welch, 2016). In terms of seismic behavior, non-structural elements can be classified as either drift-sensitive or acceleration-sensitive (Taghavi and Miranda, 2003; FEMA, 2012; Welch, 2016). Drifts are typically dealt with by stiffening the supporting building, and proper detailing of non-structural elements. Once the stiffness of the building is established, floor response spectra are typically generated to estimate the acceleration demands on non-structural elements (Sullivan *et*

al., 2013). However, recent studies have shown that current codified methods for estimating acceleration demands are inadequate, particularly because they do not account for elastic damping of the supported non-structural element and higher mode response of the supporting building (Uma *et al.*, 2010; Sullivan *et al.*, 2013; Pinkawa *et al.*, 2014; Welch, 2016; among others). Therefore, there is an increasing push towards developing improved procedures to estimate acceleration demands on non-structural elements.

This thesis addresses both points discussed above. First, an analytical investigation of the seismic response of hybrid base-rocking walls is conducted in relation to the response of RC walls. Special attention is given to the floor acceleration response of both types of structural walls as it pertains to the performance of non-structural elements. Second, several methodologies are proposed for the estimation of acceleration demands on non-structural elements that are supported by either structural wall systems.

1.2 Research Objectives and Outline of Thesis

The two main research objectives of this study are as follows:

i) To compare the seismic response of hybrid base-rocking and RC wall buildings, and

ii) To develop procedures for the estimation of floor response spectra in hybrid base-rocking and RC wall buildings responding non-linearly that can be used for the design of acceleration-sensitive non-structural elements.

Note that this study considers only light non-structural elements with a mass less than 1% of the total building mass, and one point of attachment to the supporting building.

The research objectives outlined above are addressed in the following chapters, which are outlined as follows:

Chapter 2 introduces both RC and hybrid base-rocking structural wall systems and their expected seismic behavior.

Chapter 3 presents a review of existing procedures to estimate acceleration demands on non-structural elements. The first section addresses the inherent assumptions for using floor response spectra to estimate acceleration demands on non-structural elements. The second section discusses

recent research efforts that have developed floor spectra estimation procedures for single (SDOF) and multi-degree-of-freedom (MDOF) systems responding both linearly and non-linearly. Most notably, the work of Sullivan *et al.* (2013), Calvi and Sullivan (2014), and Welch (2016) are discussed in detail. The last section discusses how several prominent code provisions determine acceleration demands on non-structural elements, and the limitations associated with each provision.

Chapter 4 discusses the design and time-history analysis of the case study RC and hybrid base-rocking wall buildings considered in this study. The layout of the case-study buildings and the seismic design loads (ASCE, 2010) are first introduced. Then, a detailed explanation of the displacement-based design of the buildings is provided. Lastly, a detailed explanation of the dynamic time-history analysis of the case-study buildings is provided.

Chapter 5 presents the results of the time history analysis of the case study buildings conducted according to Chapter 4. Using the results, the first section addresses the effectiveness of a displacement-based design approach in estimating seismic response. The second section presents an in depth comparison between the seismic response of RC and hybrid base-rocking wall buildings. Lastly, the third section details the observations made from floor response spectra atop the case-study buildings, with a focus on identifying parameters that have a significant influence of floor spectra. In addition, the dynamic interaction between non-structural elements and supporting buildings is discussed.

Chapter 6 details a two-part study into the maximum dynamic amplification of peak floor acceleration that is expected when a non-structural element and its supporting structure are in resonance. The first section investigates the performance of existing formulations for estimating the maximum dynamic amplification through time-history analysis of elastic SDOF systems, specifically focusing on the works of Sullivan *et al.* (2013) and Welch (2016). The second section investigates the effects of inelastic structural response on maximum dynamic amplification through time-history analysis of inelastic SDOF RC and hybrid base-rocking wall systems.

Chapter 7 employs the observations made in Chapter 5 and 6, and presents the development of three methodologies to estimate floor response spectra atop RC and hybrid base-rocking wall buildings responding non-linearly. The proposed procedures were based on the work of Calvi and Sullivan (2014) who proposed a simple procedure to estimate of floor response spectra in MDOF

buildings responding elastically. In this procedure, individual modal floor spectra are first generated and then combined through a simplified modal combination approach. The first two procedures proposed in the present study utilize the methodology proposed by Calvi and Sullivan (2014) and focus mostly on how to account for the influence of non-linear structural response on floor response spectra. To this end, the first procedure utilizes the concept of transitory inelastic modes of vibration (Sullivan *et al.*, 2006) to estimate floor acceleration demands during non-linear response. The second procedure utilizes empirical modal reduction factors (Welch, 2016) that can be used to reduce elastic floor acceleration demands based on the ductility expected in the system. The last procedure focuses on how to estimate acceleration demands on non-structural elements in the early design phases of a building, when the modal characteristics of the building are not known. To this end, the procedure idealizes RC and hybrid base-rocking walls as continuous distributed-mass systems to estimate their modal characteristics, which are in turn used to estimate floor acceleration demands.

Finally, Chapter 8 presents a summary of the findings from the study. The limitations of the study and areas of future research are also identified.

2 STRUCTURAL WALL SYSTEMS

2.1 Reinforced Concrete (RC) Wall Systems

Cantilever Reinforced Concrete (RC) structural walls ("RC walls") are commonly used to resist lateral loads in buildings. RC walls are economical and easy to construct and serve both architectural (i.e. they are necessary to host elevator shafts and staircases) and structural purposes (resisting vertical and lateral loads). To this end, their effectiveness at resisting lateral loads has been extensively demonstrated and buildings with RC walls have performed well in past earthquakes with structural collapse being rare (Wood *et al.,* 1987; Fintel, 1995; Mitchell *et al.,* 1995).

RC walls are cast monolithically with the foundations of the building, and commonly designed such that an inelastic mechanism (i.e. a plastic hinge) forms at the base of the wall. For these systems, the plastic hinge, and specifically the yielding of the flexural reinforcement, represents the principal source of energy dissipation. Additional energy is dissipated through cracking and crushing of concrete. To this end, it should be noted that in order to dissipate a large amount of energy (which is beneficial because it reduces the overall seismic demand on the system), it is necessary that the walls experience significant and permanent damage within the plastic hinge region.

RC walls are normally designed ensuring that undesirable failure modes, such as those due to diagonal tension or diagonal compression caused by shear, are prevented. Walls that are properly designed and detailed for flexural ductility are capable of high performance. The force-displacement response of ductile RC walls can be idealized as shown in Figure 2.1. It can be observed that once yielding occurs, cyclic loading causes significant stiffness degradation in the system as a result of increasing inelastic deformation (i.e. damage) in the plastic hinge region. Since the damage caused to the plastic hinge region is permanent, the wall can be permanently displaced even if lateral loading is removed, resulting in residual displacements. It should be noted, however, that once maximum displacement has been reached, the residual displacement could be

reduced by subsequent loading and unloading cycles depending on the characteristics of the ground motion (Christopoulos *et al.*, 2003). Figure 2.2, for example, shows how subsequent loading and unloading cycles that do not yield the system in either direction could reduce residual displacements, from r_{max} to r_{final} (Christopoulos *et al.*, 2003). In addition, the self-weight of the wall can help to re-center the wall, slightly reducing residual displacements. For a more detailed look into the seismic behavior, analysis and design of RC wall systems, refer to Paulay and Priestley (1992).

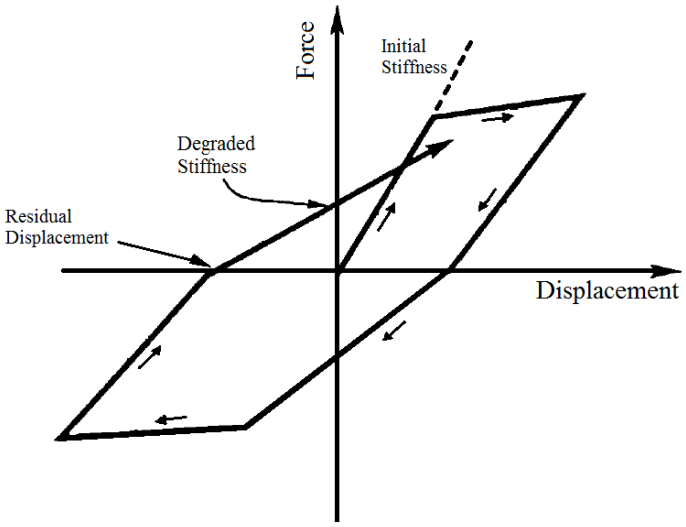

Figure 2.1 RC wall hysteretic response (adapted from Carr (2004))

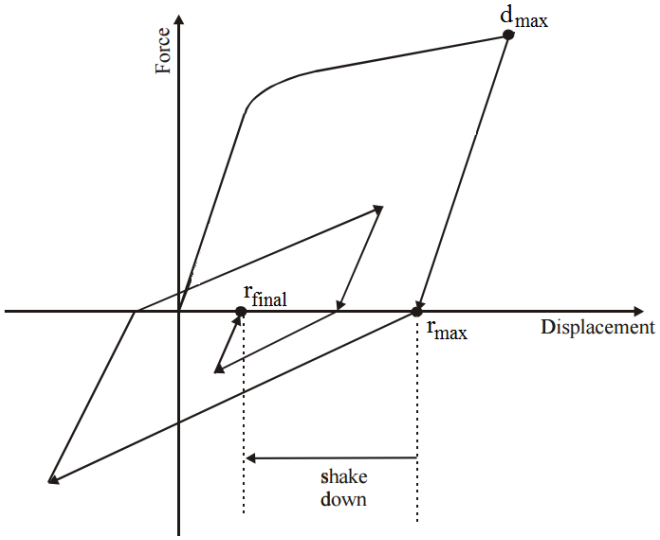

Figure 2.2 Reduction of residual displacements in RC walls during cyclic loading (adapted from Christopoulos *et al.* (2003))

2.2 Hybrid Base-Rocking Wall Systems

As discussed in the previous sub-section, RC walls (or monolithic systems in general) provide excellent energy dissipation during seismic events. However, this is accompanied by significant damage and permanent deformation that requires extensive repair to the structural system. In order to overcome this limitation, hybrid base-rocking walls ("rocking walls") have recently been developed. One of the first notable research efforts that focused on such systems is the Precast Seismic Structural Systems (PRESSS) Research Program (Priestley, 1991). In this research program, a 60 percent scale five-story precast concrete building incorporating a rocking jointed-structural wall system, developed and designed by Galusha (1999), was tested under simulated seismic loading (Priestley *et al.*, 1999). The results from the tests indicated that rocking walls had the potential for significantly reducing and even eliminating residual displacements and structural damage. Since this project, numerous analytical and experimental studies have been conducted to further develop and implement rocking walls (Rahman and Restrepo, 2000; Kurama, 2002; Holden *et al.*, 2003; Perez *et al.*, 2004; Marriott *et al.*, 2008; Wiebe, 2008; Belleri *et al.*, 2014; Sritharan et al., 2015; Gavridou, 2015; Khanmohammadi and Heydari, 2015; among others). However, relative to RC wall systems, the evidence backing the expected seismic performance of rocking wall systems is somewhat limited.

Nevertheless, several buildings have been constructed that incorporate rocking walls. The Cala building in the Dominican Republic is the first building in the literature that incorporated coupled rocking walls (Stanton *et al.*, 2003). Two other buildings incorporating coupled rocking walls have also been built in New Zealand, namely the Alan MacDiarmid Building in Wellington (Cattanach and Pampanin, 2008), and the Southern Cross Hospital Endoscopy Building in Christchurch (Pampanin *et al.*, 2011).

The rocking walls considered in the present study consist of a precast concrete panel that is reinforced with unbonded post-tensioning tendons as well as mild steel energy dissipaters crossing the wall-to-foundation interface (Figure 2.3). The post tensioning tendons are unbonded for the entire height of the wall, and anchored both at the top of the wall and at the foundation. The mild steel energy dissipaters are also unbonded for a specified length at the base of the wall. It is important to note that this type of dissipaters have some disadvantages, namely the potential for

buckling in compression and necking in tension since the dissipaters are axially loaded over an unbonded length.

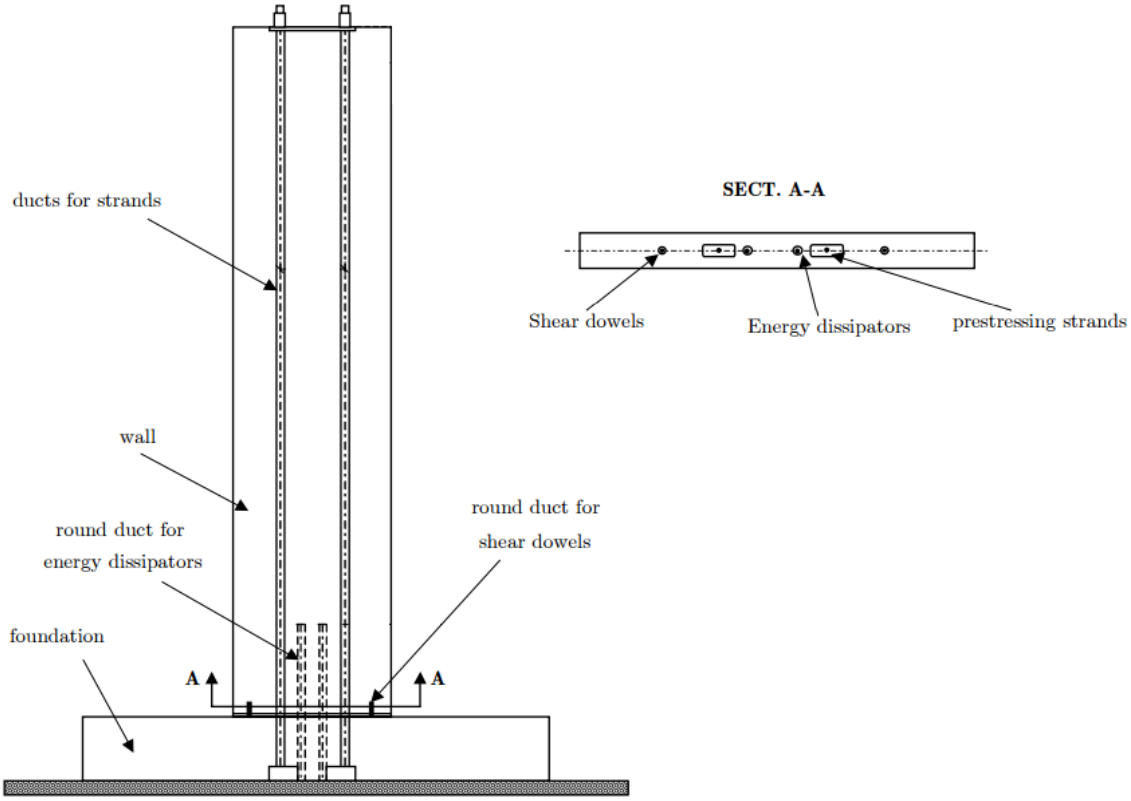

Figure 2.3 Sample schematic drawing of rocking wall (adapted from Palermo et al. (2005))

The hysteretic response of rocking walls can be idealized by the flag-shaped hysteresis shown in Figure 2.4, which was adapted from Wiebe and Christopoulos (2009). The simplified push-pull behavior presented in the figure assumes a rigid foundation, and perfectly elasto-plastic energy dissipaters crossing the wall-to-foundation joint. For clarity, the hysteresis is idealized with sharp stiffness changes, but, as experimental data shows (Figure 2.5), changes in stiffness are expected to occur more gradually (Wiebe and Christopoulos, 2009).

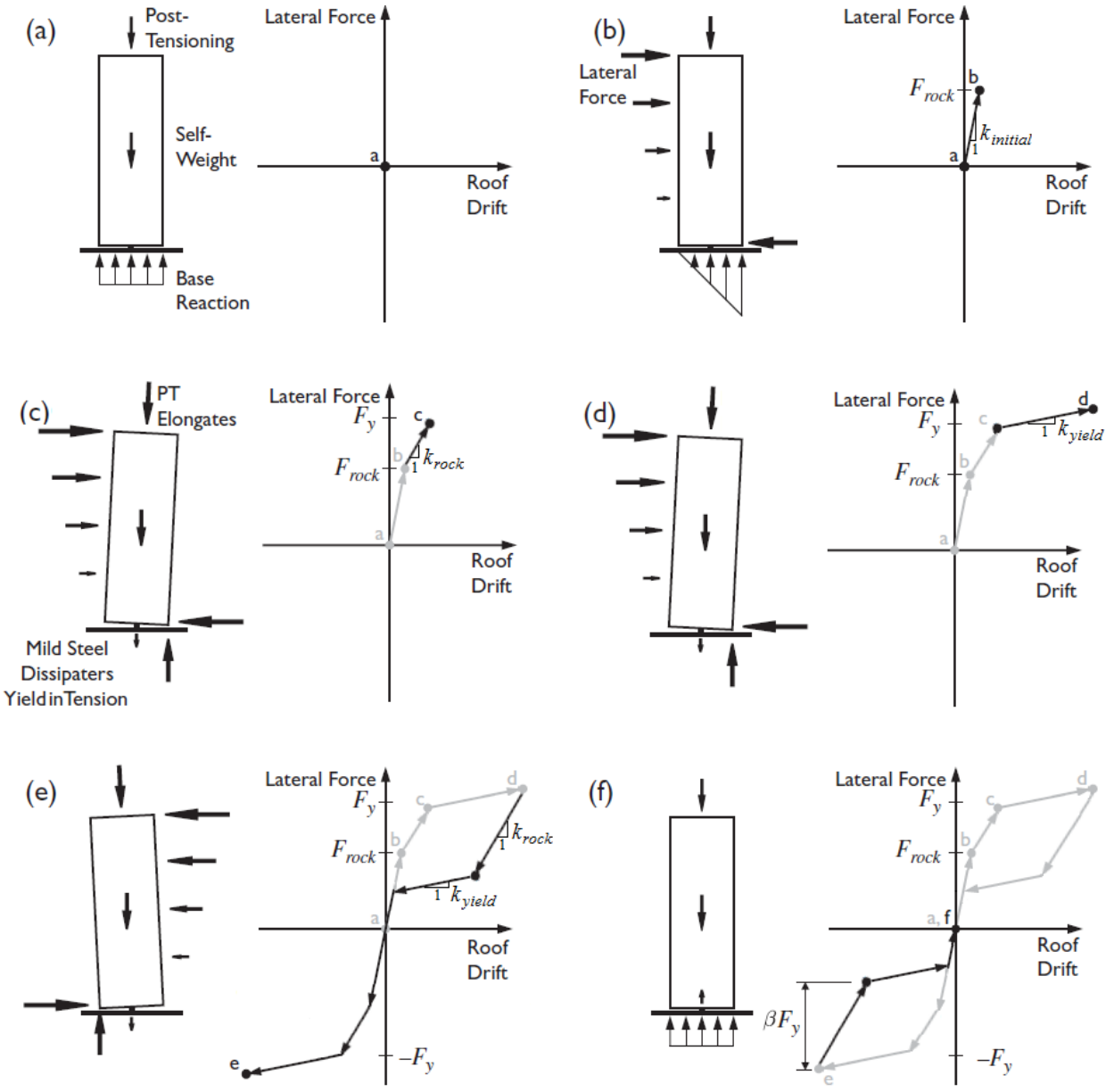

Figure 2.4 Push-pull response of base-rocking system: (a) at rest; (b) incipient rocking; (c) yield of mild steel energy dissipaters; (d) applied lateral load greater than yield load; (e) applied lateral load greater than yield load in reverse direction; (f) lateral load removed (adapted from Wiebe and Christopoulos, 2009).

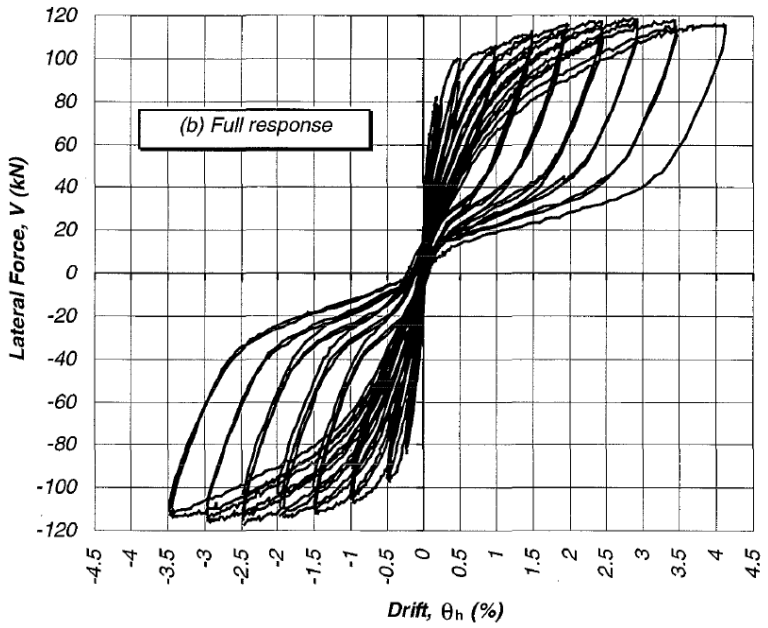

Figure 2.5 Rocking wall experimental lateral force-drift ratio response (Unit 3 tested by Rahman and Restrepo (2000))

At rest (step a), the wall in Figure 2.4 is in axial equilibrium with the base reaction counteracting the total axial load in the wall, which consists of post-tensioning force, self-weight and any additional gravity load. Upon initial loading, the wall resists lateral loads similar to an RC wall until the clamping force (total axial load) is overcome and rocking begins (step b) (Wiebe and Christopoulos, 2009). Rocking occurs because the wall is not monolithically connected to the foundation and all the reinforcement passing the wall/foundation interface is unbonded.

When rocking begins, the initial stiffness of the wall $k_{initial}$ reduces to an elastic post-rocking stiffness k_{rock} due to the opening of a gap at the rocking joint (step c). At this point, the post-tensioning tendons begin to elongate and the mild steel energy dissipaters begin resisting lateral forces elastically.

Once the dissipaters reach their yield capacity, the elastic post-rocking stiffness k_{rock} reduces to a post-yield stiffness k_{yield} (step d). At this stage, the post-tensioning tendons continue to elongate but remain elastic.

Upon load reversal, the energy dissipaters begin resisting lateral loads in compression. Since the dissipaters have been permanently deformed due to yielding in tension, they need to yield in compression in order for the joint cap to close (step e) (Wiebe and Christopoulos, 2009). Thus,

unloading occurs with the elastic post-rocking stiffness k_{rock} until yielding occurs in compression. Once the dissipaters yield in compression, the stiffness reduces to the post-yield stiffness k_{yield} until the joint gap closes (Wiebe and Christopoulos, 2009).

Since the energy dissipaters have yielded in compression, they exert an upward force upon the wall that reduces the load at which rocking begins. However, during loading in the opposite direction, the upward force must be overcome to yield the dissipaters in tension. Thus, the overall yield force of the system remains unchanged, which creates a symmetrical hysteretic behavior for loading in the opposite direction. Once applied load is removed, the wall returns back to the original position, resulting in zero residual displacements (step f) (Wiebe and Christopoulos, 2009).

The energy dissipated by the hysteretic response described above is quantified by an energy dissipation coefficient beta β (Figure 2.4f). A β of zero corresponds to the absence of energy dissipation (i.e. mild steel reinforcement), and a β of one corresponds to the maximum amount of energy dissipation while still ensuring re-centering.

The re-centering capabilities described above, which significantly reduce residual displacements, represent the main benefit of using rocking walls over RC walls. A more detailed list of benefits associated with rocking walls is presented in Table 2.1. Despite these benefits, rocking walls have been shown to attract higher floor accelerations relative to RC walls (Rodriguez *et al.*, 2002; Wiebe, 2008), which is attributed to sharp changes in stiffness during rocking (Wiebe and Christopoulos, 2010). This can be concerning for the performance of acceleration-sensitive non-structural elements. The present study addresses this concern by comparing the floor acceleration response of RC and rocking wall systems through a dynamic non-linear time-history analysis of case study buildings.

In addition, as Qureshi and Warnitchai (2016) note, both horizontal and vertical acceleration spikes have been observed in the seismic response of rocking walls during dynamic experimental tests (Toranzo, 2002; Marriott *et al.*, 2008; Schoettler *et al.*, 2009; Belleri *et al.*, 2014). These acceleration spikes are attributed to the high-velocity impact between a rocking wall and its foundation during rocking (Qureshi and Warnitchai, 2016). As reasonable to expect, this might negatively affect the performance of non-structural elements. However, this issue is not addressed in the present study and remains an area of future study.

Table 2.1 Comparison between RC and rocking wall systems (adapted from Holden et al., 2003)

System property	RC Walls	Rocking Walls
Energy dissipation capacity	Excellent	Good
Special reinforcing detailing	In potential plastic hinge zones. Congested cages to confine the concrete, prevent longitudinal reinforcing from buckling, and to prevent shear failure.	Only required at wall ends and foundation beam where rocking takes place.
Dimensional limitations	To prevent plastic hinge instability	Minimum—based on elastic theory as wall panels remain essentially crack-free
Minimum reinforcement requirements	Can significantly increase the moment capacity at the critical region. This could result in larger foundations as a result of capacity design	Temperature and shrinkage can be substituted with fiber reinforced concrete
Expected postearthquake repair work	In plastic hinge zones repair work can vary from epoxy injection of 1 mm wide cracks or less, to concrete replacement. Longitudinal bars could buckle and fracture requiring demolition. Permanent deformations.	None expected. Self-centering, permanent deflections are not expected.
Initial cost	Competitive—widely used systems	Competitive? Requires cost analysis.
Life-cycle cost	Competitive relative to other conventional systems. May require postearthquake repair, or following a severe earthquake demolition and rebuilding may be necessary.	Expected to be very competitive. No postearthquake repairs needed.

3 SEISMIC DEMANDS ON NON-STRUCTURAL ELEMENTS

Non-structural elements (NSEs) are components of buildings that are not part of the main structural system. These elements can be broadly categorized into three groups according to FEMA (2012):

- Architectural elements: partitions, ceilings, storefronts, glazing, cladding, veneers, chimney, fences, architectural ornamentation, etc.
- Mechanical, electrical and plumbing (MEP) elements: pumps, chillers, fans, air handling units, motor control centers, distribution panels, transformers, etc.
- Building contents: shelving and bookcases, industrial storage racks, retail merchandise, books, medical records, computers and desktop equipment, etc.

However, in terms of seismic design, NSEs can be separated into two main groups: drift-sensitive and acceleration-sensitive elements (Taghavi and Miranda, 2003; FEMA, 2012; Welch, 2016). Drifts are typically dealt with by stiffening the supporting building, and proper detailing of non-structural elements. However, structures tend to attract higher accelerations when stiffened, which can be limited somewhat by inelastic structural response (Sullivan *et al.*, 2013).

In general, acceleration-sensitive NSEs have proven to be more vulnerable over the course of past earthquakes (Miranda and Taghavi, 2005). In addition, numerous researches have questioned the reliability of current code provisions for this class of NSEs (Uma *et al.*, 2010; Sullivan *et al.*, 2013; Pinkawa *et al.*, 2014; Welch, 2016; among others). For these reasons, the present study focuses on acceleration-sensitive NSEs, and more specifically, how to estimate acceleration demands for this type of NSEs.

3.1 Floor Response Spectra for the Seismic Design of Non-structural Elements

In the last half century, much effort has been devoted to developing rational methods for conducting seismic analysis of NSEs. In the vast majority of practical design situations, decoupled analyses are conducted using a "cascading" approach. In this approach, it is assumed that NSEs

have minimal dynamic interaction with the supporting structure. In other words, the NSEs and the supporting structure are treated as uncoupled systems. In past research efforts, this assumption has been considered acceptable for NSEs with mass less than 1% of the total mass of the supporting structure (Singh and Ang, 1974; Sankaranarayanan, 2007; Taghavi and Miranda, 2008; Pinkawa *et al.,* 2014; Welch, 2016). However, some have suggested that interaction occurs closer to 0.1% of total mass of the supporting structure (Toro *et al.*, 1989). In the context of cascading approaches, one of the most popular methods is the Floor Response Spectrum (FRS) method (Figure 3.1). The structural response at the attachment level is considered as the input motion for the estimation of the response of the nonstructural component and used to construct the response spectra pertaining to the floor under consideration.

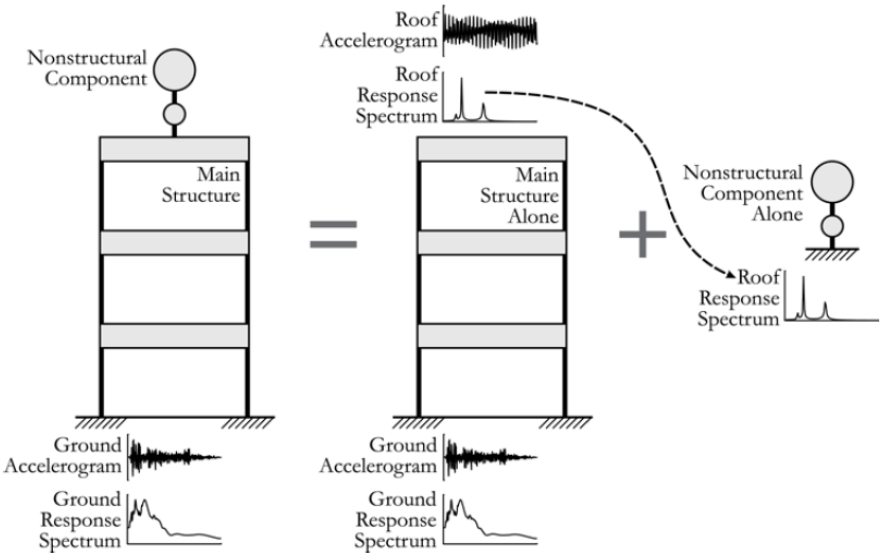

Figure 3.1 Illustration of floor response spectrum (FRS) method (Filiatrault and Sullivan, 2014)

An inherent assumption of the FRS method is that NSEs have a single point of attachment to the supporting building. As Welch (2016) and Villaverde (1997) noted, FRS methods are not suitable for NSEs with multiple points of attachment. For instance, each support or attachment can be subject to a different and out-of-phase motion, which cannot realistically be accounted for with an FRS method (Villaverde, 1997).

3.2 Novel Methods for Estimating Floor Response Spectra

One of the main objectives of the present study is to propose floor response spectra estimation procedures for RC and rocking wall buildings responding non-linearly. The proposed procedures

are based mainly on the work of Sullivan *et al.* (2013), Calvi and Sullivan (2014), and Welch (2016). Sullivan *et al.* (2013) proposed a new and simple methodology for estimating floor response spectra atop linear and non-linear single-degree-of-freedom (SDOF) structures. Then, Calvi and Sullivan (2014) extended this work to linear multi-degree-of-freedom (MDOF) structures. Most recently, Welch (2016) adapted the methodology of Calvi and Sullivan (2014) to MDOF systems responding in the non-linear range. A summary of each of these studies is presented below.

Note that numerous other procedures, not discussed here for brevity, have been proposed for the estimation of floor spectra. For a broader look into the current state-of-the-art in the estimation of floor spectra, refer to Welch (2016) who has an excellent literature review on the topic.

3.2.1 Sullivan et al. (2013) for Single-Degree-of-Freedom Systems

Sullivan *et al.* (2013) proposed a new methodology for generating floor spectra atop SDOF systems that is based on a dynamic amplification of peak floor acceleration (PFA). For a SDOF structure that has been designed for a given lateral load, the PFA can be determined by dividing the design base shear by the total mass of the structure.

To obtain the floor response spectrum, the PFA is then scaled by empirical dynamic amplification factors, which are dependent on the elastic damping of the supported element. The following empirical equations summarize the procedure:

$$a_m(T) = \begin{cases} \dfrac{T}{T_p}\left[a_{max}(DAF_{max} - 1)\right] + a_{max} & for\ T < T_p \\ a_{max} DAF_{max} & for\ T_p \leq T \leq T_e \\ a_{max} DAF & for\ T > T_e \end{cases} \tag{3.1}$$

where T is the spectral period of interest (i.e. the period of the non-structural element), and $a_m(T)$ is the spectral floor acceleration value at period T (i.e. the acceleration of the non-structural element). The term a_{max} is the PFA, and T_p is the elastic period of the primary/supporting structure. The term T_e is the effective period of the supporting structure, which is computed using a secant stiffness at design displacement. The term DAF is the dynamic amplification factor given by Equation (3.2) and DAF_{max} is the maximum dynamic amplification factor given by Equation (3.3),

which is expected to occur when the non-structural element is in resonance with the supporting structure.

$$DAF = \frac{1}{\sqrt{\left(1 - \frac{T}{T_e}\right)^2 + \xi_{NS}}} \tag{3.2}$$

$$DAF_{max} = \frac{1}{\sqrt{\xi_{NS}}} \tag{3.3}$$

where ξ_{NS} is the elastic damping of the non-structural/supported element. Note that T_e is equal to T_p if the supporting structure is responding linearly.

Both amplification factors (which are based on principles of structural dynamics) were empirically derived and successfully validated with the results of non-linear time history analyses of SDOF systems subject to a large suite of ground motions.

Figure 3.2 presents an illustration of the procedure proposed by Sullivan *et al.* (2013). Notably, maximum dynamic amplification extends from the elastic period to the effective period of the supporting structure. This was proposed by Sullivan *et al.* (2013) to take into account non-linear structural response. When a supporting structure goes through inelastic deformation, it no longer has a unique natural period of vibration. Thus, peak spectral response (i.e. resonance) occurs over a range of periods bounded by the elastic and effective periods of the supporting structure.

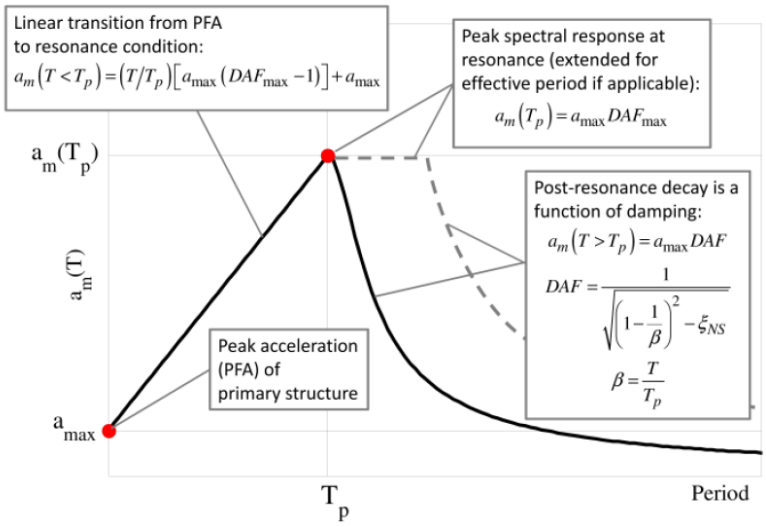

Figure 3.2 Procedure for estimating floor spectra atop SDOF systems by Sullivan et al. (2013) (Welch, 2016)

3.2.2 Calvi and Sullivan (2014) for Linear Multiple-Degree-of-Freedom Systems

The work of Calvi and Sullivan (2014) extended the methodology developed for SDOF systems by Sullivan *et al.* (2013) to MDOF systems responding in the elastic range. This was achieved by adapting the approach summarized in the previous sub-section for use with a traditional modal analysis of the supporting structure (Chopra, 2001). In this context, each of the modes is treated as an equivalent SDOF system that can be dealt with as discussed above. Thus, floor response spectra can be constructed for each mode at all floors of a structure. The effects of the individual modal floor spectra are then combined using modal superposition to generate a floor response spectrum that accounts for the effects of multiple modes.

The first step that this methodology involves is the performance of an Eigen-value analysis and the consequent calculation of periods of vibration and mode shapes (Figure 3.3a). Once the periods and mode shapes are known, a traditional modal response spectrum method is employed to determine the PFA contributions from each mode (Figure 3.3b&c) (Chopra, 2001). Mathematically, the contributions are determined by:

$$a_{max,j,i} = \frac{\phi_{j,i}}{\sum \phi_{j,i} m_j} m_{e,i} S_{a,i} \tag{3.4}$$

where $a_{max,j,i}$ is the floor acceleration at degree-of-freedom (i.e. floor level) j from mode i, $\phi_{j,i}$ is the mode shape for level j and mode i, m_j is the seismic mass at level j, and $m_{e,i}$ is the effective

modal mass for mode *i*. The term $S_{a,i}$ is the spectral acceleration value for mode *i* obtained from the design ground response spectrum.

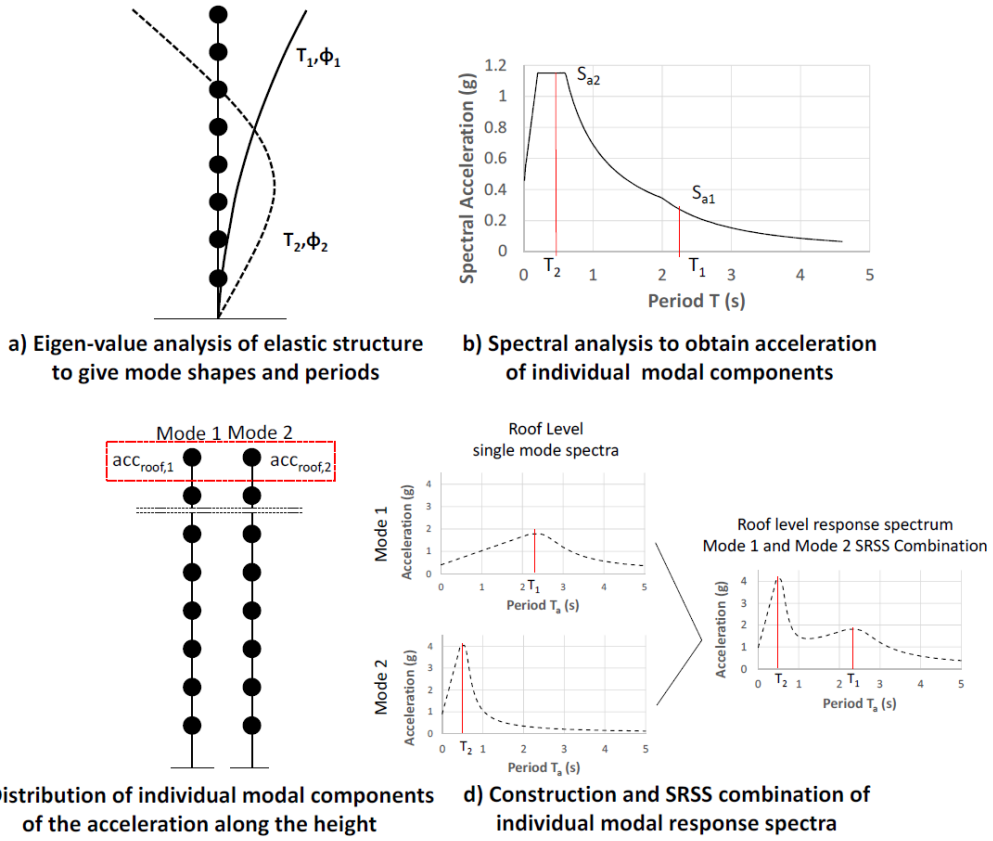

Figure 3.3 Illustration of floor spectra construction procedure for upper stories of elastic MDOF systems (Calvi and Sullivan, 2014)

Once the modal PFA contributions are determined, floor spectra can be obtained for each of the modes by using the procedure for SDOF systems outlined by Sullivan *et al.* (2013) (Section 3.2.1). At this time, the floor response spectra for upper levels are obtained by combining each of the modal floor spectra using an established modal combination rule such as square-root-of-sum-of-squares (SRSS) (Figure 3.3d).

For the lower levels, floor spectra are obtained as a curve that envelopes the floor spectra obtained using the modal combination method discussed above and the design ground response spectrum. This was proposed as a means to capture the limited higher mode filtering of the ground motion (rigid mode response) that is expected in the lower levels.

Calvi and Sullivan (2014) also proposed an adjustment to the maximum dynamic amplification factor (DAF_{max}) formulation. It was pointed out that stiff structures tend to provide little filtering

of ground motions, which was also observed by Menon and Magenes (2008) amongst others. Thus, the DAF_{max} formulation proposed by Sullivan *et al.* (2013) would overestimate the dynamic amplification of peak floor accelerations in stiff structures. To account for this phenomenon, Equation (3.5) was proposed in which the DAF_{max} is reduced for supporting structures with natural periods below $T_B = 0.3$ sec.

$$DAF_{max} = \begin{cases} \dfrac{1}{\left(1.79 - \dfrac{T_i}{T_B}\right)\sqrt{\xi_{NS}}} & if\ 0 \le T_i \le T_B \\ \dfrac{1}{\sqrt{\xi_{NS}}} & if\ T_i \ge T_B \end{cases} \tag{3.5}$$

where T_i is the elastic period of the primary structure for mode i.

3.2.3 Welch (2016) for Non-Linear Multiple-Degree-of-Freedom Systems

By building upon the works of Sullivan *et al.* (2013) and Calvi and Sullivan (2014), Welch (2016) developed a procedure to estimate floor spectra in non-linear MDOF buildings. For a supporting building responding non-linearly, floor spectra are generated by reducing elastic modal floor response spectra with empirical modal reduction factors that are dependent on the ductility of the supporting structure. Then, the reduced modal floor response spectra are combined using an established modal combination rule to obtain floor response spectra that account for the effects of multiple modes.

Since the procedure is empirical, Welch (2016) focused on two structural systems: steel moment resisting frames (MRF) and RC cantilever walls, of which only the latter is discussed here. In addition, two separate procedures were proposed by Welch (2016): a simplified procedure and an explicit procedure. The latter was not adopted in this study and, thus, not discussed here.

To develop the simplified procedure, Welch (2016) ran time history analyses of case-study structures responding both linearly and non-linearly under a large suite of ground motion records. Empirical modal reduction factors were then obtained on a record-by-record basis. A modal reduction factor is the ratio of spectral floor acceleration (SFA) from linear response to that of the corresponding non-linear response (Equation (3.6)).

$$R_{i,Single\ Record} = \frac{SFA(T_i)_L}{SFA(T_i)_{NL}} \tag{3.6}$$

where $SFA(T_i)$ is the spectral floor acceleration at the period of mode i. The subscripts L and NL represent the linear and non-linear response cases, respectively.

Once the reduction factors for each acceleration record were obtained, a non-linear regression was performed in the form of Equation (3.7).

$$R_i = \mu^{\alpha_i} \tag{3.7}$$

where R_i is the reduction factor for mode i, μ is the estimated ductility demand of the supporting structural system, and α_i is the exponent governing the rate of reduction in mode i.

Figure 3.4 presents a visual representation of how the regression analysis was conducted.

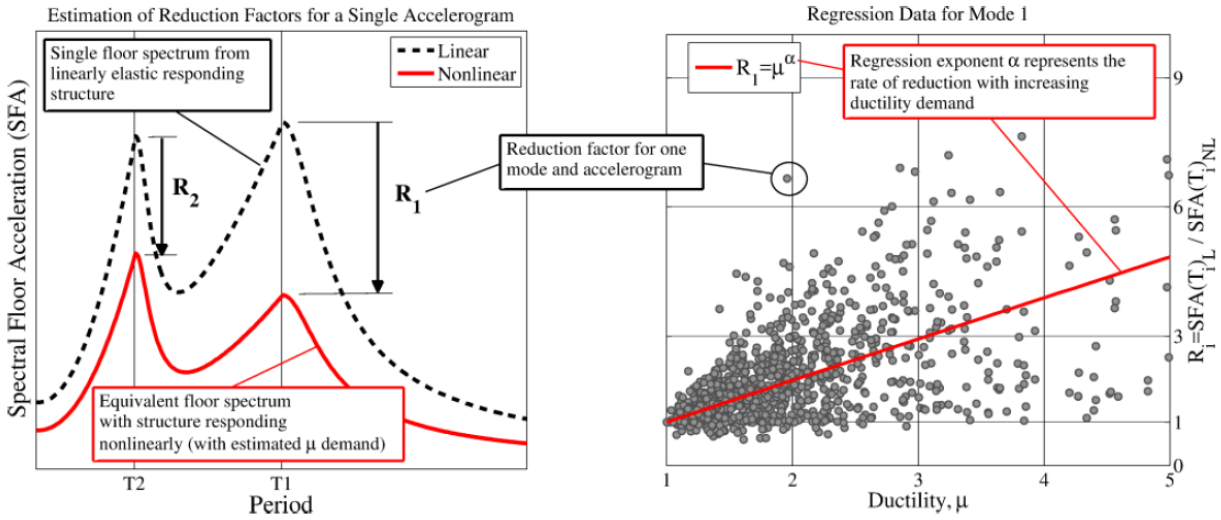

Figure 3.4 Illustration of modal reduction factors for individual accelerograms (left) and example of regression model used (right) (Welch, 2016)

The regression was conducted using only roof level floor spectra, and independent of non-structural damping ratio. Thus, the reduction factors for each of the non-structural damping ratios considered (ξ_{NS} = 0.5%, 2%, 5% and 10%) were collectively used for the regression. The analysis was conducted within a ductility range of 1.0 to 5.0, and any data point outside of this range was omitted.

The raw data was also adjusted during the regression analysis to allow for better tracking of how increasing ductility demands affect acceleration peaks. Accordingly, the reduction factor for each

accelerogram was normalized by the reduction factor at an intensity level resulting in a ductility close to 1.0 (in the range of 0.9 to 1.1). This means that for all accelerograms, a ductility of 1.0 corresponds to a reduction factor of 1.0. Table 3.1 presents the modal reduction factors obtained from the regression analysis.

Table 3.1 Generalized values of modal reduction factors from record-by-record regression for RC walls conducted by Welch (2016)

Structural System	Mode 1	Mode 2	Mode 3
	α_1	α_2	α_3
RC Walls	1.25	0.4	0.2
Modal reduction factor taken as $R_i = \mu^{\alpha}$			

To account for period elongation, Welch (2016) proposed Equations (3.8) and (3.9) to define the effective periods of modes 1 and 2 respectively. Mode 3 was assumed to have negligible period elongation.

$$T_{1,e} = T_1 \sqrt{\frac{\mu}{[1 + r(\mu - 1)]}} \tag{3.8}$$

where $T_{1,e}$ is the effective first mode period, T_1 is the elastic first mode period, and r is the global strain hardening factor.

$$T_{2,e} = \begin{cases} T_2 & for \quad \mu \leq 1.0 \\ T_2\left(1 + 0.5\left(\frac{\mu}{\mu_{pin}}\right)\right) & for \; 1.0 < \mu < \mu_{pin} \\ 1.5T_2 & for \quad \mu \geq \mu_{pin} \end{cases} \tag{3.9}$$

where $T_{2,e}$ is the effective second mode period, and T_1 is the elastic second mode period. The term μ_{pin} is the ductility limit corresponding to the pinned behavior of higher modes. Hence, when ductility reaches this limit, the RC wall is considered fully-pinned.

Welch (2016) also updated the dynamic amplification factor formulation. It was observed that damping of the supporting structure had an impact on dynamic amplification factor, albeit to a

smaller extent compared to non-structural damping. The revised formulations for DAF_{max} and DAF are given by Equations (3.10) and (3.11).

$$DAF_{max} = \begin{cases} \left(0.55 + 0.45\frac{T_i}{T_B}\right)(0.5\xi_p + \xi_{NS})^{-0.667} & if\ T_i \le T_B \\ (0.5\xi_p + \xi_{NS})^{-0.667} & if\ T_i \ge T_B \end{cases} \tag{3.10}$$

$$DAF = \begin{cases} \left(0.55 + 0.45\frac{T_i}{T_B}\right)\left[\left(1 - \frac{T}{T_{i,e}}\right)^2 + \left(0.5\xi_p + \xi_{NS}\right)\right]^{-0.667} & if\ T_i \le T_B \\ \left[\left(1 - \frac{T}{T_{i,e}}\right)^2 + \left(0.5\xi_p + \xi_{NS}\right)\right]^{-0.667} & if\ T_i \ge T_B \end{cases} \tag{3.11}$$

where T is the spectral period of interest, T_i is the elastic period of the supporting structure for mode i, $T_{i,e}$ is the effective period of the supporting structure for mode i, ξ_p is the elastic damping of the primary structure, and ξ_{NS} is the elastic damping of the non-structural element. The term T_B is taken as 0.3 sec.

Based on the findings summarized above, Welch proposed the following simplified procedure to estimate floor response spectra.

Step 1: Define the primary (ξ_p) and non-structural (ξ_{NS}) damping ratios

Welch (2016) proposed a primary damping ratio of 5% for RC walls. Even though the procedure can be applied to any non-structural damping ratio, a value of 2% was proposed if the damping of a non-structural element is not known.

Step 2: Define the input acceleration spectrum, $S_a(T,\xi_p)$

The input acceleration spectrum is the design ground response spectrum. It can also be taken as the median or mean spectrum of a target record set. At this point, T_B is also estimated as the initiation of the constant acceleration range of the input spectrum. Note that the input acceleration spectrum is defined at the primary damping ratio ξ_p.

Step 3: Perform modal analysis for the number of modes considered

For a given mode i, the following parameters need to be obtained: the fundamental period (T_i), mode shape (ϕ_i), and modal participation factor (Γ_i). Welch (2016) found that considering the first three modes was sufficient to generate reliable floor spectra estimates.

Step 4: Ductility demand, modal reduction factors and effective periods

The ductility demand (μ) needs to be estimated at the intensity of interest. The modal reduction factors can then be obtained based on Table 3.1.

The effective periods for modes 1 and 2 can be obtained using Equations (3.8) and (3.9), respectively. For modes 3 and higher, the effective period can be considered equal to the elastic period.

Step 5: Estimate modal floor accelerations, modal contributions and SRSS estimates

The modal floor acceleration $a_{max,j,i}$ for a given mode i at a floor level j is given by:

$$a_{max,j,i} = \phi_{j,i}\Gamma_i\left(\frac{S_a(T_i,\xi_p)}{R_i}\right); \quad R_i \geq 1 \tag{3.12}$$

where the elastic spectral acceleration demand $S_a(T_i,\xi_p)$ is reduced by the modal reduction factor R_i to account for non-linear demands.

The individual modal contributions $a_{m,j,i}(T)$ to the floor response spectrum are given by:

$$a_{m,j,i}(T) = \begin{cases} \left(\frac{T}{T_i}\right)^2 \left[a_{max,j,i}(DAF_{max} - 1)\right] + a_{max,j,i} & for\ T < T_i \\ a_{max,j,i}DAF_{max} & for\ T_i \leq T \leq T_{i,e} \\ a_{max}DAF & for\ T > T_{i,e} \end{cases} \tag{3.13}$$

where T is the spectral period of interest. DAF_{max} and DAF are estimated using Equations (3.10) and (3.11).

The SRSS spectral floor response at a given period T is estimated as:

$$SFA_j(T)_{SRSS} = \sqrt{\sum_{i=1}^{nm}[a_{m,j,i}(T)]^2} \tag{3.14}$$

where nm is the number of modes being considered.

Step 6: Account for rigid mode response

The final spectral floor acceleration $SFA_j(T)$ is given by Equation (3.15) which takes into account rigid mode response observed in the lower levels of RC wall buildings.

$$SFA_j(T) = \begin{cases} \max\left(SFA_j(T)_{SRSS}, S_a(T,\xi_{NS})\right) & for\ \frac{H_j}{H_n} < 0.5 \\ SFA_j(T)_{SRSS} & for\ \frac{H_j}{H_n} \geq 0.5 \end{cases} \quad (3.15)$$

where H_j is the height of floor level j, and H_n is the height of the roof level. The term $S_a(T,\xi_{NS})$ is the spectral acceleration demand at period T obtained from the input acceleration spectrum at a damping level of ξ_{NS}. If the input acceleration spectrum is obtained for a typical damping ratio of 5%, then the spectrum can be adjusted by a damping modification factor given by:

$$\eta = \left(\frac{0.1}{0.05 + \xi_{NS}}\right)^{0.5} \quad (3.16)$$

3.3 Current Code Provisions

This section provides a brief summary of exemplary code provisions regarding non-structural elements (NSEs). Specifically, the United States, Europe and New Zealand code provisions are discussed. Particular attention is given to how each provision determines acceleration demands for NSEs.

3.3.1 United States (ASCE 7-10)

In the United States, the seismic design provisions for non-structural elements/components are set forth in ASCE 7-10 (ASCE, 2010). The horizontal seismic design force for a component is determined by:

$$F_p = \frac{0.4 S_{DS} a_p W_p}{\frac{R_p}{I_p}}\left(1 + 2\frac{z}{h}\right) \quad (3.17)$$

where $0.4S_{DS}$ is the design peak ground acceleration (PGA), W_p is the weight of the component, z is the height of component attachment, and h is the average roof height of the supporting structure. The term a_p is the component amplification factor, which varies from 1.00 to 2.50. The term I_p is

the component importance factor, which varies from 1.00 to 1.50. The term R_p is the component response modification factor, which varies from 1.00 to 12.00.

The horizontal seismic design force shall not be taken less than the following limit:

$$F_p = 0.3 S_{DS} I_p W_p \tag{3.18}$$

In addition, the horizontal seismic design force need not be taken greater than the following limit:

$$F_p = 1.6 S_{DS} I_p W_p \tag{3.19}$$

NSEs are also designed for a concurrent vertical seismic design force given by:

$$F_p = \pm 0.2 S_{DS} W_p \tag{3.20}$$

The component amplification (a_p) and response reduction (R_p) factors are outlined in tables (not reproduced here for brevity) for specific NSEs. For instance, for laboratory equipment, $a_p = 1.00$ and $R_p = 2.50$, while for signs and billboards, $a_p = 2.50$ and $R_p = 3.00$. Using a lower value of a_p, other than the ones provided in the tables, is not permitted unless justified by a detailed dynamic analysis. Even so, a_p is not permitted to be taken less than 1.0.

In addition, ASCE 7-10 makes a distinction between rigid or rigidly attached, and flexible or flexibly attached components. A rigid component is defined as a NSE with fundamental period of 0.06 sec or less, while a flexible components is defined as a NSE with fundamental periods higher than 0.06 sec. For rigid component, a_p is 1.0 and for flexible components, a_p is 2.5.

Lastly, the component importance factor (I_p) is one of two values and assigned based on the criteria in Table 3.2.

Table 3.2 Non-structural element/component importance factors for ASCE 7-10 (ASCE, 2010)

Conditions	Importance Factor, I_p
• The component is required to function for life-safety purposes after an earthquake, including fire protection sprinkler systems and egress stairways. • The component conveys, supports, or otherwise contains toxic, highly toxic, or explosive substances where the quantity of the material exceeds a threshold quantity established by the authority having jurisdiction and is sufficient to pose a threat to the public if released. • The component is in or attached to a Risk Category IV (essential facilities; refer to ASCE (2010)) structure and it is needed for continued operation of the facility or its failure could impair the continued operation of the facility. • The component conveys, supports, or otherwise contains hazardous substances and is attached to a structure or portion thereof classified by the authority having jurisdiction as a hazardous occupancy.	1.5
• All other conditions	1.0

3.3.2 Europe (Eurocode 8)

In Europe, the main seismic design provisions for NSEs are set forth in Eurocode 8 (CEN, 2004). The horizontal seismic force on a NSE is given by:

$$F_a = \frac{S_a W_a \gamma_a}{q_a} \tag{3.21}$$

where W_a is the weight of the element, γ_a is the importance factor of the element, q_a is the behavior factor of the element, and S_a is the seismic coefficient applicable to NSEs, which is given by:

$$S_a = \alpha S \left[\frac{3\left(1 + \frac{z}{H}\right)}{1 + \left(1 - \frac{T_a}{T_1}\right)^2} - 0.5 \right] \geq \alpha S \tag{3.22}$$

where α is the design PGA on Soil Type A (rock) in terms of acceleration of gravity (g), S is the site soil factor, T_a is the fundamental period of the NSE, T_1 is the fundamental period of the supporting building, z is the height from the base of the supporting building to the NSE attachment, and H is the height of the supporting building.

The importance factor of the element (γ_a) is one of two values and assigned based on the criteria in Table 3.3. The behavior factor of the element (q_a) is assigned based on the criteria in Table 3.4

Table 3.3 Non-structural element importance factors for Eurocode 8 (CEN, 2004)

Type of Non-structural Element	Importance Factor, γ_a
• Anchorage elements of machinery and equipment required for life safety systems. • Tanks and vessels containing toxic or explosive substances considered to be hazardous to the safety of the general public	≥1.5
• All others.	1.0

Table 3.4 Non-structural element behavior factors for Eurocode 8 (CEN, 2004)

Type of Non-structural Element	Behavior Factor, q_a
• Cantilevering parapets or ornamentations • Signs and billboards • Chimneys, masts and tanks on legs acting as unbraced cantilevers along more than one half of their total height	1.0
• Exterior and interior walls • Partitions and facades • Chimneys, masts and tanks on legs acting as unbraced cantilevers along less than one half of their total height, or braced or guyed to the structure at or above their center of mass • Anchorage elements for permanent cabinets and book stacks supported by the floor • Anchorage elements for false (suspended) ceilings and light fixtures	2.0

3.3.3 New Zealand (NZS 1170.5)

In New Zealand, the seismic design provisions for non-structural elements/parts are set forth in NZS 1170.5 (NZS, 2004). The horizontal seismic force on a NSE is given by:

$$F_{ph} = C_p(T_p)C_{ph}R_pW_p \leq 3.6W_p \tag{3.23}$$

where $C_p(T_p)$ is the horizontal design coefficient for the part, C_{ph} is the horizontal response factor for the part, R_p is the risk factor for the part, and W_p is the weight of the part.

For parts that are sensitive to vertical acceleration, the vertical seismic force on a NSE is given by:

$$F_{pv} = C_{pv}C_{vd}R_pW_p \leq 2.5W_p \tag{3.24}$$

where C_{pv} is the vertical response factor for the part, and C_{vd} is the elastic site vertical design response spectrum value at the supporting structure's period adjusted by a structural performance factor.

The horizontal design coefficient ($C_p(T_p)$) is determined by:

$$C_p(T_p) = C(0)C_{Hi}C_i(T_p) \tag{3.25}$$

where $C(0)$ is the elastic site design response spectrum value for T = 0, C_{Hi} is the floor height coefficient for the level i supporting the part given by Equation (3.26), T_p is the period of the part, and $C_i(T_p)$ is the spectral shape factor for the part at level i given by Equation (3.27).

$$C_{Hi} = \begin{cases} 1 + \dfrac{h_i}{6}, & for\ all\ h_i < 12\ m \\ 1 + 10\dfrac{h_i}{h_n}, & for \quad h_i < 0.2h_n \\ 3.0, & for \quad h_i < 0.2h_n \end{cases} \tag{3.26}$$

where h_i is the period of the part,

$$C_i(T_p) = \begin{cases} 2.0, & for \quad T_p < 0.75\ sec \\ 2(1.75 - T_p), & for\ 0.75 < T_p < 1.5\ sec \\ 0.5, & for \quad T_p \geq 1.50\ sec \end{cases} \tag{3.27}$$

The horizontal (C_{ph}) and vertical (C_{pv}) response factors are determined based on the ductility expected in the part (Table 3.5). The risk factor for the part is determined based on

Table 3.6.

Table 3.5 Non-structural element/part response factors for NZS 1170.5 (NZS, 2004)

Ductility of the Part, μ_p	Horizontal (C_{ph}) and Vertical (C_{pv}) Response Factors
1.00	1.00
1.25	0.85
2.00	0.55
3.00 or greater	0.45

Table 3.6 Non-structural element/part risk factors for NZS 1170.5 (NZS, 2004)

Category	Criteria	Part Risk Factor, R_p
P.1	Part representing a hazard to life outside the structure [1]	1.0
P.2	Part representing a hazard to a crowd of greater than 100 people within the structure [1]	1.0
P.3	Part representing a hazard to individual life within the structure [1]	0.9
P.4	Part necessary for the continuing function of the evacuation and life safety systems within the structure	1.0
P.5	Part required for operational continuity of the structure [2]	1.0
P.6	Part for which the consequential damage caused by its failure are disproportionately great	2.0
P.7	All other parts	1.0

Notes:

1. To be considered in this category, the part must weigh more than 10 kg, and be able to fall more than 3 meters onto a publicly accessible area.
2. Only parts essential to the operational continuity of structures with importance level 4 (refer to NZS, 2004) will be classified as P.5. Non-essential parts and parts within structures of other importance levels will be otherwise classified.

3.3.4 Summary

All three code provisions have distinct procedures for establishing acceleration demands on NSEs. ASCE 7-10 takes into account the variability in acceleration demands in NSEs depending on their location within the supporting building. However, it does not account for the NSE's natural period and how it relates to the structure's natural periods (i.e. resonance condition) with the exception of broadly defining elements as either rigid or flexible.

In comparison, Eurocode 8 takes into account the fundamental natural period of NSEs with respect to the fundamental period of the supporting building. NZS 1170.5 also accounts for the natural period of the NSE but does not establish a relationship between the natural period of the NSE and the supporting building. Similar to ASCE 7-10, both NZS 1170.5 and Eurocode 8 consider the variability in acceleration demands in NSEs depending on their location within the supporting building.

The weaknesses in current code provisions have been thoroughly discussed in past research efforts (Uma *et al.*, 2010; Sullivan *et al.*, 2013; Pinkawa *et al.*, 2014; Welch, 2016; among others). Welch (2016) listed some of the important concerns regarding the code provisions, which include:

- Overestimating peak floor acceleration demands while underestimating the dynamic amplification of flexible NSEs.
- Neglecting the modal properties of the supporting building.
- Not accounting for differences in damping of the NSE and the supporting building.
- Not accounting for non-linear demands in the supporting building.

4 DISPLACEMENT-BASED DESIGN AND DYNAMIC TIME HISTORY ANALYSIS OF CASE STUDY BUILDINGS

This chapter details the design and time history analysis (THA) of the six case study buildings considered in this study. The structures were designed through a displacement-based design procedure with seismic loads from ASCE 7-10 (ASCE, 2010). Both linear and non-linear time history analyses were conducted using a lumped-plasticity modelling approach in RUAUMOKO2D (Carr, 2004).

4.1 Case-study Buildings

The structures considered for this study were 4, 8 and 12 story buildings. A general layout of the buildings is presented in Figure 4.1. The lateral load resisting systems consisted of either RC or rocking structural walls, while the gravity load resisting system consisted of columns. The columns were assumed to provide negligible lateral load resistance. In addition, the lateral and gravity load resisting systems were assumed to be uncoupled. Hence, the only gravity load the structural walls carry is self-weight.

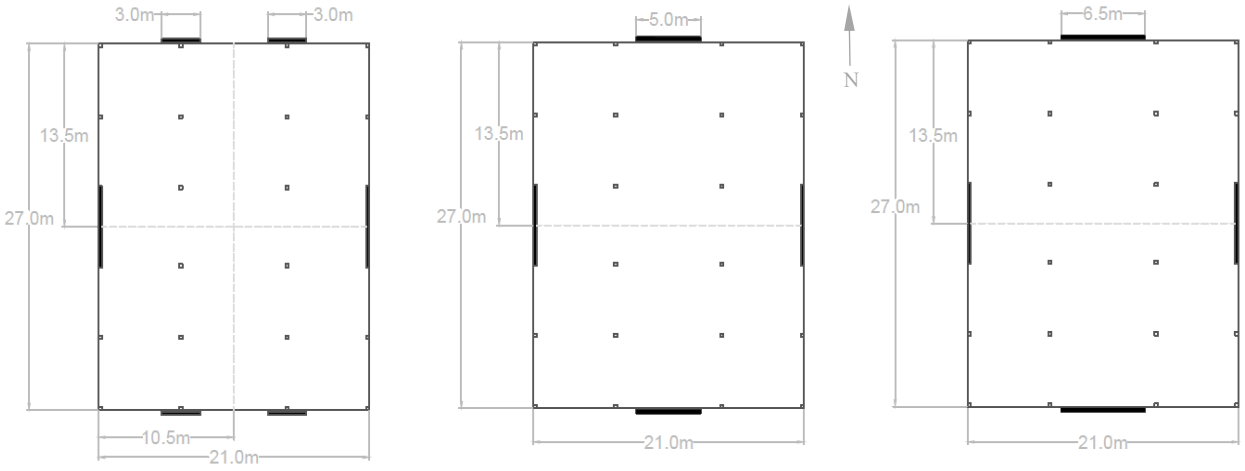

Figure 4.1 General layout of case study buildings (4, 8 and 12 stories from left to right)

The buildings were assumed to have no torsional irregularity with diaphragms that are fully rigid in plane and fully flexible out of plane. Hence, the walls in each building were designed and

analyzed separately. The walls considered in this study are the walls in the East-West direction depicted in Figure 4.1. The characteristics and material properties of these walls are presented in Table 4.1 and Table 4.2, respectively.

The concrete for all structural members was assumed to be normal-weight concrete with a unit weight of 23.5kN/m^3. The seismic mass for each floor was calculated assuming the following building characteristics:

- 0.200 m thick concrete slab,
- 0.310 m x 0.310 m concrete columns,
- 6 m x 0.310 m concrete walls in the North-South direction,
- 0.310 m thick case study concrete walls in the East-West direction, and
- a superimposed dead load of 1.5kN/m^2.

Table 4.1 Characteristics of case study structural walls

	4 Story	**8 Story**	**12 Story**
Wall Length (m)	3.0	5.0	6.5
Wall Thickness (m)	0.310	0.310	0.310
Wall Aspect Ratio (-)	4.0	4.8	5.5
Inter-story Height (m)	3.0	3.0	3.0
Total Gravity Load (kN)	263	877	1709
Typical Floor Seismic Mass Per Wall (tons)	109	210	214
Roof Seismic Mass Per Wall (tons)	100	195	197

Table 4.2 Material properties of case study structural walls

Material	Specification	Property	RC Walls	Rocking Walls
Concrete	-	Compressive Strength, *f'c (MPa)*	35	35
		Modulus of Elasticity, E_c *(GPa)*	29.6	29.6
Longitudinal Reinforcement Steel	ASTM A706M Grade 420 (ASTM International, 2016a)	Yield Stress, f_y *(MPa)*	420	420
		Ultimate Stress, f_u *(MPa)*	550	550
		Modulus of Elasticity, E_s *(GPa)*	200	200
Mild Steel	ASTM A615M Grade 280 (ASTM International, 2016b)	Yield Stress, f_{my} *(MPa)*	-	280
		Ultimate Stress, f_{mu} *(MPa)*	-	420
		Modulus of Elasticity, E_s *(GPa)*	-	200
Post-tensioning Steel	ASTM A416M Grade 1860 (ASTM International, 2016c)	Yield Stress, f_{pty} *(MPa)*	-	1670
		Ultimate Stress, f_{ptu} *(MPa)*	-	1860
		Modulus of Elasticity, E_{pt} *(GPa)*	-	195

4.2 Design Loads

The seismic loads were calculated assuming the structures are located in San Francisco, CA with a site soil property of rock, which corresponds to Site Class B property in ASCE 7-10 (ASCE, 2010). A design response spectrum (Figure 4.2) was constructed based on the location and site conditions according to ASCE 7-10 (ASCE, 2010).

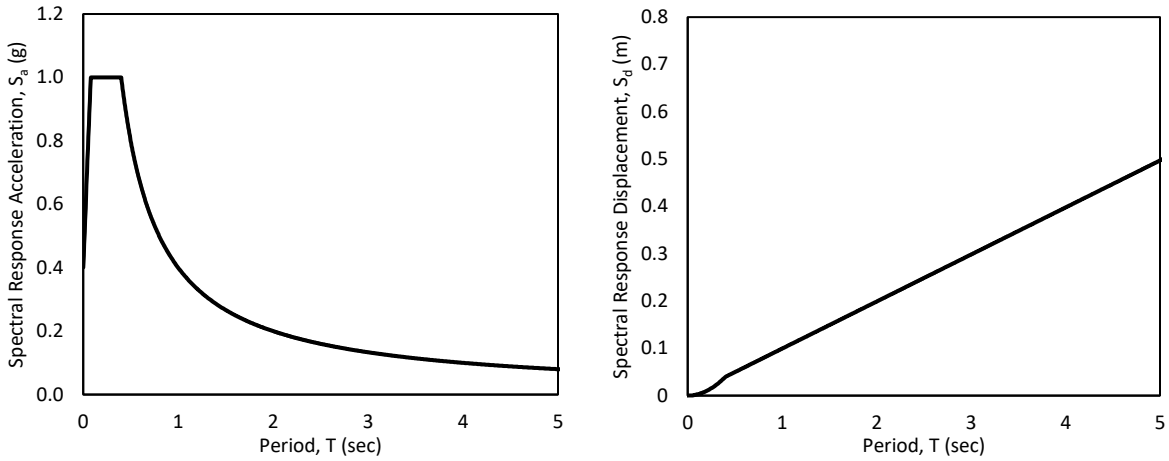

Figure 4.2 ASCE 7-10 design response spectrum

4.3 Direct Displacement-Based Design

Both the RC and rocking wall buildings were designed using a direct displacement based design (DDBD) approach. This approach was adopted because the more traditional force-based design (FBD) approach has been shown to have significant downsides for the design of precast and prestressed concrete buildings (Priestley, 1998; Conley *et al.*, 2002). In FBD, design loads are obtained using elastic structural properties, which are then reduced using reduction factors that are dependent on the ductility of the system, assuming monolithic concrete behavior (Conley *et al.*, 2002). However, energy dissipation characteristics and the concept of yielding (and therefore ductility) in precast systems are fundamentally different from monolithic concrete systems, which makes FBD procedures unable to capture the true behavior of precast systems (Priestley, 1996; Conley *et al.*, 2002; Priestley, 2002). In addition, Rahman and Sritharan (2006) showed that even if both FBD and DDBD approaches satisfied performance limits, a DDBD procedure could result in a lower design base shear, and thus a more economical design, for rocking wall systems in low-rise buildings (Pennucci *et al.*, 2009).

In DDBD, structures are designed for a target displacement selected as a function of a desired performance level. The structures are idealized as single-degree-of-freedom systems (SDOF) that achieve peak displacement at a given performance level. Since the SDOF systems are designed at peak displacement, effective system properties are used instead of elastic properties. Thus, the system is characterized by effective properties, namely a secant stiffness and an equivalent viscous damping. The equivalent damping accounts for elastic damping as well as the added hysteretic

damping resulting from inelastic deformation. A summary of the DDBD procedure adapted from Priestley *et al.* (2007) is provided in Sections 4.3.1 to 4.3.5. Figure 4.3 provides a visual summary of this procedure.

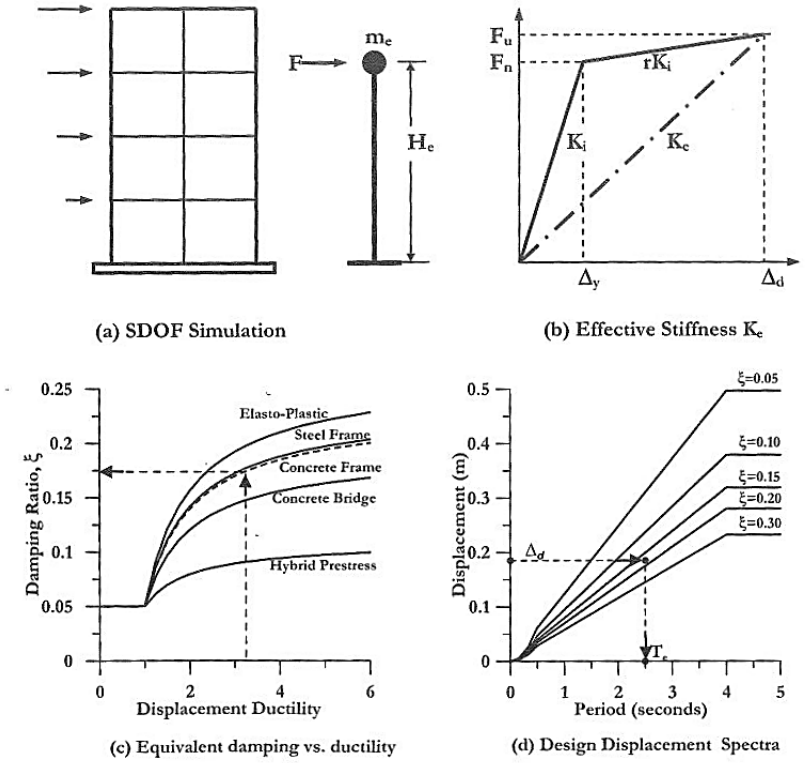

Figure 4.3 Direct displacement design of structures (Priestley et al., 2007).

4.3.1 Design Displacement

The first step of the design process is to establish the design displacement profile of the structure. This is governed by either material or drift limit states. It is also dependent upon the structural system. Hence, the displacement profiles for both RC and rocking wall buildings are addressed separately in Sections 4.3.6 and 4.3.7. Once the design displacement profile is determined, the design displacement of the equivalent SDOF system can be obtained by the expression:

$$\Delta_d = \frac{\sum_{i=1}^{n} m_i {\Delta_i}^2}{\sum_{i=1}^{n} m_i \Delta_i} \tag{4.1}$$

where m_i is the mass of each floor and Δ_i is the design displacement of each floor.

4.3.2 Effective Mass and Height

The effective mass and height of the SDOF system are calculated by Equations (4.2) and (4.3):

$$m_e = \frac{\sum_{i=1}^{n} m_i \Delta_i}{\Delta_d} \tag{4.2}$$

$$H_e = \frac{\sum_{i=1}^{n} m_i \Delta_i H_i}{\sum_{i=1}^{n} m_i \Delta_i} \tag{4.3}$$

where H_i is the height of each floor.

4.3.3 Equivalent Viscous Damping

To estimate the system's equivalent viscous damping, the system's displacement ductility needs to be calculated first. This is done using Equation (4.4):

$$\mu = \frac{\Delta_d}{\Delta_y} \tag{4.4}$$

where Δ_y is the yield displacement of the equivalent SDOF system calculated from the structure's yield displacement profile at the effective height, H_e.

The design ductility is then used to calculate the hysteretic damping expected from the system. This is dependent upon the structural system used. Thus, damping for both RC and rocking wall buildings is discussed separately in Sections 4.3.6 and 4.3.7. Once the hysteretic damping is known, the equivalent viscous damping is calculated by the expression:

$$\xi_{eq} = \xi_{el} + \xi_{hyst} \tag{4.5}$$

where ξ_{hyst} is hysteretic damping and ξ_{el} is elastic damping, assumed to be 5% for both RC and rocking wall systems.

4.3.4 Effective Period and Stiffness

The effective period of the equivalent SDOF system is obtained from a design displacement response spectrum as a function of the design displacement. However, the design spectrum

(specified for a damping ratio of 5%) is first scaled, to account for added hysteretic damping, by the factor:

$$R_\xi = \sqrt{\frac{0.07}{0.02 + \xi_{eq}}} \tag{4.6}$$

The effective stiffness of the SDOF system is then calculated using the expression:

$$k_e = \frac{4\pi^2}{T_e} m_e \tag{4.7}$$

where T_e is the effective period.

4.3.5 Design Base Shear

The design base shear is calculated as:

$$V_d = k_e \Delta_d \tag{4.8}$$

The base shear is then distributed along the height of the structure assuming a linear distribution:

$$F_i = V_d \frac{m_i \Delta_i}{\sum_{i=1}^{n} m_i \Delta_i} \tag{4.9}$$

where F_i is the equivalent static force acting at a given floor i.

Note that the force distribution obtained with this step corresponds to first mode effects only. Thus, appropriate capacity design procedures must be used to account for higher modes.

4.3.6 RC Wall Buildings

As discussed above, the design displacement profile and the hysteretic damping are dependent upon the structural system. The design displacement profile for RC wall buildings is assumed to be the result of an elastic and a plastic component. The yield displacement (i.e. the elastic component) at any given floor i can be determined as (Priestley *et al.*, 2007):

$$\Delta_{yi} = \frac{\varepsilon_y}{l_w} {H_i}^2 \left(1 - \frac{H_i}{3H_n}\right) \tag{4.10}$$

where ε_y is the yield strain of the longitudinal reinforcement, l_w is the length of the wall, and H_n is the height of the wall.

Once the yield displacement profile is determined, the design displacement profile is given by Equation (4.11), which is controlled by the 2% ASCE 7-10 (ASCE, 2010) drift limit (Priestley *et al.*, 2007).

$$\Delta_i = \Delta_{yi} + \left(\theta_c - \frac{\varepsilon_y}{l_w} H_n\right) H_i \tag{4.11}$$

where θ_c is the code drift limit.

The equivalent viscous damping for RC wall buildings is given by (Priestley *et al.*, 2007):

$$\xi_{eq} = 0.05 + 0.444\left(\frac{\mu - 1}{\mu\pi}\right) \tag{4.12}$$

Tables 4.3 and 4.4 present the design outcomes obtained using the DDBD design procedure and material properties outlined above. It should be noted that the effective periods of the case study buildings (characterized by an effective stiffness) are somewhat high. This is because the buildings were designed for the ASCE 7-10 design-level earthquake (ASCE, 2010), which is a relatively weak event in relation to the 2% drift limit (ASCE, 2010) adopted for the displacement-based design.

Table 4.3 RC wall buildings DDBD outcomes

	m_e (ton)	H_e (m)	Δ_y (m)	Δ_d (m)	μ	ξ_{eq} (%)	T_e (sec)	V_b (kN)
4 Story	338	9.11	0.043	0.151	3.5	15.1	2.38	356
8 Story	1234	17.43	0.095	0.275	2.9	14.2	4.22	754
12 Story	1827	25.85	0.162	0.390	2.4	13.3	5.79	838

Table 4.4 Design displacements, and first mode force, shear and moment distributions for the RC wall buildings

H_i (m)	4 story				8 Story				12 Story			
	Δ_i (m)	F_i (kN)	V_i (kN)	M_i (kN-m)	Δ_i (m)	F_i (kN)	V_i (kN)	M_i (kN-m)	Δ_i (m)	F_i (kN)	V_i (kN)	M_i (kN-m)
0	0.000	0	356	3243	0.000	0	754	13149	0.000	0	838	21662
3	0.041	31	356	2175	0.034	16	754	10886	0.028	7	838	19148
6	0.091	69	325	1200	0.074	35	739	8671	0.062	16	831	16656
9	0.147	112	256	432	0.120	56	704	6559	0.101	25	815	14210
12	0.207	144	144	0	0.170	80	648	4614	0.143	36	790	11840
15					0.225	105	569	2909	0.190	48	754	9579
18					0.282	131	464	1517	0.240	60	706	7461
21					0.341	159	332	520	0.292	74	646	5523
24					0.401	173	173	0	0.348	87	572	3807
27									0.405	102	485	2353
30									0.463	117	383	1204
33									0.523	131	266	405
36									0.582	135	135	0

To account for higher mode effects, a simplified capacity design procedure is recommended by Priestley *et al.* (2007). The capacity-design moment distribution is defined by a bilinear envelope as a function of the moment at the base, mid-height and top of the structure (zero). The base moment is given by Equation (4.13) while the mid-height moment is given by Equation (4.14).

$$M_B^o = \phi^o M_B \tag{4.13}$$

$$M_{0.5H_n}^o = C_{1,T} M_B^o \tag{4.14}$$

where

$$C_{1,T} = 0.41 + 0.075 T_i \left(\frac{\mu}{\phi^o} - 1\right) \geq 0.4 \tag{4.15}$$

M_B is the base moment calculated from first mode force distribution; T_i is the elastic period of the structure estimated using Equation (4.16); and ϕ^o is an overstrength factor, which is *1.0* when strain-hardening is considered in determining base flexural reinforcement (Priestley *et al.*, 2007).

$$T_i = T_e \sqrt{\frac{1 + r(\mu - 1)}{\mu}} \tag{4.16}$$

The factor, *r,* is the ratio of post-yield stiffness to elastic stiffness (approximated as 0.05 for this study).

The capacity-design shear distribution is defined by a linear envelope consisting of a shear force at the base and at the top of the structure, Equations (4.17) and (4.20), respectively.

$$V_B^o = \phi^o \omega_v V_B \tag{4.17}$$

where

$$\omega_v = 1 + \frac{\mu}{\phi^o} C_{2,T} \tag{4.18}$$

$$C_{2,T} = 0.067 + 0.4(T_i - 0.5) \leq 1.15 \tag{4.19}$$

$$V_n^o = C_3 V_B^o \tag{4.20}$$

where

$$C_3 = 0.9 - 0.3T_i \geq 0.3 \tag{4.21}$$

For shear design, the overstrength factor, ϕ^o, should account for material overstrength, strain-hardening, and excess flexural reinforcement. For simplicity, a value of *1.25,* as recommended by Priestley *et al.* (2007), was adopted.

After completing the capacity-design procedures outlined above, the following design outcomes were obtained.

Table 4.5 RC wall buildings capacity design shear and moment distributions

H_i	4 Story		8 Story		12 Story	
	V_i (kN)	M_i (kN-m)	V_i (kN)	M_i (kN-m)	V_i (kN)	M_i (kN-m)
0	955	3243	2915	13149	3898	21662
$H_{n/2}$	714	2127	1894	10091	2534	17512
H_n	474	0	874	0	1170	0

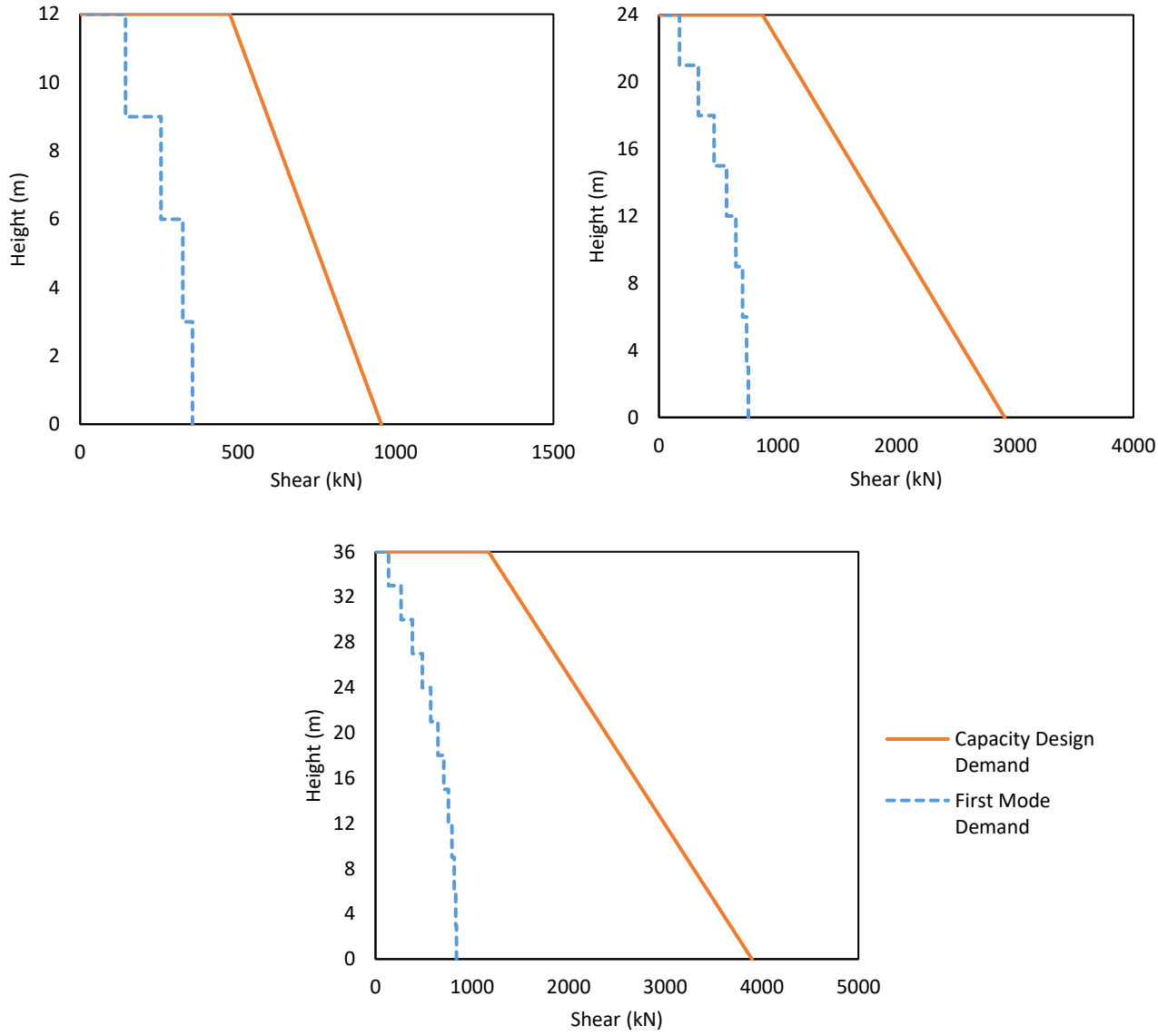

Figure 4.4 RC wall buildings DDBD shear force distribution: (a) 4-Story; (b) 8-Story; (c) 12-Story

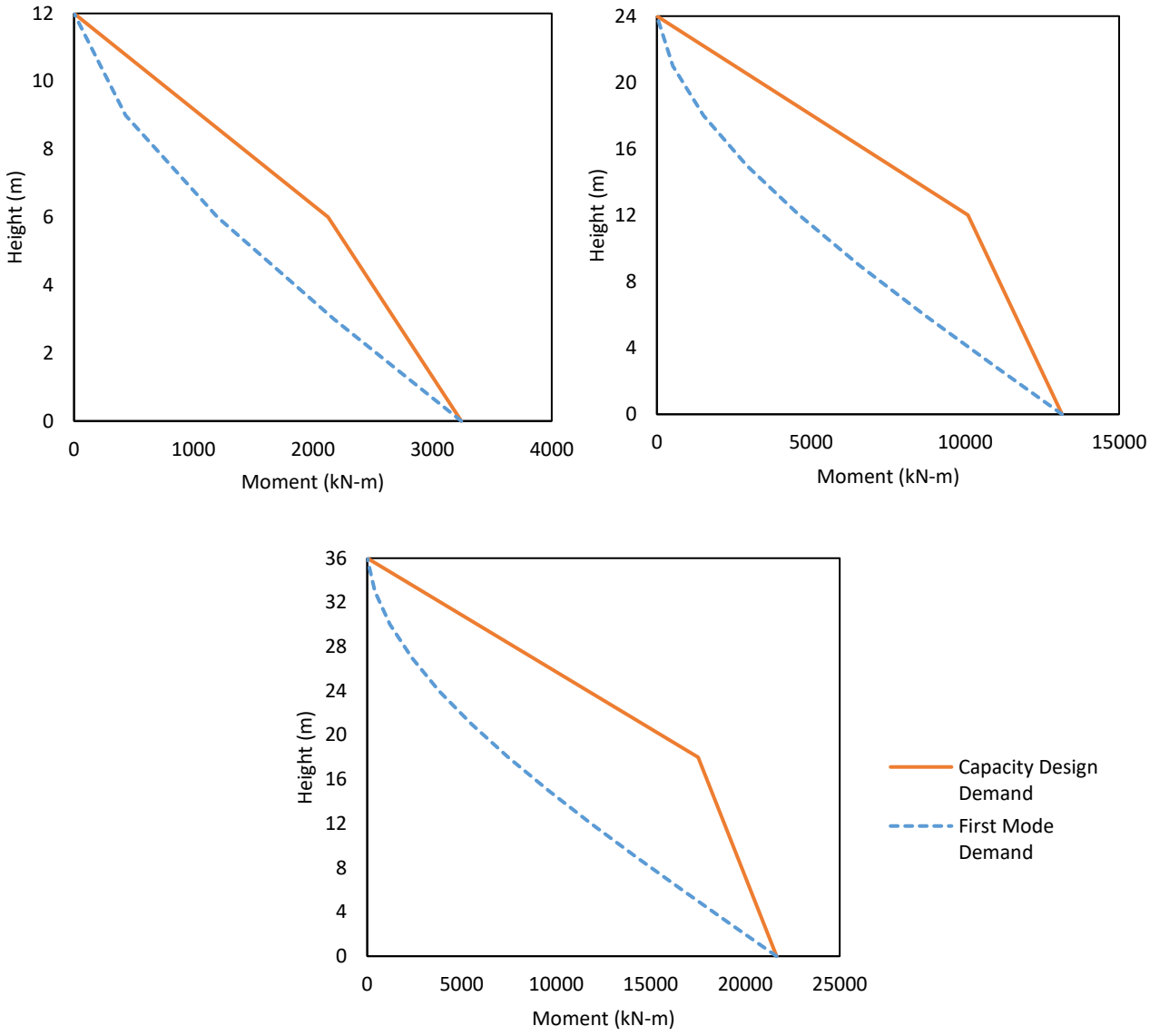

Figure 4.5 RC wall buildings DDBD moment distribution: (a) 4-Story; (b) 8-Story; (c) 12-Story

4.3.7 Rocking Wall Buildings

The displacement-based design of the rocking wall buildings was conducted following the procedure proposed by Pennucci *et al.* (2009), assuming traditional detailing of the walls as outlined by Rahman and Restepo (2000). The detailing includes longitudinal reinforcement along the height as well as confinement in the toe and heel of the wall (Figure 4.6).

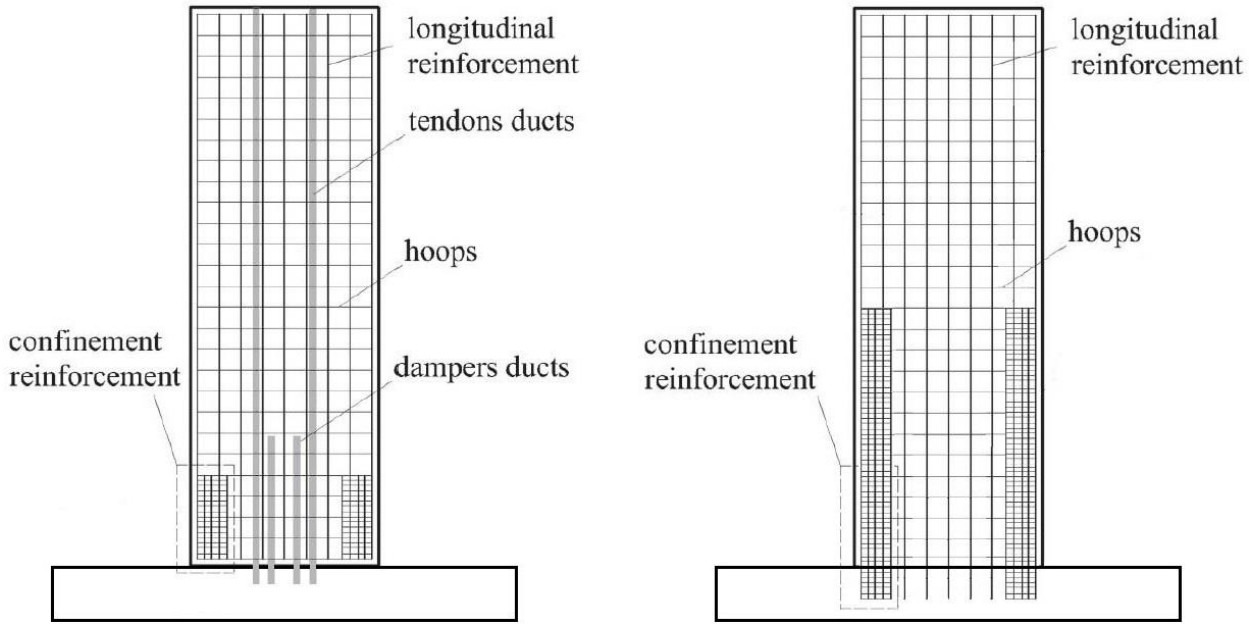

Figure 4.6 Rahman and Restepo (2000) rocking wall detailing (left) and conventional RC wall detailing (right) (adapted from Pennucci *et al.* (2009))

The displacement profile is assumed to be the result of an elastic and a plastic component. The yield displacement (i.e. the elastic component) at any given floor *i* can be determined as:

$$\Delta_{yi} = 0.5\phi_b \left[H_i^2 - \frac{H_i^3}{2H_n} + \frac{H_i^5}{20H_n^3}\right] + \theta_{y\_base} H_i \tag{4.22}$$

where H_i is the height of each floor, H_n is the height of the wall, ϕ_b is the curvature at the base of the wall, and Θ_{y_base} is the yield rotation of the wall/foundation connection. The wall base curvature is given by:

$$\phi_b = \frac{\phi_y}{\gamma} \tag{4.23}$$

where ϕ_y is the yield curvature of the wall and γ is a curvature index which is typically a value greater than *1* to allow cracking while avoiding yielding in the wall. However, a value of *2* or *3* is suggested by Pennucci *et al.* (2009) to comply with serviceability performance criteria even if cracking takes place. For this study, a value of *3* was adopted. The yield curvature is given by:

$$\phi_y = 2\frac{\varepsilon_y}{l_w} \tag{4.24}$$

where ε_y is the yield strain of the wall longitudinal reinforcement and l_w is the length of the wall.

The yield rotation of the wall/foundation connection is given by:

$$\theta_{y\_base} = \frac{\varepsilon_{my}(l_{ub\_ms} + 2\Delta_{sp})}{l_w(1-v) - d_{AS}} \tag{4.25}$$

where ε_{my} is the yield strain of mild steel, l_{ub_ms} is the mild steel unbonded length, d_{AS} is the distance from the tension face of the wall to the centroid of mild steel (Figure 4.7), v is the normalized depth of compression area at yielding and Δ_{sp} is the strain penetration which is given by:

$$\Delta_{sp} = 0.022 f_{my} d_{mb} \tag{4.26}$$

where f_{my} is the mild steel yield stress and d_{mb} is the mild steel bar diameter.

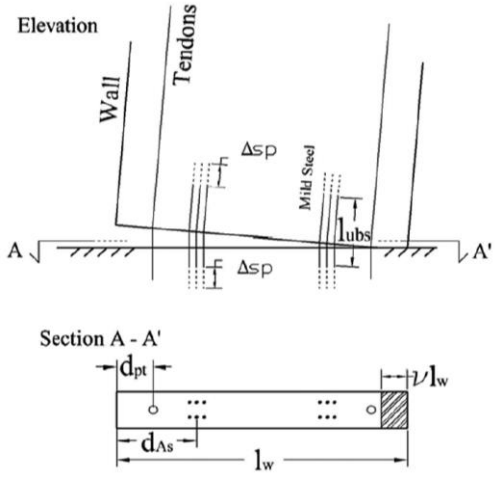

Figure 4.7 Rocking wall/foundation connection design parameters (Pennucci *et al.*, 2009)

At the beginning of the design process, the normalized depth of compression area, which is unknown at this time, was taken as *0.2* while the distance to the centroid of the mild steel reinforcement was taken as $0.35l_w$ as recommended by Pennucci *et al.* (2009). These values were then recalculated and updated once the reinforcement design was completed.

Once the yield displacement profile is calculated, the design displacement at a given floor i is obtained as:

$$\Delta_i = \Delta_{yi} + (\theta_c - \theta_{y\_n})H_i \tag{4.27}$$

where θ_c is the code drift limit and θ_{y_n} is the total roof drift at yielding given by:

$$\theta_{y\_n} = \theta_{wall} + \theta_{y\_base} \tag{4.28}$$

where θ_{wall} is the wall deformation at yielding given by:

$$\theta_{wall} = {}^{3}/_{8}\,\phi_b H_n \tag{4.29}$$

The equivalent viscous damping for rocking walls is dependent upon the factor λ, the ratio of between post-tensioning and mild steel bending resistance. In order to prevent residual displacements, λ. has to be greater than *1.0* (Figure 4.8). Thus, a value of *1.25* was adopted as suggested by Pennucci *et al.* (2009). This value ensures re-centering and the maximum amount of energy dissipation considering material over-strengths.

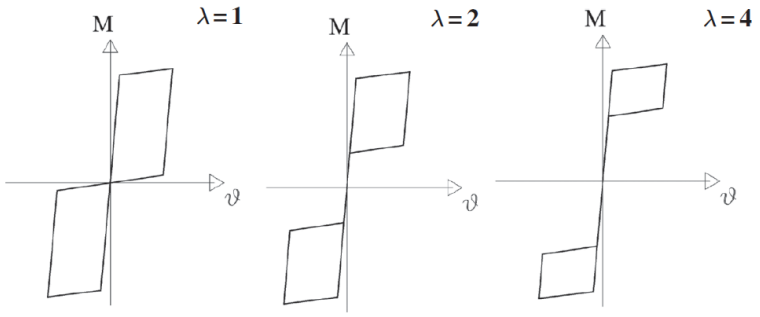

Figure 4.8 Flag-shaped hysteresis with increasing λ factors (Pennucci *et al.*, 2009)

To estimate the equivalent viscous damping for the rocking wall buildings, a damping-ductility design curve produced by Pennucci *et al.* (2009) was adopted. The design curve, developed for λ *= 1.25* and *r = 0,* is approximated by the following expression:

$$\xi_{eq} = 0.05 + 0.524\left(\frac{\mu - 1}{\mu\pi}\right) \tag{4.30}$$

Tables 4.6 and 4.7 present the design outcomes obtained using the DDBD design procedure and material properties outlined above. Similar to the RC wall buildings, it should be noted that the effective periods of the case study rocking wall buildings (characterized by an effective stiffness) are somewhat high. Again, this is because the buildings were designed for the ASCE 7-10 design-level earthquake (ASCE, 2010), which is a relatively weak event in relation to the 2% drift limit (ASCE, 2010) adopted for the displacement-based design.

Table 4.6 Rocking wall buildings DDBD outcomes

	m_e (ton)	H_e (m)	Δ_y (m)	Δ_d (m)	μ	ξ_{eq} (%)	T_e (sec)	V_b (kN)
4 Story	352	8.94	0.020	0.173	8.5	19.7	3.06	256
8 Story	1305	17.00	0.039	0.325	8.3	19.7	5.75	506
12 Story	1959	25.05	0.063	0.475	7.6	19.5	8.38	524

Table 4.7 Design displacements, and first mode force, shear and moment distributions for the rocking wall buildings

H_i (m)	4 story				8 Story				12 Story			
	Δ_i (m)	F_i (kN)	V_i (kN)	M_i (kN-m)	Δ_i (m)	F_i (kN)	V_i (kN)	M_i (kN-m)	Δ_i (m)	F_i (kN)	V_i (kN)	M_i (kN-m)
0	0.000	0	256	2292	0.000	0	506	8600	0.000	0	524	13122
3	0.056	26	256	1523	0.054	13	506	7082	0.052	6	524	11550
6	0.114	52	231	831	0.109	27	493	5604	0.106	13	517	9998
9	0.173	80	178	296	0.167	42	465	4209	0.162	19	505	8484
12	0.233	99	99	0	0.225	56	423	2939	0.218	26	485	7029
15					0.284	71	367	1839	0.276	33	459	5652
18					0.344	86	296	952	0.334	40	426	4375
21					0.404	101	209	324	0.393	47	385	3219
24					0.464	108	108	0	0.453	55	338	2205
27									0.513	62	284	1354
30									0.573	69	222	689
33									0.633	76	153	230
36									0.692	77	77	0

There is currently no simplified design procedure to account for higher mode effects in rocking wall buildings. However, as Wiebe (2008) pointed out, higher mode effects in rocking walls are likely to play a role that is analogous to that observed for RC walls. Therefore, the procedure discussed in Section 4.3.6 was applied to the rocking wall buildings to investigate its applicability. The following capacity design outcomes were obtained from the procedure.

Table 4.8 Rocking wall buildings capacity design shear and moment distributions (obtained using procedure for RC wall buildings)

H_i	4 Story		8 Story		12 Story	
	V_i (kN)	M_i (kN-m)	V_i (kN)	M_i (kN-m)	V_i (kN)	M_i (kN-m)
0	1104	2292	3982	8600	5703	13122
$H_{n/2}$	846	2508	2588	14377	3707	28001
H_n	587	0	1195	0	1711	0

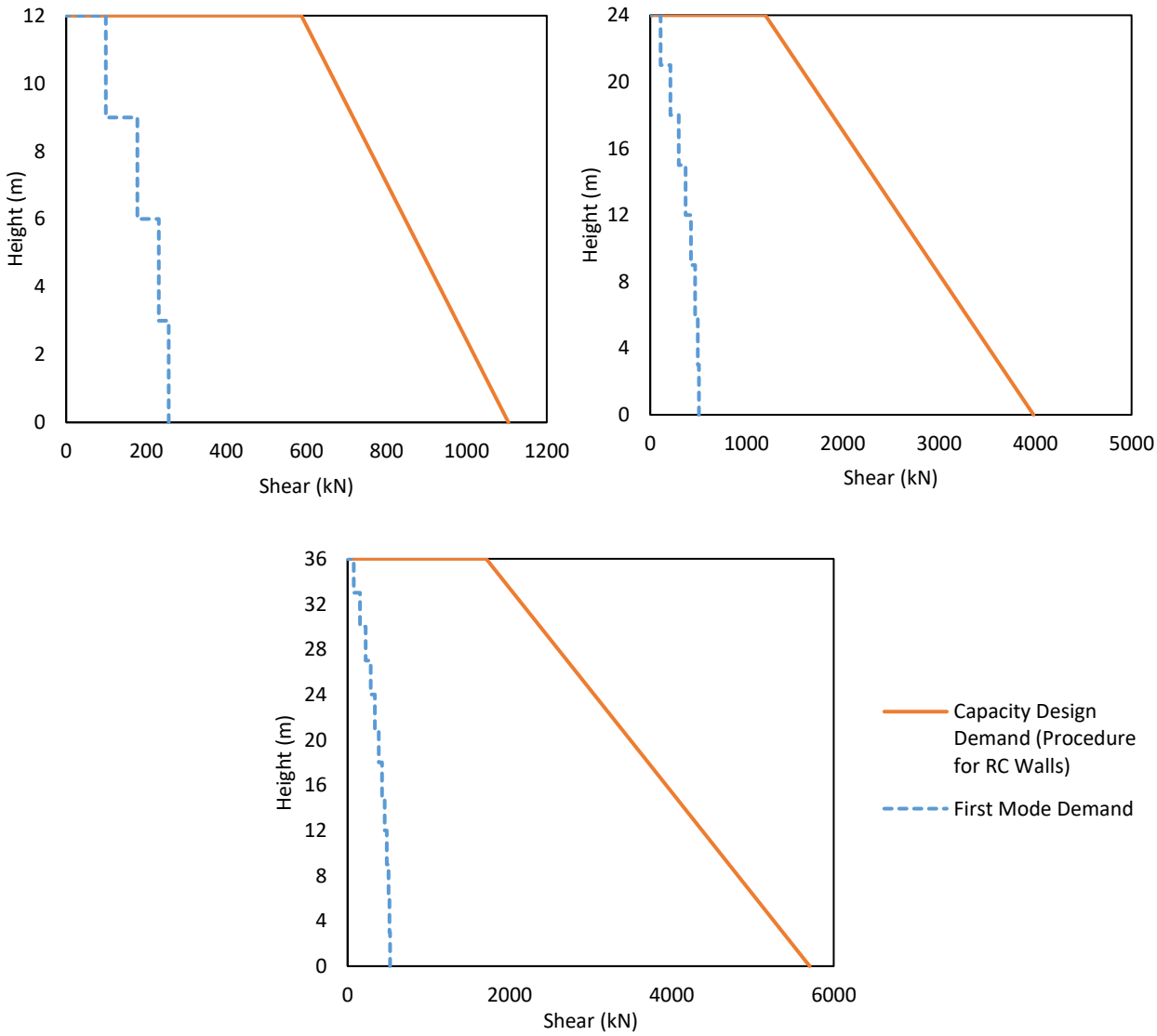

Figure 4.9 Rocking wall buildings DDBD shear distribution: (a) 4-Story; (b) 8-Story; (c) 12-Story

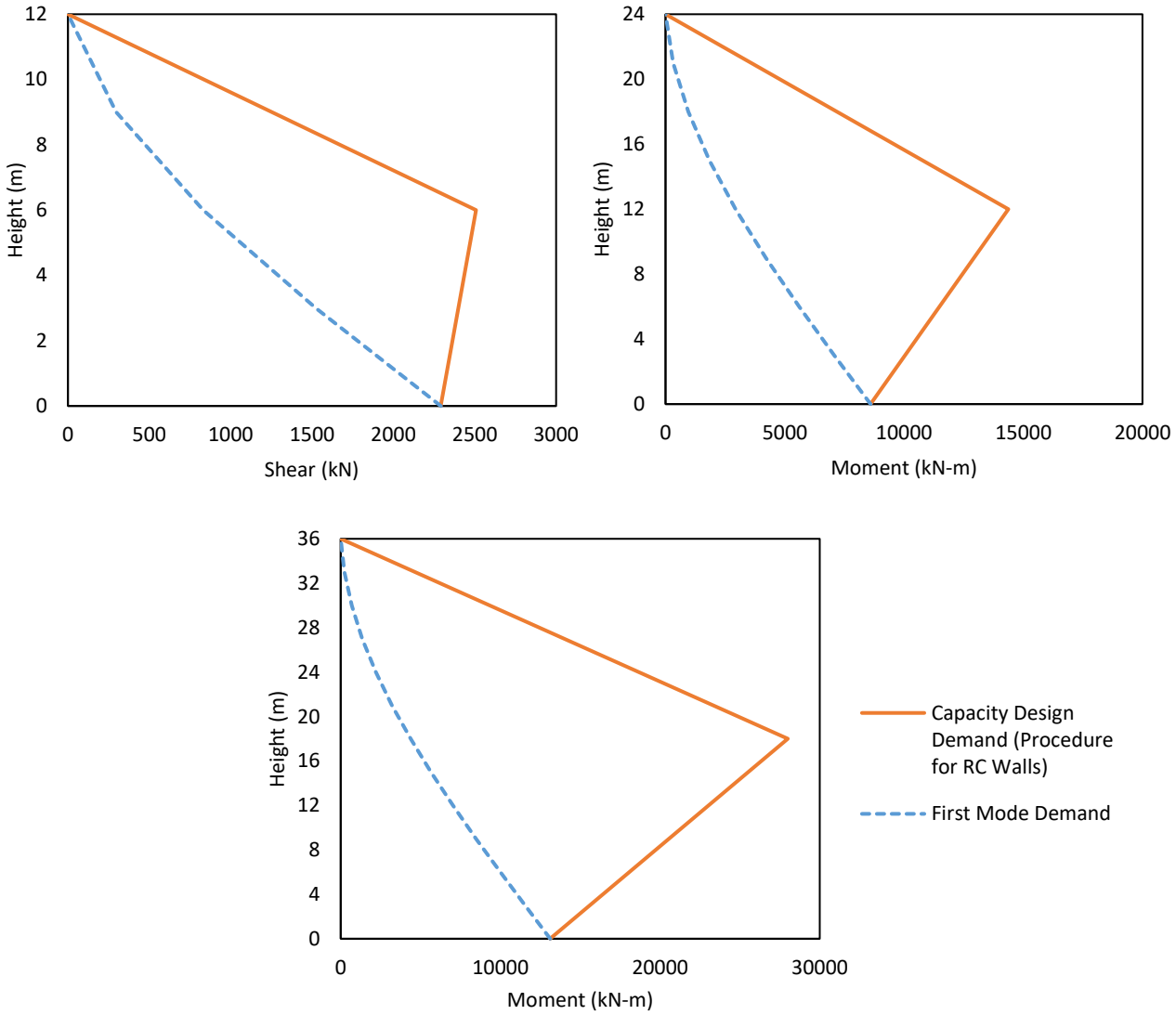

Figure 4.10 Rocking wall buildings DDBD moment distribution: (a) 4-Story; (b) 8-Story; (c) 12-Story

4.4 Reinforcement Design

The loads obtained in Section 4.3 were used to design the wall/foundation connections for both the RC and rocking walls. For simplicity, only flexural reinforcement was determined. It is assumed that the walls will have sufficient shear reinforcement and confinement to achieve the required flexural strengths. The flexural design for all case study walls is detailed in Sections 4.4.1 and 4.4.2.

4.4.1 RC Walls

For the RC walls, sectional analysis was conducted using the program CUMBIA (Montejo and Kowalsky, 2007) to determine the required flexural reinforcement and moment-curvature relationship. Traverse reinforcement was assumed to be ASTM A706M Grade 420 No. 5 bars spaced at 95mm (ASTM International, 2016a). Based on the material properties and loads outlined in the previous sections, the following design outcomes were obtained.

Table 4.9 RC walls reinforcement ratio and bilinear moment-curvature approximation

		4 Story	8 Story	12 Story
Longitudinal Reinforcement Ratio, ρ (%)		0.004	0.006	0.005
First Yield Capacity	**M_y (kN-m)**	1867	8267	14661
	ϕ_y (1/m)	0.00095	0.00058	0.00045
Nominal/Yield Capacity	**M_N (kN-m)**	2948	12072	20786
	ϕ_N (1/m)	0.00150	0.00085	0.00064
Ultimate Capacity	**M_u (kN-m)**	3464	14010	23828
	ϕ_u (1/m)	0.01938	0.01149	0.00891
Elastic Stiffness, k (kN-m^2)		1.96E+06	1.43E+07	3.26E+07
Post Yield Stiffness Ratio, r (-)		0.015	0.013	0.011

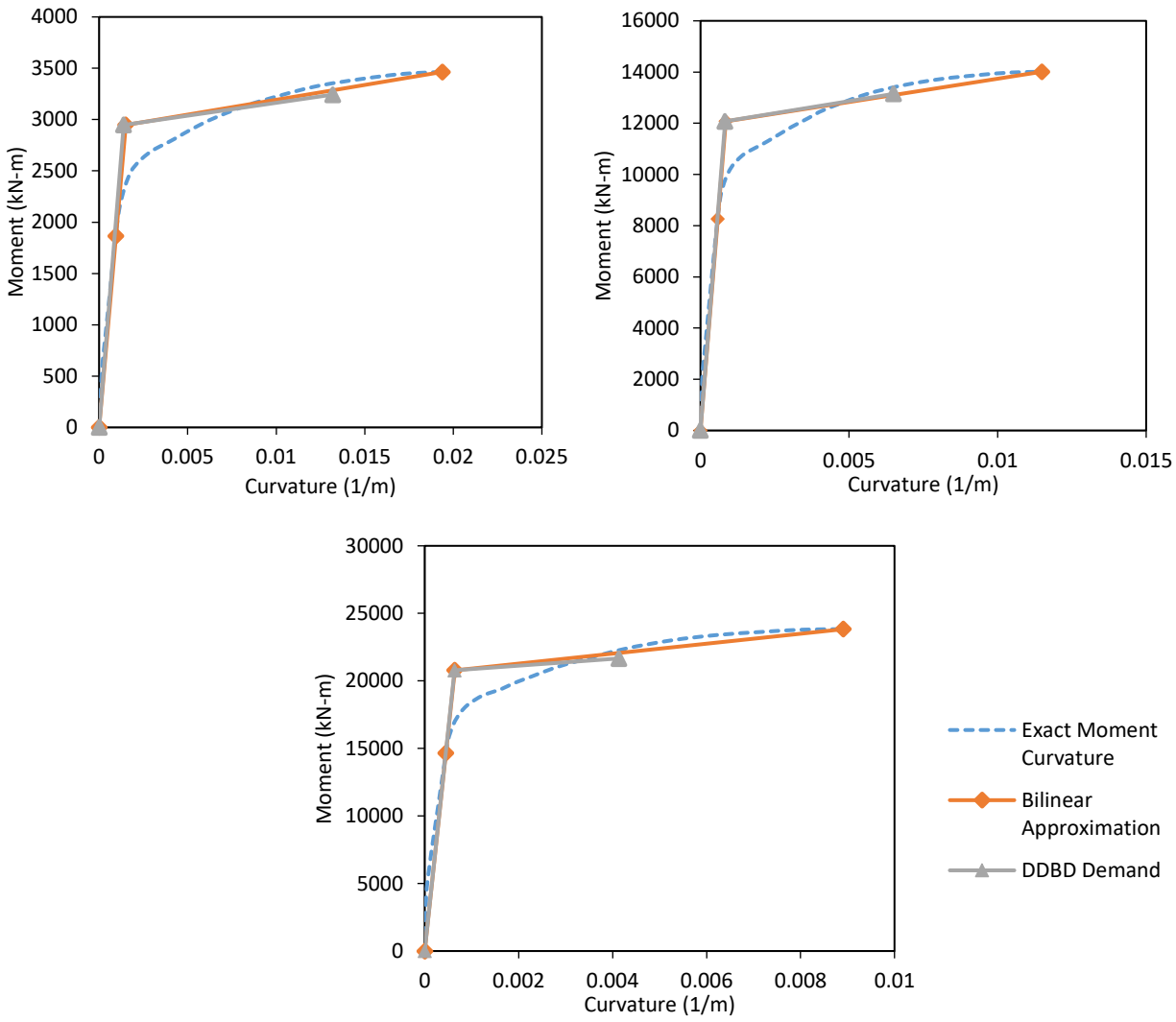

Figure 4.11 RC walls moment-curvature relationships: (a) 4-Story; (b) 8-Story; (c) 12-Story

4.4.2 Rocking Walls

The reinforcement design of the rocking wall/foundation connections was conducted according to the procedure outlined by Rahman and Restrepo (2000). The design procedure assumes that the post-tensioning tendons and mild steel energy dissipaters are placed symmetrically across the middle of the wall. Using this procedure, an idealized bilinear moment-rotation relationship was obtained. A brief summary of the procedure is presented below.

The first point (yield) of the bilinear moment-rotation relationship is the yielding of the mild steel energy dissipaters, at which point the wall/foundation separation gap has propagated through 75% of the overall depth of the wall. The moment at this point is given by the expression:

$$M_y = \left(N + f_{pti}A_{pt} + f_{my}A_m\right)\left(\frac{l_w}{2} - \frac{c_y}{3}\right) \tag{4.31}$$

where N is the gravity load on the wall, f_{pti} is the initial stress in the post-tensioning tendons after losses, A_{pt} is the total area of post-tensioning strands, A_m is the total area of mild steel, and c_y is the distance from extreme compression fiber to the neutral axis at yield given by the expression:

$$c_y \approx 0.25 l_w \tag{4.32}$$

To determine an appropriate initial post-tensioning force, the following inequality must be satisfied to ensure the tendons remain elastic at ultimate capacity.

$$f_{pti} \leq f_{ptlp} - E_{pt}\frac{\theta_c(d_{pt} - c_u)}{l_{ub\_pt}} \tag{4.33}$$

where f_{ptlp} is the nominal limit of proportionality stress of the post-tensioning tendons approximated as $0.84f_{ptu}$ as suggested by Restrepo and Rahman (2007). d_{pt} is the location of post-tensioning tendon furthest away from the extreme compression fiber, l_{ub_pt} is the total unbonded length of post-tensioning tendons taken as *1.10* times the height of the wall, and c_u is the distance from extreme compression fiber to the neutral axis at ultimate capacity given by the expression:

$$c_u \approx \frac{N + 0.9f_{ptlp}A_{pt} + f_{mu}A_m + 1.4f_c' b_e c_c}{1.4f_c' b_e} \tag{4.34}$$

where b_e is the width of the wall without concrete cover.

To determine an appropriate amount of mild steel reinforcement, the following inequality must be satisfied to ensure the tendons remain elastic up to ultimate capacity.

$$\frac{2}{5}\frac{N + f_{pti}A_{pt}}{f_{my}} < A_m \leq \frac{2}{3}\frac{N + f_{pti}A_{pt}}{f_{my}} \tag{4.35}$$

The yield rotation of the wall/foundation connection is given by the expression:

$$\theta_{y\_base} = \frac{\varepsilon_{my} l_{ub\_ms}}{\frac{l_w}{2} - c_y} \tag{4.36}$$

where I_g is moment of inertia of the gross wall cross-section and A_g is the gross cross-sectional area. In order for Equation (4.36) to be valid, the total axial load (post-tensioning plus gravity load) has to be less than $0.2A_g f'c$. When the total axial load is higher than $0.2A_g f'c$, the high compression

at the base of the wall results in a non-linear behavior of the confined concrete and mortar bed at the wall ends. This leads to a reduction of stiffness, which is not accounted for in Equation (4.36).

To determine the mild steel unbonded length, Restrepo and Rahman (2007) suggest the following range to ensure the strain in the mild steel does not exceed 2/3 of the strain at the tensile strength at ultimate capacity.

$$\frac{9}{4}\frac{\theta_c}{\varepsilon_{mu}}(d_m - c_u) \leq l_{ub\_ms} \leq \frac{3}{2}\frac{\theta_c}{\varepsilon_{mu}}(d_m - c_u) \tag{4.37}$$

where ε_{mu} is the ultimate strain of the mild steel energy dissipaters taken as 0.10, and d_m is the location of mild steel furthest away from the extreme compression fiber.

The second point (ultimate) of the bilinear moment-rotation relationship is defined as the point when the post-tensioning tendons reach a limit of proportionality. The moment at this point is given by the expression:

$$M_u = \left(N + f_{ptlp}A_{pt} + f_{mu}A_m\right)\left(\frac{l_w}{2} - \frac{a}{2} - c_c\right) \tag{4.38}$$

where c_c is the concrete cover taken as 80mm, and a is the depth of equivalent rectangular concrete stress block approximated by the expression:

$$a \approx c_u - c_c \tag{4.39}$$

The ultimate rotation of the wall/foundation connection is given by the expression:

$$\theta_{u\_base} = \frac{f_{ptlp} - f_{pti}}{E_{pt}}\frac{l_{ub\_pt}}{\frac{l_w}{2}} \tag{4.40}$$

Based on the design procedure outlined above, the following design outcomes were obtained.

Table 4.10 Rocking walls reinforcement design outcomes

		4 Story	8 Story	12 Story
Mild Steel	**Reinforcement Ratio, ρ_m (-)**	0.0017	0.0029	0.0023
	Unbonded Length, l_{ub_ms} (m)	0.400	0.600	0.750
Post-tensioning Tendons	**Reinforcement Ratio, ρ_{pt} (-)**	0.0007	0.0006	0.0005
	Initial Post-tensioning Stress/Ultimate Stress, f_{pti}/f_{ptu} (-)	0.67	0.71	0.72
	Unbonded Length, l_{ub_pt} (m)	13.2	26.4	39.6
Total Axial Load/A_gf'c (-)		0.03	0.04	0.04

Table 4.11 Rocking walls bilinear moment-rotation relationship

		4 Story	8 Story	12 Story
Yield Capacity	**M_y (kN-m)**	1965	7174	11656
	Θ_{y_base} (rad)	0.00075	0.00067	0.00065
Ultimate Capacity	**M_u (kN-m)**	2599	9244	14600
	Θ_{u_base} (rad)	0.01830	0.01821	0.01807
Elastic Stiffness, k (kN-m/rad)		2.63E+06	1.07E+07	1.80E+07
Post Yield Stiffness Ratio, r (-)		0.014	0.011	0.009

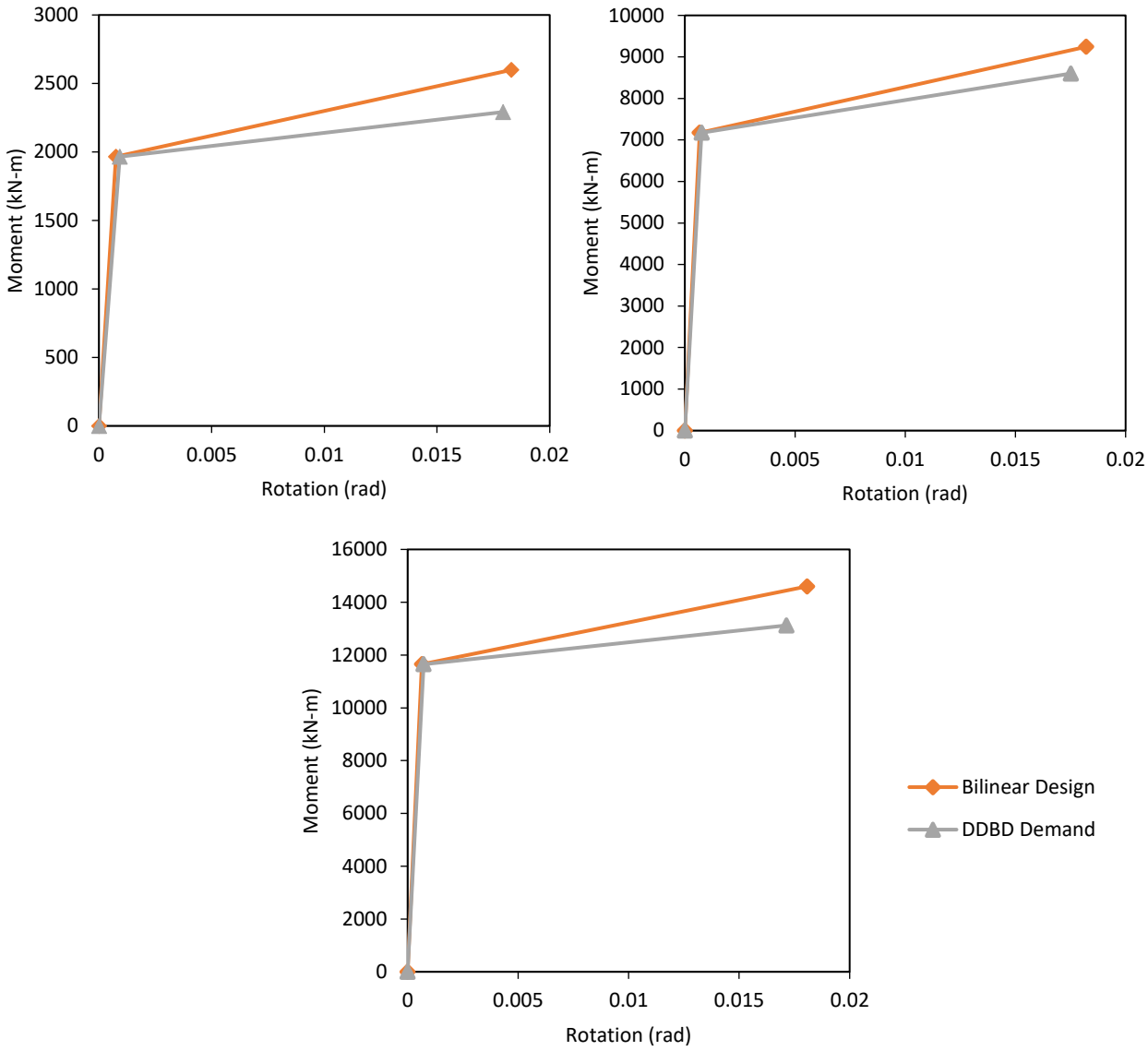

Figure 4.12 Rocking walls moment-rotation relationships: (a) 4-Story; (b) 8-Story; (c) 12-Story

4.5 Dynamic Time History Analysis Procedure

A two-dimensional time history analysis of the case study buildings was conducted using the program RUAUMOKO2D (Carr, 2004). In both the RC and rocking wall buildings, it was assumed that nonlinear behavior would occur only at the base of the systems. Thus, a lumped plasticity modelling approach was adopted. It is important to note that this approach has been previously used by others to model both types of structural wall systems (Amaris, 2002; Palermo *et al.*, 2005; Wiebe, 2008; Twigden *et al.*, 2013; Welch, 2016). The following sections detail the modelling process and ground motions used in the analysis.

4.5.1 Ground Motions

A suite of spectrum compatible ground motions were selected for the time history analysis from the Pacific Earthquake Engineering Research Center (PEER) NGA-West2 ground motion database (http://peer.berkeley.edu/ngawest2/). The ground motions were selected according to ASCE 7-10 (ASCE, 2010) two dimensional analysis guidelines. Therefore, the selected acceleration records were from events with magnitude, fault distance, and source mechanism consistent with the maximum considered earthquake (MCE) (ASCE, 2010).

In order to select seismic events with properties similar to the MCE, a deaggregation of seismic hazard was obtained for the site location and ground conditions from the United States Geological Survey (USGS) Earthquake Hazards Program online tool (https://earthquake.usgs.gov/hazards/interactive/). The following properties were obtained from the online tool and used to select the acceleration records: magnitude of 5-9, closest distance of 5-50km and mechanism of strike slip or reverse. However, the range of closest distance resulted in only a few records, so the upper limit of 50km was removed during the record selection process. The selected ground motions are listed in Table 4.12.

In addition to selecting the ground motions, the PEER website was also used to scale the acceleration records to match the ASCE 7-10 (ASCE, 2010) design response spectrum (refer to Section 4.2). Each acceleration record consisted of three components: two horizontal (H1 and H2) and one vertical (V). Since the THA is a two-dimensional analysis, only the first horizontal component (H1) was scaled. The scale factors were computed to minimize the Mean Squared Error of each record and the arithmetic mean of all records with respect to the design response spectrum (Figure 4.13). It can be noted that there is a somewhat high variability in the selected ground motions, which may not be suitable for design purposes. However, this was considered acceptable for the purpose of this study.

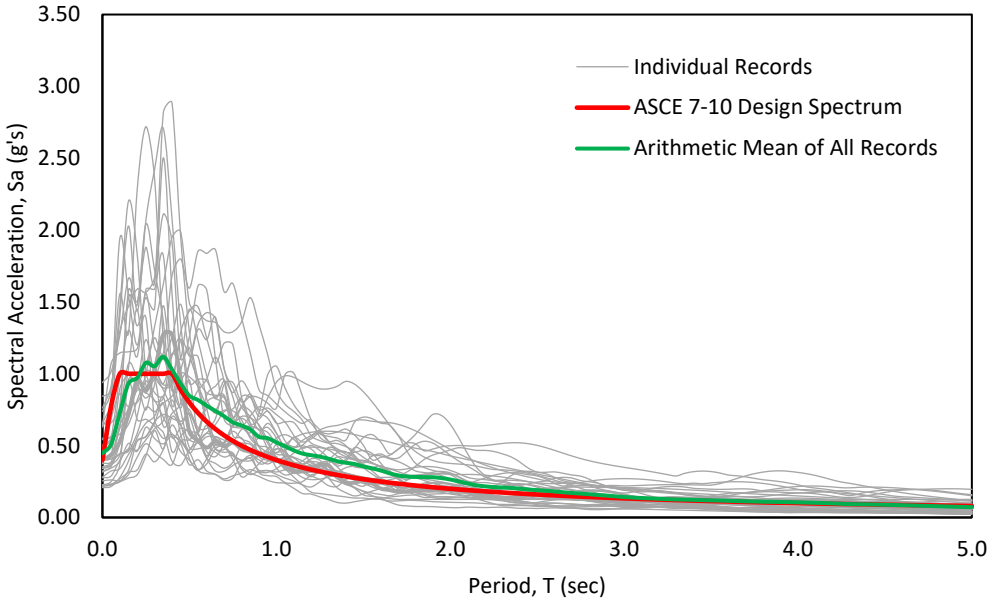

Figure 4.13 Acceleration response spectra of spectrum compatible earthquake records and ASCE 7-10 design response spectrum

Table 4.12 Characteristics of spectrum compatible earthquake records

Earthquake Name	Station Name	Year	Magnitude	Mechanism	Joyner-Boore Distance (km)	Scale Factor
Imperial Valley-02	El Centro Array #9	1940	6.95	strike slip	6.09	1.515
Northwest Calif-02	Ferndale City Hall	1941	6.6	strike slip	91.15	10.378
Borrego	El Centro Array #9	1942	6.5	strike slip	56.88	5.348
Kern County	LA - Hollywood Stor FF	1952	7.36	Reverse	114.62	4.922
Kern County	Pasadena - CIT Athenaeum	1952	7.36	Reverse	122.65	7.860
Kern County	Santa Barbara Courthouse	1952	7.36	Reverse	81.3	4.481
Kern County	Taft Lincoln School	1952	7.36	Reverse	38.42	2.484
Northern Calif-02	Ferndale City Hall	1952	5.2	strike slip	42.69	9.104
Southern Calif	San Luis Obispo	1952	6	strike slip	73.35	11.474
Northern Calif-03	Ferndale City Hall	1954	6.5	strike slip	26.72	1.697
Imperial Valley-05	El Centro Array #9	1955	5.4	strike slip	13.78	12.999
El Alamo	El Centro Array #9	1956	6.8	strike slip	121	10.123
Northern Calif-04	Ferndale City Hall	1960	5.7	strike slip	56.94	10.873
Hollister-01	Hollister City Hall	1961	5.6	strike slip	19.55	5.380
Parkfield	Cholame - Shandon Array #12	1966	6.19	strike slip	17.64	6.296
Parkfield	Cholame - Shandon Array #5	1966	6.19	strike slip	9.58	1.725
Parkfield	Cholame - Shandon Array #8	1966	6.19	strike slip	12.9	3.039
Parkfield	Temblor pre-1969	1966	6.19	strike slip	15.96	2.636
Northern Calif-06	Hollister City Hall	1967	5.2	strike slip	37.11	32.180
Borrego Mtn	El Centro Array #9	1968	6.63	strike slip	45.12	2.450
Borrego Mtn	LA - Hollywood Stor FF	1968	6.63	strike slip	222.42	20.164
Borrego Mtn	LB - Terminal Island	1968	6.63	strike slip	199.84	22.291
Borrego Mtn	Pasadena - CIT Athenaeum	1968	6.63	strike slip	207.14	32.157
Borrego Mtn	San Onofre - So Cal Edison	1968	6.63	strike slip	129.11	9.790
Lytle Creek	Colton - So Cal Edison	1970	5.33	Reverse Oblique	29.18	70.238
San Fernando	2516 Via Tejon PV	1971	6.61	Reverse	55.2	8.745
San Fernando	Bakersfield - Harvey Aud	1971	6.61	Reverse	111.88	32.583
San Fernando	Borrego Springs Fire Sta	1971	6.61	Reverse	214.32	31.655
San Fernando	Buena Vista - Taft	1971	6.61	Reverse	111.37	28.237
San Fernando	Carbon Canyon Dam	1971	6.61	Reverse	61.79	7.072
San Fernando	Cedar Springs Pumphouse	1971	6.61	Reverse	92.25	23.370
Friuli_ Italy-01	Barcis	1976	6.5	Reverse	49.13	21.782

4.5.2 Earthquake Intensity Levels

Both linear and non-linear time history analyses were conducted at six different earthquake intensities (Table 4.13). Hence, each acceleration record from Table 4.12 was scaled with the appropriate scale factor to match the intensity.

Table 4.13 Intensity levels for time history analysis

Intensity	Scale Factor	Peak Ground Acceleration, PGA (g)
1	0.50	0.225
2	0.65	0.293
3	0.75	0.338
4	0.85	0.383
5	1.00	0.450
6	1.50	0.675

Note that the case-study structures were designed for Intensity 5, which corresponds to the ASCE 7-10 Design Basis Earthquake (DBE) (ASCE, 2010). In addition, Intensity 6 corresponds to the Maximum Considered Earthquake (MCE), which is 1.5 times the DBE according to ASCE 7-10 (ASCE, 2010).

4.5.3 Modelling Assumptions

The following assumptions were made for the time history analysis.

- The structural walls were assumed elastic except for the wall/foundation connection, which behaves non-linearly according to the appropriate hysteresis model.
- The floor diaphragms were assumed fully rigid in plane and fully flexible out of plane so that each floor could be lumped at a single node.
- The gravity columns and traverse structural walls were assumed to have negligible lateral load resistance and thus were not modelled.
- The foundation was assumed fully fixed.
- P-delta effects were assumed to be negligible.

4.5.4 Integration Time-step

The integration time-step selected was 0.0005 sec, $1/10^{th}$ of the smallest acceleration record time-step, 0.005 sec (Welch, 2016). Time dependent results were also output at this time-step.

4.5.5 Elastic Damping Model

The elastic damping model adopted was based on the work by Smyrou *et al*. (2011) who conducted a thorough literature review on common damping models in non-linear analyses and proposed a suitable modelling procedure.

The proposed modelling approach involves using a user-specified modal damping model with a constant 5% for all modes except the first. For the first mode, an artificially lower value is set according to Equation (4.41) to avoid excessive damping in the post-yield phase and counter-balance the added damping introduced from using a constant damping ratio (Smyrou *et* al., 2011).

$$\xi^* = 5\% \left(\frac{1 - 0.1(\mu - 1)(1 - r)}{\sqrt{\frac{\mu}{1 + r\mu - r}}} \right) \tag{4.41}$$

where ξ* is the artificially lowered first mode damping ratio.

As noted by Pennucci *et al.* (2009), theoretically, the artificially lowered first mode damping ratio should approach zero as ductility reaches infinity. However, the empirical Equation (4.41) reaches zero at a displacement ductility of *11*. This is problematic since high displacement ductility is expected in the rocking walls (for instance μ*=8.5* for the 4-story case study wall). As a possible solution, Pennucci *et al.* (2009) used a minimum damping ratio of *1%*, which was also adopted in this study.

With the adopted elastic modelling approach, the following damping ratios were used for the time history analysis.

Table 4.14 Elastic damping values for time history analyses

		RC Walls			Rocking Walls		
		4 Story	**8 Story**	**12 Story**	**4 Story**	**8 Story**	**12 Story**
Damping Ratio (%)	**First Mode**	1.99	1.96	1.95	1.00	1.00	1.00
	All Other Modes	5.00	5.00	5.00	5.00	5.00	5.00

4.5.6 RC Wall Models

The models for the RC walls consisted of a series of elastic Giberson beam elements (Figure 4.14) with non-linearity concentrated at a plastic hinge at the base of the wall (Figure 4.15). The beam elements were characterized by a cracked, linear elastic stiffness of the wall cross-section, and the plastic hinge was characterized by a Modified Takeda hysteresis (Carr, 2004). The moment-curvature relationships from the reinforcement design (Section 4.4.1) were used as the backbone of the hysteresis. In addition, the following parameters were used to define the unloading and reloading behavior of the hysteresis (Amaris, 2002; Welch, 2016):

- Unloading stiffness factor, $\alpha = 0.5$
- Reloading stiffness factor, $\beta = 0$
- An Emori and Schnobrich unloading ($KKK = 2$)

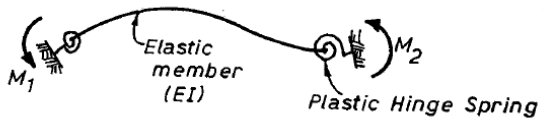

Figure 4.14 Giberson one-component beam model (Carr, 2004)

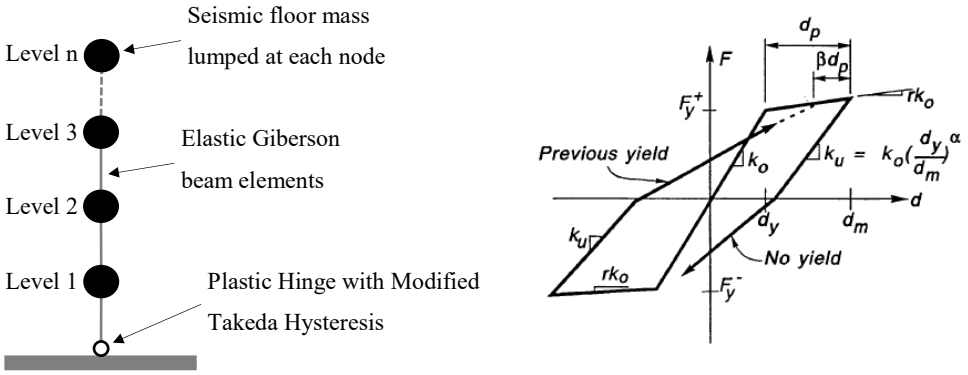

Figure 4.15 Diagram of RC wall models (left) and Modified Takeda hysteresis (Carr, 2004) (right).

The plastic hinge lengths were calculated by the following expression as suggested by Priestley *et al.* (2007).

$$l_p = kH_e + 0.1l_w + l_{sp} \tag{4.42}$$

where l_{sp} is the strain penetration length and k is a factor that takes into account the ratio between the longitudinal reinforcement ultimate and yield strengths, which is given by the expression:

$$k = 0.2\left(\frac{f_u}{f_y} - 1\right) \leq 0.08 \tag{4.43}$$

The strain penetration length is given by the expression:

$$l_{sp} = 0.022 f_{ye} d_b \ \ (f_{ye}\ in\ MPa) \tag{4.44}$$

where f_{ye} is the expected yield stress of longitudinal reinforcement taken as $1.1f_y$ (Priestley *et al.*, 2007), and d_b is the diameter of longitudinal reinforcement.

Concrete shear modulus was taken as 0.43 times the Young's modulus of concrete (Montejo and Kowalsky, 2007). Effective shear area was taken as 5/6th of total cross-sectional area (Welch, 2016). The moment of inertia for the elastic beam elements was calculated by Equation (4.45), which takes into account concrete cracking (Priestley *et al.*, 2007 and Welch, 2016). A summary of all the model properties is presented in Table 4.15.

$$I_e = \frac{M_N}{E_c \phi_N} \tag{4.45}$$

Table 4.15 RUAUMOKO2D model parameters for the RC walls

	4 Story	8 Story	12 Story
Plastic Hinge Length, l_p (m)	0.99	1.77	2.44
Yield Moment, M_N (kN-m)	2948	12072	20786
Post Yield Stiffness Ratio, r (-)	0.015	0.013	0.011
Moment of Inertia, I_e (m^4)	0.07	0.48	1.10
Gross Cross-sectional Area, A_g (m^2)	0.93	1.55	2.02
Effective Shear Area, A_{sh} (m^2)	0.78	1.29	1.68

The modal characteristics of the RC wall buildings obtained using the models described in this sub-section are presented in Appendix A.

4.5.7 Rocking Wall Models

The models for the rocking walls consisted of a series of elastic Giberson beam elements (Figure 4.14) for the wall panel and a zero length rotational spring for the wall/foundation connection (Figure 4.16). The beam elements were characterized by a cracked, linear elastic stiffness of the wall cross-section, and the rotational spring was characterized by a Flag-Shaped Bi-Linear Hysteresis (Carr, 2004). The moment-rotation relationships from the reinforcement design (Section 4.4.2) were used as the backbone of the hysteresis.

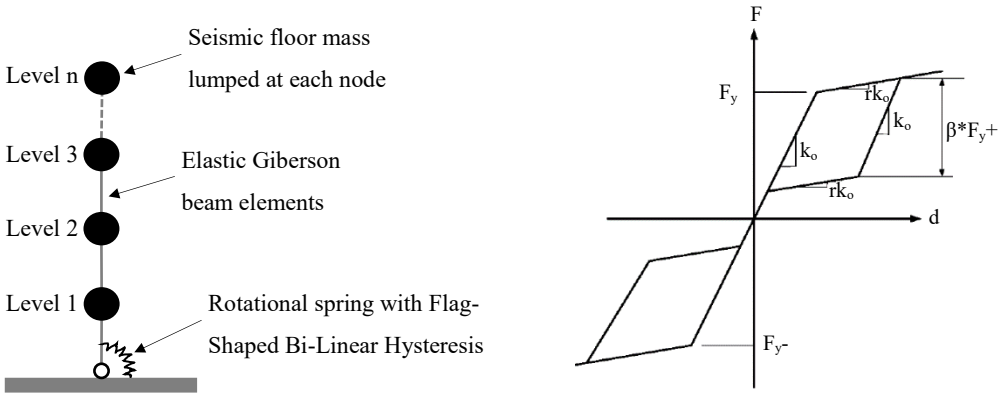

Figure 4.16 Diagram of rocking wall models (left) and flag-shaped bi-linear hysteresis (Carr 2004) (right).

The energy dissipation coefficient β was calculated to be *0.888* from Equation (4.46). The expression was derived by equating an equivalent hysteretic damping model in terms of β, Equation (4.47), and a model in terms of λ, Equation (4.48). The latter was used to generate the damping-ductility curve in Section 4.3.7 (Pennucci *et al.*, 2009). The damping model in terms of β was adopted from Priestley and Grant (2005).

$$\beta = \frac{2}{\lambda + 1} \; for \; r = 0 \tag{4.46}$$

where λ*=1.25* from the displacement based design of the rocking walls (refer to Section 4.3.7).

$$\xi_{hyst} = \frac{(\mu - 1)\beta}{\pi\mu(1 + r(\mu - 1))} \tag{4.47}$$

$$\xi_{hyst} = \frac{2(\mu - 1)}{\pi\mu(\lambda + 1)} \; for \; r = 0 \tag{4.48}$$

The concrete shear modulus was taken as 0.43 times the Young's modulus of concrete (Montejo and Kowalsky, 2007). Effective shear area was taken as 5/6th of total cross-sectional area (Welch, 2016). The moment of inertia for the beam elements was taken as 85% of the gross moment of inertia. Even though rocking walls have been shown to exhibit little to no cracking in experimental investigations (Priestley *et* al., 1999; Rahman and Restrepo, 2000; Belleri *et al.*, 2014; Gavridou, 2015; amongst others), a 15% reduction in stiffness was introduced to account for slight cracking. A summary of all the model properties are presented in Table 4.16.

Table 4.16 RUAUMOKO2D model parameters for the rocking walls

	4 Story	**8 Story**	**12 Story**
Elastic Stiffness, k_o (kN-m/rad)	2.63E+06	1.07E+07	1.80E+07
Yield Moment, M_y (kN-m)	1965	7174	11656
Post Yield Stiffness Ratio, r (-)	0.014	0.011	0.009
Moment of Inertia, I_e (m^4)	0.59	2.74	6.03
Gross Cross-sectional Area, A_g (m^2)	0.93	1.55	2.02
Effective Shear Area, A_{sh} (m^2)	0.78	1.29	1.68

The modal characteristics of the rocking wall buildings obtained using the models described in this sub-section are presented in Appendix A.

4.5.8 Non-structural Elements Modelled with Supporting Structure

When included in the rocking and RC wall models, non-structural elements (NSEs) were modelled as elastic SDOF, mass-spring-damper systems. The springs were modelled with longitudinal spring members and the dampers were modelled with longitudinal dashpot members (Carr, 2004) (Figure 4.17). The spring and damper, which were modeled in parallel, were fixed to the floor level of interest on one end and fixed to the lumped mass of the NSE on the other end. The lumped mass was free to move only in the longitudinal direction. This modelling process was the same for both the RC and rocking walls.

For a non-structural element with a specified mass and natural period, the stiffness of the longitudinal spring member was determined using the fundamental relationship:

$$k = m\left(\frac{2\pi}{T}\right)^2 \tag{4.49}$$

where m is the mass and T is the natural period of the non-structural element.

Subsequently, for a specified damping ratio, the damping coefficient of the longitudinal dashpot member was determined using the fundamental relationship:

$$c = \xi\left(2\sqrt{km}\right) \tag{4.50}$$

where ξ is the damping ratio of the non-structural element.

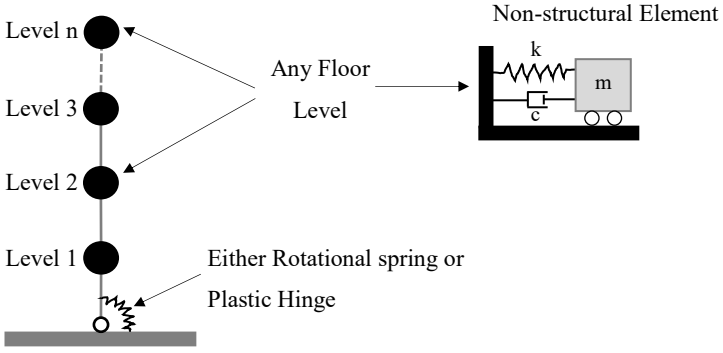

Figure 4.17 Diagram of non-structural element modelled with supporting structural wall

5 DYNAMIC TIME HISTORY ANALYSIS RESULTS

This chapter presents the results of both the linear (LTHA) and non-linear time history analysis (NLTHA) of the case-study RC and rocking wall buildings. From these results, the first section assesses the effectiveness of the displacement based design approach in predicting structural response. The second section addresses the seismic response of rocking wall systems in comparison to RC wall systems. Lastly, the third section presents the key observations that were made from floor response spectra obtained from time history analyses of case study buildings.

The analysis results were collected for all 32 ground acceleration records. Mean values were then computed and used as representative of expected response for the specific earthquake intensity. The dispersion in the data is presented in the form of coefficients of variation.

5.1 Comparison between Analysis Results and Displacement Based Design

This section aims to analyze how well a displacement-based design (DBD) procedure predicts structural response. To this end, NLTHA results for the DBE intensity are compared to DBD outcomes with respect to displacement, interstory drift, moment, and shear envelopes.

5.1.1 RC Wall Buildings

The displacement-based design approach is expected to provide an accurate estimation of displacement profiles, as discussed in Section 4.3. Displacement estimates for the 8- and 12-story RC wall buildings were found to be in good agreement with the analysis results (Figure 5.1). However, the estimates were somewhat non-conservative for the 4- and 8-story buildings. Both buildings had mean interstory drifts exceeding the 2% design drift (Figure 5.2).

Even though base moments were predicted very well, the moment estimates along the height of the buildings (obtained from the capacity design procedure discussed in Section 4.3.6) were found to be somewhat non-conservative for all case study buildings (Figure 5.3), particularly at mid-

height where the higher modes seem to play a predominant role. In contrast, the shear estimates from the procedure compared well to the analysis results (Figure 5.4).

Figure 5.5 summarizes the variability in the analyses results. The coefficients of variation were somewhat high for peak displacement, peak interstory drift and peak base shear. This is to be expected since there is significant variability in earthquake records used in NLTHA even if they are scaled to similar intensities, as also noted by Wiebe (2008). The variability for peak base moments were generally low and decreased with increasing building height.

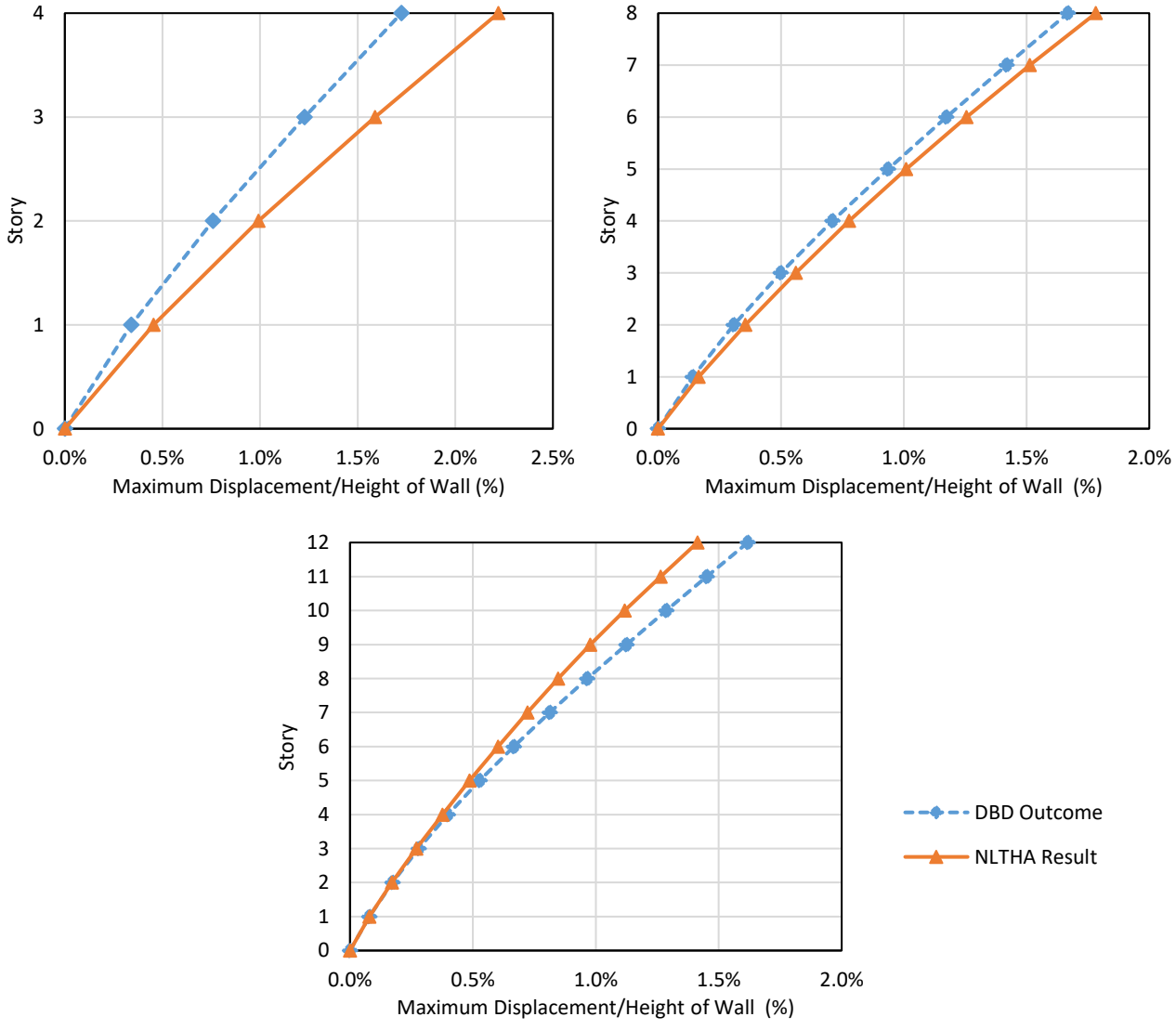

Figure 5.1 Maximum displacement envelope of RC wall buildings from DBD and NLTHA under DBE intensity: (a) 4-Story; (b) 8-Story; (c) 12-story

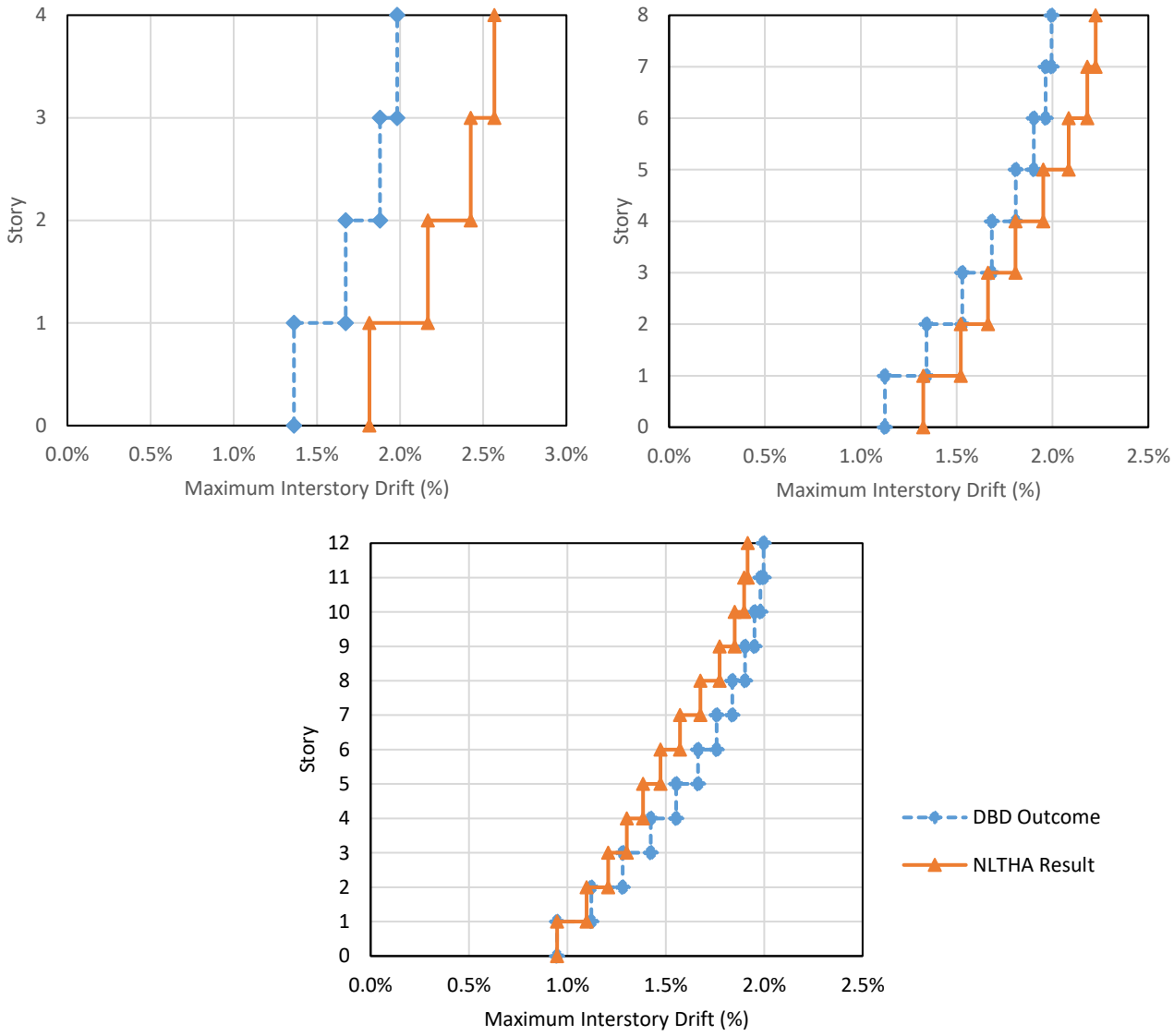

Figure 5.2 Maximum interstory drift envelope of RC wall buildings from DBD and NLTHA under DBE intensity: (a) 4-Story; (b) 8-Story; (c) 12-story

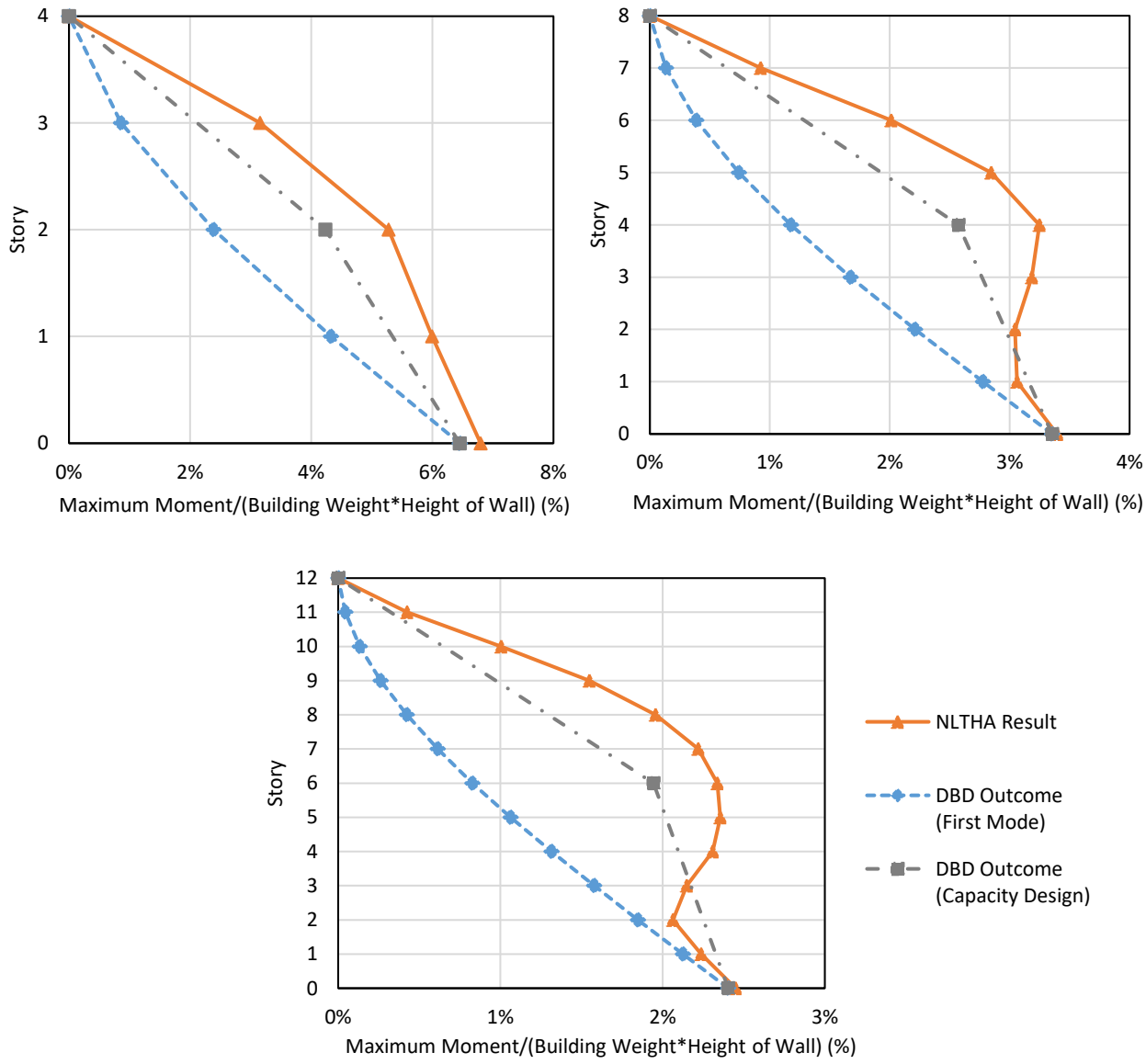

Figure 5.3 Maximum moment envelope of RC wall buildings from DBD and NLTHA under DBE intensity: (a) 4-Story; (b) 8-Story; (c) 12-story

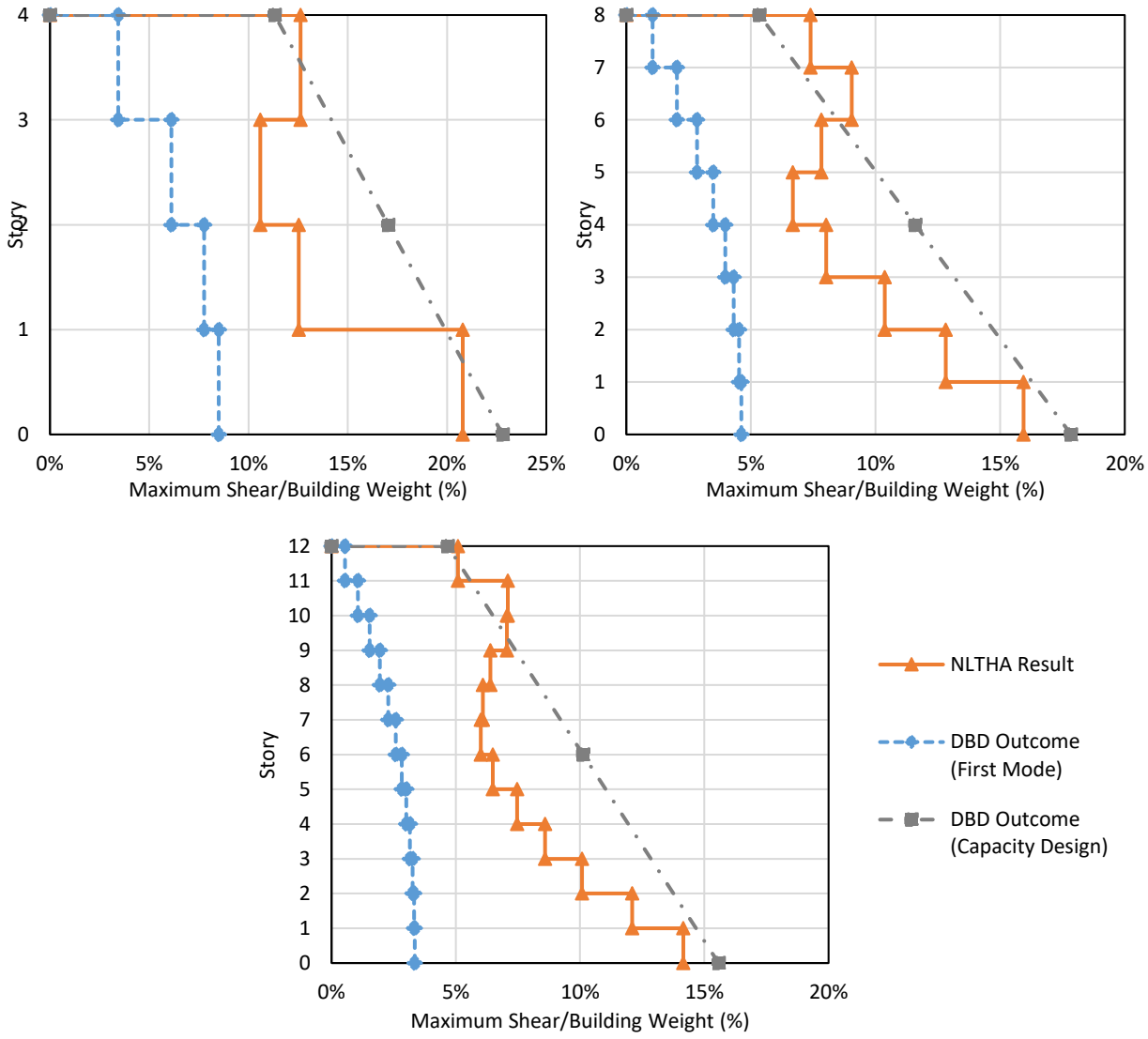

Figure 5.4 Maximum shear envelope of RC wall buildings from DBD and NLTHA under DBE intensity: (a) 4-Story; (b) 8-Story; (c) 12-story

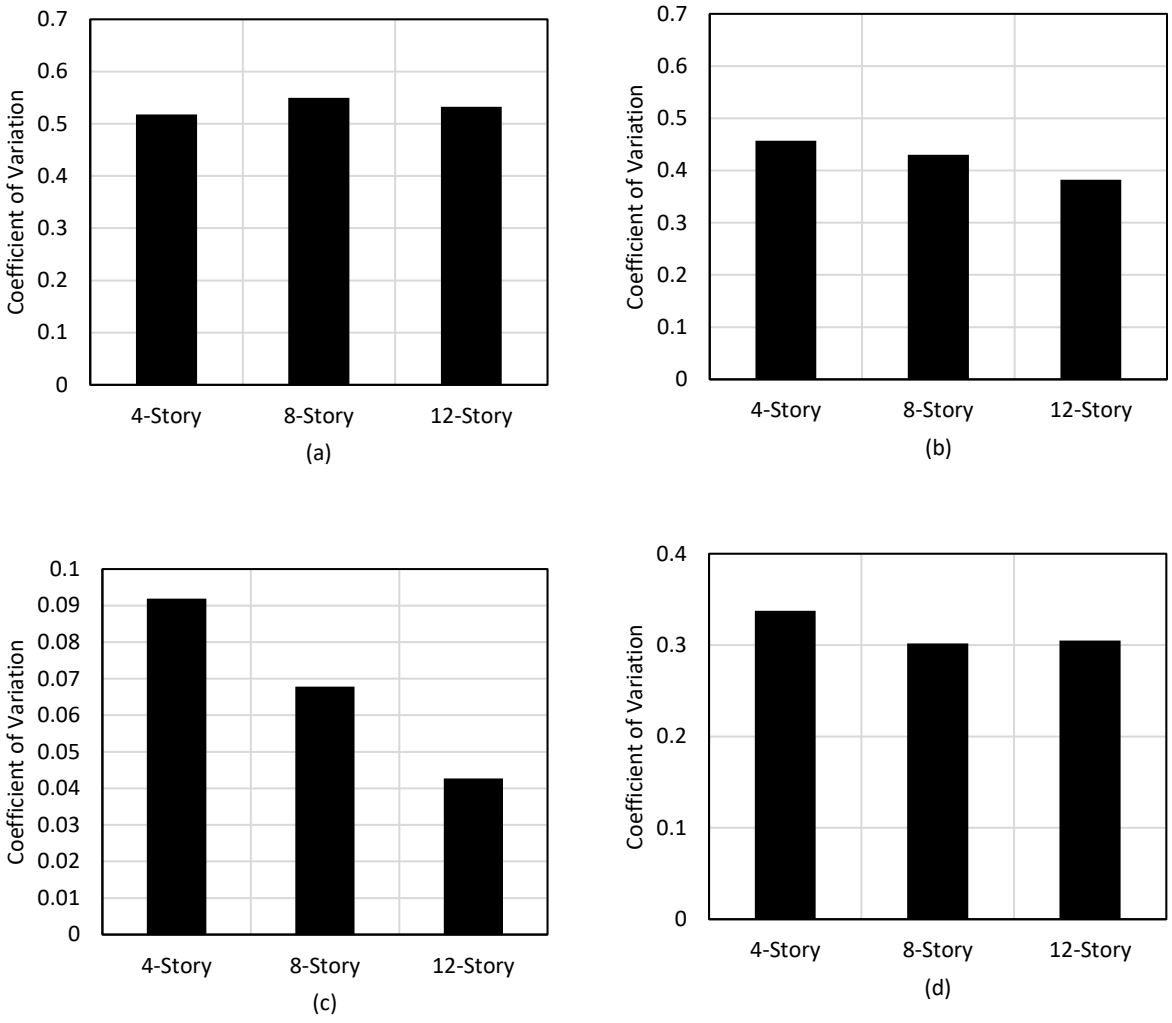

Figure 5.5 RC wall buildings under DBE intensity, variability for: (a) peak roof displacement; (b) peak roof interstory drift; (c) peak base moment; (d) peak base shear

5.1.2 Rocking Wall Buildings

For the rocking wall buildings, displacement estimates were generally acceptable, slightly non-conservative for the 4-story building, but conservative for the 8- and 12-story buildings (Figure 5.6). This is in contrast with the results presented by Pennucci *et al.* (2009) who found that displacement estimates, using the same DBD approach, were in very good agreement with the analysis results regardless of building height. There are two possible explanations for the greater disparity between DBD estimates and analysis results in this study. First, the moment-rotation relationships used in the models were slightly different from the DBD outcomes (Figure 4.12). More specifically, the post-yield stiffness for all three case-study walls was higher in the models.

This could explain the disparity between DBD estimates and analysis results since the majority of wall rotation and displacement is expected post-yield. Secondly, Pennucci *et al.* (2009) used a multi-spring modelling approach, which has been shown to capture the cyclic response of rocking walls with increased accuracy compared to the lumped plasticity modelling approach used in this study (Twigden *et al.*, 2013). In addition, Pennucci *et al.* (2009) could have made different assumptions regarding the elastic stiffness for the wall panels (not explicitly provided in the paper) compared to the 85% of gross stiffness assumed in this study (refer to Section 4.5.7).

The base moment estimates for the 8- and 12-story buildings were in very good agreement with the analysis results (Figure 5.8). However, the estimates for the 4-story wall fell short on the non-conservative side, compared to the analysis results (Figure 5.8). For all case study buildings, the moment and shear distributions above the base of the walls were significantly higher than the first-mode DBD estimates (Figures 5.8 and 5.9). This response is due to higher mode effects and requires appropriate capacity design measures, as discussed by Pennucci *et al.* (2009).

In Section 4.3.7, the RC wall capacity-design procedures were adapted and used for the rocking walls to provide some design means of accounting for the effects of higher modes. This brought a remarkable improvement in the results, with the magnitudes of the "magnified" capacity-design moments approaching those extracted from the analyses. It can be seen in Figure 5.8 that the design values are still somewhat non-conservative, but this is not surprising considering that the procedure was developed and calibrated for RC walls.

Analogous improvements can be observed with respect to the shear force distributions. It can be noted that the "magnified" capacity-design shear profiles represent conservative envelopes of the shear forces obtained from the analyses (Figure 5.9). This suggests that the capacity-design procedure developed for RC walls has potential for use with rocking walls, but more work is needed before the approach can be generalized. To this end, special attention should be given to the modal superposition capacity-design approach (refer to Priestley *et al.* (2007)), which was the basis for the simple design procedure presented in Section 4.3.6.

Figure 5.10 summarizes the variability in the analyses results. Similar to the RC wall buildings, the coefficients of variation for the rocking wall buildings were somewhat high for peak displacement, peak interstory drift and peak base shear, but low for the peak base moment.

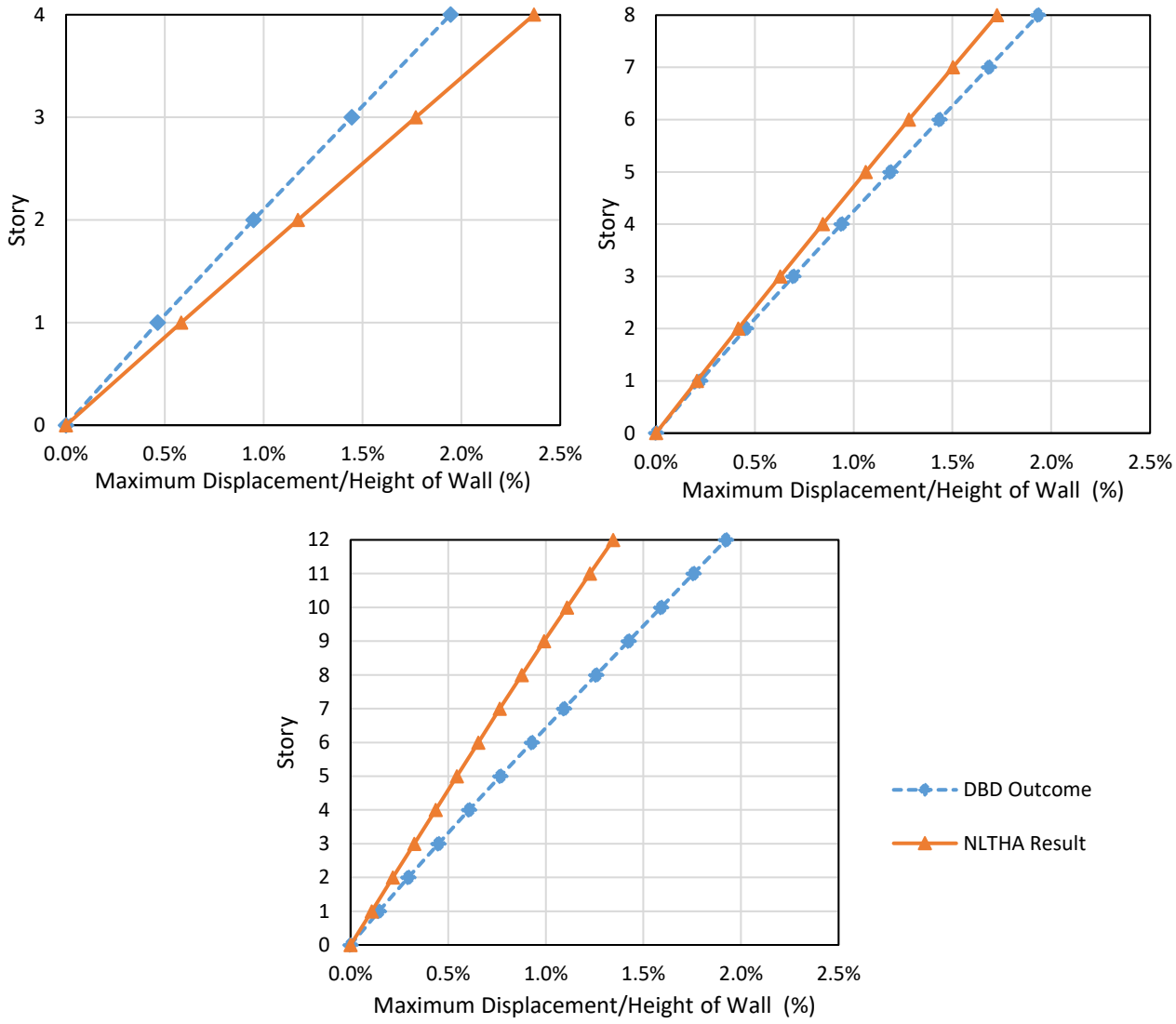

Figure 5.6 Maximum Displacement Envelope of Rocking Walls from DBD and NLTHA under DBE Intensity: (a) 4-Story; (b) 8-Story; (c) 12-story

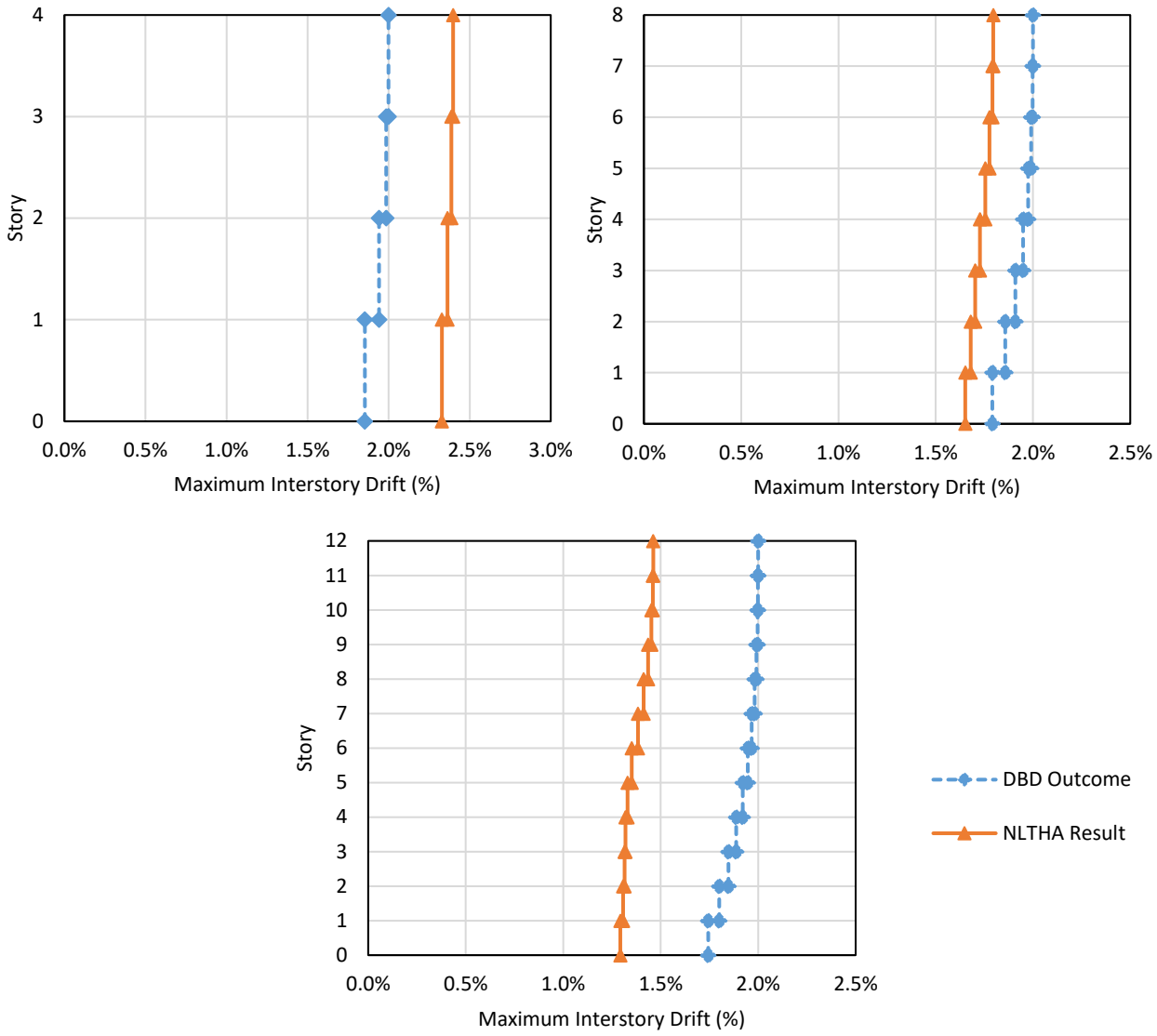

Figure 5.7 Maximum Interstory Drift Envelope of Rocking Walls from DBD and NLTHA under DBE Intensity: (a) 4-Story; (b) 8-Story; (c) 12-story

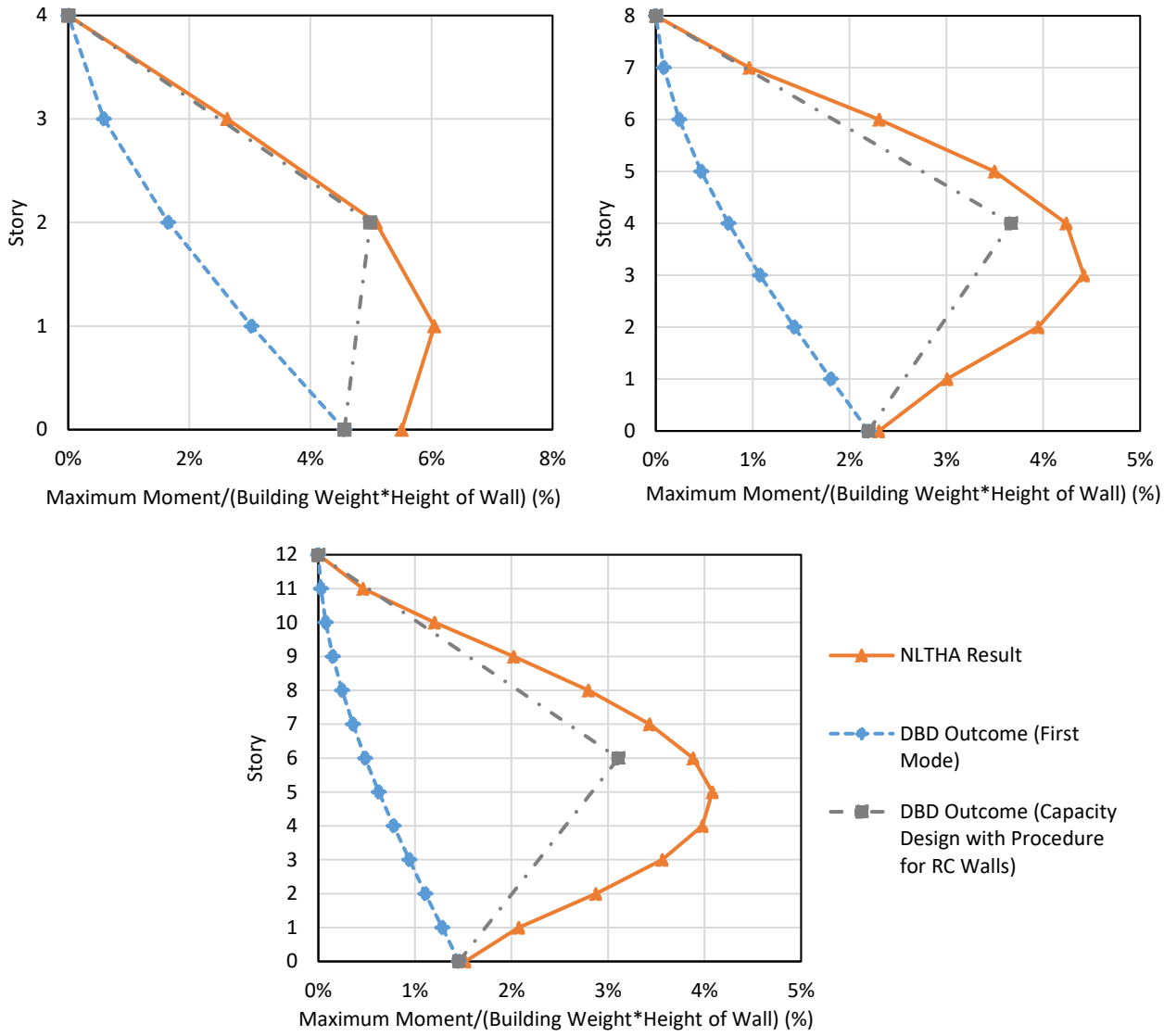

Figure 5.8 Maximum Moment Envelope of Rocking Walls from DBD and NLTHA under DBE Intensity: (a) 4-Story; (b) 8-Story; (c) 12-story

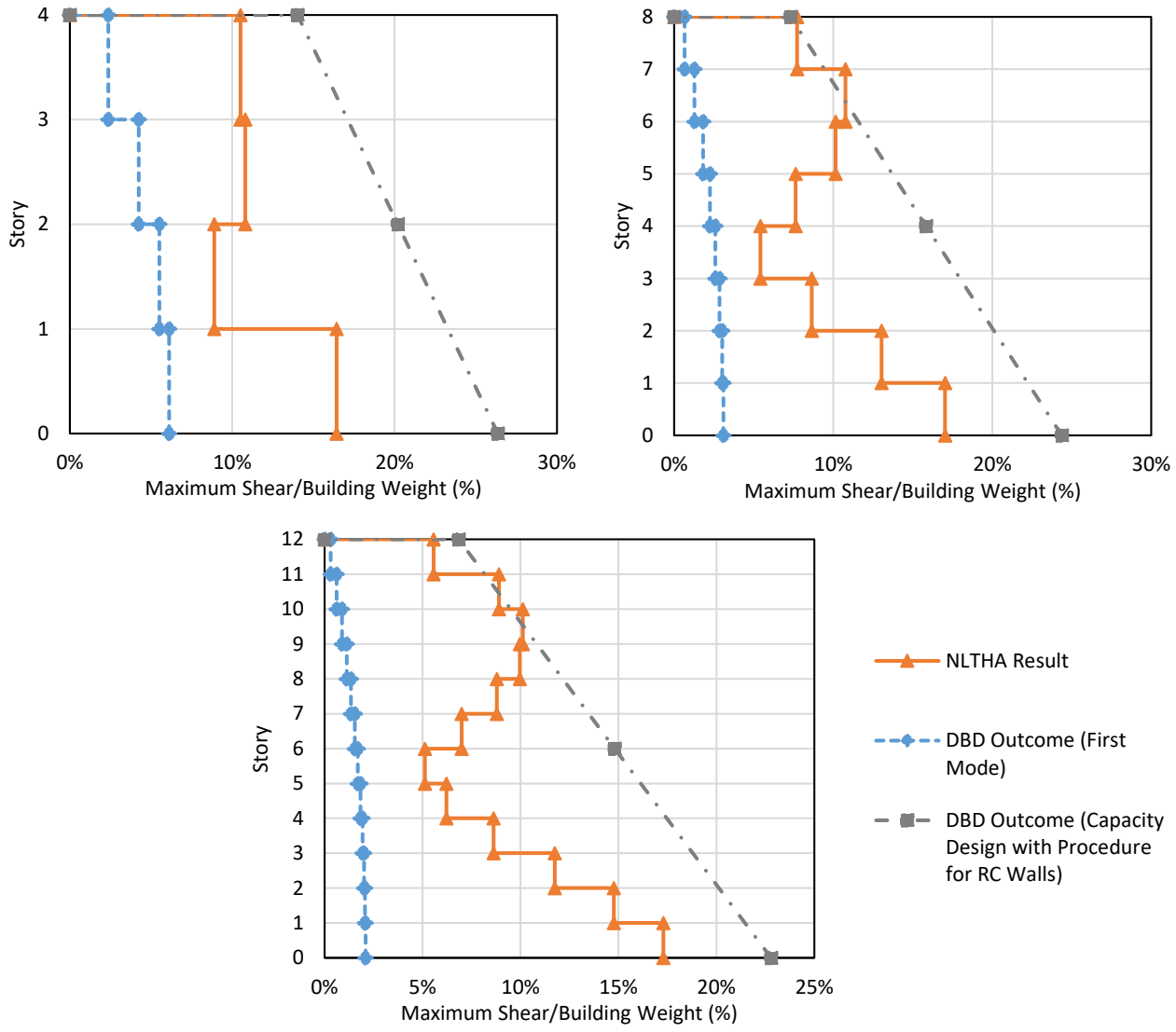

Figure 5.9 Maximum Shear Envelope of Rocking Walls from DBD and NLTHA under DBE Intensity: (a) 4-Story; (b) 8-Story; (c) 12-story

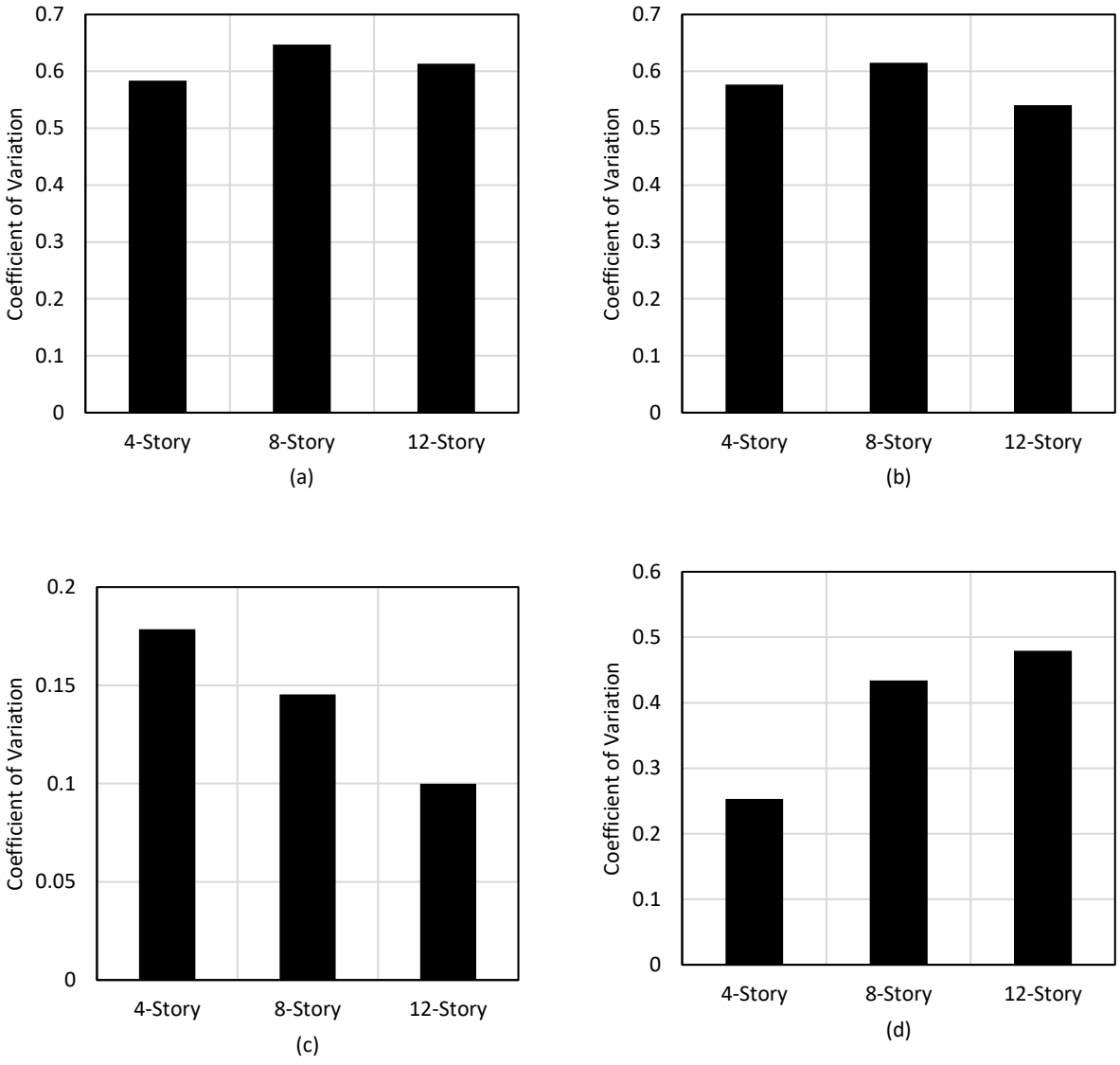

Figure 5.10 Rocking Walls under DBE Intensity, Variability for: (a) Peak Roof Displacement; (b) Peak Roof Interstory Drift; (c) Peak Base Moment; (d) Peak Base Shear

5.2 Comparison between RC and Rocking Wall Buildings

This section aims to compare the seismic response of rocking and RC wall systems based on the results of the non-linear time history analyses at two intensity levels, namely the DBE and the MCE.

5.2.1 Displacement Response

The mean peak displacement responses for the DBE and MCE Intensities are presented in Figures 5.11 and 5.12. Rocking wall peak displacements were comparable to RC wall displacements for the DBE intensity. This is to be expected since both structural systems were designed for a 2% design drift.

Peak displacements were also comparable for the MCE intensity with rocking wall displacements slightly higher than RC wall displacements. This might be an indication that both structural systems are responding similarly to the applied ground motions. The Modified Takeda Hysteresis that was used to model the RC walls is expected to dissipate more energy leading to smaller displacements compared to the flag-shaped hysteresis used to model the rocking walls. However, the rocking walls are much stiffer compared to the RC walls, which might also be reducing the rocking wall displacements, albeit to a smaller extent compared to the impact of hysteresis rules.

Wiebe (2008) found that shorter rocking walls had higher peak displacements than the corresponding RC walls. However, Khanmohammadi and Heydari (2015) found that rocking wall displacements were generally lower than RC wall displacements. It is important to note that both Wiebe (2008) and Khanmohammadi and Heydari (2015) had distinct design and modelling assumptions relative to each other and this study. It is likely that these differences are causing the differences in the findings of each study.

Figure 5.13 summarizes the variability in peak displacement results for both the rocking and RC walls. Both structural systems had somewhat high but similar coefficients of variation.

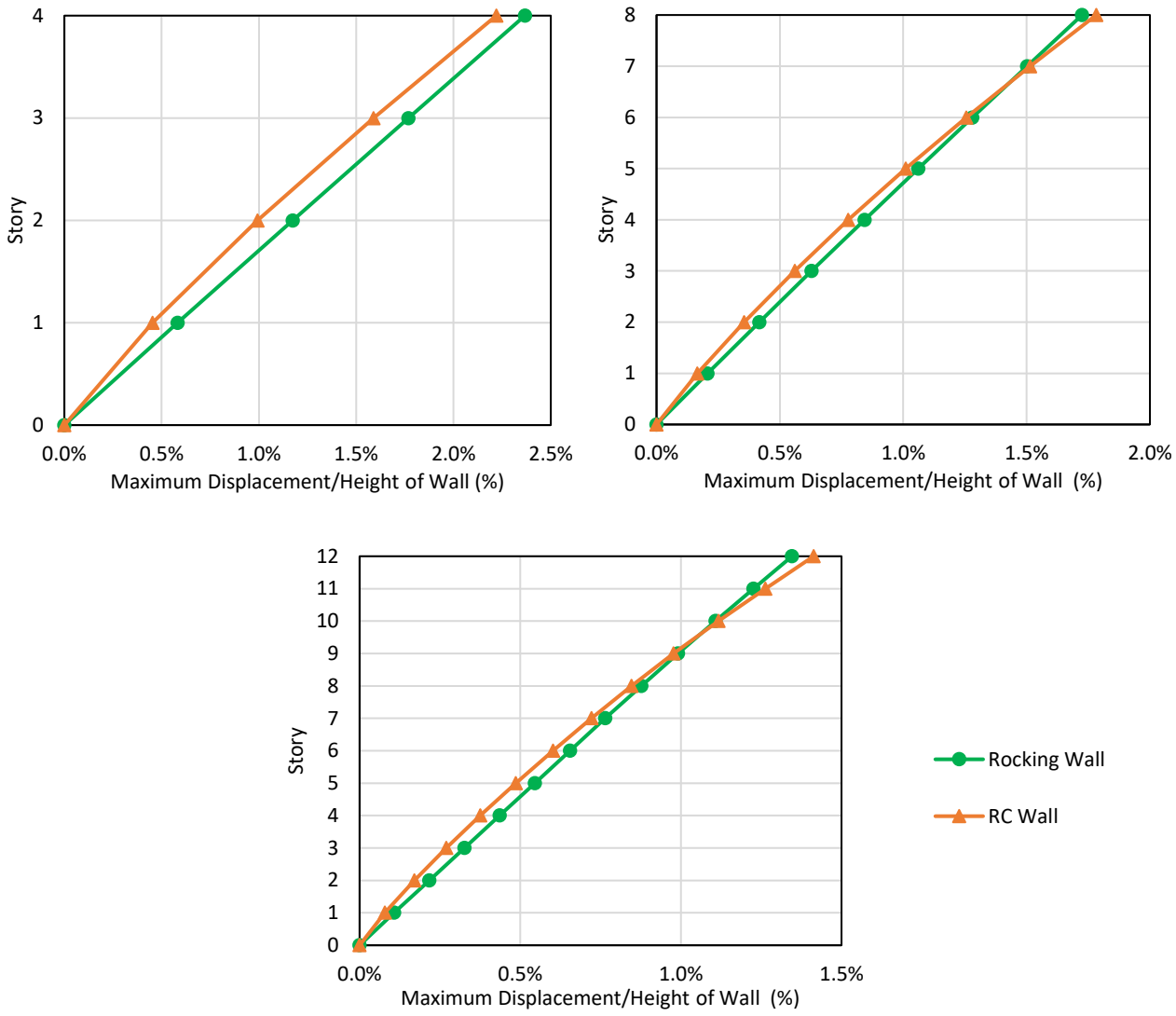

Figure 5.11 Maximum displacement envelope under DBE intensity: (a) 4-Story; (b) 8-story; (c) 12-story

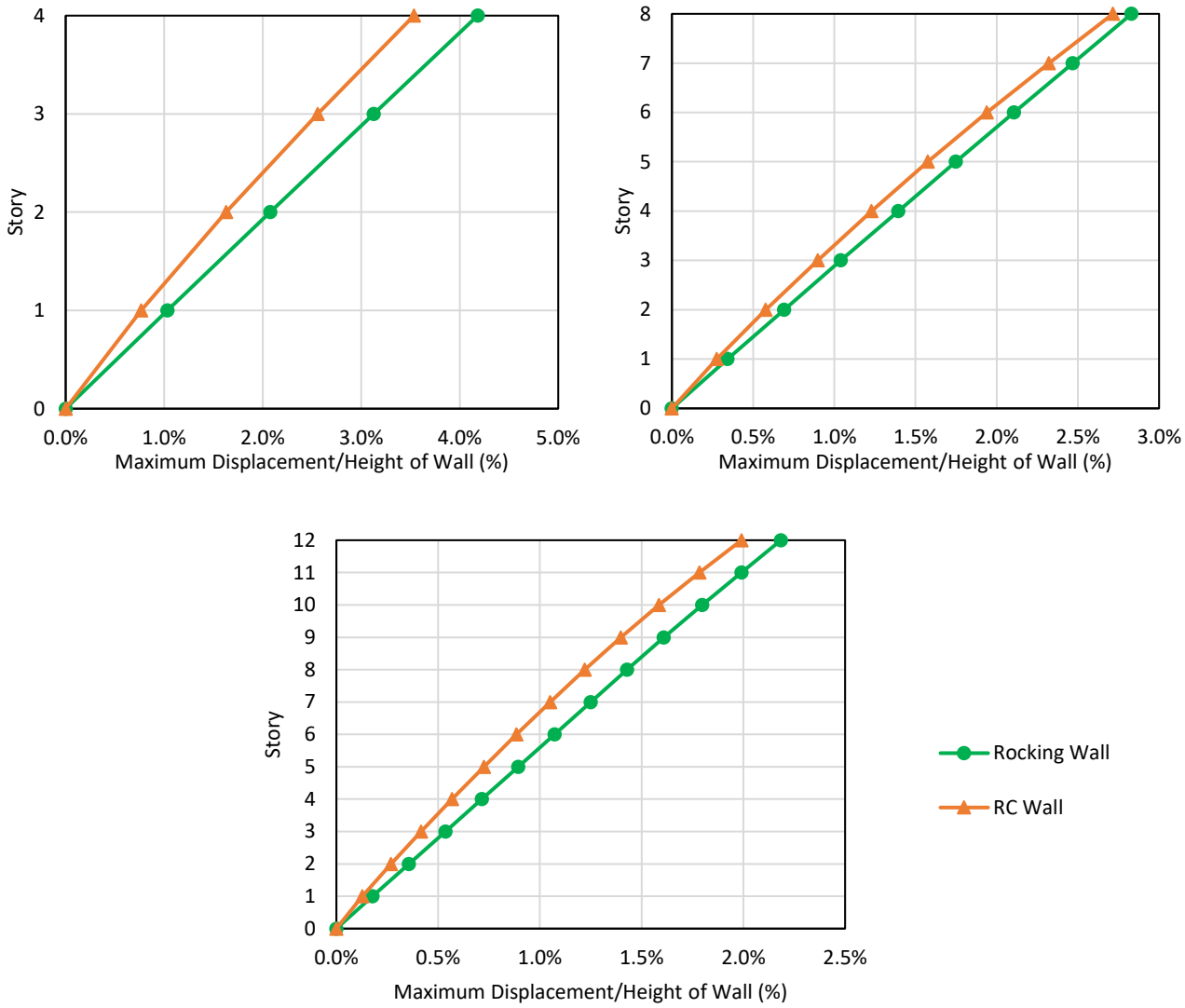

Figure 5.12 Maximum displacement envelope under MCE intensity: (a) 4-Story; (b) 8-story; (c) 12-story

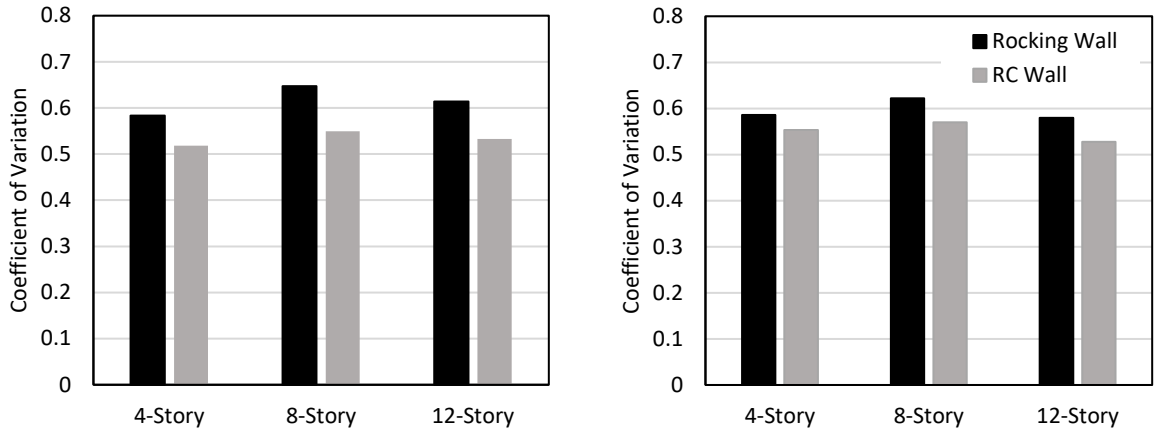

Figure 5.13 Variability in peak roof displacement under DBE (left) and MCE (right) intensities

5.2.2 Interstory Drift Response

The mean peak interstory drift responses for the DBE and MCE intensities are presented in Figures 5.14 and 5.15. Interstory drifts in the rocking walls remained approximately constant regardless of wall height, but the highest values were recorded at the top of the walls. This indicates that the majority of the wall displacement is coming from the rigid body rotation of the wall at the base, which was expected since the wall panels were designed to undergo minor elastic deformation.

In contrast, peak interstory drifts in the RC walls had a more gradual increase from low drift at the base of the walls towards a maximum drift at the top of the walls. This indicates that the deformation in RC walls is more distributed along the height of the walls and not concentrated at the base of the walls.

Figure 5.16 summarizes the variability in peak displacement results for both the rocking and RC walls. Both structural systems had somewhat high coefficients of variation with rocking walls having slightly higher values.

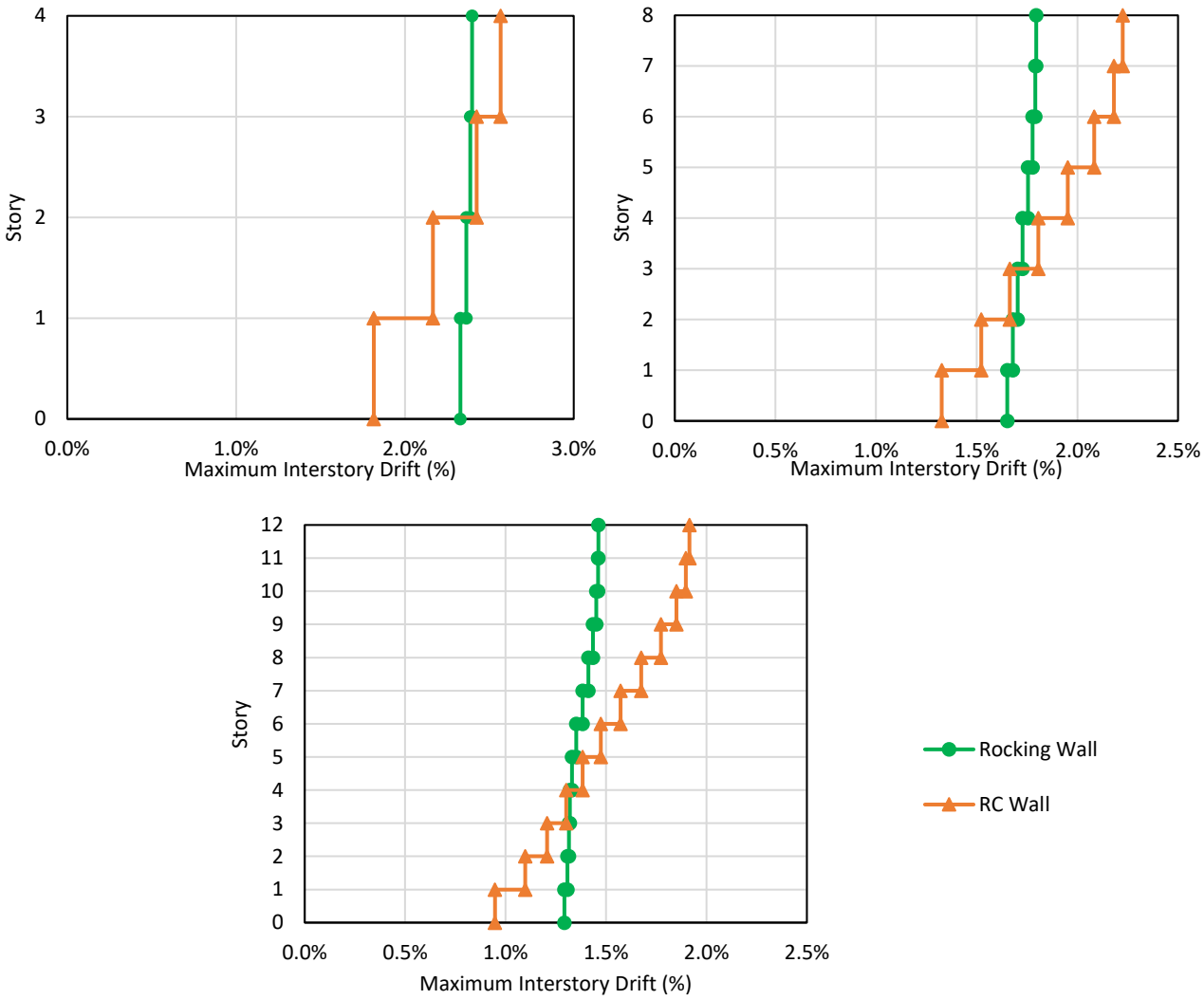

Figure 5.14 Maximum interstory drift envelope under DBE intensity: (a) 4-Story; (b) 8-story; (c) 12-story

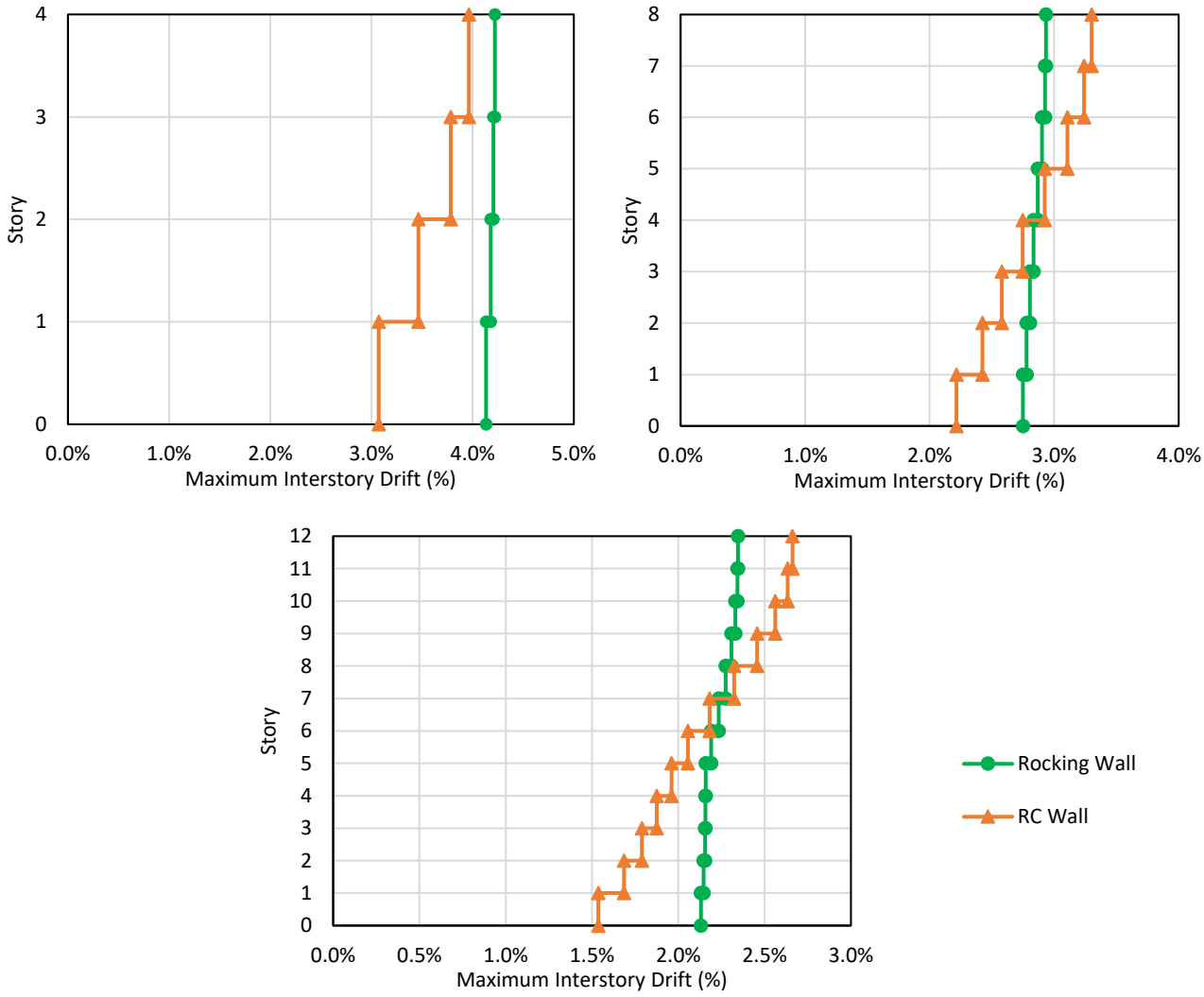

Figure 5.15 Maximum interstory drift envelope under MCE intensity: (a) 4-Story; (b) 8-story; (c) 12-story

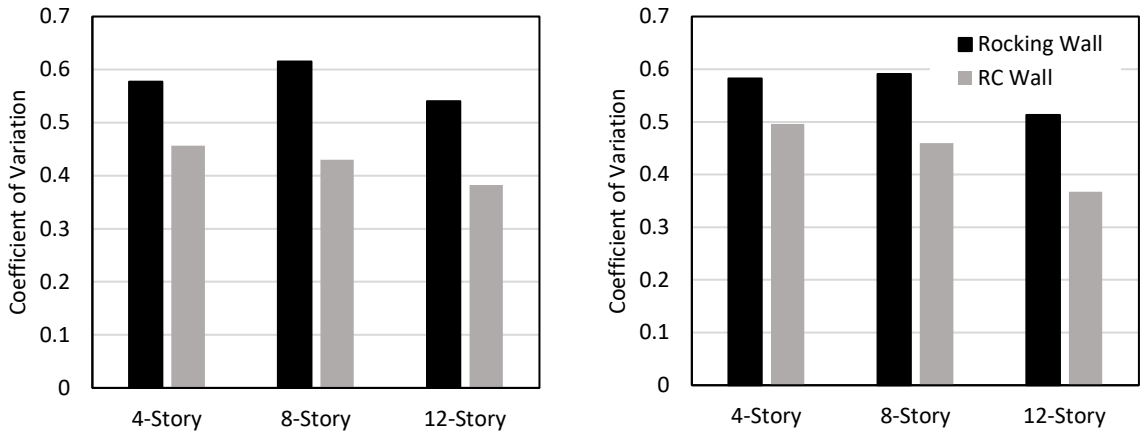

Figure 5.16 Variability in peak Roof interstory drift under DBE (left) and MCE (right) intensities

5.2.3 Residual Displacement Response

The residual displacement responses for the DBE and MCE intensities are presented in Figures 5.17 and 5.18. The rocking walls were found to have significantly less residual displacements compared to the RC walls, which was also observed by Khanmohammadi and Heydari (2015) and Wiebe (2008) amongst many others. This is to be expected since the primary benefit of using a rocking system instead of a traditional monolithic system is the re-centering capability, which leads to a reduction or elimination of residual displacements.

The maximum residual displacements recoded were 0.021% of wall height for the rocking walls and 0.24% of wall height for the RC walls. As reasonable to expect, the highest residual displacements in the RC walls were recorded for the MCE intensity. However, the residual displacements for the rocking walls remained approximately constant for both the DBE and MCE intensities. This indicates very good self-centering properties, which do not depend upon the earthquake intensity or the maximum displacement reached by the structure.

Figure 5.19 summarizes the variability in residual displacement results for both the rocking and RC walls. Both structural systems had high coefficients of variation. This was unexpected for the rocking walls since there was no strength degradation introduced in the models. Once the earthquake excitation is removed, the rocking walls are expected to remain elastic and go into free vibration, which should dampen to a residual displacement of zero regardless of the ground motion applied. Thus, the high variability in the rocking walls could be an indication of insufficient analysis run-time to allow for the dampening of free vibration.

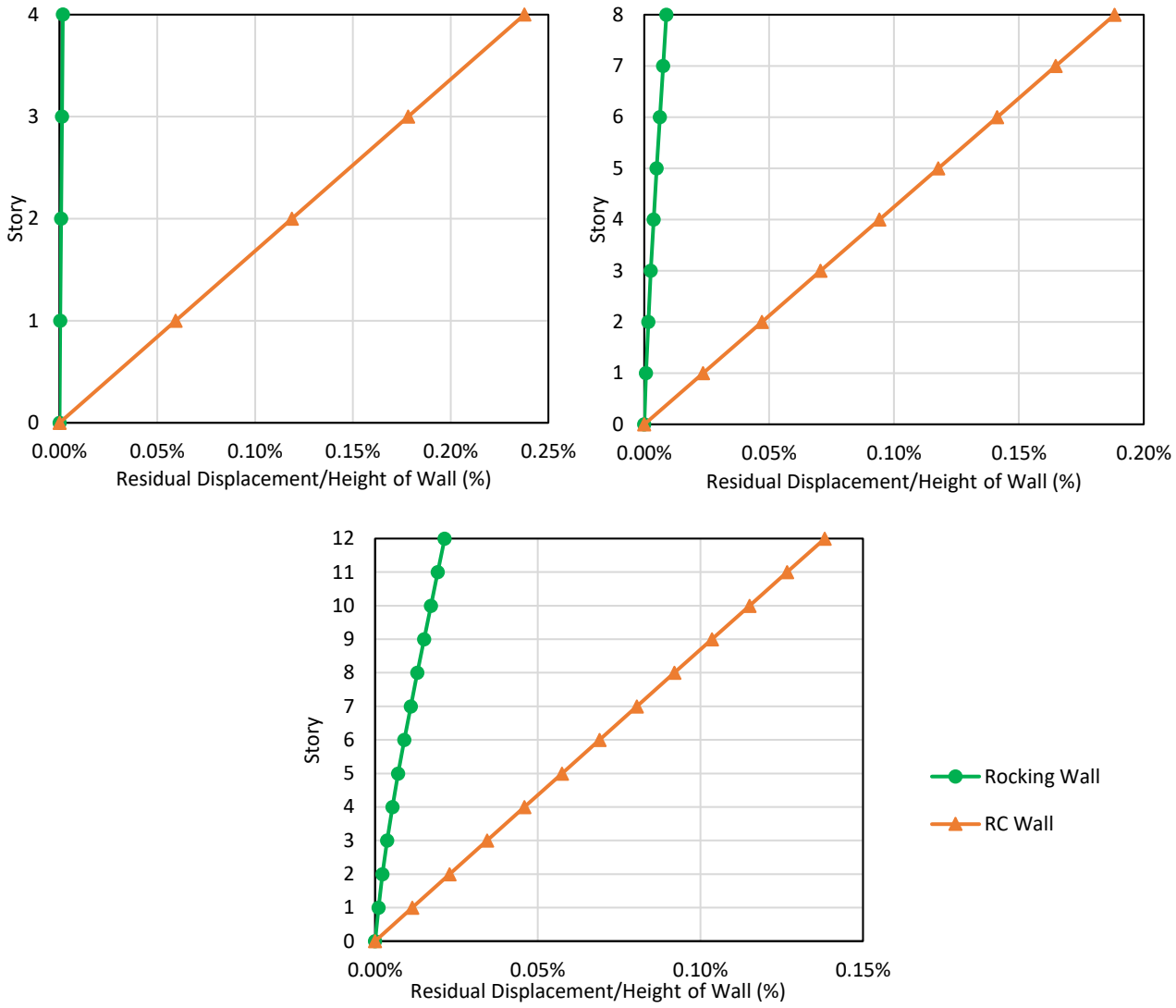

Figure 5.17 Maximum residual displacement envelope under DBE intensity: (a) 4-Story; (b) 8-story; (c) 12-story

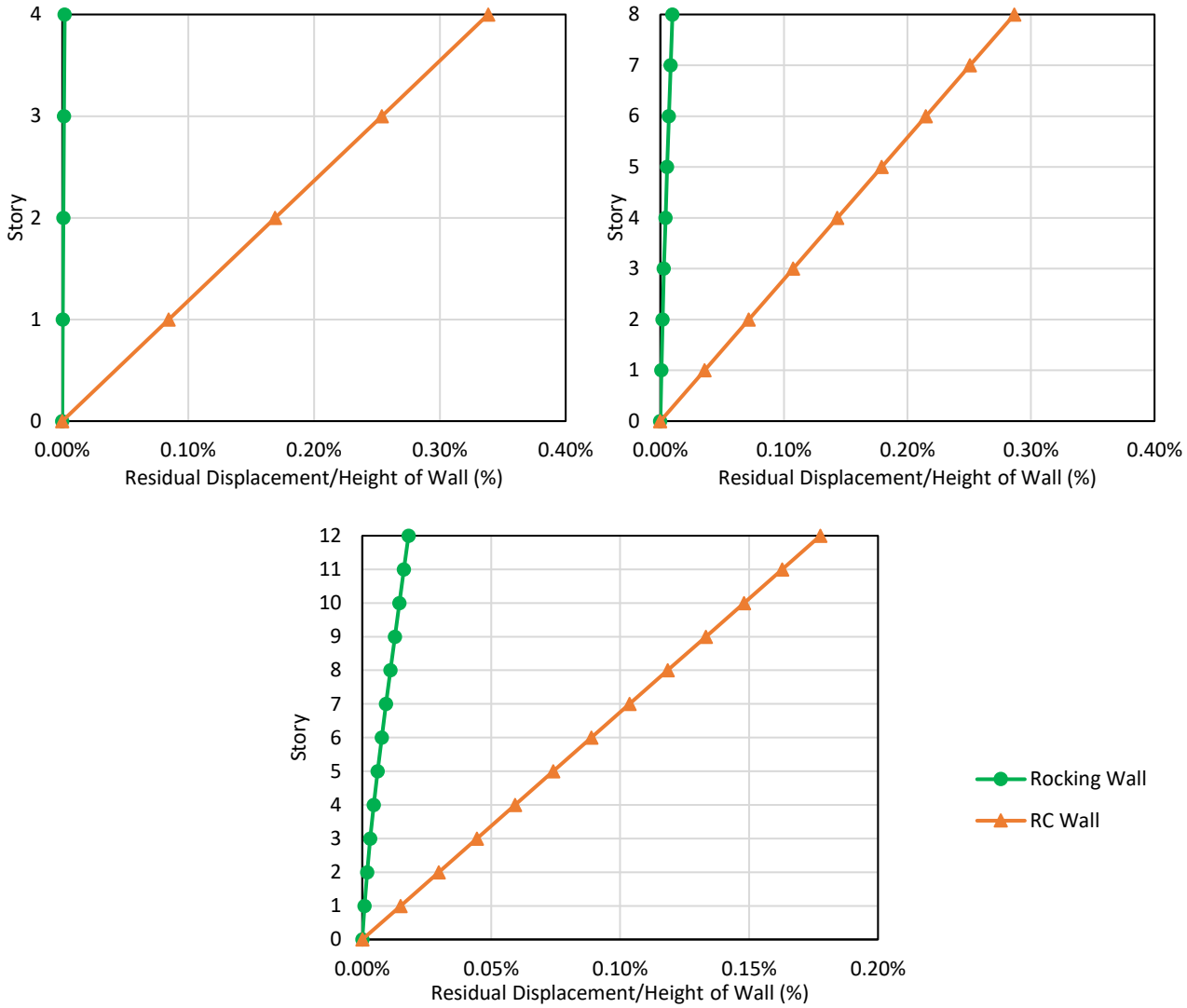

Figure 5.18 Maximum residual displacement envelope under MCE intensity: (a) 4-Story; (b) 8-story; (c) 12-story

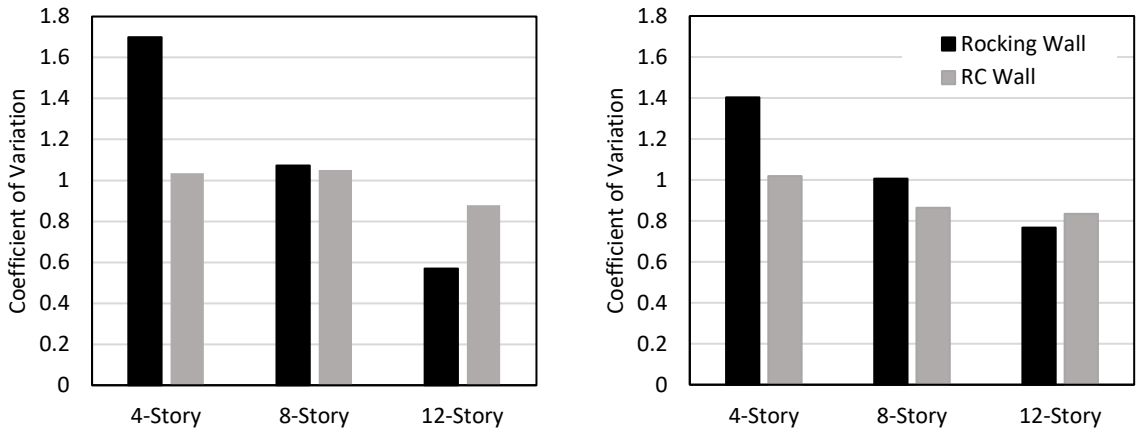

Figure 5.19 Variability in roof residual displacement drift under DBE (left) and MCE (right) intensities

5.2.4 Peak Floor Acceleration Response

The peak floor accelerations (PFAs) for the DBE and MCE intensities are presented in Figures 5.20 and 5.21. The 4-story rocking wall PFAs were found to be comparable to or slightly less than PFAs in the corresponding RC walls for both the DBE and MCE intensities. This trend was also observed in the 8- and 12-story walls but only in the upper half of the walls. For the lower half of the walls and the top two floor levels, the rocking wall PFAs were found to be slightly higher than PFAs from the RC walls.

These results are consistent with results from Khanmohammadi and Heydari (2015) in which PFAs in rocking walls were either comparable to or less than PFAs in the corresponding RC walls. In contrast, Wiebe (2008) found that rocking walls generally had higher PFAs compared to RC walls. As Wiebe (2008) noted, this might be an indication of rocking joints causing an amplification in floor acceleration. However, this was not observed in this study or by Khanmohammadi and Heydari (2015). Wiebe (2008) also pointed out that the high PFAs in rocking systems may be partially due to numerical issues that arise because of modelling assumptions, and specifically because of the decision to idealize a flag-shaped hysteresis using sharp corners. However, this same assumption was maintained in this study and high PFAs were not observed in rocking walls. Thus, the accurate modelling of flag-shaped hysteresis remains an open question and the subject of ongoing research studies.

Figure 5.22 summarizes the variability in PFA results for both the rocking and RC walls. Both structural systems had somewhat high coefficients of variation with rocking walls having slightly higher values.

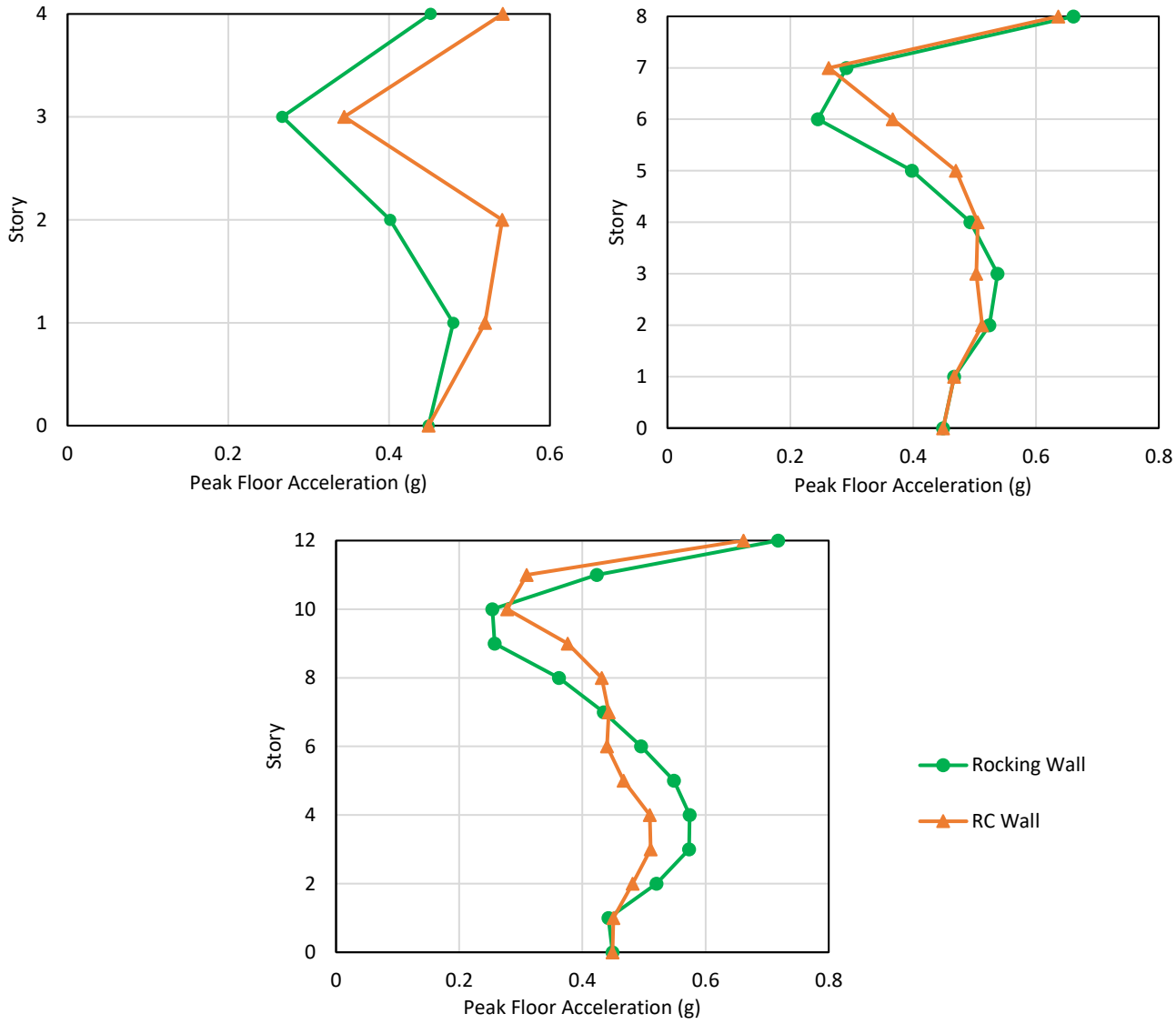

Figure 5.20 Peak floor acceleration envelope under DBE intensity: (a) 4-Story; (b) 8-story; (c) 12-story

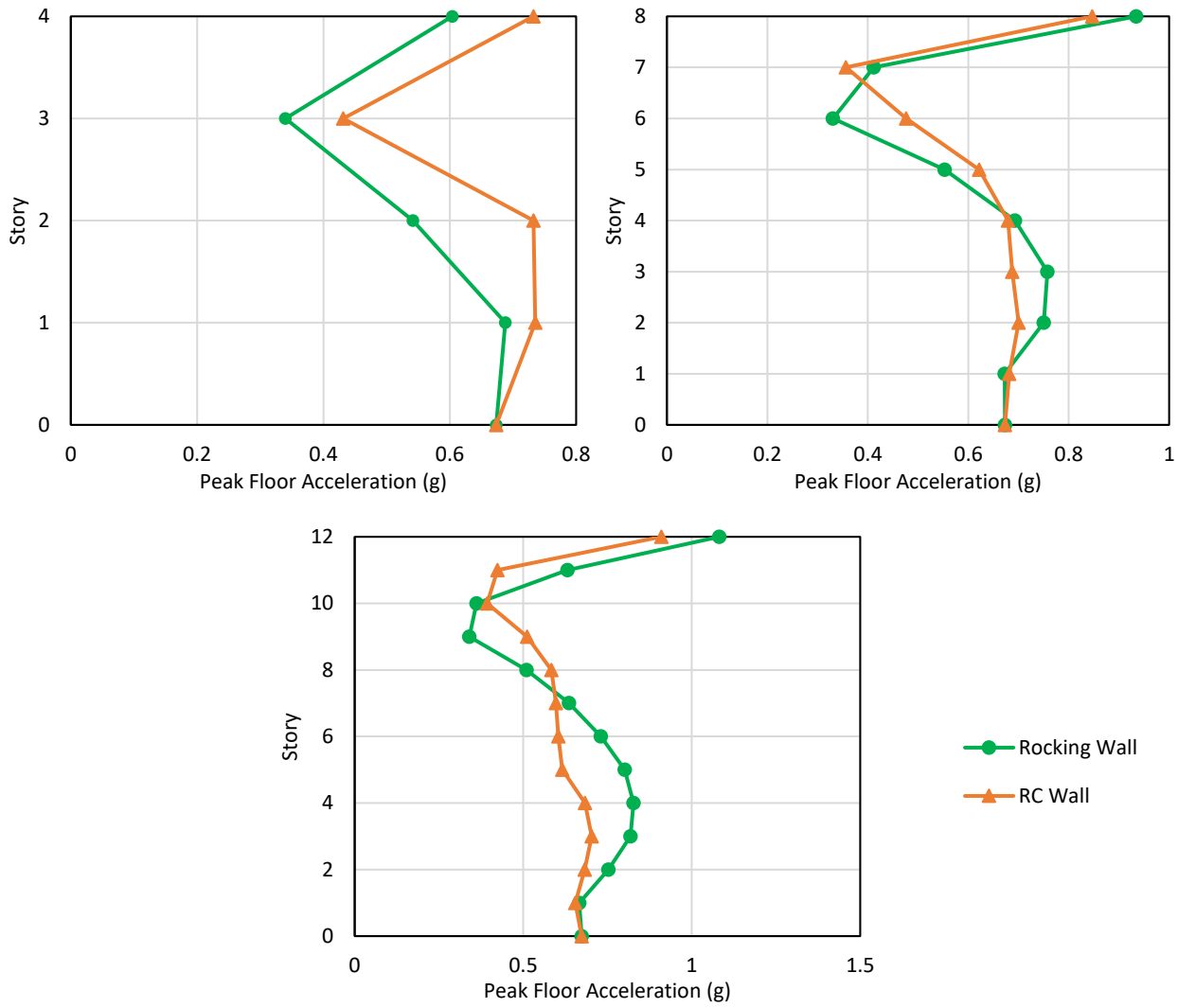

Figure 5.21 Peak floor acceleration envelope under MCE intensity: (a) 4-Story; (b) 8-story; (c) 12-story

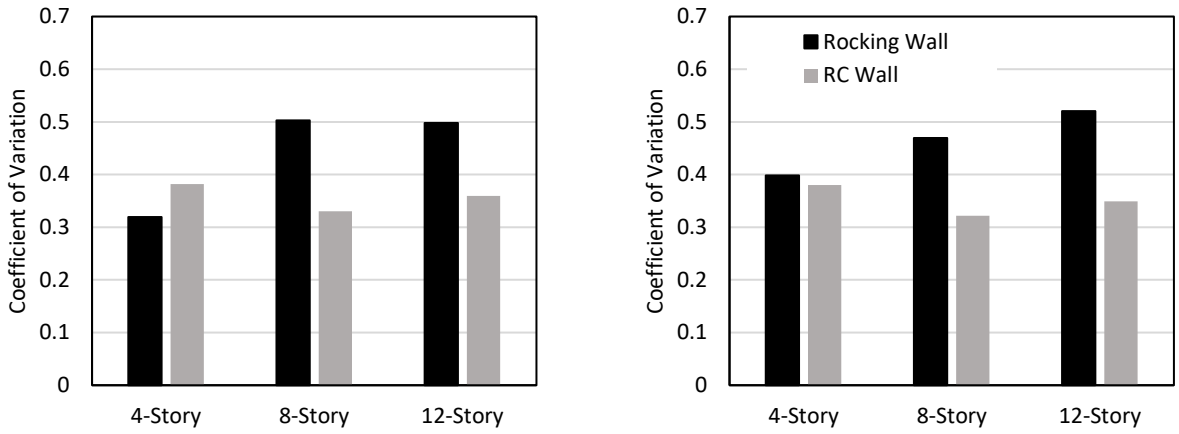

Figure 5.22 Variability in peak roof acceleration under DBE (left) and MCE (right) intensities

5.2.5 Bending Moment Response

The bending moment responses for the DBE and MCE intensities are presented in Figures 5.23 and 5.24. For better comparison, the moment values for all walls were normalized by the base moment resulting from a point load equal to the wall seismic weight acting at the roof. For both the DBE and MCE intensities, the base moments for the rocking walls were lower than the base moments from the corresponding RC walls. This was expected and attributed to the high ductility capacity of the rocking walls (Table 4.6). For a given wall height, the rocking walls had a higher design ductility and effective period than the RC walls, which led to a lower base moment and shear.

In contrast, the rocking wall moment envelopes were either comparable to or higher than the moment envelopes for the RC walls. This suggests that the higher mode effects are more pronounced in rocking than in RC wall systems. In addition, as the height of the walls increased, the rocking wall moments were progressively larger than the RC wall moments over the height of the walls. These results are consistent with results from Khanmohammadi and Heydari (2015) but in contrast with the observations of Wiebe (2008).

Wiebe (2008) obtained rocking wall moments that were similar to RC wall moments over the height of the walls, regardless of wall height. However, it is important to note that Wiebe (2008) modelled the RC walls with an elastoplastic hysteresis, which is in contrast with the Modified Takeda Hysteresis that was used in this study. In addition, the elastic stiffness of the elastoplastic hysteresis was set equal to the elastic stiffness of the flag-shaped hysteresis used to model the

rocking walls. As Sullivan *et al.* (2008) and others note, higher mode response is not affected by inelastic deformation to the same extent as first mode response. This means that higher modes can respond somewhat elastically even when the structure achieves high ductility. Since Wiebe (2008) assumed similar elastic properties for both structural systems, this might explain why higher mode effects were found to be similar for both systems.

Figure 5.25 summarizes the variability in peak bending moment results for both the rocking and RC walls. Both structural systems had low coefficients of variation with rocking walls having slightly higher values.

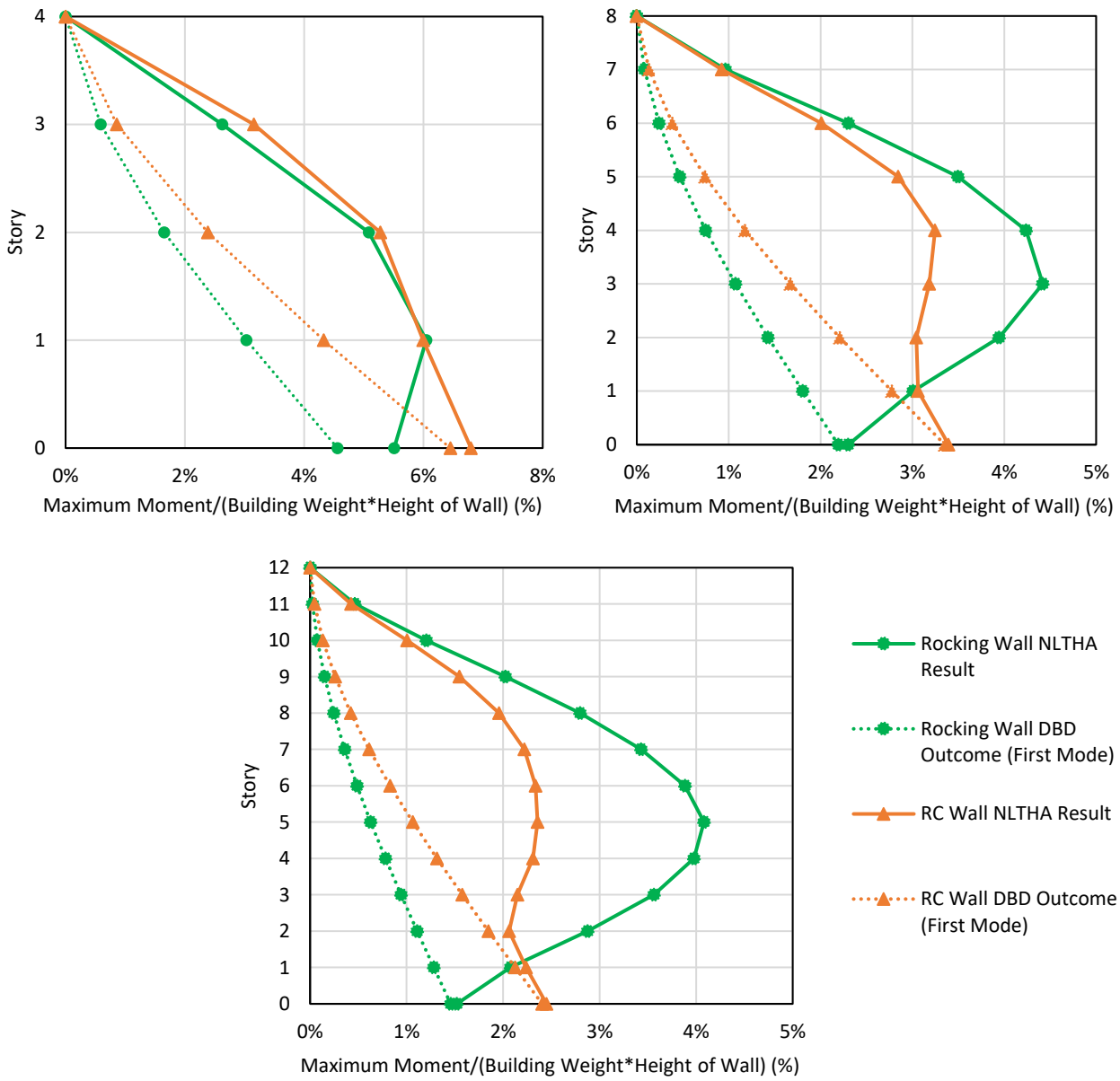

Figure 5.23 Maximum moment envelope under DBE intensity: (a) 4-Story; (b) 8-story; (c) 12-story

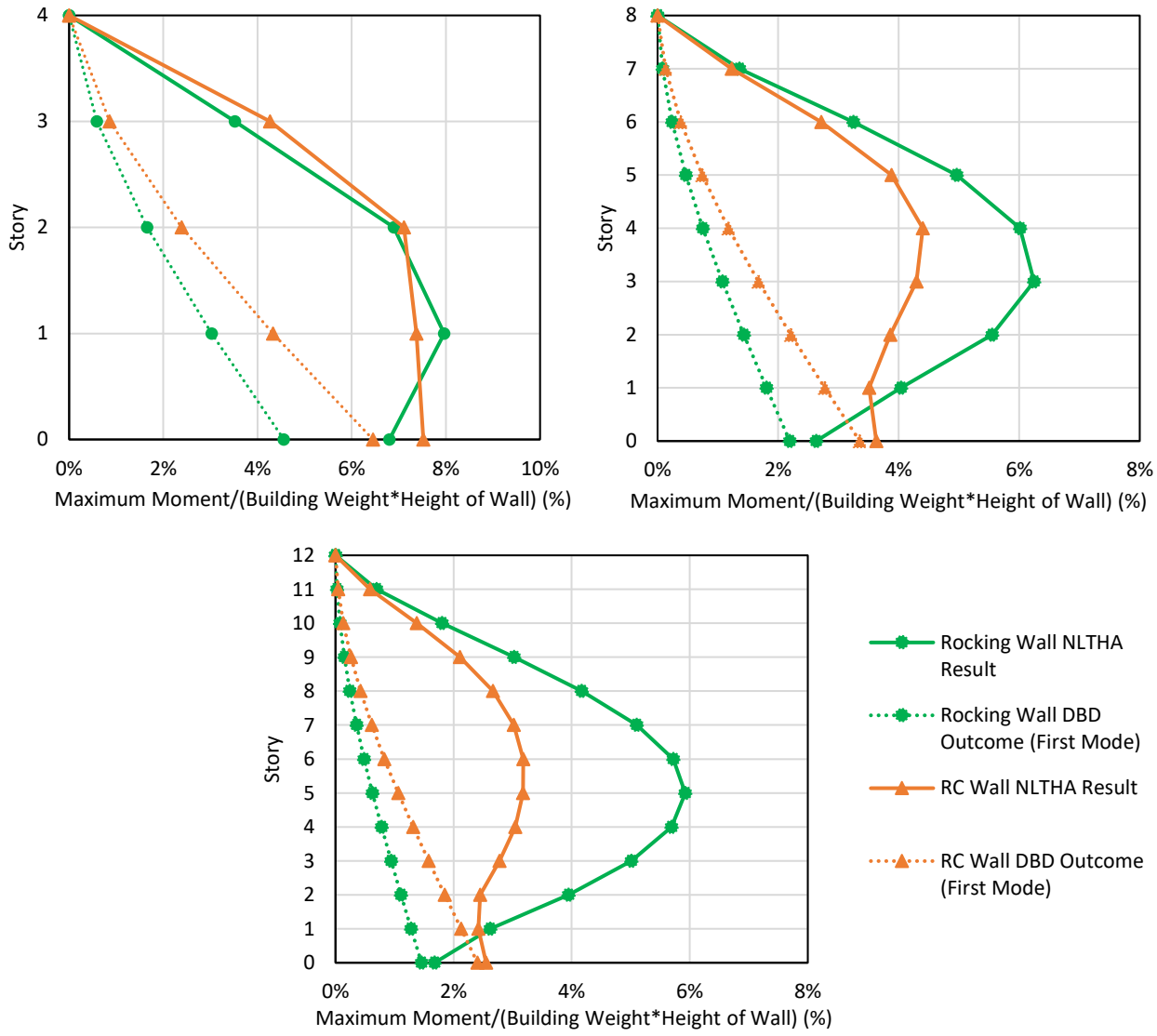

Figure 5.24 Maximum moment envelope under MCE intensity: (a) 4-Story; (b) 8-story; (c) 12-story

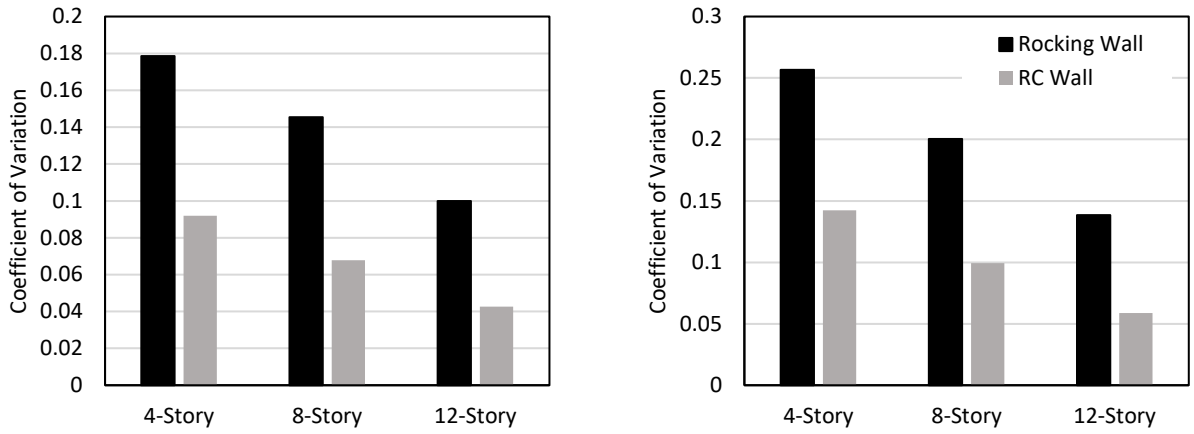

Figure 5.25 Variability in peak base moment under DBE (left) and MCE (right) intensities

5.2.6 Shear Response

The shear responses for the DBE and MCE intensities are presented in Figures 5.26 and 5.27. For better comparison, the shear values for all walls were normalized with respect to the total seismic weight of the wall. As mentioned in the previous section, the rocking walls had lower first mode design shears compared to the RC walls, which is attributed to their high ductility capacity (Figures 5.26 and 5.27). However, for both the DBE and MCE intensities, shear values were generally higher over the entire height of the rocking walls compared to the RC walls, with the exception of the 4-story walls. This suggests that higher mode effects are more pronounced in rocking systems, which is consistent with the observations made in the bending moment response of rocking walls in the previous section.

Figure 5.28 summarizes the variability in peak shear results for both the rocking and RC walls. Both structural systems had somewhat high coefficients of variation with rocking walls having generally higher values.

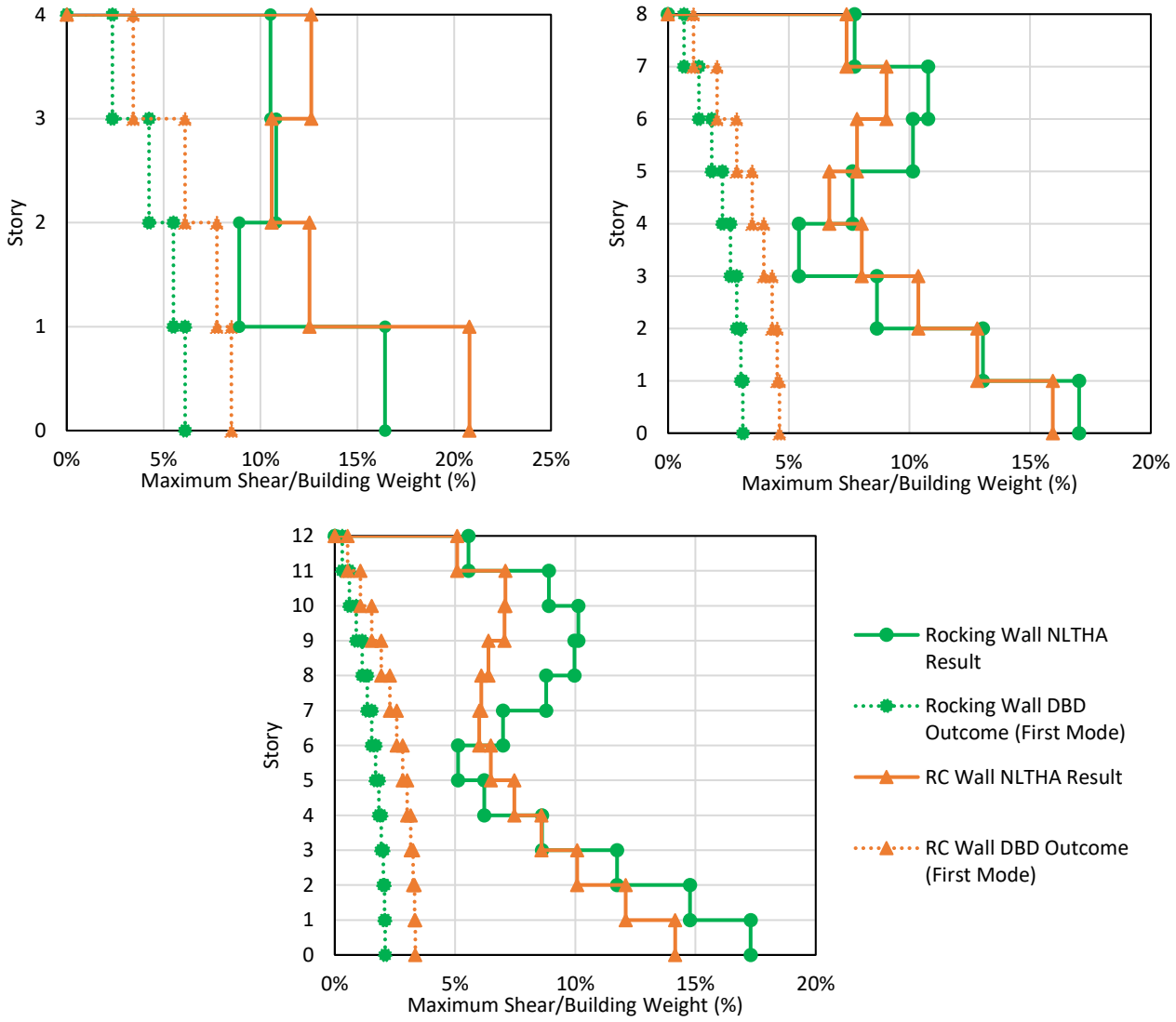

Figure 5.26 Maximum shear envelope under DBE intensity: (a) 4-Story; (b) 8-story; (c) 12-story

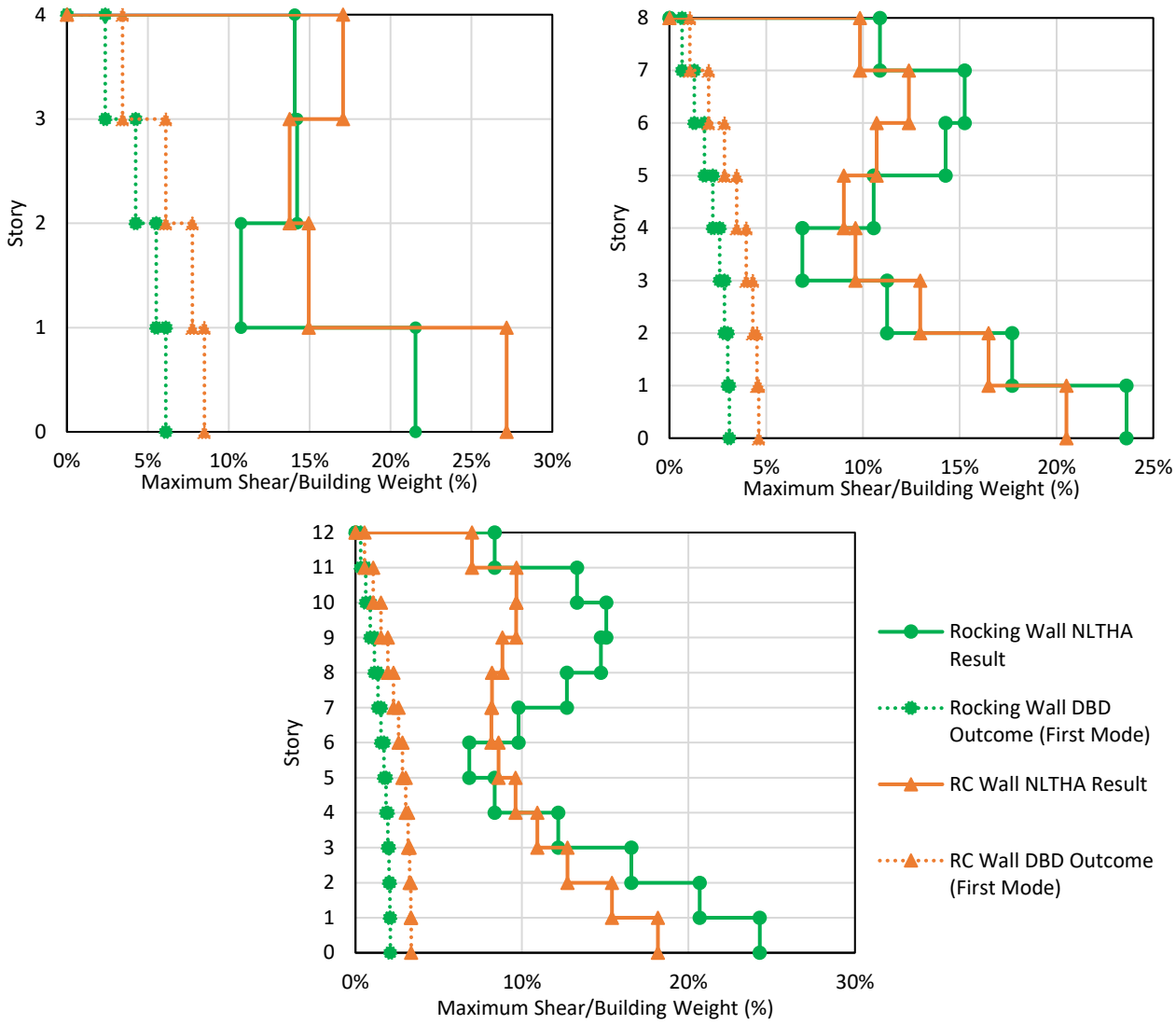

Figure 5.27 Maximum shear envelope under MCE intensity: (a) 4-Story; (b) 8-story; (c) 12-story

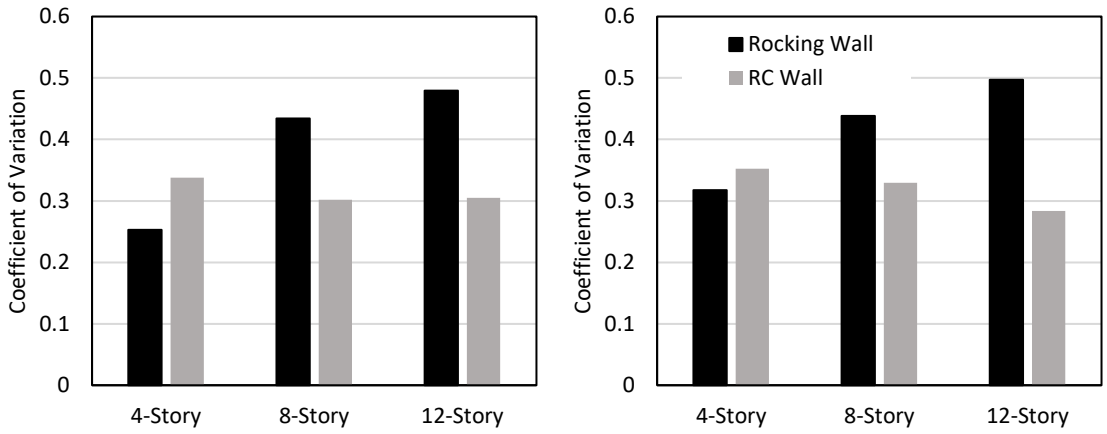

Figure 5.28 Variability in peak base shear under DBE (left) and MCE (right) intensities

5.2.7 Summary

Both structural systems experienced analogous peak displacements and peak floor accelerations. However, the rocking walls had negligible residual displacements compared to the RC walls. This represents the main benefit that rocking systems have over RC systems. The results of the analyses also suggest that the effects of higher modes are more significant in rocking walls, but it is believed that these effects could be mitigated through appropriate capacity design measures.

5.3 Observations of Floor Response Spectra atop RC and Rocking Wall Buildings

This section details the key observations that were made from floor response spectra obtained from both linear (LTHA) and non-linear (NLTHA) time history analyses of the case study buildings. After the time history analyses were conducted, floor response spectra were obtained using DYNAPLOT (Carr, 2004) at four damping levels of 2%, 5%, 10% and 20% of critical damping. From the NLTHA results, floor response spectra were obtained for each floor level at Intensities 1, 5, and 6 (refer to Table 4.13). From the LTHA results, floor response spectra were obtained for each floor level at Intensity 5.

This section also presents the results of the NLTHA that were conducted with non-structural elements modelled with the case-study buildings. Using these results, the dynamic interaction between non-structural elements and supporting structures is discussed.

5.3.1 Parameters Influencing Floor Response Spectra

This section aims to discuss three parameters that have a strong influence on floor response spectra. This includes non-structural element damping, modal characteristics of the supporting building, and inelastic structural response.

5.3.1.1 Non-structural Element Damping

As previously mentioned, floor response spectra were generated at four damping levels of 2%, 5%, 10% and 20% of critical damping for each of the case study buildings. Figure 5.29 shows the effect of non-structural damping ξ_{NS} on the floor response spectra of the 4-story RC wall building responding elastically at Intensity 5, which is representative of overall trends. Corresponding figures for all case-study buildings, and types of structural response (i.e. elastic or inelastic) is provided in Appendix B.

As Figure 5.29 shows, spectral floor acceleration (SFA) demands are strongly dependent on the non-structural element damping ξ_{NS} under consideration. As reasonable to expect, low ξ_{NS} values result in the highest amplification of SFA demands. The influence of ξ_{NS} is highest at modal periods where the spectral demands are also highest since the non-structural element and the supporting structure are in resonance. For very low and high spectral periods as well as spectral periods in between modal periods, the influence of ξ_{NS} is low.

Sample non-structural damping ratios ξ_{NS} and periods T_{NS} are provided in Table 5.1 and Figure 5.30. These values are provided to show the wide range of dynamic properties of non-structural elements that can be expected in buildings.

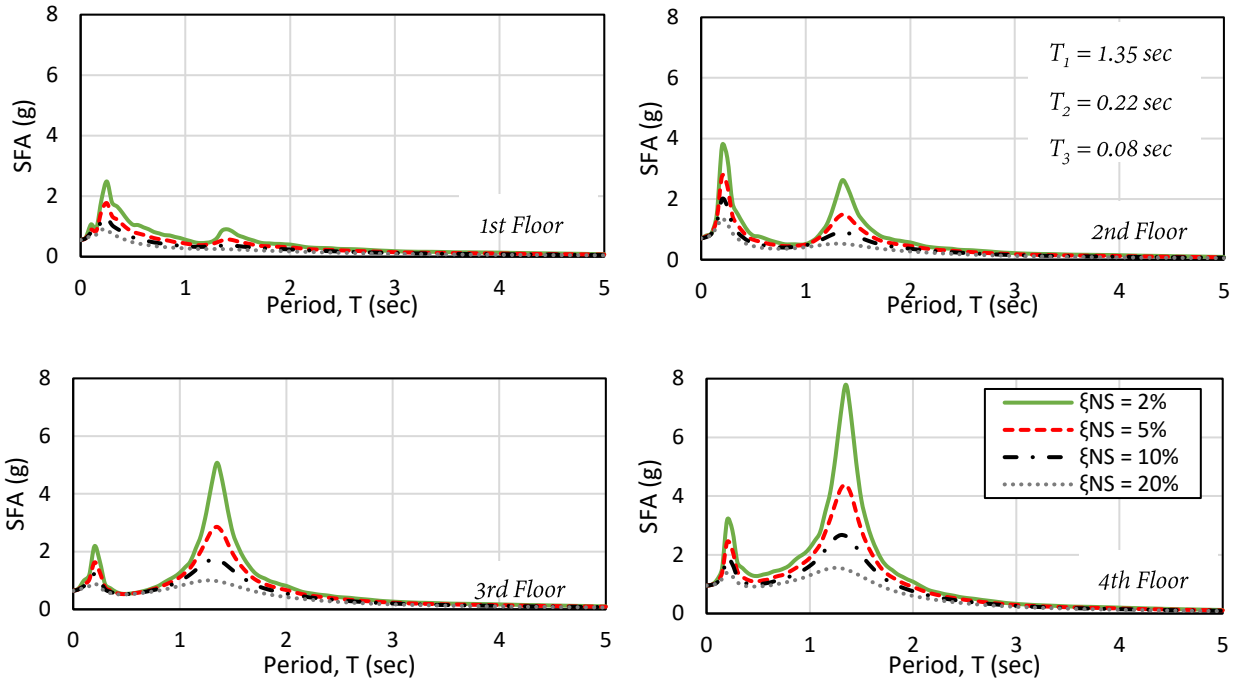

Figure 5.29 Mean floor response spectra atop 4-story RC wall building for fully elastic structural response at Intensity 5 (PGA = 0.450 g)

Table 5.1 Sample non-structural damping ratios and periods from previous studies (Welch, 2016)

Component Type	ξ_{NS} (%)	T_{NS} (%)*	Reference	Notes
Suspended Ceiling	14% - 30%	0.07 – 0.1	Ryu *et al.* (2012)	Analytical/ Experimental
Vibration Isolated Chiller	1% - 3%	0.65 – 0.85	Fathali and Filiatrault (2008)	Experimental
Large HVAC Equipment - Fixed base - Vibration Isolated	 1% 1%	 0.2 1.0	Wanitkorkul and Filiatrault (2008)	Analytical
Sprinkler Piping System** - Black iron, threaded - CPVC, cement joints - Steel, groove joints	9% 13% 10%	0.46 – 0.58 1.87 -2.20 0.80 -0.97	Tian *et al.* (2015)	Experimental
Computer Servers	2%	0.025	Gidaris *et al.* (2016)	Analytical
Filing Cabinet - Fixed-base - Free-standing	13% 17%	0.4 0.5	Marsantyo *et al.* (2000)	Experimental
Unreinforced Masonry Wall with Wood Backing*** (Out of plane motion)	9%	0.16	Paquette *et al.* (2001)	Experimental

* Period correspond to translational modes in horizontal direction.
** Includes main lines, branch lines and bracing; period ranges correspond to the first four modes of branch lines
*** Not included in the original table adapted from Welch (2016)

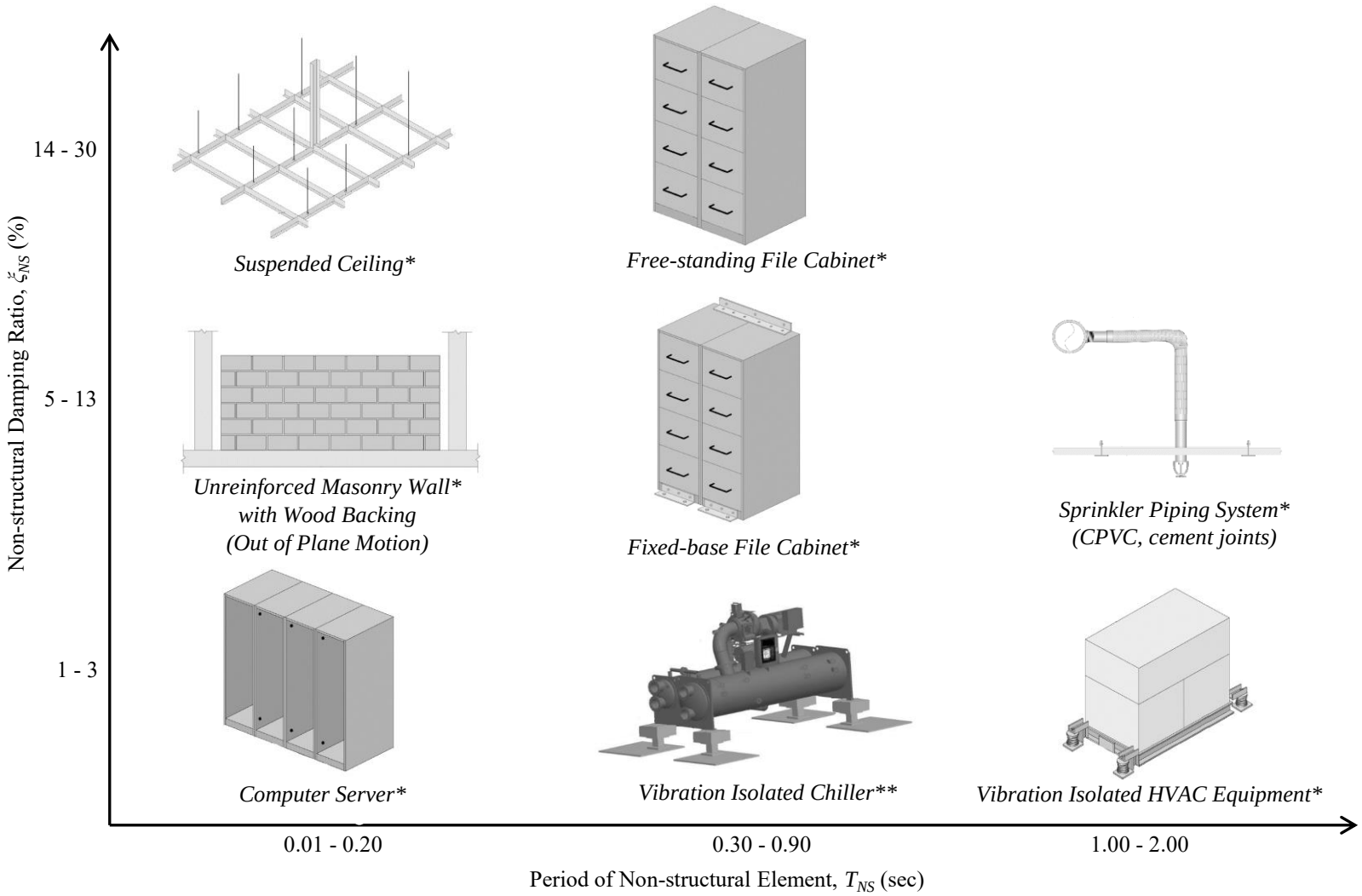

* Image adapted from FEMA (2012) ** Image adapted from Fathali and Filiatrault (2008)

Figure 5.30 Illustration of sample non-structural damping ratio and period ranges (exact values and references provided in Table 5.1)

5.3.1.2 Modal Characteristics of the Supporting Building

Floor response spectra can vary significantly depending on the floor level under consideration. For each floor level, the contributions of each mode to the peak floor acceleration (PFA) depends on the modal coordinates for that floor. Accordingly, SFA demands are also dependent on the modal contributions for the specific floor. The highest SFA demands for each mode occur at the floor level with the highest modal coordinate for the specific mode under consideration.

This is illustrated using the floor response spectra of the 4-story RC wall building responding elastically at Intensity 5 (Figure 5.29), which is representative of overall trends. In the 4-story RC wall building, the highest SFA demands occurred at roof level for the first mode, the second floor for the second mode, and the first floor for the third mode. For all three modes, these floor levels correspond to the floor level with the highest modal coordinate for the respective mode (Figure 5.31).

This observation can be directly used to select the location of non-structural elements. If a non-structural element has a natural period close to the modal periods of the supporting building, it could be placed on floors with the least modal coordinates of the corresponding mode to reduce acceleration demands. For example, if a non-structural element in the 4-story RC wall building has a period close to the second modal period, it could be placed on the first or third floor to reduce acceleration demands. As Figure 5.31 shows, the second and third floors have the lowest modal coordinates for the second mode. This can also be observed in the floor response spectra of the 4-story RC wall building. As Figure 5.29 shows, the lowest acceleration demands for the second mode occur on the first and third floors.

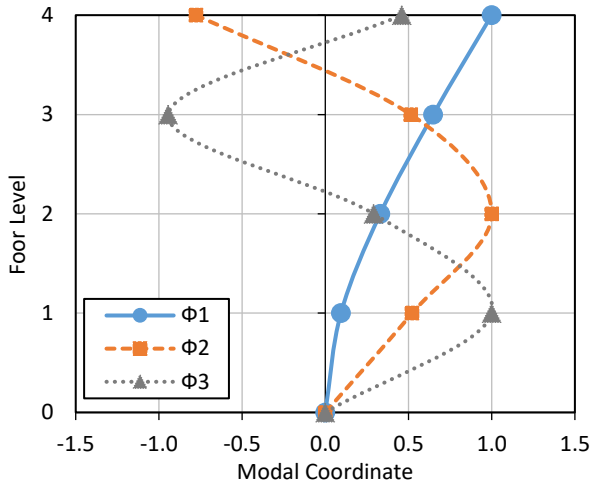

Figure 5.31 Mode shapes of the 4-story RC wall building

5.3.1.3 Inelastic Structural Response

Inelastic structural response has a significant impact of peak SFA demands. As a structure deforms into the inelastic range, energy is dissipated and SFA demands can be reduced. This can be observed in Figures 5.32 and 5.33 in which there is significant reduction in peak SFA demands for inelastic response compared to elastic response for the 8-story RC and rocking wall buildings at Intensity 5. These figures are representative of overall trends and corresponding figures for all case-study buildings are provided in Appendix B.

For both types of structural walls, the reduction is SFA demands is highest in the first mode region. For the RC walls, there is also a significant reduction in SFA demands in the second mode region, albeit to a smaller extent compared to the first mode region. However, for the rocking walls, there is only a minor decrease in SFA demands in the second mode region. This indicates that higher mode response might be more significant in rocking walls, which is consistent with the observations made regarding the bending moment and shear response of rocking walls in Chapter 5.

The third mode contribution to spectral acceleration demands remains nearly elastic for both types of structural walls. This supports the notion that the higher mode response is not affected by inelastic deformation to the same extent as the first mode response.

In addition, inelastic structural response leads to peak SFA demands occurring over a range of periods in the form of a “plateau”. This is due to the modal periods of the supporting structure

lengthening as the supporting structure goes into inelastic deformation. Hence, the resonance condition between the non-structural element and the supporting structure, which leads to peak SFA demands, occurs over a range of periods starting from the elastic period and ending at the effective period of the supporting structure. The extent of period elongation is highest for the first mode and significantly decreases in higher modes.

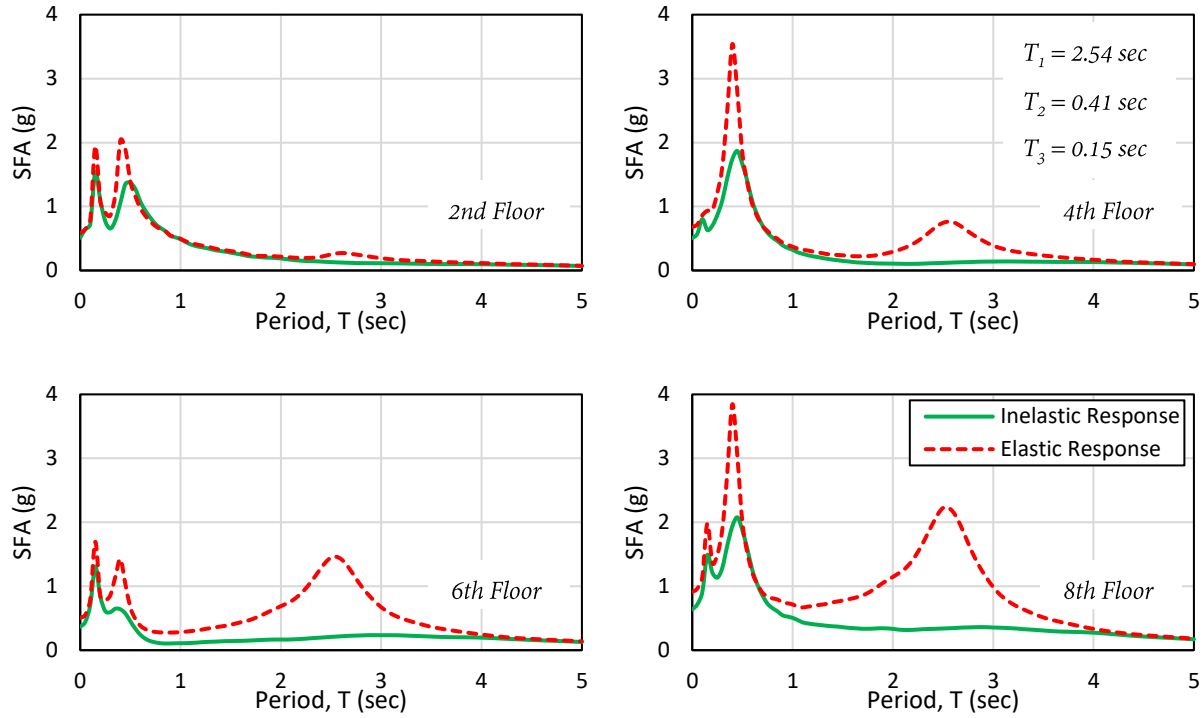

Figure 5.32 Mean floor response spectra atop 8-story RC wall building for fully elastic and inelastic structural response at Intensity 5 (PGA = 0.450 g); ξ_{NS} = 5%

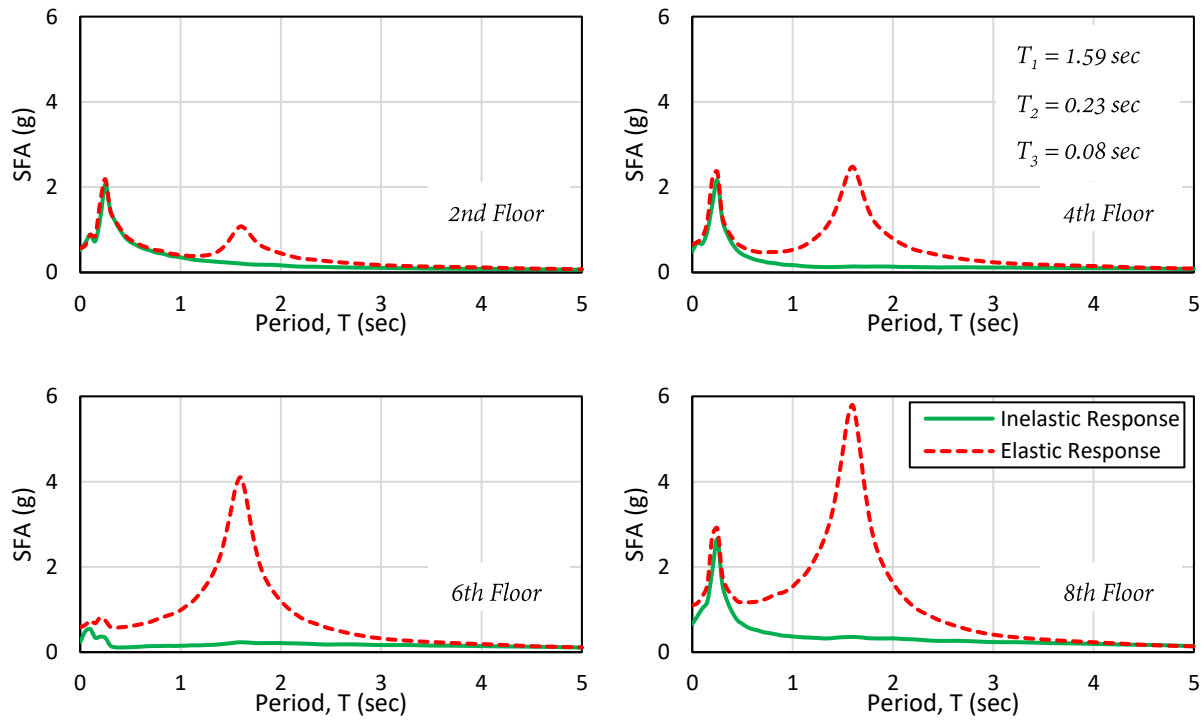

Figure 5.33 Mean floor response spectra atop 8-story rocking wall building for fully elastic and inelastic structural response at Intensity 5 (PGA = 0.450 g); ξ_{NS} = 5%

5.3.2 Dynamic Interaction between Non-structural Elements and Supporting Buildings

One of the main objectives of this present study is to develop procedures for the estimation of floor response spectra (FRS), which can be used for the design of acceleration-sensitive non-structural elements (NSEs). As discussed in Section 3.1, an FRS method is commonly employed for NSEs that have negligible dynamic interaction with the supporting building, and thus FRS are usually obtained from a decoupled analysis. This assumption has typically been considered acceptable for a ratio of NSE mass to total building mass (referred to as mass ratio) of 1% or less (Singh and Ang, 1974; Sankaranarayanan, 2007; Taghavi and Miranda, 2008; Pinkawa *et al.*, 2014; Welch, 2016). However, some have suggested that NSEs and supporting buildings may need to be treated as coupled for mass ratios higher than 0.1% (Toro *et al.*, 1989). Noting the large difference in the mass ratios considered acceptable, this section aims to understand the mass ratio at which dynamic interaction can be considered negligible.

To this end, a coupled NLTHA was conducted in which NSEs with varying mass ratios (MR) were modelled with the case-study buildings according to the modelling procedure in Section 4.5.8. The analysis was conducted using the ground motions from Section 4.5.1 at Intensity 5. The analysis was limited to the 4- and 12-story RC and rocking wall buildings and only included NSEs located at the roof and mid-height floor levels. The NSEs had mass ratios of 0.12% and 0.06%. Each NSE was modelled at four damping levels ξ_{NS}: 0.1%, 2%, 10% and 20% of critical damping. A wide range of NSE natural periods was considered which included the first three modal periods of the supporting building.

Note that for each combination of NSE mass ratio, period, damping, and floor level, a separate model was created that only included the NSE of interest and the supporting building. After the coupled NLTHA was conducted, mean accelerations of the NSEs were obtained, which were then compared to values from a mean floor response spectra obtained from a decoupled NLTHA. The comparisons presented in this section are for the roof level of the case-study buildings. Corresponding figures for mid-height floor levels are presented in Appendix B.

For NSEs with very low damping (0.1%) in the 4-story RC wall building, mean NSE accelerations were approximately equal to acceleration demands from the 5% damped FRS for a wide range of natural periods with the exception of periods close to the fundamental period of the supporting

building (Figure 5.34). This indicates that the coupled models were non-classically damped, and thus the damping of the supporting primary structure was contributing to the damping of the supported NSE. This trend was also observed in the 4-story rocking wall building (Figure 5.35).

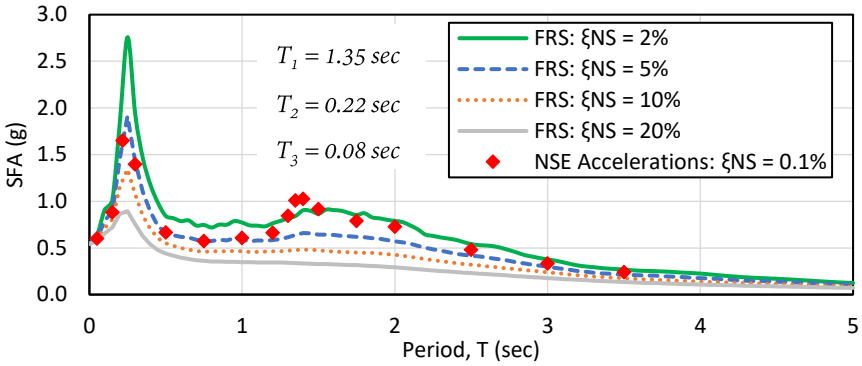

Figure 5.34 Comparison between mean NSE accelerations from coupled analysis (MR=0.12%; ξ_{NS} = 0.1%) and mean FRS at various levels of ξ_{NS} from decoupled analysis; roof level of 4-story RC wall building, inelastic structural response at Intensity 5 (PGA = 0.450 g)

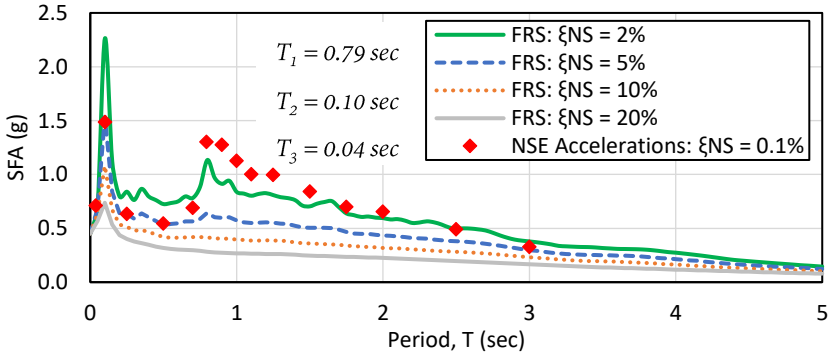

Figure 5.35 Comparison between mean NSE accelerations from coupled analysis (MR=0.12%; ξ_{NS} = 0.1%) and mean FRS at various levels of ξ_{NS} from decoupled analysis; roof level of 4-story rocking wall building, inelastic structural response at Intensity 5 (PGA = 0.450 g)

In general, FRS obtained from the decoupled analyses gave conservative acceleration demand estimates for a wide range of NSE periods. However, FRS estimates were non-conservative for NSEs with periods close to the fundamental period of the supporting building (Figures 5.36 and 5.37). This trend was observed for both mass ratios of 0.06% and 0.12% as well as in all floor levels and case study buildings considered. Interestingly, the lower mass ratio was associated with higher accelerations. This indicates that dynamic interaction between NSEs and supporting structures might be significant even for mass ratios as low as 0.06%.

However, FRS estimates from the decoupled analyses were conservative for NSEs with periods close to the second or third modal periods. This indicates that dynamic interaction may only need to be accounted for NSEs with natural periods close to the fundamental period of the structure.

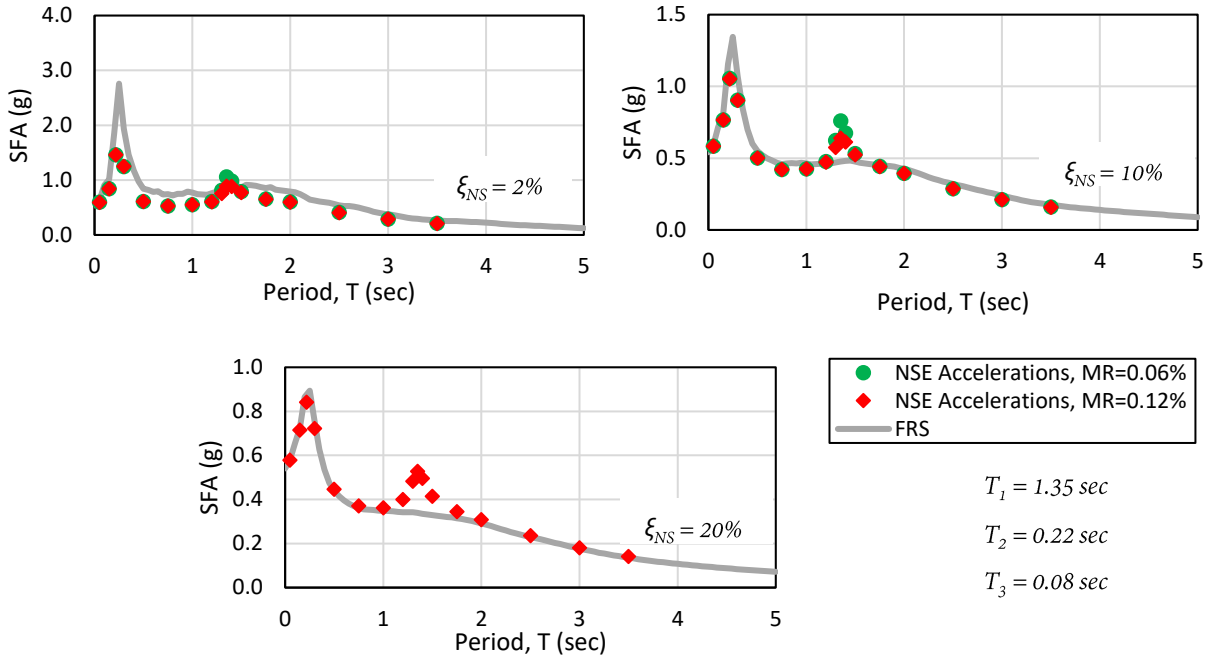

Figure 5.36 Comparison between mean NSE accelerations from coupled analysis and mean FRS from decoupled analysis for roof level of 4-story RC wall building; inelastic structural response at Intensity 5 (PGA = 0.450 g)

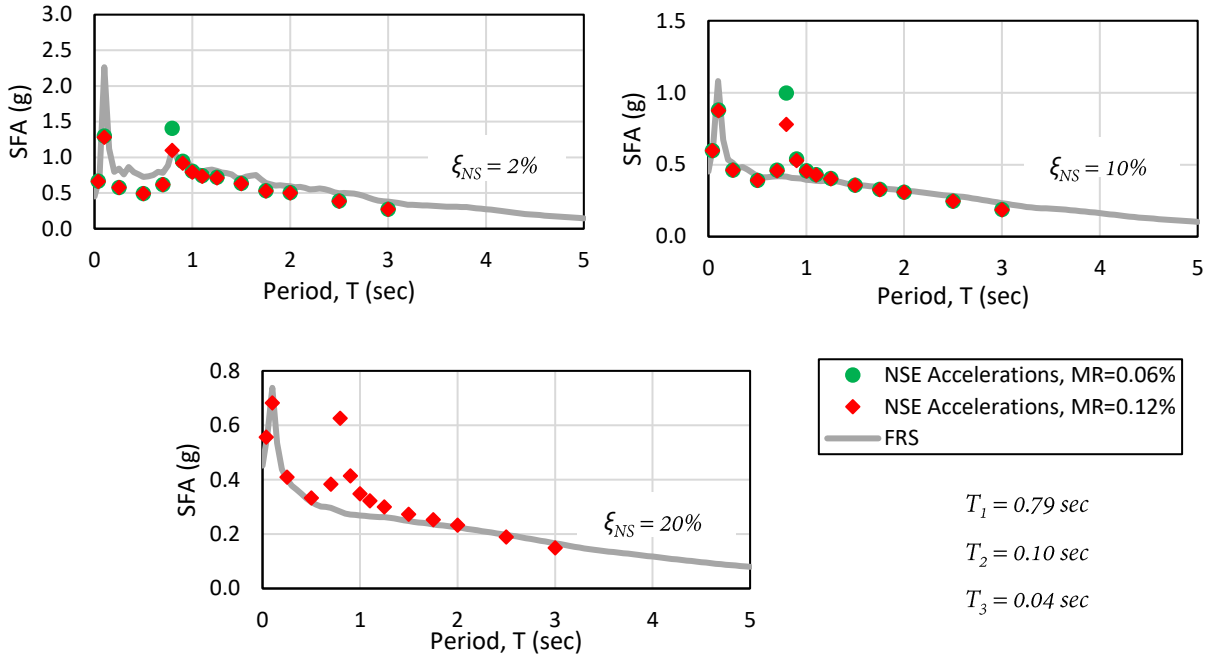

Figure 5.37 Comparison between mean NSE accelerations from coupled analysis and mean FRS from decoupled analysis for roof level of 4-story rocking wall building; inelastic structural response at Intensity 5 (PGA = 0.450 g)

The effect of dynamic interaction was also observed to diminish with increasing height of the supporting building. For both the 12-story RC and rocking wall buildings, the accelerations from the decoupled analyses were higher than spectral acceleration demands from the coupled analyses for NSEs with periods close to the fundamental period of the supporting building, but to a much smaller degree compared to the 4-story buildings (Figures 5.38 and 5.39).

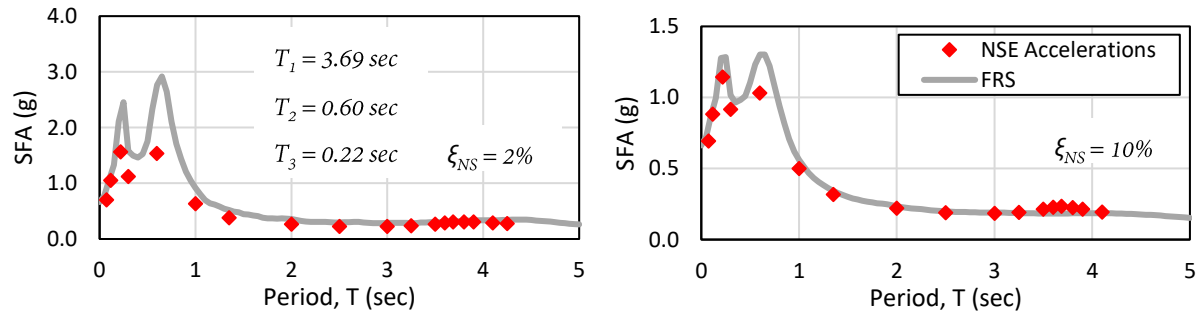

Figure 5.38 Comparison between mean NSE accelerations from coupled analysis (MR = 0.12%) and mean FRS from decoupled analysis for roof level of 12-story RC wall building; inelastic structural response at Intensity 5 (PGA = 0.450 g)

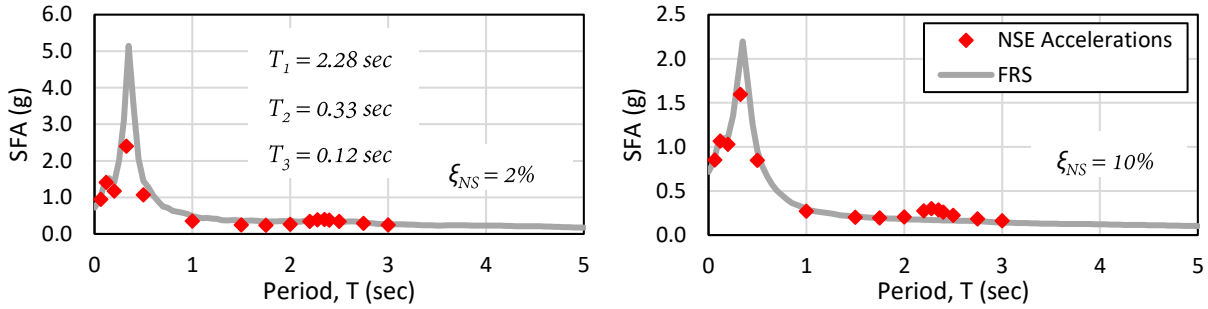

Figure 5.39 Comparison between mean NSE accelerations from coupled analysis (MR = 0.12%) and mean FRS from decoupled analysis for roof level of 12-story rocking wall building; inelastic structural response at Intensity 5 (PGA = 0.450 g)

6 MAXIMUM DYNAMIC AMPLIFICATION OF PEAK FLOOR ACCELERATION

The current chapter details the investigative efforts into the maximum dynamic amplification of peak floor acceleration that occurs when a non-structural element is in resonance with the supporting structure. The work in this chapter applies to non-structural elements that can be considered uncoupled from the supporting structure, which, as discussed in Section 5.3.2, is typically considered acceptable for a mass ratio of 1% or less (Singh and Ang, 1974; Sankaranarayanan, 2007; Taghavi and Miranda, 2008; Pinkawa *et al.,* 2014; Welch, 2016). The observations made in this chapter were directly utilized in the development of methodologies to estimate floor response spectra atop RC and rocking wall buildings responding non-linearly in Chapter 7.

Maximum dynamic amplification occurs when a non-structural element (NSE) and the primary structure are in resonance. The maximum dynamic amplification factor (DAF_{max}) is defined as the ratio between maximum spectral acceleration and peak floor acceleration (PFA), which is shown in Figure 6.1. The term *p* stands for primary/supporting structure and the term *NS* stands for non-structural/supported element.

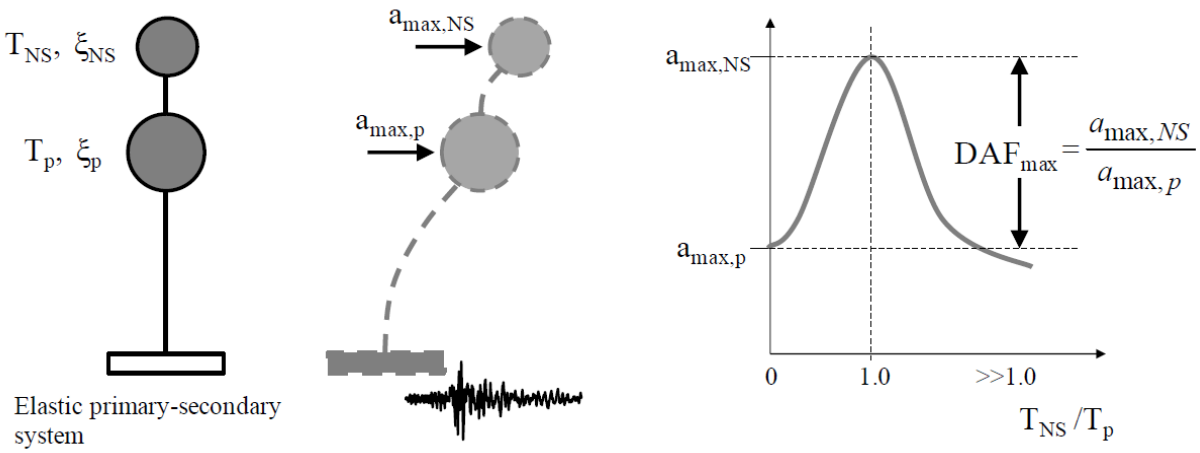

Figure 6.1 Illustration of the peak dynamic amplification of acceleration for an elastic primary-secondary SDOF system at the resonant condition (Welch, 2016)

In recent years, maximum dynamic amplification has been mostly studied and quantified empirically (Sullivan *et al.*, 2013; Calvi and Sullivan, 2014; Vukobratović, 2015; Welch, 2016). This is partly because earthquake excitations apply neither harmonic nor a clearly defined impulse loading (Sullivan *et al.*, 2013), and closed form formulations of maximum dynamic amplification have been shown to overestimate the amplification of PFA at resonance (Welch, 2016).

As discussed in Section 3.2, Sullivan *et al.* (2013), Calvi and Sullivan (2014), and Welch (2016) (amongst others) proposed empirical formulations for DAF_{max}. Sullivan *et al.* (2013) formulated DAF_{max} as a function of non-structural element damping and assumed DAF_{max} was independent of the supporting structure's properties (Equation (6.1)). Calvi and Sullivan (2014) kept the formation made in their previous work but introduced a reduction of DAF_{max} for stiff supporting structures with periods less than 0.3 sec (Equation (6.2)). Most recently, Welch (2016) updated the formulations of the two previous studies to take into account the damping of the primary structure in addition to the damping of the non-structural element (Equation (6.3)).

$$DAF_{max} = \frac{1}{\sqrt{\xi_{NS}}} \tag{6.1}$$

where ξ_{NS} is the elastic damping of the non-structural/supported element.

$$DAF_{max} = \begin{cases} \dfrac{1}{\left(1.79 - \dfrac{T_i}{T_B}\right)\sqrt{\xi_{NS}}} & if\ 0 \le T_i \le T_B \\ \dfrac{1}{\sqrt{\xi_{NS}}} & if\ T_i \ge T_B \end{cases} \tag{6.2}$$

where T_i is the elastic period of the primary structure for mode i. The term T_B is taken as 0.3 sec.

$$DAF_{max} = \begin{cases} \left(0.55 + 0.45\dfrac{T_i}{T_B}\right)(0.5\xi_p + \xi_{NS})^{-0.667} & if\ T_i \le T_B \\ (0.5\xi_p + \xi_{NS})^{-0.667} & if\ T_i \ge T_B \end{cases} \tag{6.3}$$

where $T_{i,e}$ is the effective period of the supporting structure for mode i, and ξ_p is the elastic damping of the primary structure.

For a better understanding of maximum dynamic amplification of peak floor acceleration, a study of floor spectra atop both elastic and inelastic SDOF systems was conducted through time history analysis. The main objectives of the study were as follows:

i. Investigate the performance of existing formulations for DAF_{max} with a new suite of ground motions not used in the development of the formulations for primary structure periods beyond $T_B = 0.3$ sec, specifically focusing on the works of Sullivan *et al.* (2013) and Welch (2016);

ii. Investigate the effects of inelastic structural response on DAF_{max}.

6.1 Time History Analysis of SDOF Systems

Both the elastic and inelastic SDOF systems were modeled as mass-spring-damper systems. For the earthquake excitation, the 32 ground motions in Section 4.5.1 were used in the time history analysis. The following sections detail the modelling process of the SDOF systems.

6.1.1 Modelling of Elastic SDOF Systems

The SDOF systems considered for the elastic analysis had primary structure periods T_p of 0.3, 0.5, 1.0, 2.0, 3.0, 4.0 and 5.0 sec. Each SDOF system was modelled considering primary structure damping ratios ξ_p of 1%, 3% and 5% of critical damping. These damping ratios represent commonly assumed values for typical buildings (Welch, 2016). Damping was modelled using a

Rayleigh tangent-stiffness proportional damping model, consistent with the studies on DAF_{max} conducted by Sullivan *et al.* (2013) and Welch (2016).

The ground acceleration records were applied at an intensity level of 1.0. For each combination of ground acceleration record, primary structure period and damping ratio, floor spectra were generated at five non-structural element damping ratios ξ_{NS} of 0.5%, 1%, 2%, 5%, and 10% of critical damping.

6.1.2 Modelling of Inelastic SDOF Systems

The inelastic SDOF systems were modelled in RUAUMOKO2D with two distinct hysteretic characteristics: Modified Takeda and flag-shaped hysteresis (Carr, 2004). The flag-shaped hysteresis was selected to represent the behavior of a rocking wall. The post-yield stiffness ratio was set at 10% and the energy dissipation coefficient β was set at 0.888. The adopted β value corresponds to a ratio of between post-tensioning and mild steel bending resistance λ of 1.25 as suggested by Pennucci *et al.* (2009). This provides the maximum amount of energy dissipation possible whilst ensuring re-centering of the wall and taking material over-strengths into account (refer to Sections 4.3.7 and 4.5.7 for more details). The Modified Takeda hysteresis was selected to represent the behavior of an RC wall. The post-yield stiffness ratio was also set at 10% and the following parameters were used to define the unloading and reloading behavior of the hysteresis (Amaris, 2002; Welch, 2016):

- Unloading stiffness factor, $\alpha = 0.5$
- Reloading stiffness factor, $\beta = 0$
- An Emori and Schnobrich unloading ($KKK = 2$)

The SDOF systems considered had primary structure periods T_p of 0.5, 1.0, 2.0, 3.0, 4.0 and 5.0 sec. Each SDOF system was modelled with a structural damping ratio ξ_p of 3%, 5% and 7% of critical damping. These values were selected to create a reasonable range of damping ratios around 5% damping, which is typically assumed for both types of structural walls. Damping was modelled using a Rayleigh tangent-stiffness proportional damping model, consistent with the studies on DAF_{max} conducted by Sullivan *et al.* (2013) and Welch (2016).

To study the effects of increasing inelastic deformation on DAF_{max}, the intensity of each of the ground acceleration records was gradually increased starting from an intensity resulting in elastic response. Displacement ductility was utilized to measure the level of inelastic deformation. For each combination of intensity level, ground acceleration record, primary structure period and damping ratio, floor spectra were generated using DYNAPLOT (Carr, 2004) at four non-structural element damping ratios ξ_{NS} of 0.5%, 1%, 2% and 5% of critical damping.

6.1.3 Monitoring of Maximum Dynamic Amplification Factor

For both the elastic and inelastic SDOF systems, DAF_{max} was obtained through floor spectra by taking the ratio of maximum spectral floor acceleration (SFA_{max}) and peak floor acceleration (PFA), as defined in Equation (6.4).

$$DAF_{max} = \frac{SFA_{max}}{PFA} = \frac{SFA_{max}}{SFA(0)} \tag{6.4}$$

where *SFA(0)* is the spectral acceleration value at spectral period of 0 sec.

6.2 Maximum Dynamic Amplification Factor in Elastic SDOF Systems

The performance of existing formulations for DAF_{max} beyond T_B = 0.3 sec was investigated using the results of the time history analysis of the elastic SDOF systems. Sullivan *et al.* (2013) proposed a formulation for DAF_{max} as a function of non-structural damping ξ_{NS} (Equation (6.1)). This formulation is presented along with the data from the present study in Figure 6.2. A regression analysis was conducted to find the best fit for the data in the form of $DAF_{max} = {\xi_{NS}}^{x}$ where *x* is the dependable variable. Equation (6.5) was found to be the best fit with an R^2 value of 0.51. The highest disparity between Equation (6.5) and the Sullivan *et al.* (2013) formulation occurs at low non-structural element damping ratios. This is reasonable since the scatter in the data is also highest at low non-structural element damping ratios, consistent with analysis results from Sullivan *et al.* (2013) and Welch (2016). Considering this scatter, the Sullivan *et al.* (2013) formulation can be considered an acceptable approximation for DAF_{max} for the data presented in this study.

$$DAF_{max} = \frac{1}{{\xi_{NS}}^{0.559}} \tag{6.5}$$

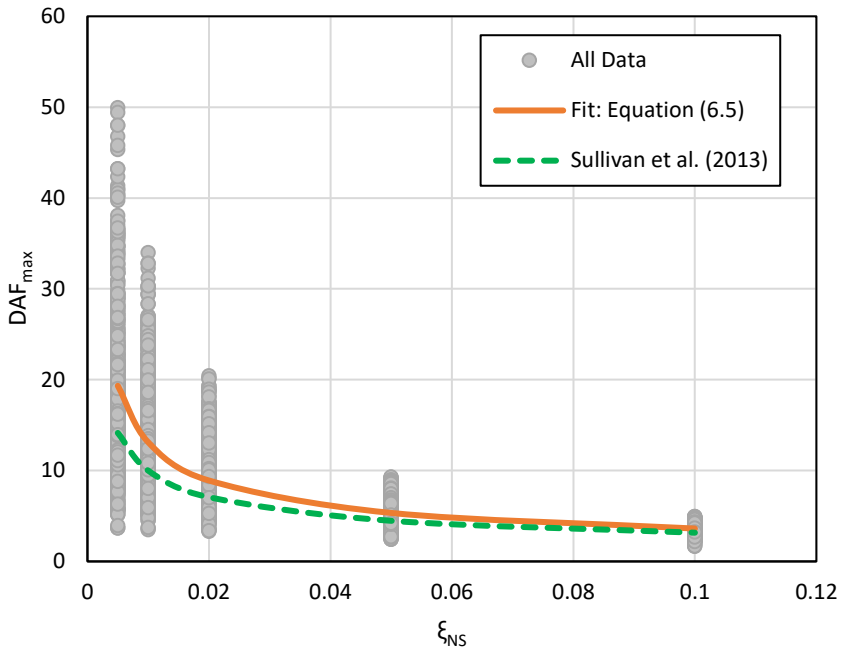

* All Data represents DAF_{max} values for each combination of ground acceleration record, primary structure period, primary structure damping ratio, and non-structural element damping ratio.

Figure 6.2 Comparison between the DAF_{max} formulation of Sullivan et al. (2013) and best fit for the results of time history analyses of elastic SDOF systems

Most recently, Welch (2016) updated the DAF_{max} formulations of Sullivan *et al.* (2013), and Calvi and Sullivan (2014) to include the influence of the primary structure damping ξ_p along with non-structural damping ξ_{NS} (Equation (6.3)). This formulation is presented along with the data from this current study in Figure 6.3. A regression analysis was conducted to find the best fit for the data in the form of $DAF_{max} = (a\xi_p + \xi_{NS})^b$ where a and b are the dependable variables. Equation (6.6) was found to be the best fit with an R^2 value of 0.61. This is a better fit to the data set compared to Equation (6.5), which only included the effects of non-structural damping, consistent with the observations of Welch (2016). The disparity between the Welch (2016) formulation and best fit of the data is small and limited to a small range of primary and non-structural damping ratios. Thus, an updated formulation for DAF_{max} based on the best fit of the current data set was not warranted, and the Welch (2016) formulation was adopted in this study.

$$DAF_{max} = (0.25\xi_p + \xi_{NS})^{-0.646} \quad for \;\; T_i \geq T_B \tag{6.6}$$

where T_i is the elastic period of the primary structure for mode *i*.

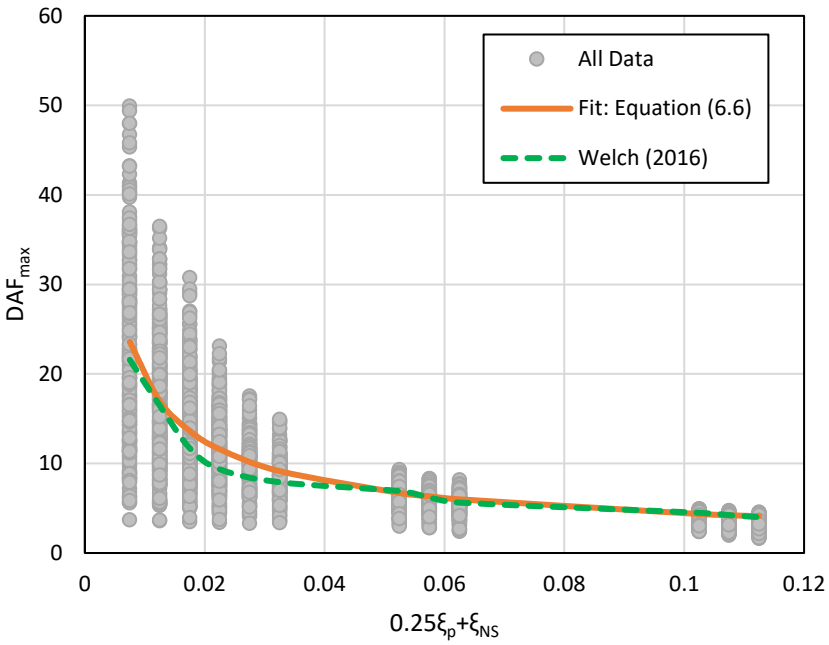

* All Data represents DAF_{max} values for each combination of ground acceleration record, primary structure period, primary structure damping ratio, and non-structural element damping ratio.

Figure 6.3 Comparison between the DAF_{max} formulation of Welch (2016) and best fit for the results of time history analyses of elastic SDOF systems

6.3 Maximum Dynamic Amplification Factor in Inelastic SDOF Systems

To investigate the effects of inelastic structural response on DAF_{max}, non-linear time history analysis (NLTHA) of inelastic SDOF systems was conducted at varying levels of intensity. Figures 6.4 and 6.5 are representative of the trends observed in the analysis results for the various combinations of primary structure period, primary structure damping ratio, and non-structural element damping ratio.

As Figures 6.4 and 6.5 show, DAF_{max} values generally decrease with increasing ductility for both the Modified Takeda and flag-shaped hysteresis models (Carr, 2004). This indicates that the existing formulations for DAF_{max}, which were empirically derived from elastically responding SDOF systems, represent an upper bound for DAF_{max}. Thus, the existing formulations are expected to be conservative and suitable for use in buildings responding non-linearly.

However, for the flag-shaped hysteresis, there is a sharp increase in DAF_{max} when going from elastic deformation (ductility less than 1.0) to low levels of inelastic deformation (ductility slightly

higher than 1.0). This increase in DAF_{max} might be caused by numerical issues arising from the idealization of the flag-shaped hysteresis with sharp corners (briefly discussed in Section 5.2.4). Floor acceleration spikes in rocking systems have been shown to be sensitive to the roundness of the flag-shaped hysteresis with sharper corners potentially causing higher spikes (Wiebe and Christopoulos, 2011). Applying rounded corners has been shown to mitigate this issue so future work could replicate the NLTHA with a round-cornered flag-shaped hysteresis to check if the increase in DAF_{max} for low ductility values is a numerical issue

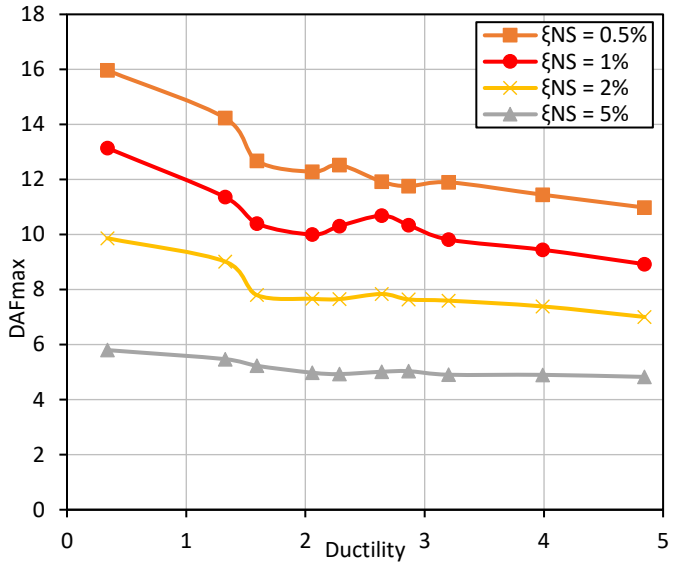

* Each data point represents mean DAF_{max} and ductility values of 32 records scaled to the same intensity.

Figure 6.4 The influence of increasing ductility demands on DAF_{max} for SDOF systems modelled with a Modified Takeda hysteresis (Carr, 2004) at varying levels of non-structural element damping; T_p = 1 sec; ξ_p = 5%

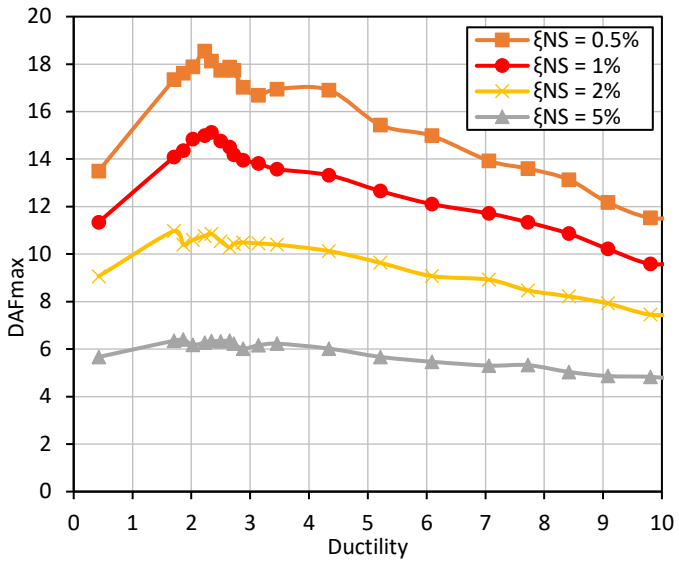

* Each data point represents the mean DAF_{max} and ductility values of 32 records scaled to the same intensity.

Figure 6.5 The influence of increasing ductility demands on DAF_{max} for SDOF systems modelled with a Flag-Shaped hysteresis (Carr, 2004) at varying levels of non-structural element damping; T_p = 1 sec; ξ_p = 5%

6.4 Concluding Remarks

The DAF_{max} formulations of Sullivan *et al.* (2013) and Welch (2016) were in good agreement with the current data set for primary structural periods beyond T_B = 0.3 sec. Thus, the most recent relationship for DAF_{max} proposed by Welch (2016) was adopted in this study.

Furthermore, the effects of inelastic structural response on DAF_{max} were investigated. Increasing ductility demands were generally associated with lower DAF_{max} values. Hence, the simplified DAF_{max} formulations for elastic systems can be considered conservative and acceptable for buildings responding non-linearly.

Noting the strong relationship between DAF_{max} and damping, future studies should explore the sensitivity of the proposed DAF_{max} formulations to the damping model employed. In this study, the elastic damping the primary structure was modelled using a Rayleigh tangent-stiffness proportional damping model. Thus, future studies could replicate the study described in this chapter using different damping models to study the relationship between DAF_{max} and the damping model employed.

7 METHODOLOGIES FOR THE ESTIMATION OF FLOOR RESPONSE SPECTRA IN RC AND ROCKING WALL BUILDINGS RESPONDING NON-LINEARLY

In this chapter, several methodologies are developed for the estimation of floor response spectra in RC and rocking wall buildings. As discussed in Section 3.2.2, Calvi and Sullivan (2014) proposed a simple procedure for the estimation of floor response spectra in MDOF buildings responding elastically. The work summarized in this chapter extends this procedure to RC and rocking wall buildings responding non-linearly.

7.1 Estimation of Ductility Demand

In order to develop procedures for the estimation of floor response spectra in buildings responding non-linearly, it is important to have a reliable estimate of the buildings' ductility as it quantifies the extent of inelastic behavior. From the NLTHA of the case-study buildings, ductility was measured on a record-by-record basis for each earthquake intensity under consideration (Intensities 1, 5, and 6). This is in line with the work of Welch (2016) who also found that ductility demands estimated using approximate procedures such as the ones presented below were comparable to simpler practice-oriented estimates of ductility demand. The following sections detail how ductility was estimated for the two types of structural systems considered.

7.1.1 RC Wall Buildings

For RC walls, displacement ductility is defined as the maximum displacement of the wall at the effective height divided by the yield displacement of the wall at the effective height (Priestley *et al.,* 2007). The effective height of the walls is determined as:

$$H_e = \frac{\sum_{i=1}^{n} m_i \Delta_i H_i}{\sum_{i=1}^{n} m_i \Delta_i} \tag{7.1}$$

where m_i is the mass of each floor, Δ_i is the design displacement of each floor, and H_i is the height of each floor.

The yield displacement at the effective height of the wall is given by:

$$\Delta_{y,H_e} = \frac{\varepsilon_y}{l_w} {H_e}^2 \left(1 - \frac{H_e}{3H_n}\right) \tag{7.2}$$

where ε_y is the yield strain of the longitudinal reinforcement, l_w is the length of the wall, and H_n is the height of the wall.

Effective heights and yield displacements were calculated during the displacement-based design of the case study buildings (refer to Section 4.3). For clarity, the design outcomes have been repeated in this section as Table 7.1.

Table 7.1 Effective heights and yield displacements at effective height for the RC wall buildings

	H_e (m)	H_e/H_n	$\Delta_{y,He}$ (m)
4 Story	9.11	0.759	0.043
8 Story	17.43	0.726	0.095
12 Story	25.85	0.718	0.162

7.1.2 Rocking Wall Buildings

Similar to the RC walls, displacement ductility of rocking walls can be defined as the maximum displacement of the wall at the effective height divided by the yield displacement of the wall at the effective height (Pennucci *et al.*, 2009). The effective height is calculated with Equation (7.1). The yield displacement at the effective height can be determined as:

$$\Delta_{y,He} = 0.5\phi_b \left[H_e^2 - \frac{H_e^3}{2H_n} + \frac{H_e^5}{20H_n^3}\right] + \theta_{y\_base} H_e \tag{7.3}$$

where H_n is the height of the wall, ϕ_b is the curvature at the base of the wall, and Θ_{y_base} is the yield rotation of the wall/foundation connection. The wall base curvature is given by:

$$\phi_b = \frac{\phi_y}{\gamma} \tag{7.4}$$

where ϕ_y is the yield curvature of the wall and Υ is a curvature index which was taken as 3 in this current study (refer to Section 4.3.7 for more details). The yield curvature is given by:

$$\phi_y = 2\frac{\varepsilon_y}{l_w} \tag{7.5}$$

where ε_y is the yield strain of the wall longitudinal reinforcement and l_w is the length of the wall.

The yield rotation of the wall/foundation connection is given by:

$$\theta_{y\_base} = \frac{\varepsilon_{my}(l_{ub\_ms} + 2\Delta_{sp})}{l_w(1-v) - d_{AS}} \tag{7.6}$$

where ε_{my} is the yield strain of mild steel, l_{ub_ms} is the mild steel unbonded length, d_{AS} is the distance from the tension face of the wall to the centroid of mild steel, v is the normalized depth of compression area at yielding and Δ_{sp} is the strain penetration which is given by:

$$\Delta_{sp} = 0.022\mathrm{f}_{my}\mathrm{d}_{mb} \tag{7.7}$$

where f_{my} is the mild steel yield stress and d_{mb} is the mild steel bar diameter.

Effective heights and yield displacements were calculated during the displacement-based design of the case study buildings (refer to Section 4.3). For clarity, the design outcomes have been repeated in this section as Table 7.2.

Table 7.2 Effective heights and yield displacements at effective height for the rocking wall buildings

	H_e (m)	H_e/H_n	$\Delta_{y,He}$ (m)
4 Story	8.94	0.745	0.020
8 Story	17.00	0.708	0.039
12 Story	25.05	0.696	0.063

7.1.3 Summary of Ductility Demands from NLTHA

Using the procedures in the previous sub-sections, ductility was computed on a record-by-record basis for each of the earthquake intensities under consideration. Mean ductility demands were then calculated for each combination of case study building and earthquake intensity, which are presented in Table 7.3.

Table 7.3 Mean ductility demand estimates from the NLTHA of case study buildings

		Ductility Demand, μ		
Structural System	**Intensity**	**4-story**	**8-story**	**12-story**
RC Walls	**1**	2.02	1.43	1.15
	5*	4.52	3.04	2.06
	6**	7.28	4.71	2.96
Rocking Walls	**1**	3.80	3.25	2.40
	5*	10.44	7.36	5.28
	6**	18.46	12.12	8.58

* Design basis earthquake (DBE) intensity
** Maximum considered earthquake (MCE) intensity

7.2 Estimation of Floor Response Spectra using Transitory Inelastic Modal Characteristics

Calvi and Sullivan (2014) proposed a procedure for estimating floor response spectra atop elastic MDOF systems in which individual modal floor spectra are combined using modal superposition to generate floor response spectra at each floor level. The modal floor spectra are generated by first obtaining the elastic PFA contributions from each mode using a traditional modal response spectrum method. The modal PFA contributions are then scaled by empirical dynamic amplification factors (DAF) to obtain spectral floor acceleration demands for each mode (refer to Section 3.2.2 for a more details on the procedure).

To adapt this procedure to MDOF buildings responding non-linearly, it is proposed that inelastic modal PFA contributions be obtained using transitory modal characteristics instead of elastic modal characteristics to take into account the inelastic response of the building. The concept of transitory inelastic modes of vibration was put forward by Sullivan *et al.* (2006) to estimate the higher mode response of ductile structures. It was hypothesized that the development of inelasticity in structures is controlled by the first mode response. Thus, higher mode response must be characterized by taking into account the inelasticity caused by the first mode response (Sullivan *et al.*, 2008). To this end, higher mode response is determined using transitory modal characteristics that are obtained through an eigen-value analysis using a tangent or unloading stiffness (instead of

the elastic stiffness) for the plastic hinge region. Therefore, this approach takes into account the loss of stiffness that is expected in plastic hinge regions due to inelastic response.

Once the modal PFA contributions are determined using transitory inelastic modal characteristics, they can then be scaled by the same empirical dynamic amplification factors (DAF) calibrated for elastic systems to obtain spectral floor acceleration demands for each mode. As discussed in Section 6.3, the DAF_{max} formulations that were adopted in the present study were shown to be conservative for structures responding non-linearly. Thus, if PFAs can be accurately estimated using transitory modal characteristics, the existing formulations for DAF can be used to generate a floor response spectrum for a structure responding non-linearly.

7.2.1 Estimation of Transitory Inelastic Modal Characteristics

In order to obtain the transitory inelastic modal periods and mode shapes, an eigen-value analysis can be conducted on a model of the supporting structure with a rotational spring placed at the location of concentrated inelastic behavior (i.e. plastic hinge regions and rocking joints). The rotational spring is then assigned the secant stiffness of the structural system, which can be calculated based on the expected ductility of the structural system. For both types of structural systems studied, Figure 7.1 shows a schematic representation of the RUAUMOKO2D models used to obtain the transitory modal characteristics.

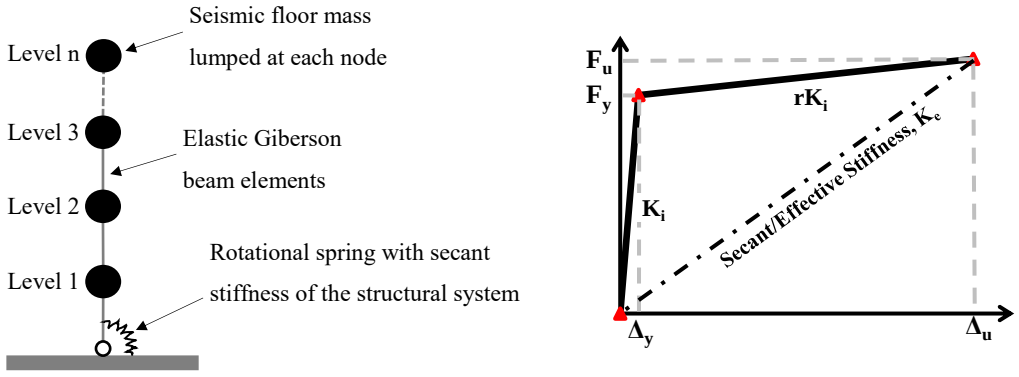

Figure 7.1 Diagram of the model used to obtain transitory modal characteristics for the case study buildings (left) and diagram showing the secant stiffness of a structural system (right)

For RC wall buildings, the secant stiffness $K_{e,RC}$ can be calculated as:

$$K_{e,RC} = \frac{M_y + r\frac{K_{i,\phi}}{L_p}\left[\frac{(\mu-1)\Delta_{y,H_e}}{H_e}\right]}{\phi_y L_p + \frac{(\mu-1)\Delta_{y,H_e}}{H_e}} \; ; \quad \mu \geq 1 \tag{7.8}$$

where M_y is the yield moment capacity of the wall, r is the global post yield stiffness ratio, and $K_{i,\phi}$ is the elastic stiffness of the wall in terms of moment-curvature. The term μ is the expected ductility of the structural system. ϕ_y is the yield curvature of the wall, and L_p is the plastic hinge length. The term H_e is the effective height of the wall which can be determined using Equation (7.1). The term $\Delta_{y,He}$ is the yield displacement of the wall at the effective height of the wall determined using Equation (7.2). Note that if $\mu = 1$, the secant stiffness K_e is equal to the elastic stiffness of the wall.

For rocking wall buildings, the secant stiffness $K_{e,rock}$ can be calculated as:

$$K_{e,rock} = \frac{M_y + rK_{i,\theta}\left[\frac{(\mu-1)\Delta_{y,H_e}}{H_e}\right]}{\theta_{y\_base} + \frac{(\mu-1)\Delta_{y,H_e}}{H_e}} \; ; \quad \mu \geq 1 \tag{7.9}$$

where $K_{i,\theta}$ is the elastic stiffness of the rocking joint in terms of moment-rotation, and Θ_{y_base} is the yield base rotation of the wall. The term H_e is the effective height of the wall which can be determined using Equation (7.1). The term $\Delta_{y,He}$ is yield displacement of the wall at the effective height of the wall determined using Equation (7.3).

Based on the relationships outlined above and the estimated ductility of the case-study buildings in Table 7.3, the secant stiffness values were calculated for all case-study buildings and earthquake intensities considered (Table 7.4). The secant stiffness values were then used in an Eigen-value analysis of the case-study buildings (using the RUAUMOKO2D model depicted in Figure 7.1) to obtain the transitory modal characteristics, which are presented in Appendix A.

Table 7.4 Secant stiffness values for the case study buildings

		Secant Stiffness, K_e (MN-m/rad)		
Structural System	**Intensity**	**4 Story**	**8 Story**	**12 Story**
RC Walls	**1**	491	3209	8425
	5*	189	1045	2650
	6**	122	651	1635
Rocking Walls	**1**	313	1336	2938
	5*	125	583	1182
	6**	85	389	754
* Design basis earthquake (DBE) intensity ** Maximum considered earthquake (MCE) intensity				

7.2.2 Estimation of Peak Floor Accelerations

Once the transitory modal periods and mode shapes are determined using eigen-value analysis, the modal contributions to the PFA can be determined using a traditional modal response spectrum method. Mathematically, the contributions are determined by:

$$a_{max,j,i} = \begin{cases} \phi_{t,j,i}\Gamma_{t,i}S_a\left(T_{i,e},\xi_{p,eq}\right) & for\ i = 1 \\ \phi_{t,j,i}\Gamma_{t,i}S_a\left(T_{i,e},\xi_p\right) & for\ i > 1 \end{cases} \tag{7.10}$$

where $a_{max,j,i}$ is the floor acceleration at floor level j from mode i, $\phi_{t,j,i}$ is the transitory mode shape for floor level j and mode i, and $\Gamma_{t,i}$ is transitory modal participation factor for mode i. The term $T_{i,e}$ is the effective period of the supporting structure for mode i, which is to be taken as the transitory modal period for mode i. The term $S_a(T_{i,e},\xi_p)$ is the spectral acceleration demand for higher mode i obtained from the design ground response spectrum at the elastic primary damping ratio ξ_p. The term $S_a(T_{i,e},\xi_{p,eq})$ is spectral acceleration demand for the first mode obtained from the design ground response spectrum at the equivalent viscous damping ratio of the primary structure, which is given by Equation (7.11).

$$\xi_{p,eq} = \xi_p + \xi_{hyst} \tag{7.11}$$

where ξ_{hyst} is hysteretic damping and ξ_p is elastic primary damping of the structure, assumed to be 5% for both RC and rocking walls.

An equivalent viscous damping is proposed for the first mode to take into account the added hysteretic damping resulting from inelastic deformations. The hysteretic damping is dependent on the structural system in use and the expected ductility of the system (refer to Section 4.3.3 for more details). As Sullivan *et al.* (2008) and others note, the higher mode response is not affected by inelastic deformation to the same extent as the first mode response. Thus, the consideration of hysteretic damping is not proposed for the higher modes.

The equivalent viscous damping for RC walls is given by (Priestley *et al.*, 2007):

$$\xi_{eq,RC} = 0.05 + 0.444\left(\frac{\mu - 1}{\mu\pi}\right) \tag{7.12}$$

where μ is the expected ductility.

The equivalent viscous damping for rocking walls can be approximated by Equation (7.13), which was derived for a ratio between post-tensioning and mild steel bending resistance $\lambda = 1.25$ and post-yield global stiffness factor $r = 0$ (Pennucci *et al.*, 2009). Refer to Section 4.3.7 for more details on equivalent viscous damping in rocking walls.

$$\xi_{eq,rock} = 0.05 + 0.524\left(\frac{\mu - 1}{\mu\pi}\right) \tag{7.13}$$

Once the modal contributions to the PFA are determined following the steps summarized above, the PFA can be calculated using the SRSS rule as:

$$PFA_{SRSS,j} = \sqrt{\sum_{i=1}^{nm} [a_{max,t,j,i}]^2} \tag{7.14}$$

Where *nm* is the number of modes under consideration.

In line with the recommendations of Calvi and Sullivan (2014) and Welch (2016), it is proposed that the PFA for the lower half of MDOF buildings be taken as the maximum of the peak ground acceleration (PGA) and the SRSS PFA determined by the modal superposition approach discussed above. This is proposed to capture the limited higher mode filtering of ground motions (rigid mode response) that is expected in the lower levels of MDOF buildings (Calvi and Sullivan, 2014; Welch, 2016). Thus, the PFA at any given floor level *j* can be determined as:

$$PFA_j = \begin{cases} \max\left(PFA_{SRSS,j}, PGA\right) & for \dfrac{H_j}{H_n} < 0.5 \\ PFA_{SRSS,j} & for \dfrac{H_j}{H_n} \geq 0.5 \end{cases} \quad (7.15)$$

where H_j is the height of floor level j, and H_n is the height of the roof level.

To analyze how well transitory modal characteristics predict the PFA, mean PFAs from the NLTHA of the case study buildings were compared to PFAs estimated using the steps outlined above.

The comparisons for the RC wall buildings at Intensities 1, 5 and 6 are presented in Figures 7.2 to 7.4. It can be seen that the PFA estimates are comparable to the mean PFA values from the NLTHA for all three earthquake intensities, with slightly non-conservative estimates at all floor levels. However, the estimates improved with increasing earthquake intensity, which might be an indication that transitory modal properties are better at estimating structural response at high ductility demands.

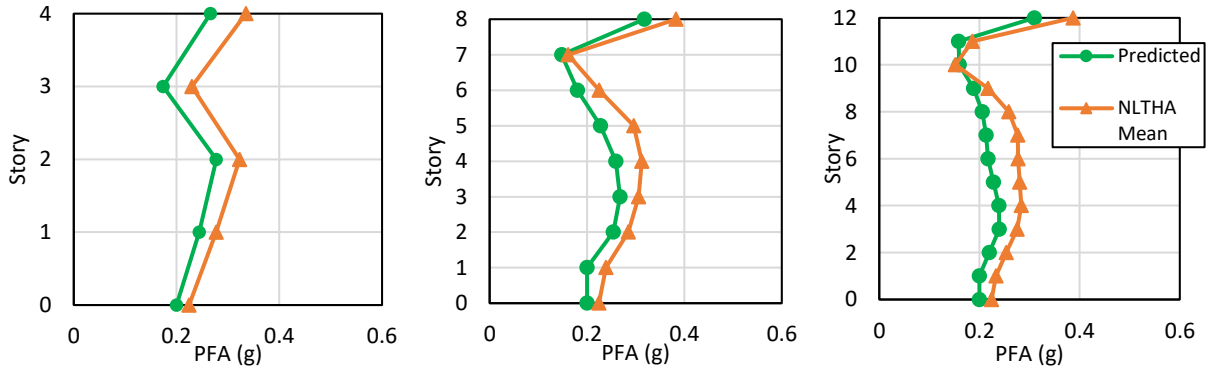

Figure 7.2 Comparison between PFA estimates using transitory modes and NLTHA mean PFA for RC wall buildings under Intensity 1: (a) 4-Story; (b) 8-story; (c) 12-story

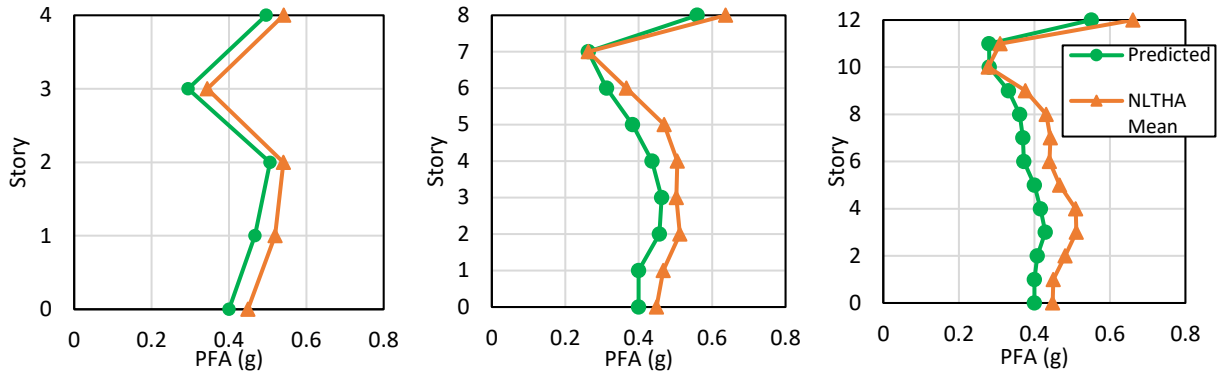

Figure 7.3 Comparison between PFA estimates using transitory modes and NLTHA mean PFA for RC wall buildings under Intensity 5: (a) 4-Story; (b) 8-story; (c) 12-story

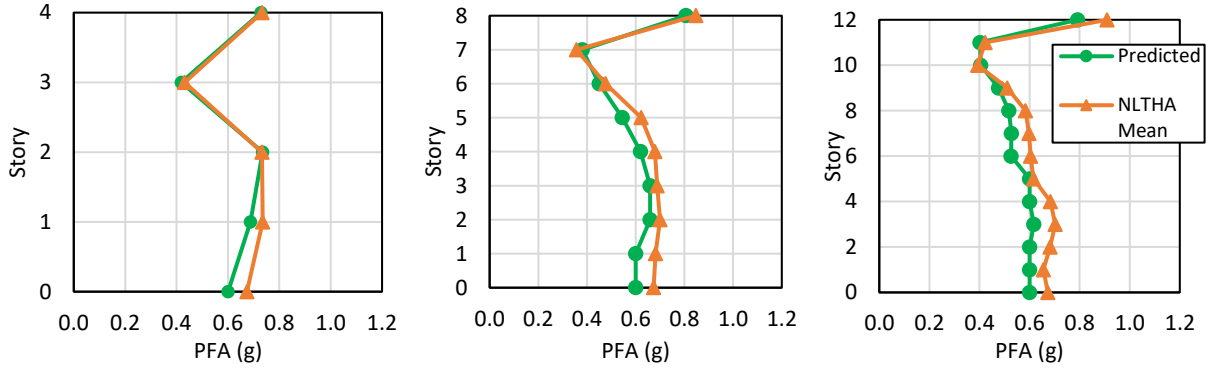

Figure 7.4 Comparison between PFA estimates using transitory modes and NLTHA mean PFA for RC wall buildings under Intensity 6: (a) 4-Story; (b) 8-story; (c) 12-story

The comparisons for the rocking wall buildings at Intensities 1, 5 and 6 are presented in Figures 7.5 to 7.7. Overall, there was very good agreement between the PFA estimates and the mean PFA values from the NLTHA, with slightly non-conservative estimates for the lower floor levels. This trend was consistent over all three earthquake intensities.

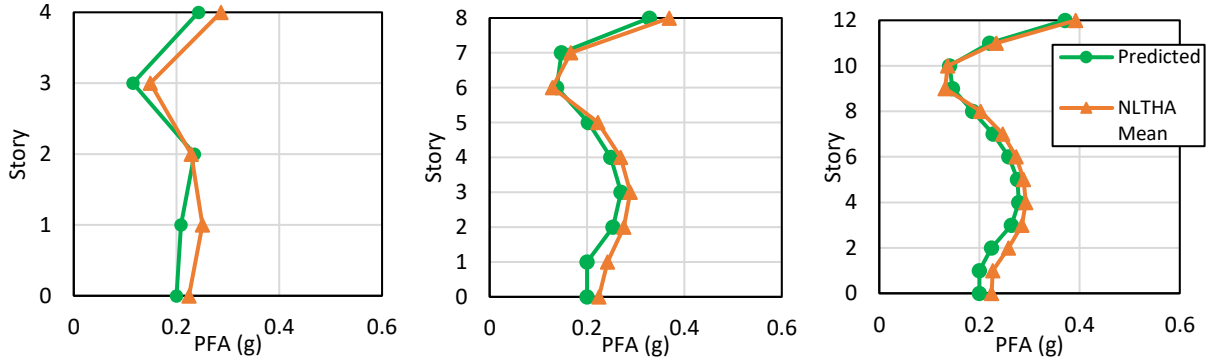

Figure 7.5 Comparison between PFA estimates using transitory modes and NLTHA mean PFA for rocking wall buildings under Intensity 1: (a) 4-Story; (b) 8-story; (c) 12-story

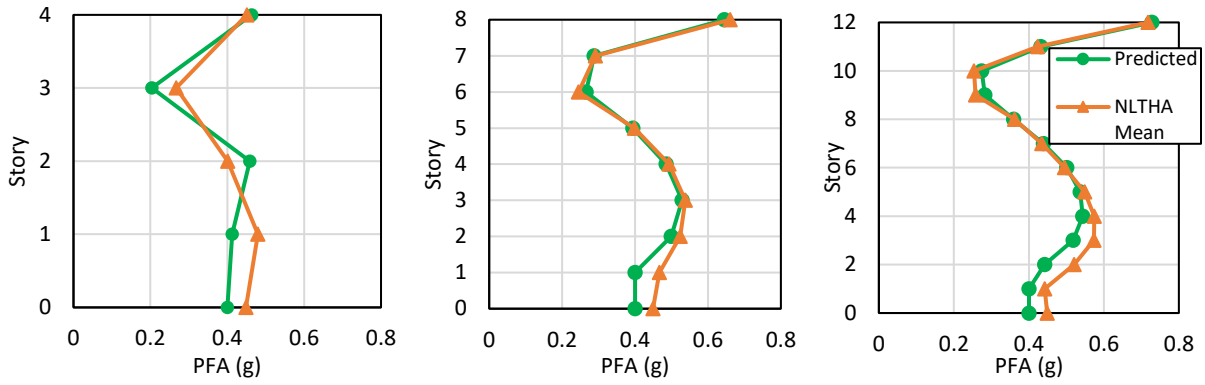

Figure 7.6 Comparison between PFA estimates using transitory modes and NLTHA mean PFA for rocking wall buildings under Intensity 5: (a) 4-Story; (b) 8-story; (c) 12-story

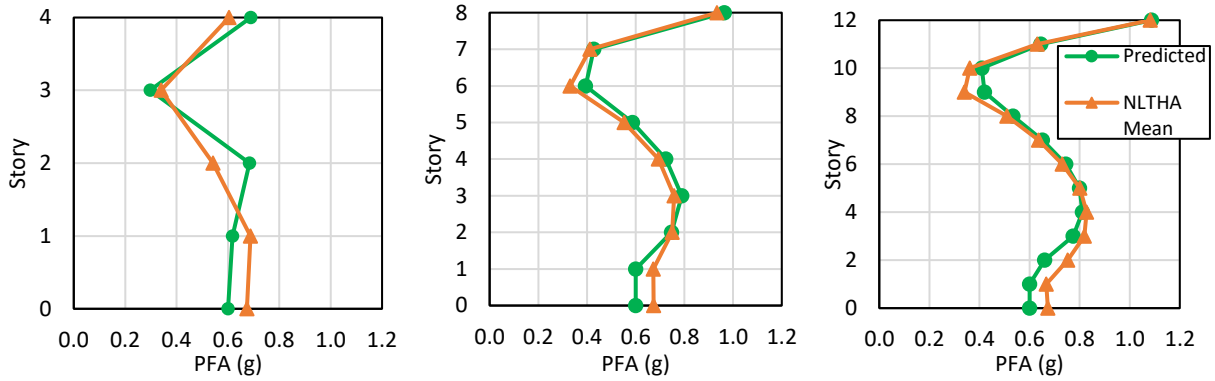

Figure 7.7 Comparison between PFA estimates using transitory modes and NLTHA mean PFA for rocking wall buildings under Intensity 6: (a) 4-Story; (b) 8-story; (c) 12-story

7.2.3 Estimation of Floor Response Spectra

Once the modal contributions to the PFA are determined using transitory modes, the individual modal contributions $a_{m,j,i}(T)$ to the floor response spectrum are given by:

$$a_{m,j,i}(T) = \begin{cases} \left(\frac{T}{T_i}\right)\left[a_{max,j,i}(DAF_{max} - 1)\right] + a_{max,j,i} & for\ T < T_i \\ a_{max,j,i}DAF_{max} & for\ T_i \le T \le T_{i,e} \\ a_{max}DAF & for\ T > T_{i,e} \end{cases} \quad (7.16)$$

where T is the spectral period of interest, and T_i is the elastic period of the supporting structure for mode i, which is obtained through traditional eigen-value analysis of the supporting structure. DAF_{max} and DAF are estimated using Equations (7.17) and (7.18), respectively (Welch, 2016).

$$DAF_{max} = \begin{cases} \left(0.55 + 0.45\frac{T_i}{T_B}\right)(0.5\xi_p + \xi_{NS})^{-0.667} & if\ T_i \le T_B \\ (0.5\xi_p + \xi_{NS})^{-0.667} & if\ T_i \ge T_B \end{cases} \tag{7.17}$$

$$DAF = \begin{cases} \left(0.55 + 0.45\frac{T_i}{T_B}\right)\left[\left(1 - \frac{T}{T_{i,e}}\right)^2 + \left(0.5\xi_p + \xi_{NS}\right)\right]^{-0.667} & if\ T_i \le T_B \\ \left[\left(1 - \frac{T}{T_{i,e}}\right)^2 + \left(0.5\xi_p + \xi_{NS}\right)\right]^{-0.667} & if\ T_i \ge T_B \end{cases} \tag{7.18}$$

where ξ_p is the elastic damping of the primary structure, and ξ_{NS} is the elastic damping of the non-structural element. The term T_B is taken as 0.3 sec.

The individual modal contributions to the floor response spectrum are then combined using modal superposition to give the SRSS spectral floor response at a given period T:

$$SFA_j(T)_{SRSS} = \sqrt{\sum_{i=1}^{nm}[a_{m,j,i}(T)]^2} \tag{7.19}$$

where *nm* is the number of modes being considered.

The final spectral floor acceleration $SFA_j(T)$ is given by Equation (7.20) which takes into account rigid mode response observed in the lower levels of MDOF systems (Calvi and Sullivan, 2014; Welch, 2016).

$$SFA_j(T) = \begin{cases} \max\left(SFA_j(T)_{SRSS}, S_a(T, \xi_{NS})\right) & for\ \frac{H_j}{H_n} < 0.5 \\ SFA_j(T)_{SRSS} & for\ \frac{H_j}{H_n} \ge 0.5 \end{cases} \tag{7.20}$$

where H_j is the height of floor level j, and H_n is the height of the roof level. The term $S_a(T,\xi_{NS})$ is the spectral acceleration demand at period T obtained from the design ground response spectrum at the elastic non-structural element damping ratio ξ_{NS}.

7.2.4 Comparison between Floor Response Spectra Estimates and NLTHA Results

The following section presents the floor response spectra estimates obtained using the procedures outlined in the previous sub-sections along with the mean floor response spectra from the NLTHA

of the case study buildings. The comparisons are presented for the 4-story case study buildings at Intensities 1, 5 and 6, and 2% non-structural damping ξ_{NS}. Corresponding comparisons for all case study buildings and non-structural damping ratios can be found in Appendix C.

The comparisons for the 4-story RC wall building are shown in Figures 7.8 to 7.10. These results are considered representative of the results of the 8- and 12-story case study buildings. Only the first three modes of vibration were used to estimate floor spectra. In general, there was very good agreement between floor spectra estimates and NLTHA results. Peak spectral acceleration demands were well predicted using the proposed procedure. Period elongation and the resulting "plateau" in peak spectral acceleration demands were also well predicted. However, for Intensity 1, the first mode contribution was underestimated for the 4-story building (Figure 7.8). For Intensities 5 and 6, the second mode contribution was slightly overestimated at some floor levels (Figures 7.9 and 7.10).

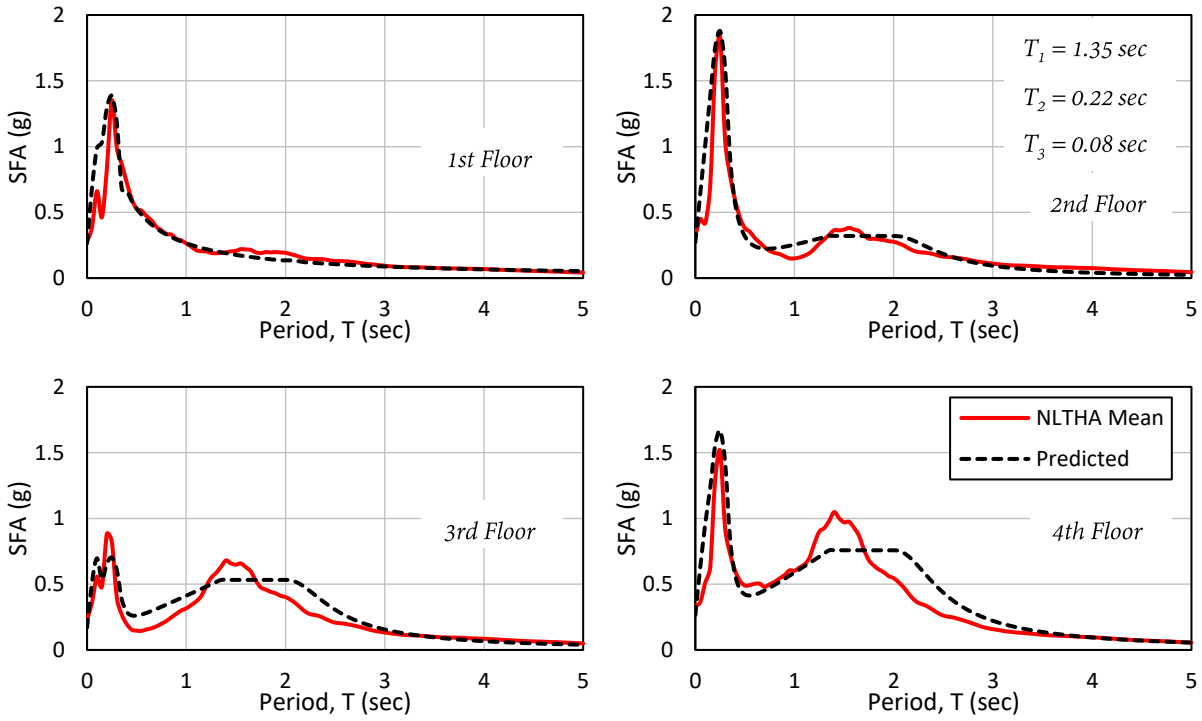

Figure 7.8 Comparison between mean floor spectra from NLTHA and estimates using transitory modal properties; 4-story RC wall building, Intensity 1 (PGA = 0.225 g), ξ_{NS} = 2%

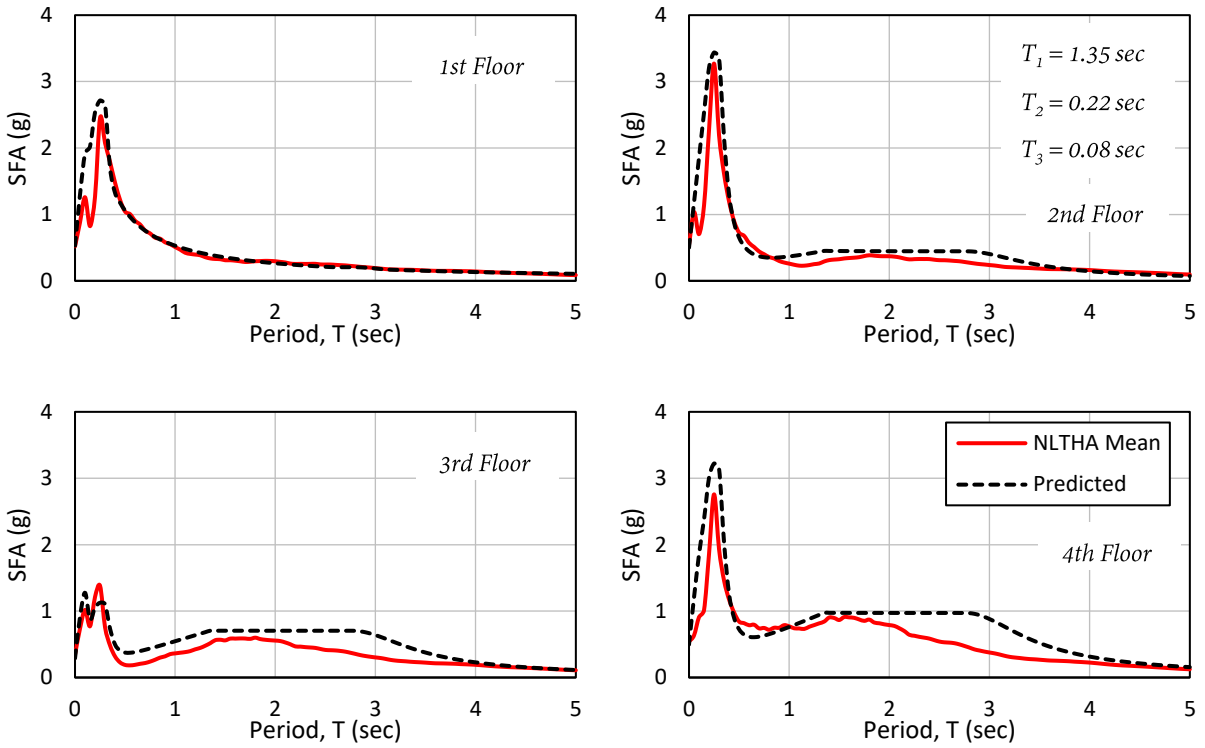

Figure 7.9 Comparison between mean floor spectra from NLTHA and estimates using transitory modal properties; 4-story RC wall building, Intensity 5 (PGA = 0.450g), ξ_{NS} = 2%

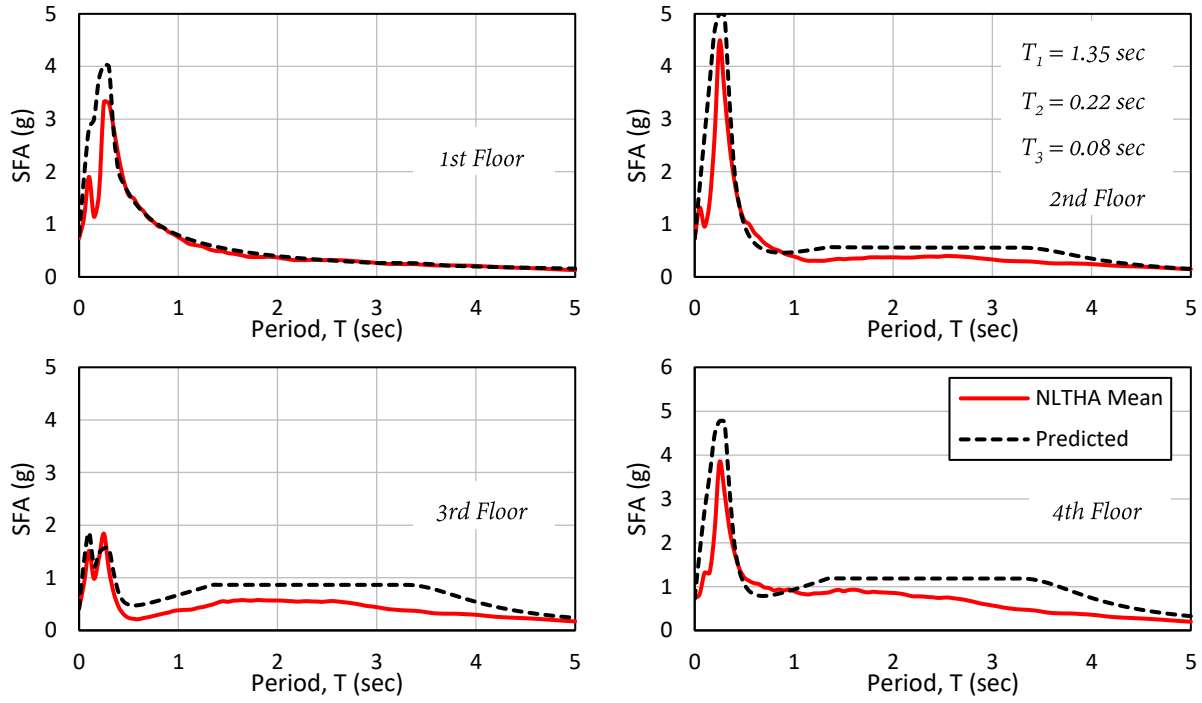

Figure 7.10 Comparison between mean floor spectra from NLTHA and estimates using transitory modal properties; 4-story RC wall building, Intensity 6 (PGA = 0.675g), ξ_{NS} = 2%

The comparisons for the 4-story rocking wall building are presented in Figures 7.11 to 7.13. These results are considered representative of the results of the 8- and 12-story case study buildings. Similar to the RC wall buildings, only the first three modes of vibration were used to estimate the floor response spectra in the rocking wall buildings. This appears to be satisfactory in giving reasonable floor spectra estimates. Both peak spectral acceleration demands and period elongation were well predicted for all case-study buildings. However, first mode contributions were underestimated for the 4- and 8-story buildings at Intensity 1 (Figure 7.11).

Rigid mode response was observed in the lower levels of the rocking wall buildings. This is most apparent in the first floor of the 4-story building in which the NLTHA mean floor response spectra resembles the design ground spectrum with the exception of the second modal peak (Figure 7.11). To this end, it can be observed that taking an envelope of the design ground spectrum and the floor response spectrum obtained through modal superposition appears to capture the rigid body response very well.

Consistent with the trends observed in the estimation of PFA, floor spectra estimates improved with increasing earthquake intensity (i.e. ductility), which indicates that transitory modal properties might be better at estimating structural response at high ductility demands (Figures 7.12 and 7.13).

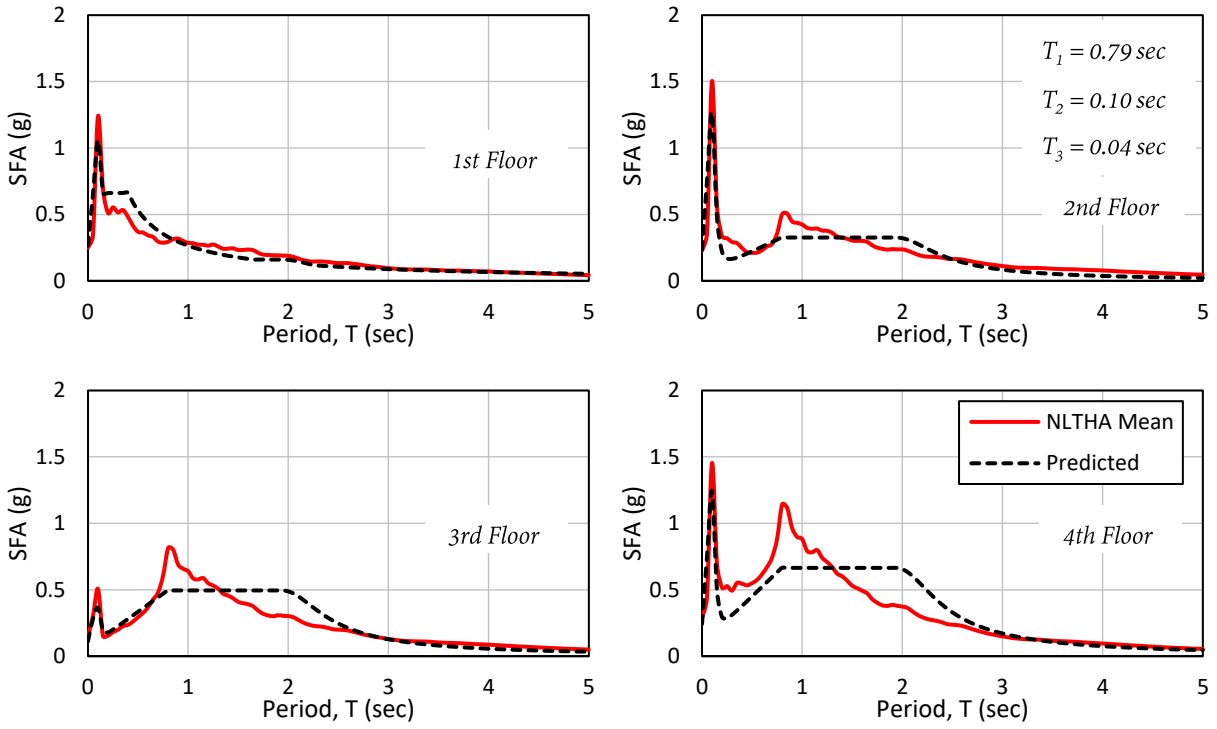

Figure 7.11 Comparison between mean floor spectra from NLTHA and estimates using transitory modal properties; 4-story rocking wall building, Intensity 1 (PGA = 0.225 g), ξ_{NS} = 2%

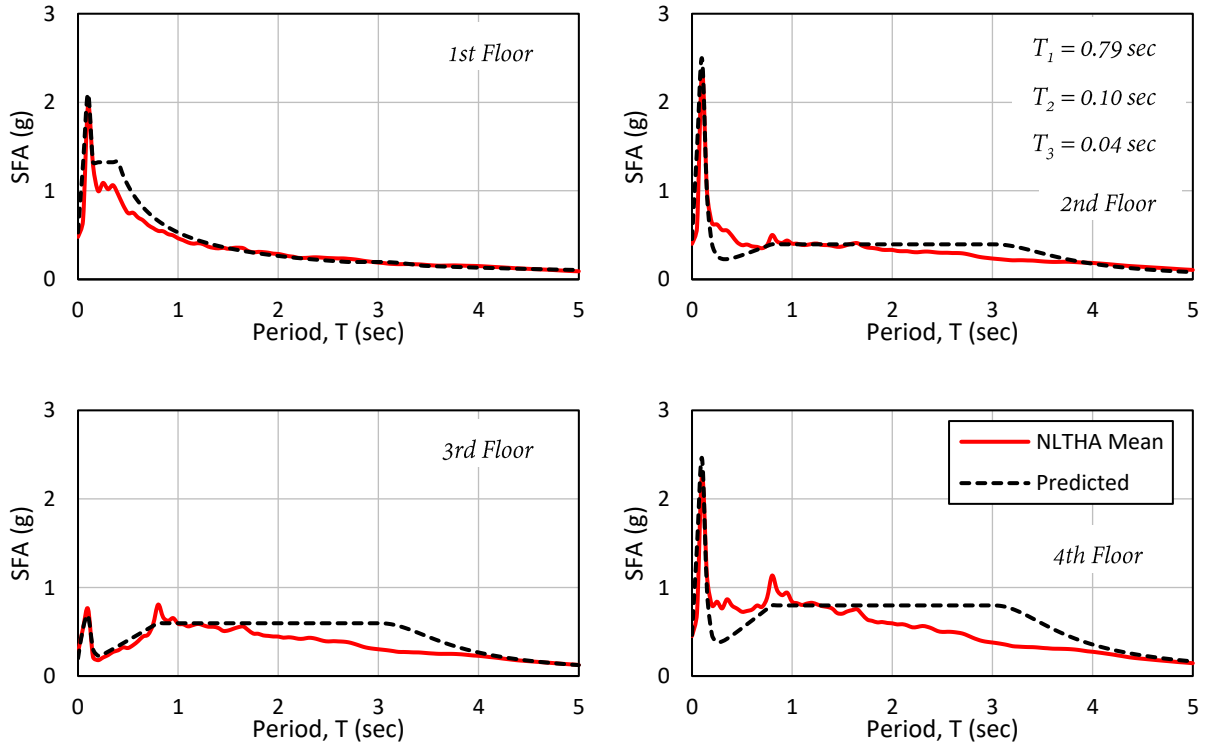

Figure 7.12 Comparison between mean floor spectra from NLTHA and estimates using transitory modal properties; 4-story rocking wall building, Intensity 5 (PGA = 0.450g), ξ_{NS} = 2%

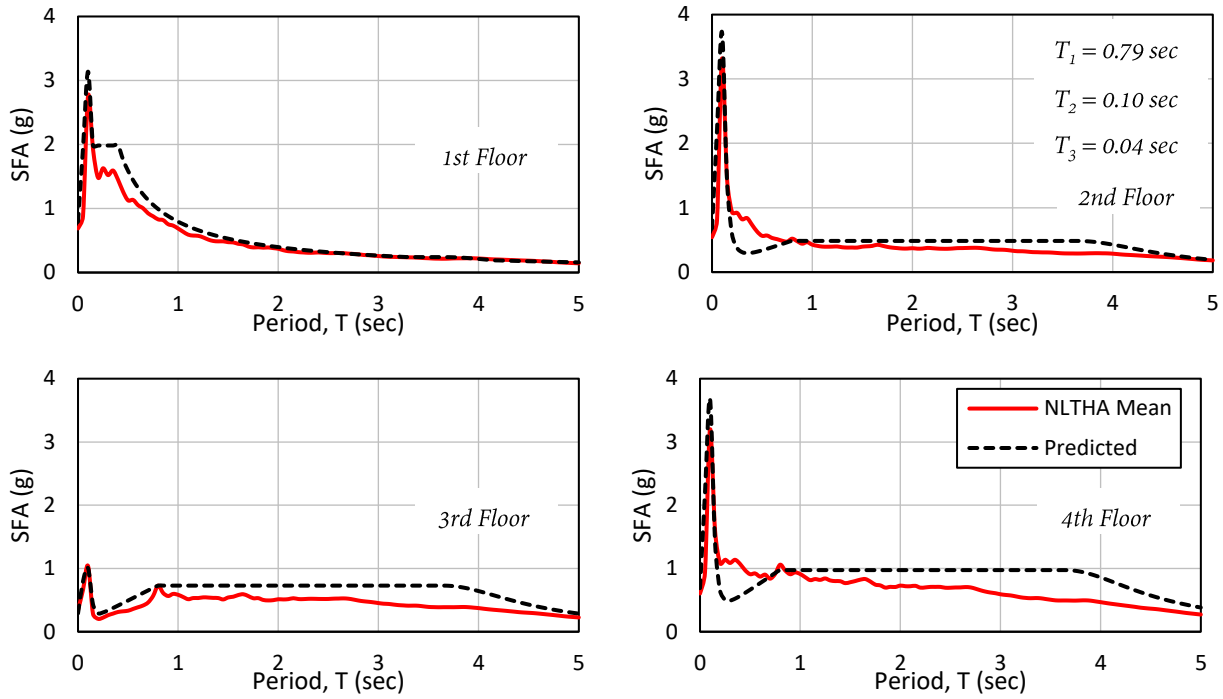

Figure 7.13 Comparison between mean floor spectra from NLTHA and estimates using transitory modal properties; 4-story rocking wall building, Intensity 6 (PGA = 0.675g), ξ_{NS} = 2%

7.2.5 Issues with Using Transitory Modal Characteristics

In the previous sub-sections, it has been proposed that different modal contributions be combined using an SRSS modal superposition in both the estimation of PFAs and floor response spectra. However, as Sullivan *et al.* (2008) note, traditional modal superposition methods, including SRSS, are not theoretically valid for inelastic systems since they were developed with linear random vibration theory. Nevertheless, Sullivan *et al.* (2008) used an SRSS approach and were able to show improved characterization of higher modes acting during non-linear response using transitory modal properties compared to elastic modal properties. Similarly, it has been shown in the previous sub-sections that reasonable estimates of the PFA and the floor response spectra can be obtained using transitory modal characteristics and an SRSS modal superposition method.

It is important to note that the procedure outlined in the previous sub-sections may not be suitable for structural systems characterized by the activation of more than one plastic mechanism, such as moment frames or dual systems. For instance, Sullivan *et al.* (2008) looked at RC Frame-Wall structures, and noted that a number of different stiffness distributions need to be accounted for when determining transitory modal characteristics in systems with multiple plastic hinge locations.

Assuming the first mode causes the development of a plastic mechanism, determining the stiffness of each of the plastic hinges is not straightforward. Thus, Sullivan *et al.* (2008) proposed that the transitory modal characteristics be determined at maximum response assuming a tangent stiffness (approximated as zero) at all plastic hinge locations. This is expected to provide an upper bound for the transitory modal characteristics. Thus, inelastic behavior and consequently floor response spectra may be estimated with this approach but might be limited to maximum structural response for structural systems with more than one location of concentrated inelastic behavior. In any case, the development of procedures to estimate transitory modal characteristics for structural systems with more than one plastic mechanism is not within the scope of this work and should be addressed in future research efforts.

7.3 Estimation of Floor Response Spectra using Empirical Modal Reduction Factors

A common practice in the seismic design of structures is to obtain the seismic design loads assuming a structure will respond elastically and then reducing the loads by means of empirical response modification factors to account for the structure's non-linear response. Typically, the modification factors are dependent on the expected ductility of the structural system in use. Some researchers (Sankaranarayanan, 2007; Welch, 2016; amongst others) have proposed a similar design process for light acceleration sensitive non-structural elements. In this context, it has been proposed that the floor response spectra be first determined assuming the supporting structure behaves elastically, and that the floor spectra be subsequently reduced based on the inelasticity expected in the system. This section explores such a procedure, which was proposed by Welch (2016) for RC wall and steel moment resisting frame (MRF) buildings.

The procedure discussed by Welch (2016) to estimate floor spectra in non-linear MDOF systems involves reducing the elastic modal floor response spectra using empirical modal reduction factors that are dependent on the ductility of the supporting structure. The reduced modal floor response spectra are then combined using an SRSS modal combination rule to obtain floor response spectra that account for the effects of multiple modes and the inelasticity expected in the primary structural system. In this section, the procedure that Welch (2016) proposed for RC wall buildings is tested using a new set of ground motions and case study buildings. In addition, the procedure is extended for use with rocking wall buildings.

7.3.1 Quantifying Modal Reduction Factors

The use of distinct reduction factors for each mode was proposed by Welch (2016) to account for the decreased rate of reduction in spectral acceleration response observed with increasing order of modes during non-linear response. This was also observed in this study (refer to Section 5.3.1) as well as by Sankaranarayanan (2007), amongst others.

In order to account for the non-linear response expected in the primary structure, Welch (2016) proposed a simple relationship between the reduction in spectral acceleration demand and the expected ductility of the primary structure. The reduction was quantified through a regression analysis in the form of Equation (7.21).

$$R_i = \mu^{\alpha_i} \tag{7.21}$$

where R_i is the reduction factor for mode i, μ is the estimated ductility demand of the primary/supporting structural system, and α_i is the exponent governing the rate of reduction in mode i.

For the regression analysis, Welch (2016) ran time history analyses of case-study structures responding both linearly and non-linearly under a large suite of ground motion records. Empirical modal reduction factors were then obtained on a record-by-record basis. A modal reduction factor is the ratio of the spectral floor acceleration (SFA) from linear response to that of the corresponding non-linear response (Equation (7.22)). Figure 7.14 presents an illustration of how this regression analysis was conducted.

$$R_{i,Single\ Record} = \frac{SFA(T_i)_L}{SFA(T_i)_{NL}} \tag{7.22}$$

where $SFA(T_i)$ is the spectral floor acceleration at the period of mode i. The subscripts L and NL represent the linear and non-linear response cases, respectively.

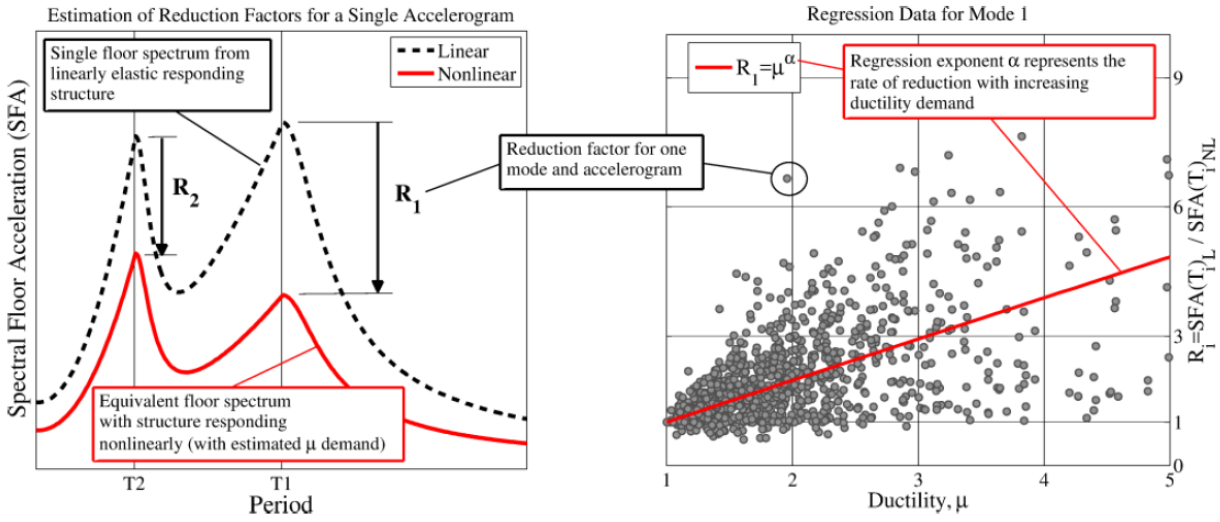

Figure 7.14 Illustration of modal reduction factors for individual accelerograms (left) and example of regression model used (right) (Welch, 2016)

The regression analysis described above was replicated in this study for RC and rocking wall buildings. Both linear and non-linear time history analyses of the case-study buildings were conducted at six intensity levels (refer to Section 4.5.2). The results of these analyses were then used to perform the regression analysis.

The regression analysis was conducted using floor response spectra at the roof level. This is consistent with the analysis conducted by Welch (2016) who noted that mode shapes are typically normalized to the roof level, which should allow for differences in mode shapes to be reasonably accounted for, during modal superposition. The analysis was conducted for ductility values ranging from 1.0 to 5.0 for the RC walls (Welch, 2016) and from 1.0 to 15.0 for the rocking walls. Any data point outside of this range was omitted from the analysis. The raw data was also adjusted during the regression analysis to allow for better tracking of how increasing ductility demands affect acceleration peaks (Welch, 2016). Each reduction factor corresponding to an acceleration record was normalized by a reduction factor obtained at an intensity level resulting in a ductility closest to 1.0 (in the range of 0.9 to 1.1). Thus, a ductility of 1.0 corresponds to a reduction factor of 1.0 for each acceleration record.

The regression analysis was independent of building height and non-structural damping ratio. Thus, the reduction factors for each of the case study buildings (4-, 8- and 12-stories) and non-structural damping ratios (ξ_{NS} = 2%, 5%, 10% and 20%) were collectively used for the regression.

Figures 7.15 and 7.16 present the results of the regression analysis for the RC and rocking wall buildings, respectively. For the RC wall buildings, the results from this study are shown alongside the recommendations of Welch (2016).

For all three modes, the scatter in the reduction factors increased with increasing ductility for both structural wall systems. In addition, the reduction in SFA resulting from inelastic structural response significantly reduced with increasing order of modes. Comparing the two structural systems, for the same increment in ductility, a higher reduction should be expected in the RC wall buildings for all three modes. This supports the notion that RC wall buildings dissipate more energy compared to their rocking wall counterparts, for the same ductility demand.

For the RC wall buildings, the α_i values recommended by Welch (2016) have very good agreement with the data from the present study with the exception of the third mode. For the third mode, Welch (2016) recommended an α_i value of zero based on observations made through a regression analysis of local maxima of median response, which was not conducted in the present study. In addition to the record-by-record regression, Welch (2016) conducted a regression on median floor response spectra in which reduction factors were still quantified in the form of Equation (7.22), but $SFA(T_i)_{NL}$ was determined as a local maximum. Thus, $SFA(T_i)_{NL}$ was obtained as the maximum SFA around the vicinity of the elastic modal period instead of the SFA at the elastic modal period. This was done to capture the influence of period elongation on the reduction of SFA during non-linear response. From this regression analysis, Welch (2016) observed negligible reduction and in some cases even amplification in SFA demands for the third mode, which prompted the recommendation of $\alpha_i = 0$ for the third mode.

In general, the RC wall modal reduction factors recommended by Welch (2016) were slightly conservative for the current data set. Thus, updated values based on the best fit of the current data set were not warranted, and the recommendations of Welch (2016) were adopted in the current

study. A summary of the modal reduction factors recommended for both RC and rocking wall buildings is presented in Table 7.5.

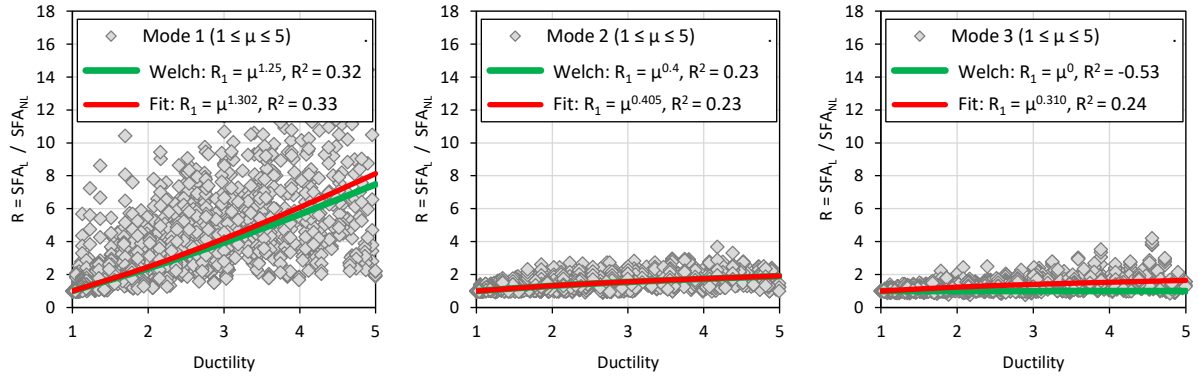

Figure 7.15 Regression analysis results to estimate SFA reduction factors for the first three modes of the RC wall case study buildings; fit using adjusted data at roof level and all non-structural damping ratios

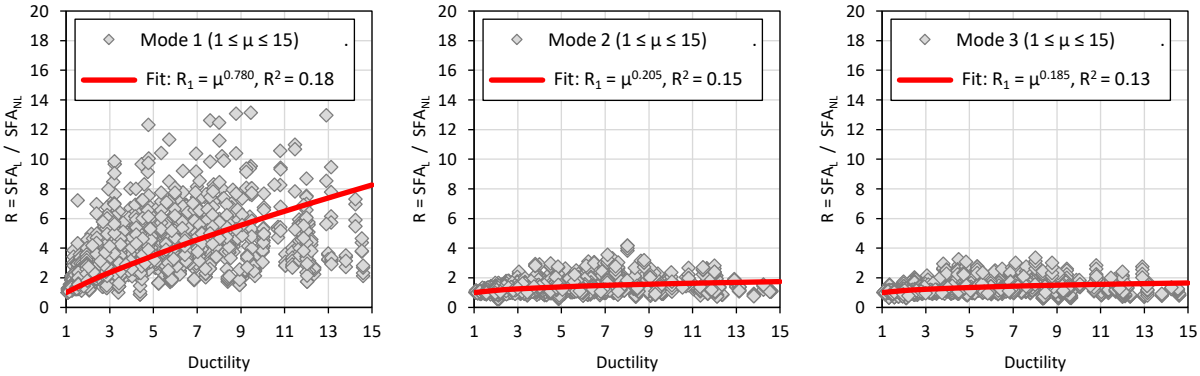

Figure 7.16 Regression analysis results to estimate SFA reduction factors for the first three modes of the rocking wall case study buildings; fit using adjusted data at roof level and all non-structural damping ratios

Table 7.5 Generalized values of modal reduction factors for RC and rocking walls to estimate the expected reduction in SFA during non-linear structural response

Structural System	**Mode 1**	**Mode 2**	**Mode 3**
	α_1	**α_2**	**α_3**
RC Walls *	1.25	0.4	0
Rocking Walls	0.75	0.20	0.18
*Proposed by Welch (2016) Modal reduction factor taken as $R_i = \mu^{\alpha}$			

7.3.2 Quantifying Period Elongation

As discussed in Section 5.3.1, inelastic structural response leads to a "plateau" of peak SFA demands at modal periods. This is due to the modal periods of the supporting structure lengthening as the supporting structure deforms non-linearly. Thus, peak SFA demands occur over a range of periods starting at the elastic period and ending at the effective period of the primary structure. It was also observed that the extent of period elongation decreases with increasing order of modes. In order to capture this "plateau" in peak SFA demands, approximations for the effective periods of RC and rocking wall buildings are proposed in this section.

For both RC and rocking wall buildings, the effective period for the first mode can be calculated as:

$$T_{1,e} = T_1 \sqrt{\frac{\mu}{[1 + r(\mu - 1)]}} \tag{7.23}$$

where $T_{1,e}$ is the effective first mode period, T_1 is the elastic first mode period, and r is the global strain hardening factor.

For the effective second mode period of RC wall buildings, Welch (2016) proposed an approximation based on continuum mechanics of fully-fixed and fully-pinned cantilever beams with the same distributed mass and sectional properties. For fully-fixed cantilever beams, the theoretical second mode period can be approximated by Equation (7.24) (Chopra, 2001). If a fully-fixed cantilever beam goes through inelastic deformation and becomes a fully-pinned cantilever beam, the second mode period can be approximated by Equation (7.25) (Pennucci *et al.*, 2015).

$$T_{2,fix} = 0.285L^2 \sqrt{\frac{m}{EI}} \tag{7.24}$$

where L is the length, m is the uniformly distributed mass, and EI is the stiffness of the beam.

$$T_{2,pin} = 0.407L^2 \sqrt{\frac{m}{EI}} \tag{7.25}$$

By comparing the coefficients of Equations (7.24) and (7.25), it can be seen that a 44% period elongation could be expected in the second mode when transitioning from a fully-fixed to a fully-pinned cantilever beam.

In order to define a limit at which the plastic hinge of an RC wall building can be considered fully-pinned, a ductility demand μ_{pin} of 5 was suggested by Pennucci *et al.* (2015). However, a lower value of 3.5 has also been suggested for coupled walls by Pennucci *et al.* (2011). For simplicity, Welch (2016) adopted a μ_{pin} of 5 and approximated the second mode period elongation as 50% at fully-pinned case. Mathematically, this is presented as Equation (7.26), which was adopted in this study.

$$T_{2,e} = \begin{cases} T_2 & for \quad \mu \leq 1.0 \\ T_2\left(1 + 0.5\left(\frac{\mu}{\mu_{pin}}\right)\right) & for \; 1.0 < \mu < \mu_{pin} \\ 1.5T_2 & for \quad \mu \geq \mu_{pin} \end{cases} \tag{7.26}$$

where $T_{2,e}$ is the effective second mode period, and T_2 is the elastic second mode period. The term μ_{pin} is the ductility limit corresponding to the pinned behavior of higher modes.

Similar to RC wall buildings, the second mode period for rocking wall buildings is also bounded by the periods of fully-fixed and fully-pinned cantilever beams. The difference between RC and rocking walls is in the ductility limit at which the wall can be considered fully-pinned. To the author's knowledge, an appropriate ductility limit μ_{pin} has not be proposed in the literature. From the displacement-based design of rocking wall buildings, maximum ductility demands of 8.5 and 13.3 were obtained in this study and by Pennucci *et al.* (2009), respectively. By considering these values, a conservative value of 13 is proposed for μ_{pin} until a reasonable estimate is proposed in future studies.

As discussed in Section 5.3.1, negligible period elongation was observed in the third and higher modes for both the RC and rocking wall case study buildings. Thus, the inclusion of a "plateau" in peak SFA demands is not proposed for the third and higher modes for both RC and rocking wall buildings.

7.3.3 Estimation of Floor Response Spectra

The modal floor acceleration contributions $a_{max,j,i}$ for a given mode i at a floor level j is given by:

$$a_{max,j,i} = \phi_{j,i}\Gamma_i\left(\frac{S_a\left(T_i, \xi_p\right)}{R_i}\right); \quad R_i \geq 1 \tag{7.27}$$

where $S_a(T_i, \xi_p)$ is the elastic spectral acceleration demand for the mode *i* obtained from the design ground response spectrum at the primary damping ratio. The term R_i is the modal reduction factor for mode *i* that accounts for the non-linear demands of the primary structure.

Once the modal contributions to the PFA are determined, the individual modal contributions $a_{m,j,i}(T)$ to the floor response spectrum are given by:

$$a_{m,j,i}(T) = \begin{cases} \left(\frac{T}{T_i}\right)\left[a_{max,j,i}(DAF_{max} - 1)\right] + a_{max,j,i} & for\ T < T_i \\ a_{max,j,i} DAF_{max} & for\ T_i \le T \le T_{i,e} \\ a_{max} DAF & for\ T > T_{i,e} \end{cases} \tag{7.28}$$

where T is the spectral period of interest, and T_i is the elastic period of the primary structure for mode *i*, and $T_{i,e}$ is the effective period of the primary structure for mode *i*. DAF_{max} and DAF are estimated using Equations (7.29) and (7.30), respectively (Welch, 2016).

$$DAF_{max} = \begin{cases} \left(0.55 + 0.45\frac{T_i}{T_B}\right)(0.5\xi_p + \xi_{NS})^{-0.667} & if\ T_i \le T_B \\ (0.5\xi_p + \xi_{NS})^{-0.667} & if\ T_i \ge T_B \end{cases} \tag{7.29}$$

$$DAF = \begin{cases} \left(0.55 + 0.45\frac{T_i}{T_B}\right)\left[\left(1 - \frac{T}{T_{i,e}}\right)^2 + \left(0.5\xi_p + \xi_{NS}\right)\right]^{-0.667} & if\ T_i \le T_B \\ \left[\left(1 - \frac{T}{T_{i,e}}\right)^2 + \left(0.5\xi_p + \xi_{NS}\right)\right]^{-0.667} & if\ T_i \ge T_B \end{cases} \tag{7.30}$$

where ξ_p is the elastic damping of the primary structure, and ξ_{NS} is the elastic damping of the non-structural element. The term T_B is taken as 0.3 sec.

The individual modal contributions to the floor response spectrum are then combined using modal superposition to give the SRSS spectral floor response at a given period *T*:

$$SFA_j(T)_{SRSS} = \sqrt{\sum_{i=1}^{nm} [a_{m,j,i}(T)]^2} \tag{7.31}$$

where *nm* is the number of modes being considered.

The final spectral floor acceleration $SFA_j(T)$ is given by Equation (7.32), which takes into account rigid mode response observed in the lower levels of MDOF systems (Calvi and Sullivan, 2014; Welch, 2016).

$$SFA_j(T) = \begin{cases} \max\left(SFA_j(T)_{SRSS}, S_a(T,\xi_{NS})\right) & for\ \frac{H_j}{H_n} < 0.5 \\ SFA_j(T)_{SRSS} & for\ \frac{H_j}{H_n} \geq 0.5 \end{cases} \quad (7.32)$$

where H_j is the height of floor level j, and H_n is the height of the roof level. The term $S_a(T,\xi_{NS})$ is the spectral acceleration demand at period T obtained from the design ground response spectrum at the elastic non-structural element damping ratio ξ_{NS}.

7.3.4 Comparison between Floor Response Spectra Estimates and NLTHA Results

The following section presents the floor response spectra estimates obtained using the procedures outlined above along with the mean floor response spectra from the NLTHA of the case study buildings. The comparisons are presented for Intensity 5 and 2% non-structural damping ξ_{NS}. Corresponding comparisons for all intensities and non-structural damping ratios are presented in Appendix C.

The comparisons for the RC wall buildings are presented in Figures 7.17 to 7.19. In general, the floor response spectra predictions were in good agreement with NLTHA results. Peak spectral accelerations as well as the "plateau" of the peaks were well predicted for the 8- and 12-story buildings. However, the first and second mode peak spectral accelerations were slightly underestimated for the 4-story building. This is reasonable considering the high ductility observed in the 4-story building relative to the 8- and 12-story buildings. As discussed Section 7.3.1, more scatter was observed in modal reduction factors for high ductility demands during the regression analysis.

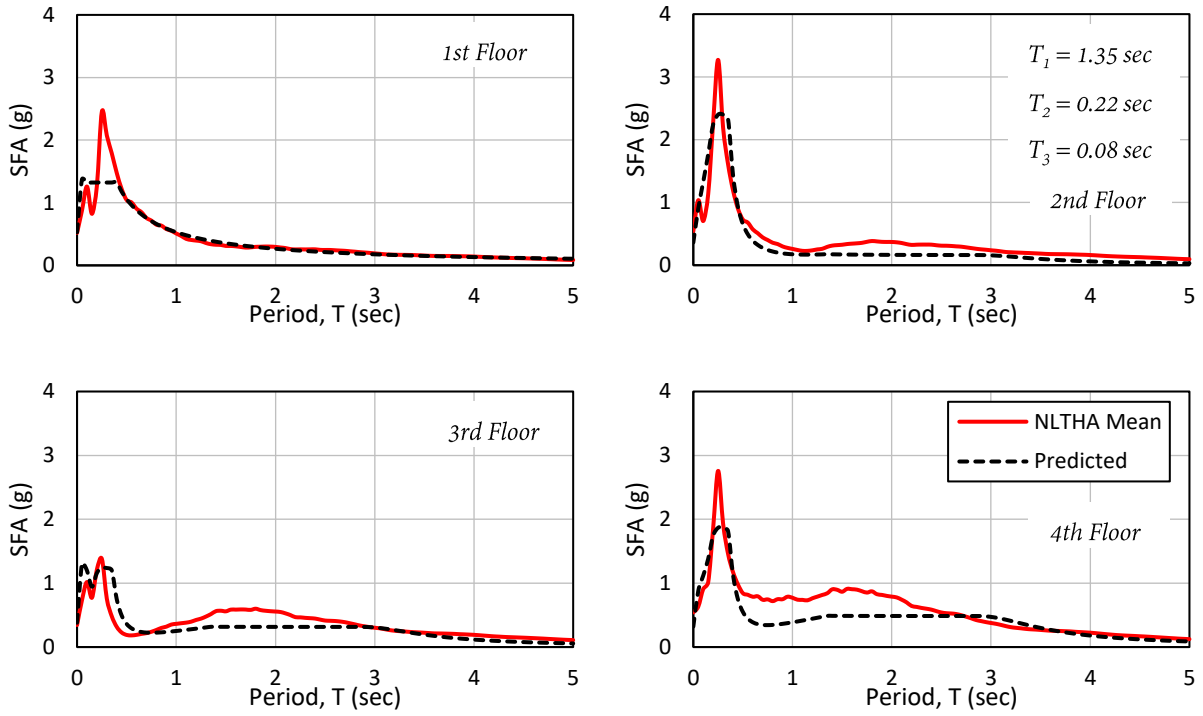

Figure 7.17 Comparison between mean floor spectra from NLTHA and estimates using modal reduction factors; 4-story RC wall building, Intensity 5 (PGA = 0.450 g), ξ_{NS} = 2%

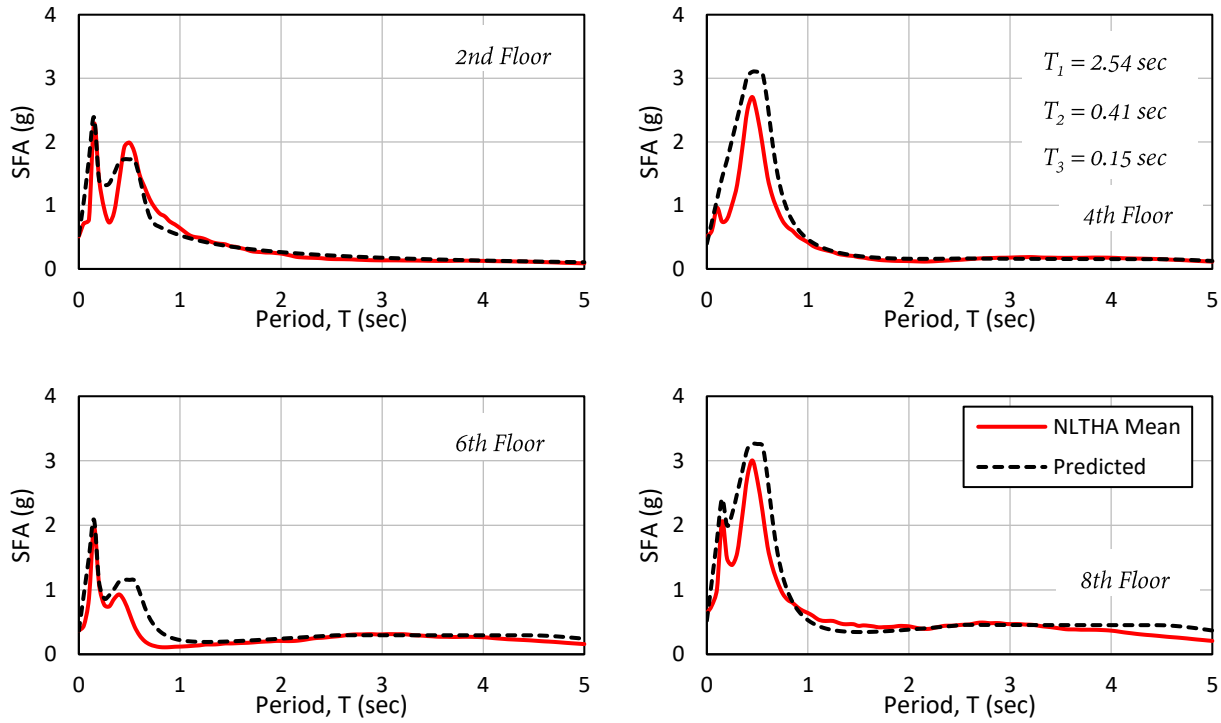

Figure 7.18 Comparison between mean floor spectra from NLTHA and estimates using modal reduction factors; 8-story RC wall building, Intensity 5 (PGA = 0.450 g), ξ_{NS} = 2%

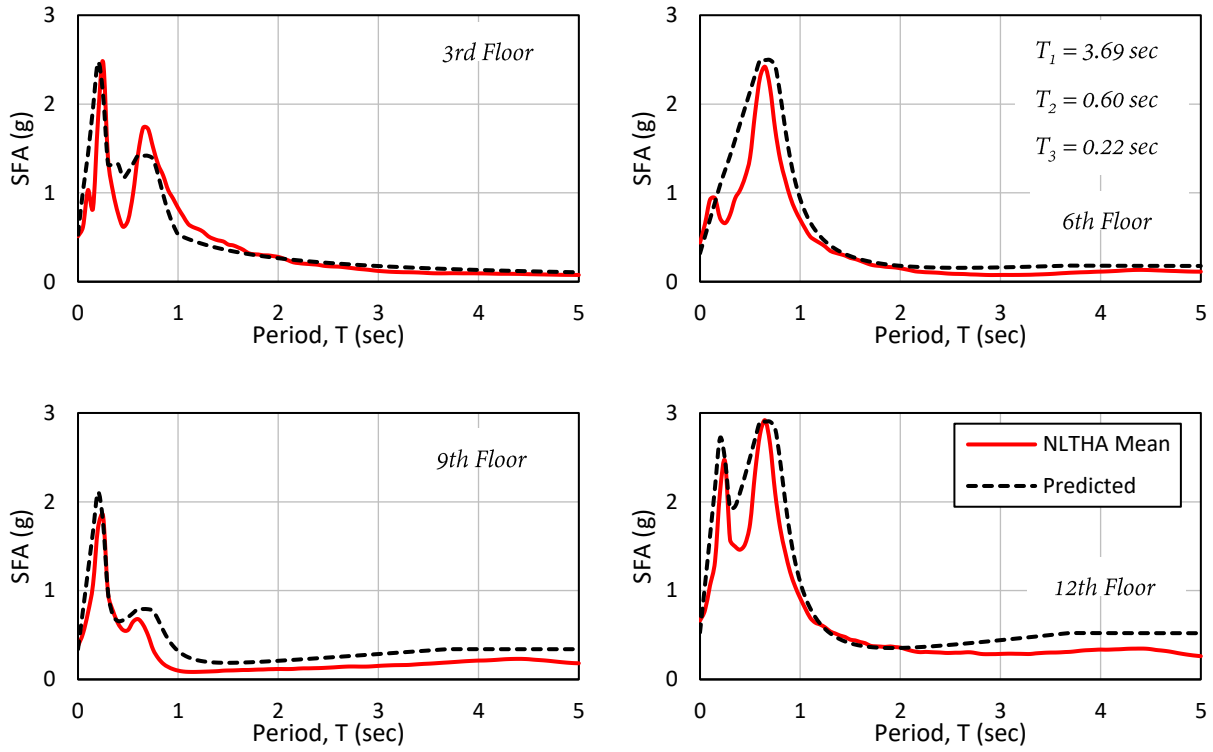

Figure 7.19 Comparison between mean floor spectra from NLTHA and estimates using modal reduction factors; 12-story RC wall building, Intensity 5 (PGA = 0.450 g), ξ_{NS} = 2%

The comparisons for the rocking wall buildings are presented in Figures 7.20 to 7.22. Overall, the proposed procedure provided reasonable estimates for floor response spectra atop rocking wall buildings. Specifically, the first and third mode contributions to the floor response spectra were well predicted for all case study buildings. However, the second mode contribution was slightly underestimated for all case study buildings.

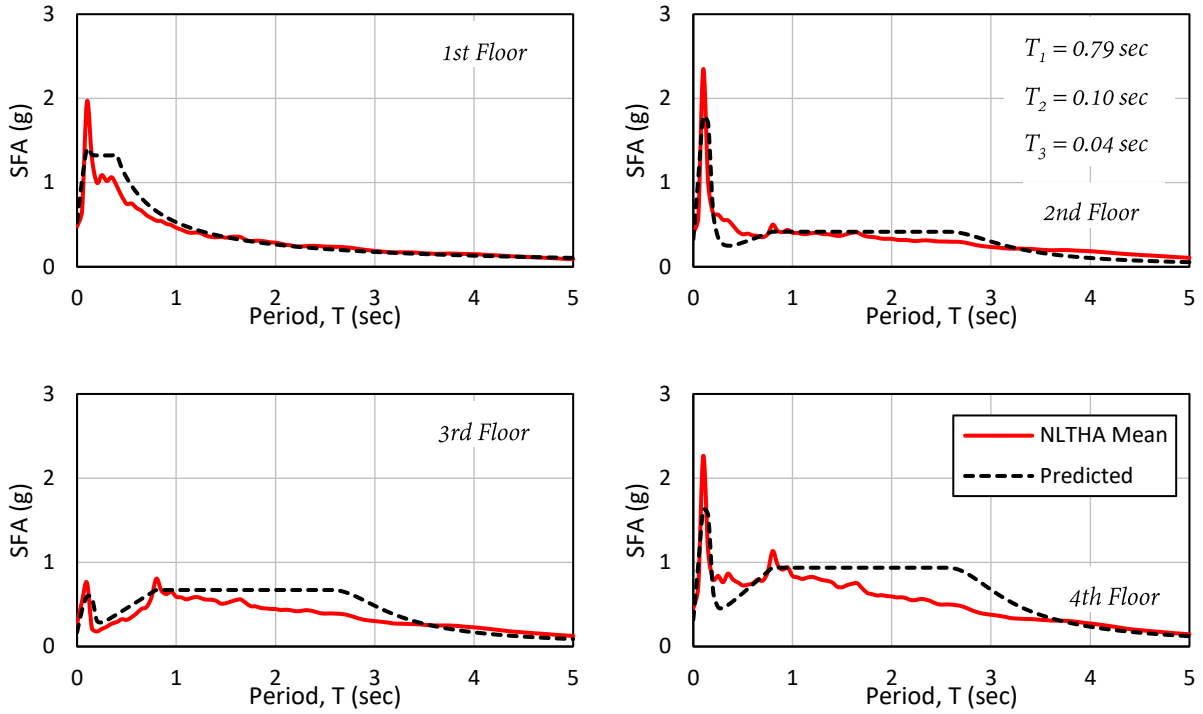

Figure 7.20 Comparison between mean floor spectra from NLTHA and estimates using modal reduction factors; 4-story rocking wall building, Intensity 5 (PGA = 0.450 g), ξ_{NS} = 2%

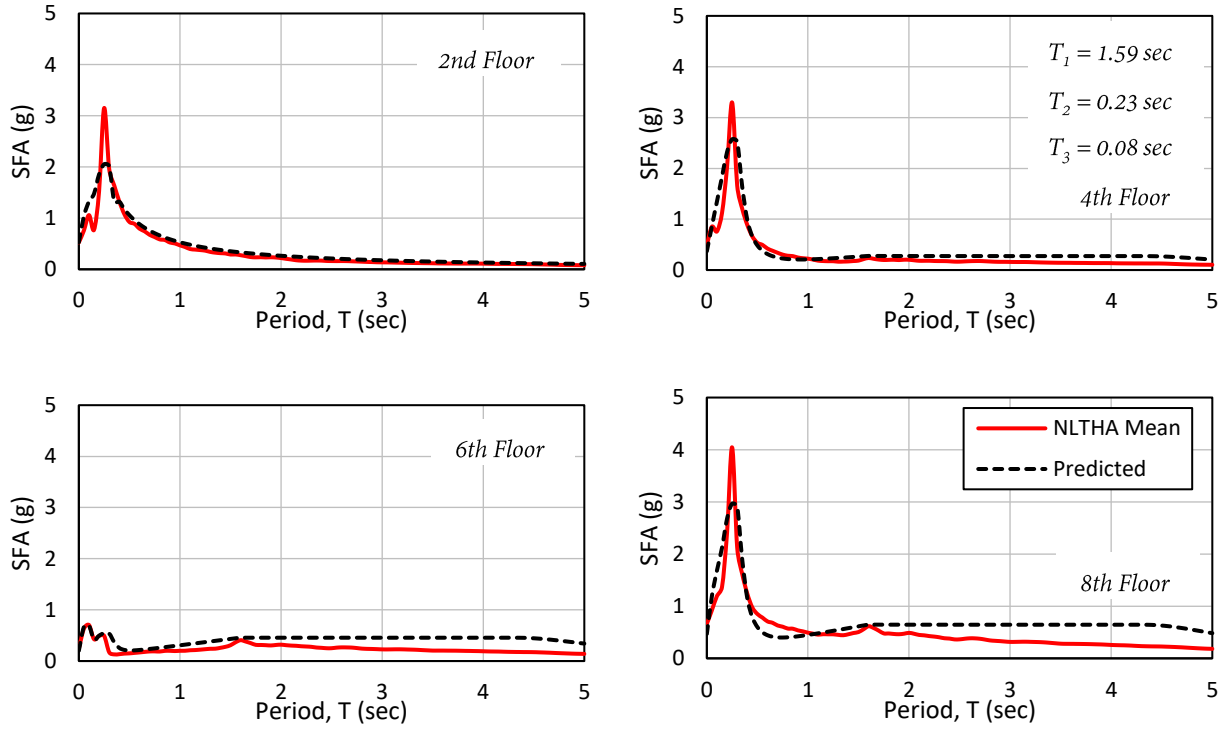

Figure 7.21 Comparison between mean floor spectra from NLTHA and estimates using modal reduction factors; 8-story rocking wall building, Intensity 5 (PGA = 0.450 g), ξ_{NS} = 2%

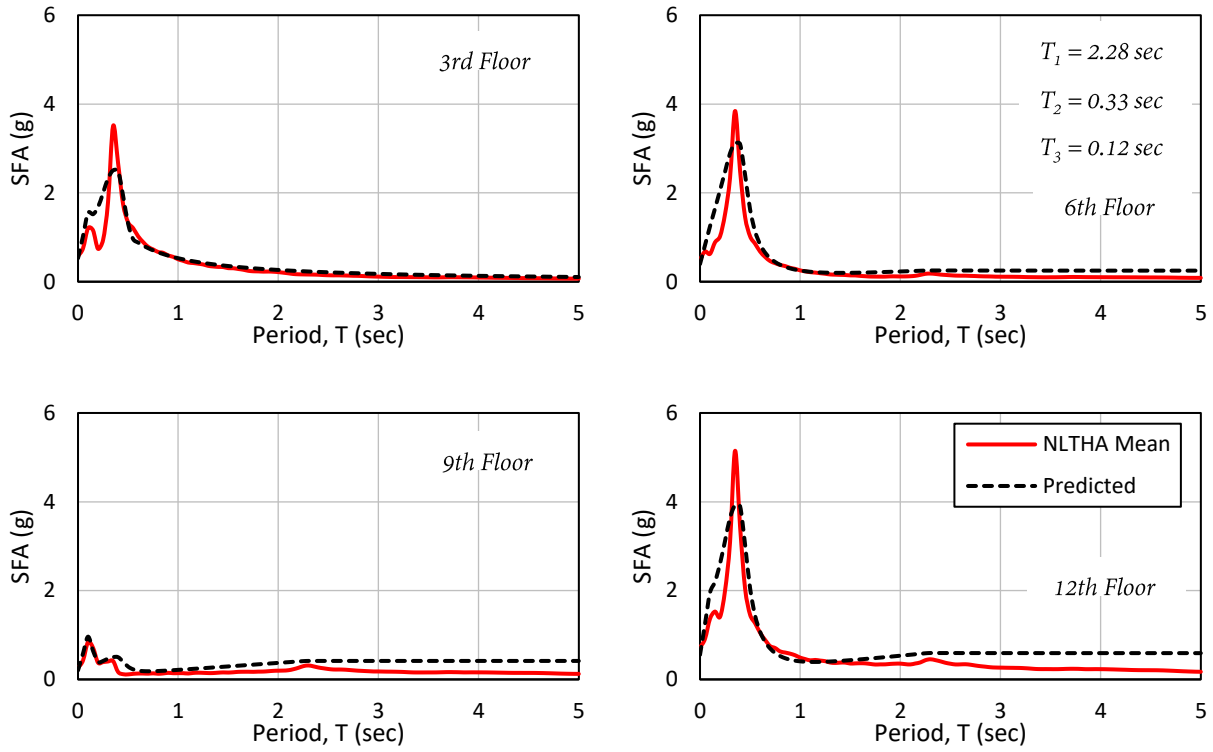

Figure 7.22 Comparison between mean floor spectra from NLTHA and estimates using modal reduction factors; 12-story rocking wall building, Intensity 5 (PGA = 0.450 g), ξ_{NS} = 2%

7.4 Estimation of Floor Response Spectra using Dynamics of Distributed-Mass Systems

This section explores the feasibility of approximating floor response spectra atop RC and rocking wall buildings using the dynamic properties of continuous distributed-mass beams. This approach can be useful for the consideration of non-structural elements (NSEs) during the early design phases of a building when there is limited knowledge about the dynamic characteristics of the building, such as right after the completion of a direct displacement-based design (DDBD). Other approximate and closed-form methods to estimate acceleration demands on NSEs have been proposed in the literature such as the work of Miranda and Taghavi (2005) who proposed approximate methods to estimate PFAs in MDOF buildings responding elastically.

The floor response spectra estimation procedure discussed in this section is based on the procedure proposed by Calvi and Sullivan (2014). Thus, floor response spectra are generated by combining individual modal response spectra using modal superposition. In order to generate the modal response spectra, the modal properties of the building need to be known. Therefore, the first two

sub-sections focus on how the modal characteristics of RC and rocking wall buildings can be approximated using closed-form modal properties of continuous distributed-mass beams. For this, it was assumed that the only information available to the designer is the direct displacement-based design (DDBD) outcomes. Then, procedures to approximate floor response spectra for RC and rocking wall buildings are proposed and verified.

7.4.1 Approximate Elastic Modal Characteristics for RC Wall Buildings

To estimate their modal characteristics, RC wall buildings can be idealized as continuous cantilever beams with uniform stiffness *EI* and uniform distributed mass per unit length *m*. Thus, the concentrated masses at each floor level are assumed distributed across the whole height of the wall. For uniform cantilever beams with length *L*, the natural period T_i and mode shape ϕ_i for mode *i* are given by Equations (7.33) and (7.34) respectively (Chopra, 2001).

$$T_i = \alpha_i L^2 \sqrt{\frac{m}{EI}} \tag{7.33}$$

where $\alpha_i = 1.787, 0.285, 0.102, 0.052, etc.$

$$\phi_i(x) = \cosh \beta_i x - \cos \beta_i x - \frac{\cosh \beta_i L + \cos \beta_i L}{\sinh \beta_i L + \sin \beta_i L}(\sinh \beta_i x - \sin \beta_i x) \tag{7.34}$$

where $\beta_i L = 1.8751, 4.6941, 7.8548, 10.996, etc.$

After the preliminary design of an RC wall building is completed (e.g. using a DDBD approach), only the total mass of the building, the effective first mode period $T_{1,e}$ and the expected ductility μ are known (refer to Section 4.3). The elastic stiffness of the wall *EI* is not known. In order to estimate *EI*, the elastic fundamental mode period is first estimated using Equation (7.35), which assumes that the global post-yield stiffness factor *r* is zero.

$$T_1 = T_{1,e}\sqrt{\mu} \tag{7.35}$$

Once the elastic first mode period is known, the elastic stiffness of the wall *EI* can be approximated by rearranging Equation (7.33) for the first mode, which is illustrated in Equation (7.36).

$$EI = m\left(\frac{1.787L^2}{T_1}\right)^2 \tag{7.36}$$

With the elastic stiffness of the wall approximated, the elastic modal characteristics of the RC wall building can be easily obtained using Equations (7.33) and (7.34).

The procedure outlined above was used to obtain approximate elastic modal properties for the RC wall case study buildings, which are presented in Appendix A. The approximations were then compared to modal properties obtained through traditional modal analysis. The comparisons for the first three modal periods and mode shapes are presented in Table 7.6 and Figure 7.23 respectively.

It can observed that reasonable approximations of both modal periods and mode shapes were obtained by idealizing RC wall buildings as continuous cantilever beams. The approximations were better for lower order of modes, with the first mode shape approximation almost identical to the one obtained through modal analysis (Figure 7.23). It should also be noted that the approximations significantly improved with increasing building height. This was expected because as the number of degrees-of-freedom (i.e. floor levels) increases, approximating a lumped-mass system as a continuous beam with a distributed mass becomes more realistic.

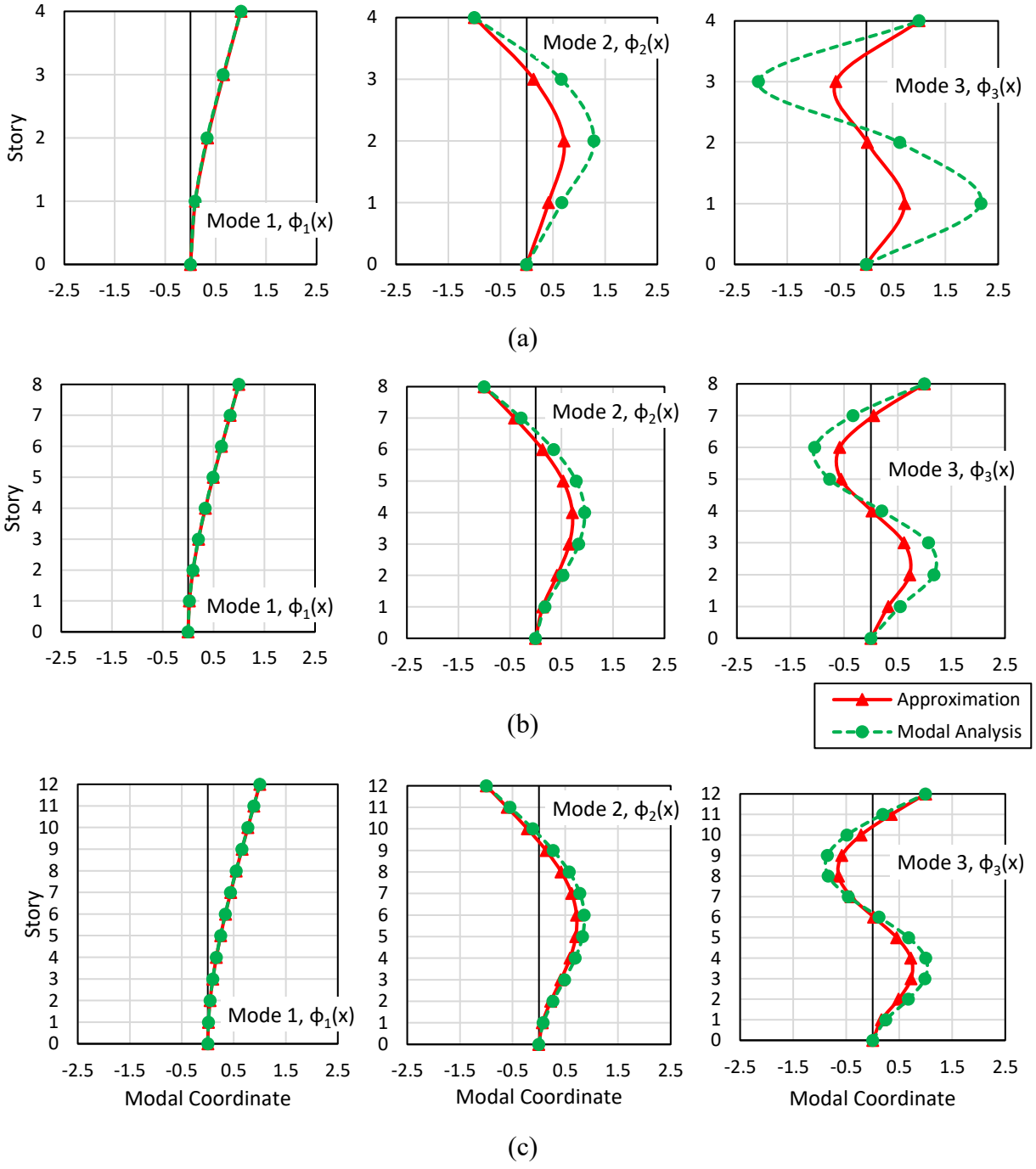

Figure 7.23 Comparison between mode shapes obtained through modal analysis and approximate mode shapes of continuous cantilever beams; (a) 4-story; (b) 8-story; (c) 12-story

Table 7.6 Comparison between modal periods obtained through modal analysis and approximate modal periods of continuous cantilever beams

	Modal Periods (sec)								
	4 Story			8 Story			12 Story		
	T_1	T_2	T_3	T_1	T_2	T_3	T_1	T_2	T_3
Approximation	1.27	0.20	0.07	2.48	0.40	0.14	3.73	0.60	0.21
Modal Analysis	1.35	0.22	0.08	2.54	0.41	0.15	3.69	0.60	0.22
Difference	-6.2%	-6.9%	-9.8%	-2.4%	-4.0%	-6.5%	1.3%	-0.2%	-2.3%

7.4.2 Approximate Elastic Modal Characteristics for Rocking Wall Buildings

To estimate the modal characteristics of rocking wall buildings, rocking walls can be idealized as spring-hinged (at the foundation) uniform continuous beams. Again, the concentrated masses at each floor level of the rocking wall buildings are assumed to be distributed evenly along the height of the wall.

For a spring-hinged uniform beam with length *L*, uniform stiffness *EI*, uniform distributed mass per unit length *m*, and base rotational spring stiffness *K*, the modal period for mode *i* is given by (Chun, 1972):

$$T_i = \frac{2\pi L^2}{(\beta_i L)^2}\sqrt{\frac{m}{EI}} \tag{7.37}$$

where the $\beta_i L$ terms are the roots of Equation (7.38).

$$\frac{KL}{EI}\frac{1}{\beta_i L}\left(\frac{1}{\cos\beta_i L * \cosh\beta_i L} + 1\right) - \tan\beta_i L + \tanh\beta_i L = 0 \tag{7.38}$$

The mode shape for mode *i* is given by (Chun, 1972; Jacobson and Ayre, 1958):

$$\phi_i(x) = \frac{-KL}{EI}\frac{1}{\beta_i L}\left(\frac{C}{D}\right)_i(\cos\beta_i x - \cosh\beta_i x) + \left(\frac{C}{D}\right)_i(\sin\beta_i x + \sinh\beta_i x) + (\sin\beta_i x - \sinh\beta_i x) \tag{7.39}$$

where

$$\left(\frac{C}{D}\right)_i = \frac{\sin\beta_i L + \sinh\beta_i L}{\frac{KL}{EI}\frac{1}{\beta_i L}(\cos\beta_i L + \cosh\beta_i L) + \sinh\beta_i L - \sin\beta_i L} \tag{7.40}$$

Again, following the displacement based design of a rocking wall building, the total mass of the building, the effective first mode period $T_{1,e}$ and the expected ductility μ are known (refer to Section 4.3). However, analogously to the case of RC wall systems, the elastic stiffness of the wall *EI* and the elastic rotational spring stiffness *K* are not known.

Recognizing that rocking wall panels have been observed to sustain minor to no cracking during experimental investigations (Priestley *et* al., 1999; Rahman and Restrepo, 2000; Belleri *et al.*, 2014; Gavridou, 2015; amongst others), it is proposed that the elastic stiffness of the wall *EI* be approximated as 85% of gross stiffness. In order to approximate the elastic base rotational spring stiffness *K*, the elastic fundamental mode period is first estimated using Equation (7.41), which assumes that the global post-yield stiffness factor *r* is zero.

$$T_1 = T_{1,e}\sqrt{\mu} \tag{7.41}$$

Once the elastic first mode period is known, $\beta_1 L$ can be calculated by rearranging Equation (7.37). Then, the elastic base rotational spring stiffness *K* can be estimated by rearranging Equation (7.39) and plugging in $\beta_1 L$. Equation (7.42) summarizes these steps into one equation.

$$K = \frac{\beta_1 L\, EI(\tan\beta_1 L - \tanh\beta_1 L)}{L\left(\frac{1}{\cos\beta_1 L * \cosh\beta_1 L} + 1\right)} \tag{7.42}$$

where

$$\beta_1 L = \sqrt{\frac{2\pi L^2}{T_1}\sqrt{\frac{m}{EI}}} \tag{7.43}$$

With the elastic stiffness values of the wall and the base rotational spring approximated, the modal properties of the rocking walls can be estimated using Equations (7.37) and (7.39).

Even though the modal properties of rocking wall buildings can be estimated with the procedure outline above, the process is somewhat complicated and time consuming. In order to simplify the procedure, the base rotational spring stiffness can be assumed as zero (*K = 0*). Thus, the rocking

walls are idealized as fully-pinned continuous cantilever beams. For such systems, the modal properties can be easily computed using Equations (7.44) and (7.45) (Pennucci *et al.*, 2011).

$$T_i = \alpha_i L^2 \sqrt{\frac{\overline{m}}{EI}} \tag{7.44}$$

where $\alpha_i = 0.407, 0.126, 0.060, etc.$

$$\phi_i(x) = \sin \beta_i x + \frac{\sin \beta_i L}{\sinh \beta_i L} \sinh \beta_i x \tag{7.45}$$

where $\beta_i L = \frac{\pi}{4} + i\pi$

The first mode of vibration for a fully-pinned cantilever beam corresponds to the second mode of vibration for the rocking walls. The first mode of vibration for the rocking walls is approximated as a rigid body rotation and thus cannot be determined with Equations (7.44) and (7.45). Instead, the first mode period is approximated from the displacement-based design outcomes by using Equation (7.41). The first mode shape (i.e. rigid body rotation) can be obtained with a simple linear function (Equation (7.46)) that linearly increases the modal coordinates from a value of zero at the base of the wall to a value of one at the roof level.

$$\phi_1(x) = \frac{x}{L} \tag{7.46}$$

Both procedures outlined above were utilized to obtain approximate elastic modal properties for the rocking wall case-study buildings, which are presented in Appendix A. Comparisons between the approximations and modal properties obtained through traditional modal analysis are presented for the first three modes in Table 7.7 and Figure 7.24.

Compared to the RC wall buildings, there was significantly more error in the approximation of modal periods for the rocking wall buildings (Table 7.7). However, idealizing the rocking walls as spring-hinged cantilever beams resulted in better estimates of modal periods. This was expected since idealizing a rocking wall as a sprung-base cantilever is a more realistic representation of rocking behavior compared to a fully-pinned cantilever. In addition, the estimates improved with increasing height, consistent with the observations in the RC wall buildings. In terms of mode shapes, both the fully-pinned and sprung-base cantilever beams resulted in almost identical approximations (Figure 7.24).

As mentioned above, idealizing the rocking walls as sprung-base cantilever beams was relatively time consuming. Thus, it is proposed that rocking walls be idealized as fully-pinned cantilever beams. The additional error in modal periods is considered acceptable noting the relative ease of obtaining modal properties for fully-pinned cantilever beams.

Table 7.7 Comparison between modal periods obtained through modal analysis and approximate modal periods of spring-hinged and fully-pinned cantilever beams

	Modal Periods (sec)								
	4 Story			**8 Story**			**12 Story**		
	T_1	**T_2**	**T_3**	**T_1**	**T_2**	**T_3**	**T_1**	**T_2**	**T_3**
Approximation, Spring-Hinged Base (K≠0)	1.05	0.08	0.03	2.00	0.20	0.07	3.04	0.31	0.10
Modal Analysis	0.79	0.10	0.04	1.59	0.23	0.08	2.28	0.33	0.12
Difference	32%	- 20%	-34%	26%	-10%	-22%	34%	-4%	-16%
Approximation, Fully-Pinned Base (K=0)	1.05	0.07	0.02	2.00	0.17	0.05	3.04	0.27	0.08
Modal Analysis	0.79	0.10	0.04	1.59	0.23	0.08	2.28	0.33	0.12
Difference	32%	-35%	-48%	26%	-25%	-37%	34%	-19%	-31%

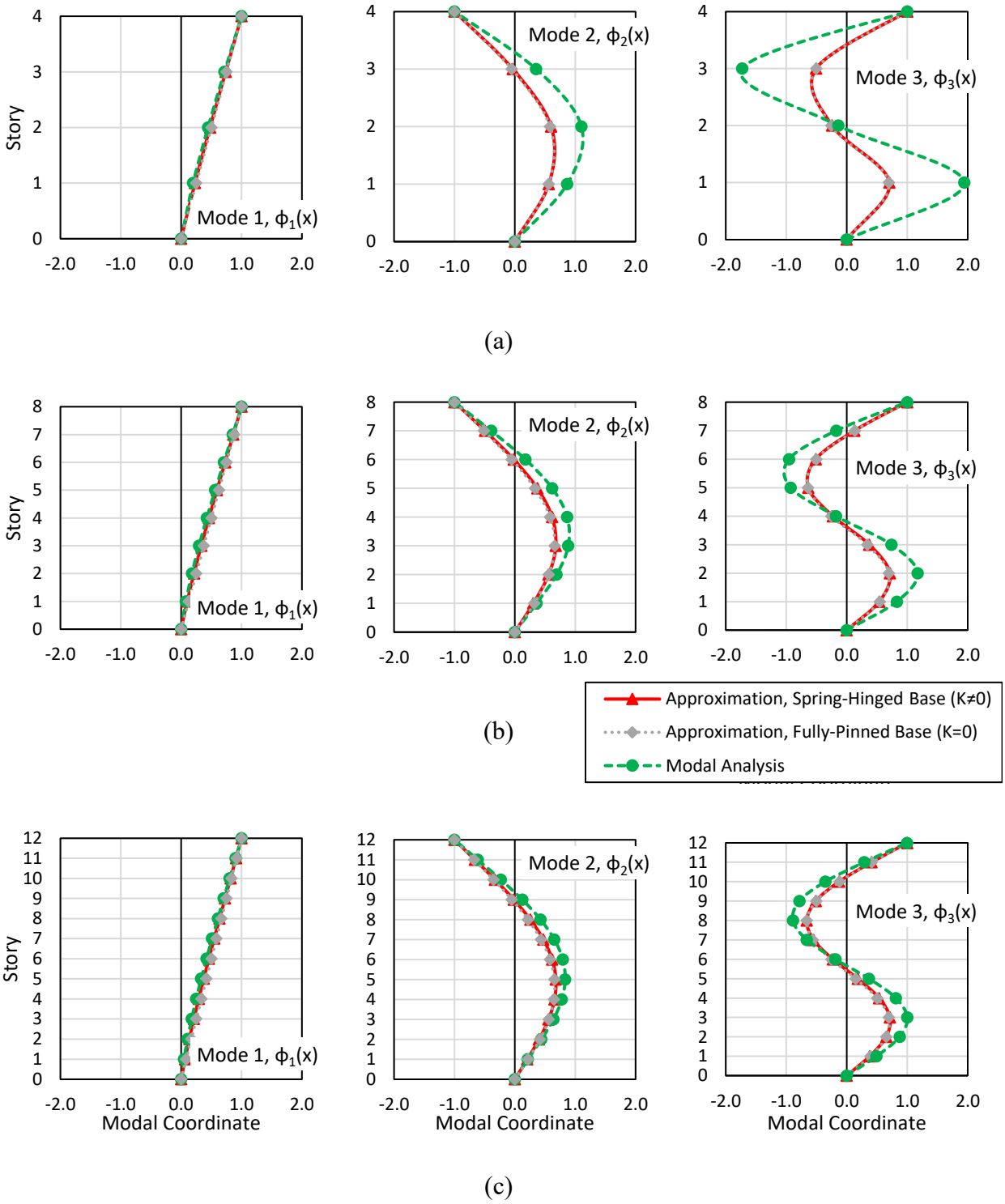

Figure 7.24 Comparison between mode shapes obtained through modal analysis and approximate mode shapes of spring-hinged and fully-pinned cantilever beams; (a) 4-story; (b) 8-story; (c) 12-story

7.4.3 Quantifying Period Elongation

As discussed in Section 5.3.1, inelastic structural response leads to a "plateau" of peak SFA demands at modal periods. This is due to modal periods elongating as the structure goes through non-linear deformations. It was also noted that for both RC and rocking wall buildings, the period elongation was only observed for the first and second modes. Thus, this section provides approximations for the effective periods of the first and second mode.

For the first mode, the effective period is known from the displacement-based design of the structural wall as discussed in the previous two sub-sections. For the second mode, the effective period can be approximated using Equation (7.47) (refer to Section 7.3.2 for the derivation).

$$T_{2,e} = \begin{cases} T_2 & for \quad \mu \leq 1.0 \\ T_2\left(1 + 0.5\left(\frac{\mu}{\mu_{pin}}\right)\right) & for \; 1.0 < \mu < \mu_{pin} \\ 1.5T_2 & for \quad \mu \geq \mu_{pin} \end{cases} \tag{7.47}$$

where $T_{2,e}$ is the effective second mode period, and T_2 is the approximate elastic second mode period. The term μ_{pin} is the ductility limit corresponding to the pinned behavior of higher modes. μ_{pin} is taken as *5.0* for RC wall buildings and *13.0* for rocking wall buildings.

7.4.4 Estimation of Floor Response Spectra

In the previous sub-sections, procedures to estimate the elastic modal properties of the RC and rocking wall buildings were proposed. However, using elastic modal properties to generate floor response spectra will lead to excessively conservative results, and, in some regions of the spectra, possibly leading to non-conservative estimates. When a modal period of the supporting structure lengthens due to inelastic deformation, spectral acceleration demands for the effective periods could be higher relative to the elastic period. For instance, if the elastic period is within the initial ramp-up portion of the ground response spectrum, the effective period could lengthen past the ramp-up potion into the constant acceleration range of the ground spectrum, and thus attract higher accelerations. However, as discussed in Section 5.3.1, inelastic structural response generally leads to a significant reduction of spectral floor acceleration demands relative to elastic structural response. This reduction is most significant for the first mode while the higher modes tend to exhibit only minor reductions in spectral floor acceleration demands.

In order to account for the effect of inelastic structural response on the first mode, it is proposed that the modal floor acceleration contributions be obtained from the equivalent lateral force distribution of the design base shear. If the RC or rocking wall building is designed using a displacement-based design approach (refer to Section 4.3), the equivalent lateral force distribution is obtained using Equation (7.48), which only takes into account first-mode response.

$$F_j = V_d \frac{m_j \Delta_j}{\sum_{j=1}^{n} m_j \Delta_j} \tag{7.48}$$

where F_j is the equivalent static force acting at a given floor j, V_d is the design base shear, m_j is the seismic mass of floor j, and Δ_j is the design displacement of floor j.

From this force distribution, the first mode contributions to the peak floor acceleration at a given floor j $a_{max,j,1}$ can be estimated as:

$$a_{max,j,1} = \frac{F_j}{m_j}; \tag{7.49}$$

For higher modes, it is proposed that the modal contributions to the peak floor acceleration be determined by a traditional modal response spectrum method using the approximate elastic modal properties. Assuming that the higher mode response remains elastic is potentially conservative but overall reasonable considering the minor reductions in spectral floor acceleration demands observed in higher modes during inelastic structural response. Thus, the higher mode contributions to the peak floor acceleration can be determined by the expression:

$$a_{max,j,i} = \phi_{j,i} \Gamma_i S_a(T_i, \xi_p); \;\; i \geq 1 \tag{7.50}$$

where $\phi_{j,i}$ is the approximate mode shape for floor level j and mode i, and Γ_i is the approximate modal participation factor for mode i. The term $S_a(T_i, \xi_p)$ is the elastic spectral acceleration demand for the mode i obtained from the design ground response spectrum at the primary damping ratio.

Once the modal contributions to the PFA are determined, the individual modal contributions $a_{m,j,i}(T)$ to the floor response spectrum are given by:

$$a_{m,j,i}(T) = \begin{cases} \left(\frac{T}{T_i}\right)\left[a_{max,j,i}(DAF_{max} - 1)\right] + a_{max,j,i} & for\ T < T_i \\ a_{max,j,i}DAF_{max} & for\ T_i \le T \le T_{i,e} \\ a_{max}DAF & for\ T > T_{i,e} \end{cases} \tag{7.51}$$

where T is the spectral period of interest, and T_i is the approximate elastic period of the primary structure for mode i, and $T_{i,e}$ is the approximate effective period of the primary structure for mode i. DAF_{max} and DAF are estimated using Equations (7.52) and (7.53) respectively (Welch, 2016).

$$DAF_{max} = \begin{cases} \left(0.55 + 0.45\frac{T_i}{T_B}\right)(0.5\xi_p + \xi_{NS})^{-0.667} & if\ T_i \le T_B \\ (0.5\xi_p + \xi_{NS})^{-0.667} & if\ T_i \ge T_B \end{cases} \tag{7.52}$$

$$DAF = \begin{cases} \left(0.55 + 0.45\frac{T_i}{T_B}\right)\left[\left(1 - \frac{T}{T_{i,e}}\right)^2 + \left(0.5\xi_p + \xi_{NS}\right)\right]^{-0.667} & if\ T_i \le T_B \\ \left[\left(1 - \frac{T}{T_{i,e}}\right)^2 + \left(0.5\xi_p + \xi_{NS}\right)\right]^{-0.667} & if\ T_i \ge T_B \end{cases} \tag{7.53}$$

where ξ_p is the elastic damping of the primary structure, and ξ_{NS} is the elastic damping of the non-structural element. The term T_B is taken as 0.3 sec.

The individual modal contributions to the floor response spectrum are then combined using modal superposition to give the SRSS spectral floor response at a given period T:

$$SFA_j(T)_{SRSS} = \sqrt{\sum_{i=1}^{nm}[a_{m,j,i}(T)]^2} \tag{7.54}$$

where nm is the number of modes being considered.

The final spectral floor acceleration $SFA_j(T)$ is given by Equation (7.55), which takes into account rigid mode response observed in the lower levels of MDOF systems (Calvi and Sullivan, 2014; Welch, 2016).

$$SFA_j(T) = \begin{cases} \max\left(SFA_j(T)_{SRSS}, S_a(T, \xi_{NS})\right) & for \dfrac{H_j}{H_n} < 0.5 \\ SFA_j(T)_{SRSS} & for \dfrac{H_j}{H_n} \geq 0.5 \end{cases} \quad (7.55)$$

where H_j is the height of floor level j, and H_n is the height of the roof level. The term $S_a(T,\xi_{NS})$ is the spectral acceleration demand at period T obtained from the design ground response spectrum at the elastic non-structural element damping ratio ξ_{NS}.

7.4.5 Comparison between Floor Response Spectra Estimates and NLTHA Results

The following section presents the floor response spectra estimates obtained using the procedures outlined above along with the mean floor response spectra from the NLTHA of the case study buildings. The comparisons are presented for Intensity 5 and 2% non-structural damping ξ_{NS}. Corresponding comparisons for all non-structural damping ratios are presented in Appendix C. The comparisons are only presented for Intensity 5 because the displacement-based design of the case study buildings (refer to Section 4.3) was conducted for this intensity.

The comparisons for the RC wall buildings are presented in Figures 7.25 to 7.27. Consistent with the previous two methodologies proposed for the estimation of floor response spectra, only the first three modes of vibration were used for the current estimation procedure. In the previous sub-section, it was proposed that the first mode contributions to the peak floor accelerations be estimated from the equivalent lateral force distribution of the design base shear. With this approach, the first mode peak spectral accelerations were well predicted for all RC wall buildings.

The second and third mode peak spectral accelerations were also well predicted for the 8- and 12-story RC wall buildings, with slightly conservative estimates for the roof levels. There was less agreement between floor response spectra estimates and NLTHA results for the 4-story RC wall building. The second modal peaks were underestimated while the third modal peaks were overestimated. This was expected since the error in the mode shape approximations significantly increased with decreasing height of the RC wall buildings (Figure 7.23).

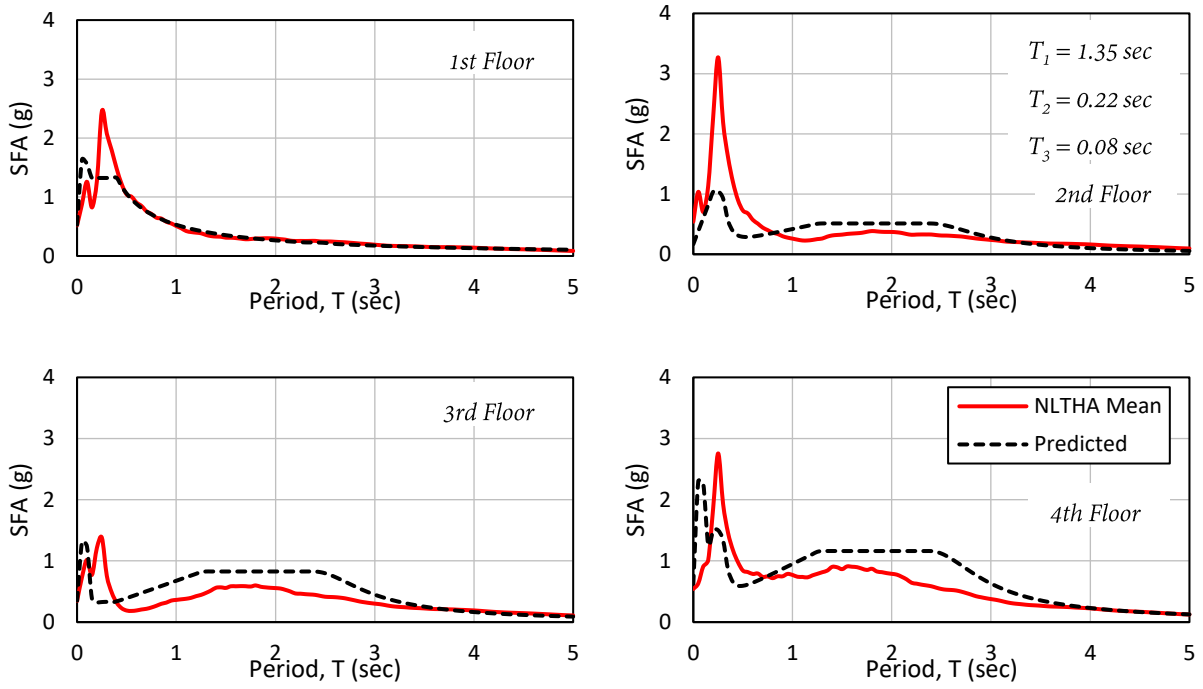

Figure 7.25 Comparison between mean floor spectra from NLTHA and estimates using closed-form modal properties of a continuous cantilever beam; 4-story RC wall building, Intensity 5 (PGA = 0.450 g), ξ_{NS} = 2%

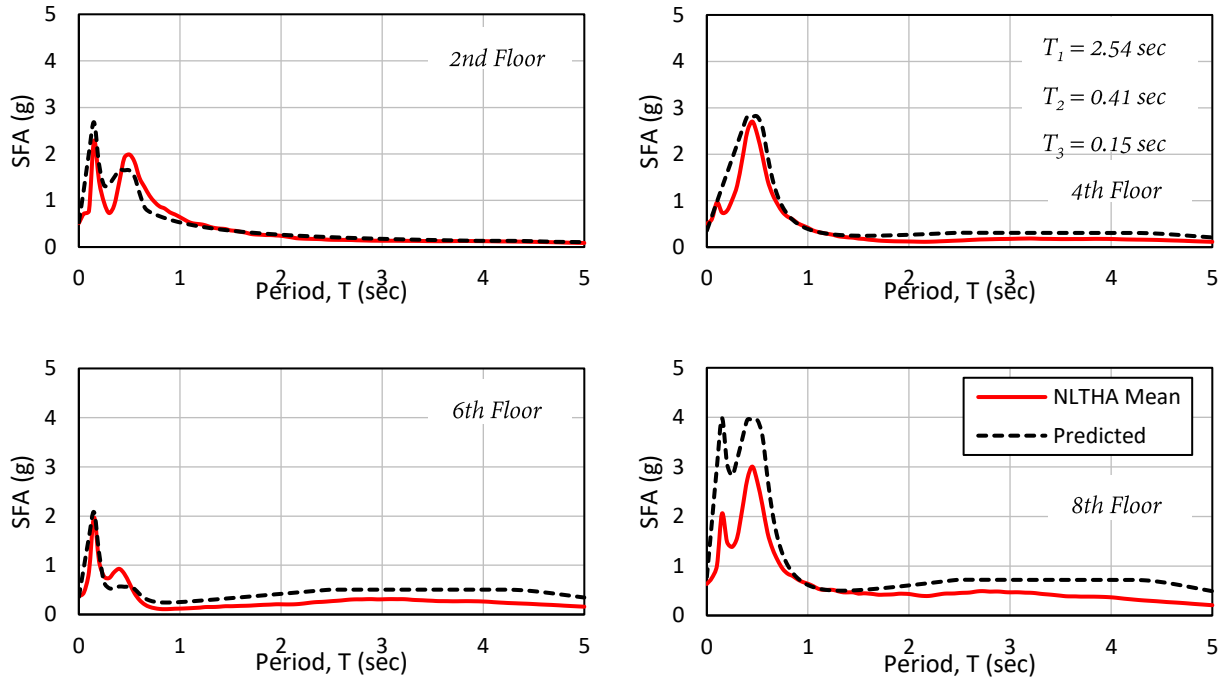

Figure 7.26 Comparison between mean floor spectra from NLTHA and estimates using closed-form modal properties of a continuous cantilever beam; 8-story RC wall building, Intensity 5 (PGA = 0.450 g), ξ_{NS} = 2%

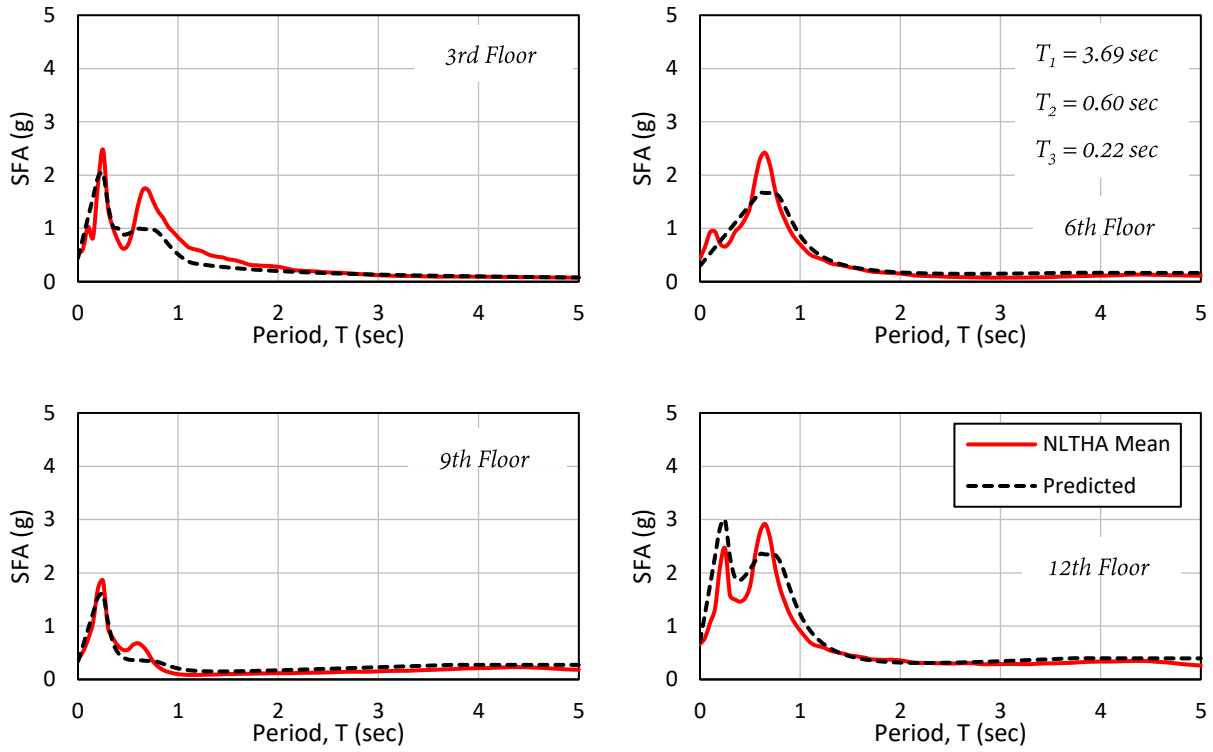

Figure 7.27 Comparison between mean floor spectra from NLTHA and estimates using closed-form modal properties of a continuous cantilever beam; 12-story RC wall building, Intensity 5 (PGA = 0.450 g), ξ_{NS} = 2%

The comparisons for the rocking wall buildings are presented in Figures 7.28 to 7.30. Again, only the first three modes of vibration were used to estimate floor response spectra. For all three rocking wall buildings, the first mode peak spectral accelerations were well predicted from the design equivalent lateral force distribution. However, the beginning of the "plateau" in peak spectral acceleration was not captured since the first modal periods were overestimated (Table 7.7).

In addition, the second modal peaks were underestimated while the third mode peaks were slightly overestimated for all three rocking wall buildings. However, the estimates improved with increasing building height, consistent with the observations of the RC wall buildings.

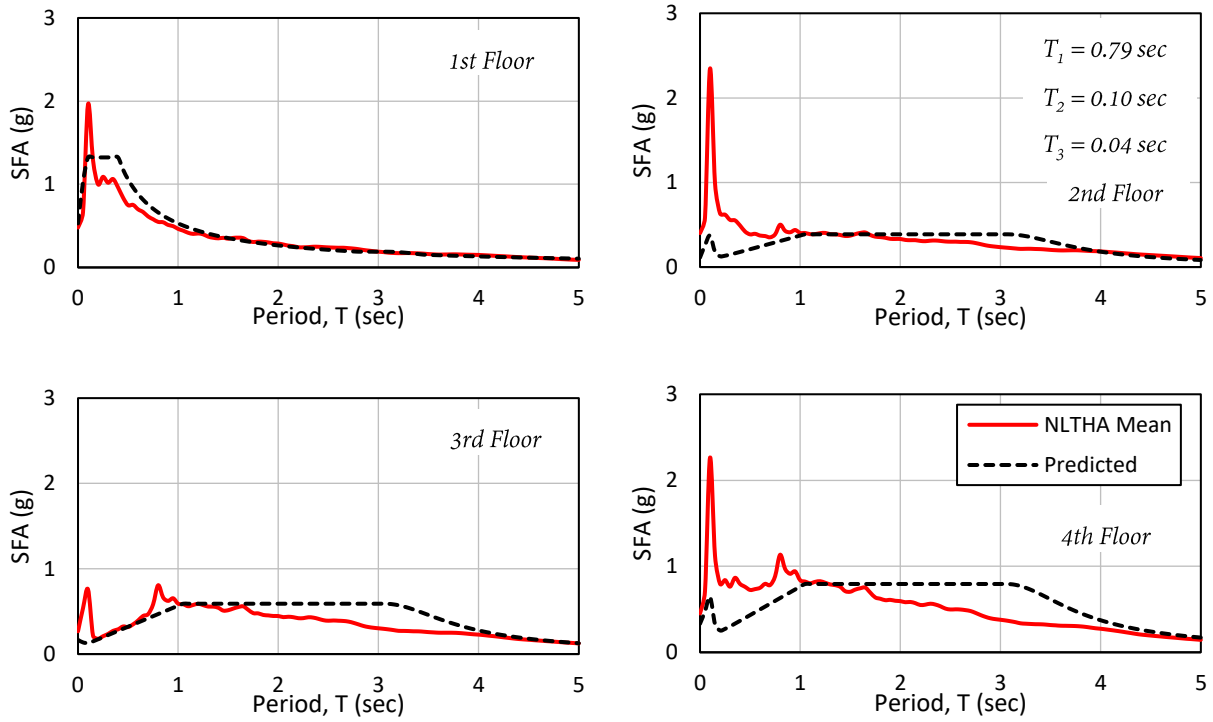

Figure 7.28 Comparison between mean floor spectra from NLTHA and estimates using closed-form modal properties of a fully-pinned continuous cantilever beam; 4-story rocking wall building, Intensity 5 (PGA = 0.450 g), ξ_{NS} = 2%

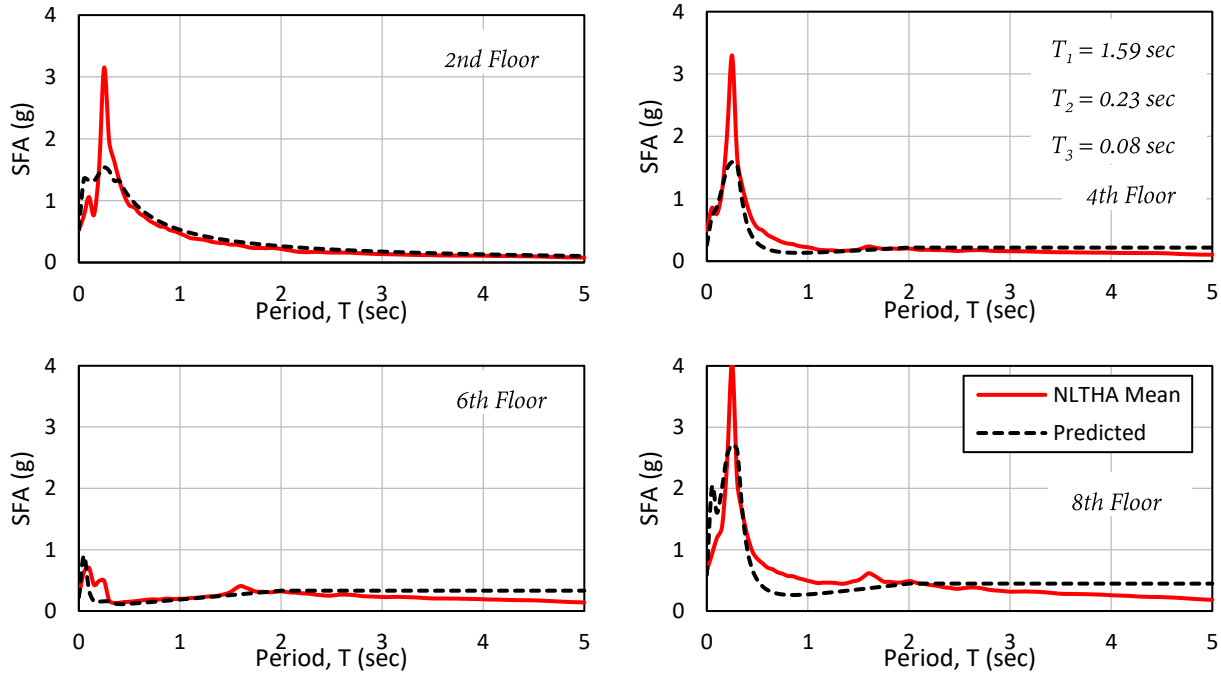

Figure 7.29 Comparison between mean floor spectra from NLTHA and estimates using closed-form modal properties of a fully-pinned continuous cantilever beam; 8-story rocking wall building, Intensity 5 (PGA = 0.450 g), ξ_{NS} = 2%

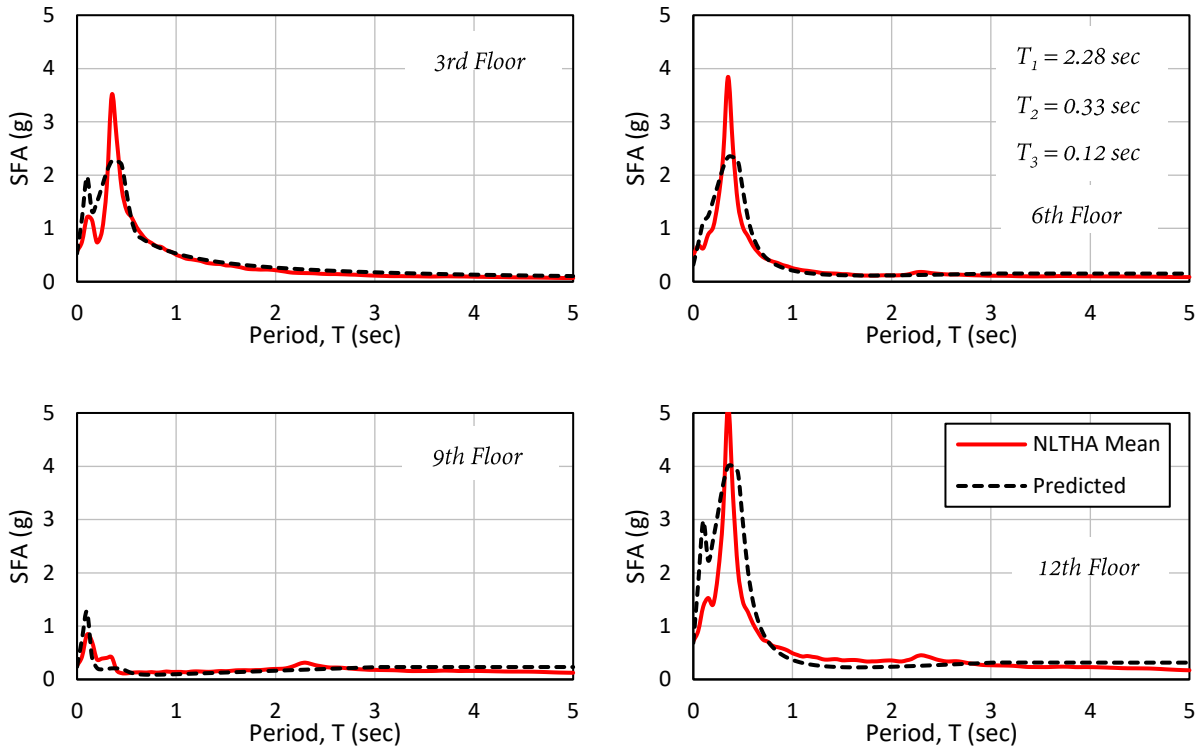

Figure 7.30 Comparison between mean floor spectra from NLTHA and estimates using closed-form modal properties of a fully-pinned continuous cantilever beam; 12-story rocking wall building, Intensity 5 (PGA = 0.450 g), ξ_{NS} = 2%

Overall, the floor response spectra estimates obtained in this section matched well with the results of the NLTHA especially considering the limited amount of information available regarding the modal characteristics of the buildings after displacement-based design. Even though some of the estimates were non-conservative for higher mode response, the floor response spectra obtained through the simple procedure outlined above can still be very useful for the consideration of non-structural elements in the early design phases of RC and rocking wall buildings.

The main source of error in the floor response spectra estimates were the mode shape approximations. Thus, the application of reasonable correction factors to the mode shapes obtained from continuous distributed-mass beams could improve the proposed procedure.

7.5 Summary of Methodologies to Estimate Floor Response Spectra

This section summarizes the three floor response spectra estimation procedures proposed in the previous sub-sections. The required steps for each procedure are presented below with the necessary equations replicated for clarity. Since all three procedures were developed based on the

work of Calvi and Sullivan (2014), some of the steps are the same for all three procedures and thus only presented once. The steps that are unique to each of the proposed methods have been designated with the following markers:

Method (a): Procedure that utilizes transitory inelastic modal characteristics
Method (b): Procedure that utilizes empirical modal reduction factors
Method (c): Procedure that utilizes dynamics of distributed-mass systems

Step 1: Define the primary (ξ_p) and non-structural (ξ_{NS}) damping ratios

For both RC and rocking wall buildings, the primary damping ratio can be taken as 5% of critical. Even though the procedure can be applied to any non-structural damping ratio, a value of 2% is proposed if the damping of a non-structural element is not known (Welch, 2016).

Step 2: Define the input acceleration spectrum, $S_a(T,\xi_p)$

The input acceleration spectrum is the design ground response spectrum. It can also be taken as the median or mean spectrum of a target record set (Welch, 2016). Note that the input acceleration spectrum is defined at the primary damping ratio ξ_p.

Step 3, Method (a): Perform modal analysis for the number of modes considered

For a given mode i, the following parameters need to be obtained:

- elastic modal period (T_i)
- transitory modal period ($T_{i,e}$)
- transitory mode shape ($\phi_{t,i}$), and
- transitory modal participation factor ($\Gamma_{t,i}$).

To obtain the transitory modal characteristics, modify the model used to obtain elastic modal characteristics by adding a zero-length rotational spring at the location of concentrated inelastic behavior (i.e. plastic hinge region or rocking joint). The rotational spring is assigned the secant stiffness of the structural system K_e at the expected ductility demand μ.

For RC and rocking wall buildings, the secant stiffness can be estimated with Equations (7.56) and (7.57) respectively.

$$K_{e,RC} = \frac{M_y + r\frac{K_{i,\phi}}{L_p}\left[\frac{(\mu-1)\Delta_{y,H_e}}{H_e}\right]}{\phi_y L_p + \frac{(\mu-1)\Delta_{y,H_e}}{H_e}} \; ; \quad \mu \geq 1 \tag{7.56}$$

where M_y is the yield moment capacity of the wall, r is the global post yield stiffness ratio, and $K_{i,\phi}$ is the elastic stiffness of the wall in terms of moment-curvature. ϕ_y is the yield curvature of the wall, and L_p is the plastic hinge length. The term H_e is the effective height of the wall which can be determined using Equation (7.1). The term $\Delta_{y,He}$ is yield displacement of the wall at the effective height of the wall determined using Equation (7.2).

$$K_{e,rock} = \frac{M_y + rK_{i,\theta}\left[\frac{(\mu-1)\Delta_{y,H_e}}{H_e}\right]}{\theta_{y\_base} + \frac{(\mu-1)\Delta_{y,H_e}}{H_e}} \; ; \quad \mu \geq 1 \tag{7.57}$$

where $K_{i,\theta}$ is the elastic stiffness of the rocking joint in terms of moment-rotation, and Θ_{y_base} is the yield base rotation of the wall. The term $\Delta_{y,He}$ is yield displacement of the wall at the effective height of the wall determined using Equation (7.3).

Step 3, Method (b): Perform modal analysis for the number of modes considered

For a given mode *i*, the following parameters need to be obtained:

- elastic modal period (T_i)
- elastic mode shape (ϕ_i), and
- elastic modal participation factor (Γ_i).

Step 3, Method (c): Estimate elastic modal characteristics

RC Wall Buildings

For an RC wall building, the approximate modal period for mode *i* is given by the expression:

$$T_i = \begin{cases} T_{1,e}\sqrt{\mu} & for\ i = 1 \\ \alpha_i L^2 \sqrt{\dfrac{m}{EI}} & for\ i > 1 \end{cases} \tag{7.58}$$

where $\alpha_i = 1.787, 0.285, 0.102, 0.052, etc.$ The effective first mode period $T_{1,e}$ and expected ductility μ are obtained from the displacement-based design of the RC wall building. The term *EI* is the elastic stiffness of the wall, which is estimated by the expression:

$$EI = m\left(\frac{1.787L^2}{T_1}\right)^2 \tag{7.59}$$

For an RC wall building, the approximate mode shape for mode *i* is given by the expression:

$$\phi_i(x) = \cosh \beta_i x - \cos \beta_i x - \frac{\cosh \beta_i L + \cos \beta_i L}{\sinh \beta_i L + \sin \beta_i L}(\sinh \beta_i x - \sin \beta_i x) \tag{7.60}$$

where $\beta_i L = 1.8751, 4.6941, 7.8548, 10.996, etc.$

Rocking Wall Buildings

For a rocking wall building, the approximate modal period for mode *i* is given by the expression:

$$T_i = \begin{cases} T_{1,e}\sqrt{\mu} & for\ i = 1 \\ \alpha_{i-1} L^2 \sqrt{\dfrac{m}{EI}} & for\ i > 1 \end{cases} \tag{7.61}$$

where $\alpha_i = 0.407, 0.126, 0.060, etc.$ The effective first mode period $T_{1,e}$ and expected ductility μ are obtained from the displacement-based design of the rocking wall building. The term *EI* is the elastic stiffness of the wall approximated as 85% of the gross stiffness of the wall.

For a rocking wall building, the approximate mode shape for mode *i* is given by the expression:

$$\phi_i(x) = \begin{cases} \dfrac{x}{L} & for\ i = 1 \\ \sin\beta_i x + \dfrac{\sin\beta_i L}{\sinh\beta_i L}\sinh\beta_i x & for\ i > 1 \end{cases} \tag{7.62}$$

where $\beta_i L = \frac{\pi}{4} + (i-1)\pi$

Step 4, Method (a): Estimate Effective periods

For this method, effective modal periods are taken as the transitory modal periods.

Step 4, Method (b): Estimate Effective periods

For both RC and rocking wall buildings, the effective periods for the first and second modes can be estimated using Equations (7.63) and (7.64).

$$T_{1,e} = T_1\sqrt{\frac{\mu}{[1 + r(\mu - 1)]}} \tag{7.63}$$

$$T_{2,e} = \begin{cases} T_2 & for \quad \mu \le 1.0 \\ T_2\left(1 + 0.5\left(\dfrac{\mu}{\mu_{pin}}\right)\right) & for\ 1.0 < \mu < \mu_{pin} \\ 1.5T_2 & for \quad \mu \ge \mu_{pin} \end{cases} \tag{7.64}$$

The global strain hardening factor r may be omitted. The term μ_{pin} is taken as *5.0* for RC wall buildings and *13.0* for rocking wall buildings.

Step 4, Method (c): Estimate Effective periods

For both RC and rocking wall buildings, the effective period for the first mode is determined from the displacement-based design of the building. The effective period for the second mode is estimated by Equation (7.64).

Step 5; Method (a): Estimate modal floor accelerations

The modal floor acceleration $a_{max,j,i}$ for a given mode i at a floor level j is given by:

$$a_{max,j,i} = \begin{cases} \phi_{t,j,i}\Gamma_{t,i}S_a\left(T_{i,e}, \xi_{p,eq}\right) & for\ i = 1 \\ \phi_{t,j,i}\Gamma_{t,i}S_a\left(T_{i,e}, \xi_p\right) & for\ i > 1 \end{cases} \tag{7.65}$$

The term $S_a(T_{i,e})$ is the spectral acceleration demand for mode *i* obtained from the design ground response spectrum at either the elastic primary damping ratio ξ_p or the equivalent viscous damping ratio $\xi_{p,eq}$ of the primary structure, which is given by Equation (7.66).

$$\xi_{p,eq} = \xi_p + \xi_{hyst} \tag{7.66}$$

where ξ_{hyst} is hysteretic damping, which can be calculated using Equation (7.67) for RC wall buildings and Equation (7.68) for rocking wall buildings.

$$\xi_{eq,RC} = 0.05 + 0.444\left(\frac{\mu - 1}{\mu\pi}\right) \tag{7.67}$$

$$\xi_{eq,rock} = 0.05 + 0.524\left(\frac{\mu - 1}{\mu\pi}\right) \tag{7.68}$$

Note that Equation (7.68) is valid for a ratio between post-tensioning and mild steel bending resistance $\lambda = 1.25$ and will need to be updated based on the reinforcement design of the rocking walls.

Step 5; Method (b): Estimate modal floor accelerations

The modal floor acceleration $a_{max,j,i}$ for a given mode *i* at a floor level *j* is given by:

$$a_{max,j,i} = \phi_{j,i}\Gamma_i\left(\frac{S_a\left(T_i, \xi_p\right)}{R_i}\right); \quad R_i \geq 1 \tag{7.69}$$

where the elastic spectral acceleration demand $S_a(T_i, \xi_p)$ is reduced by the modal reduction factor R_i to account for non-linear demands. The modal reduction factors are determined as:

$$\begin{aligned} R_1 = R_{i=1} \approx \mu^{1.25} \;\; RC\ Wall\ ;\ R_1 = R_{i=1} \approx \mu^{0.75} \quad Rocking\ Wall \\ R_2 = R_{i=2} \approx \mu^{0.4} \;\; RC\ Wall\ ;\ R_2 = R_{i=2} \approx \mu^{0.20} \quad Rocking\ Wall \\ R_{HM} = R_{i>2} \approx \mu^{0} \quad RC\ Wall\ ;\ R_{HM} = R_{i>2} \approx \mu^{0.18} \;\; Rocking\ Wall \end{aligned} \tag{7.70}$$

Step 5; Method (c): Estimate modal floor accelerations

The modal floor acceleration $a_{max,j,i}$ for a given mode *i* at a floor level *j* is given by:

$$a_{max,j,i} = \begin{cases} \dfrac{F_j}{m_j} & for\ i = 1 \\ \phi_{j,i}\Gamma_i S_a(T_i, \xi_p) & for\ \ i \geq 1 \end{cases} \tag{7.71}$$

where F_j is the equivalent static force acting at a given floor j and m_j is the seismic mass of floor j.

Step 6: Estimate modal contributions and SRSS estimates of floor response spectra

The individual modal contributions $a_{m,j,i}(T)$ to the floor response spectrum are given by:

$$a_{m,j,i}(T) = \begin{cases} \left(\dfrac{T}{T_i}\right)\left[a_{max,j,i}(DAF_{max} - 1)\right] + a_{max,j,i} & for\ T < T_i \\ a_{max,j,i} DAF_{max} & for\ T_i \leq T \leq T_{i,e} \\ a_{max} DAF & for\ T > T_{i,e} \end{cases} \tag{7.72}$$

where T is the spectral period of interest. DAF_{max} and DAF are estimated using Equations (7.73) and (7.74), respectively.

$$DAF_{max} = \begin{cases} \left(0.55 + 0.45\dfrac{T_i}{T_B}\right)(0.5\xi_p + \xi_{NS})^{-0.667} & if\ T_i \leq T_B \\ (0.5\xi_p + \xi_{NS})^{-0.667} & if\ T_i \geq T_B \end{cases} \tag{7.73}$$

$$DAF = \begin{cases} \left(0.55 + 0.45\dfrac{T_i}{T_B}\right)\left[\left(1 - \dfrac{T}{T_{i,e}}\right)^2 + \left(0.5\xi_p + \xi_{NS}\right)\right]^{-0.667} & if\ T_i \leq T_B \\ \left[\left(1 - \dfrac{T}{T_{i,e}}\right)^2 + \left(0.5\xi_p + \xi_{NS}\right)\right]^{-0.667} & if\ T_i \geq T_B \end{cases} \tag{7.74}$$

The term T_B is taken as 0.3 sec.

The SRSS spectral floor acceleration response at a given period T is estimated as:

$$SFA_j(T)_{SRSS} = \sqrt{\sum_{i=1}^{nm} [a_{m,j,i}(T)]^2} \tag{7.75}$$

where nm is the number of modes being considered.

Step 7: Account for rigid mode response

The final spectral floor acceleration $SFA_j(T)$ is given by Equation (7.76) which takes into account rigid mode response observed in the lower levels of MDOF buildings.

$$SFA_j(T) = \begin{cases} \max\left(SFA_j(T)_{SRSS}, S_a(T, \xi_{NS})\right) & for \dfrac{H_j}{H_n} < 0.5 \\ SFA_j(T)_{SRSS} & for \dfrac{H_j}{H_n} \geq 0.5 \end{cases} \tag{7.76}$$

where H_j is the height of floor level j, and H_n is the height of the roof level. The term $S_a(T,\xi_{NS})$ is the spectral acceleration demand at period T obtained from the input acceleration spectrum at a damping level of ξ_{NS}. If the input acceleration spectrum is obtained for a typical damping ratio of 5%, then the spectrum can be adjusted by a damping modification factor given by:

$$R_\xi = \sqrt{\frac{0.07}{0.02 + \xi_{NS}}} \tag{7.77}$$

8 CONCLUSIONS

This study had two main objectives: (i) comparing the seismic response of RC and rocking wall buildings; and (ii) proposing methodologies for the estimation of acceleration demands on non-structural elements supported by both structural systems.

In order to achieve these objectives, the behavior of both structural systems as well background information regarding the estimation of seismic demands on non-structural elements were first discussed in Chapters 2 and 3.

In Chapter 4, the displacement based design (DBD) and time history analysis of six RC and rocking wall case study buildings were carried out. In Chapter 5, the results of the time history analyses were used to assess the performance of a DBD seismic design approach as well as the seismic response of rocking wall buildings relative to RC wall buildings. In addition, floor response spectra obtained from the analyses were used to gain a better understanding of the parameters affecting spectral acceleration demands and the dynamic interaction between non-structural elements and supporting buildings.

Chapter 6 investigated the dynamic amplification of peak floor acceleration at the resonance of a non-structural element and its supporting structure. The accurate estimation of this dynamic amplification is a critical part of estimating peak spectral acceleration demands that occur at modal periods. In Chapter 7, the findings from Chapter 5 and 6 were utilized in the development of three procedures to estimate floor response spectra atop RC and rocking wall buildings.

The following two sections summarize the findings and the limitations of the study summarized above. Areas of future research are also identified.

8.1 Overview of Findings

8.1.1 Performance of a Displacement-Based Seismic Design Approach

A direct displacement-based design (DDBD) procedure was utilized for the design of both the RC and rocking wall case study buildings considered in the present study. The design of the RC and rocking wall buildings was conducted according to the procedures proposed by Priestley *et al.* (2007) and Pennucci *et al.* (2009), respectively. A dynamic non-linear time history analysis of each of the case study buildings was then conducted under a suite of spectrum compatible ground motions. The results of the analysis were used to investigate the effectiveness of the DDBD approach in predicting structural response.

For the RC wall buildings, the following observations were made regarding the DDBD approach:

- In general, displacement estimates from the DDBD procedure were found to be in good agreement with the analysis results, with slightly non-conservative estimates for the 4- and 8-story buildings.
- The DDBD base moment estimates were in very good agreement with the analysis results for all case study buildings.
- The capacity design procedure proposed by Priestley *et al.* (2007) was found to underestimate moment values along the height of each of the case study walls, particularly at mid-height where the higher modes seem to play a predominant role. However, the shear estimates from the same procedure compared well to the analysis results.

For the rocking wall buildings, the following observations were made regarding the DDBD approach:

- Compared to the analysis results, the displacement estimates from the DDBD procedure were generally acceptable. However, the estimates were found to be slightly non-conservative for the 4-story building, but conservative for the 8- and 12-story buildings.
- The DDBD base moment estimates were in very good agreement with the analysis results except for the 4-story building.

- As a means of accounting for higher modes in the rocking wall buildings, the RC wall capacity-design procedures proposed by Priestley *et al.* (2007) were adapted and used for the rocking walls. Despite being developed and calibrated for RC walls, the procedure was able to provide reasonable, albeit non-conservative, estimates to the moment distribution along the height of the rocking wall buildings. The shear force distribution estimates from the procedure were also found to be in good agreement with analysis results.

8.1.2 Seismic Response of Rocking Wall Systems

Rocking wall systems are currently being developed as an alternative to traditional monolithic RC wall systems, which are prone to damage and residual drifts following strong earthquakes. RC walls are designed such that an inelastic mechanism forms at the base of the wall, commonly referred to as the plastic hinge region. In order to dissipate energy during a seismic event, RC walls rely on the yielding of longitudinal reinforcement, as well as the cracking and crushing of concrete, in the plastic hinge region. However, this causes significant damage to the plastic hinge region leading to residual displacements. Rocking wall systems, on the other hand, avoid this type of damage because they are not monolithically cast with the foundation, and incorporate unbonded reinforcement. To this end, rocking walls consists of precast wall panels that are post-tensioned to the foundation such that controlled rocking occurs during seismic events. Energy dissipation is also provided through unbonded mild-steel reinforcement that crosses the wall/foundation interface. Since the post-tensioning tendons and energy dissipaters are unbonded, damage is avoided to the wall panels during seismic events. In addition, after lateral loading is removed, the post-tensioning force re-centers the wall panels eliminating any residual drifts.

In the present study, the seismic response of rocking and RC wall systems was compared through non-linear time history analysis of case study buildings (4, 8 and 12 stories) modelled using a simplified lumped-plasticity approach. The buildings were designed using a direct displacement-based design (DDBD) approach for a 2% drift limit and a design-basis earthquake per ASCE 7-10 standards (ASCE, 2010). The seismic response of both structural systems was compared for both design-basis and maximum-considered earthquake intensities (ASCE, 2010). Compared to the RC wall buildings, the following observations were made about the rocking wall buildings:

i) The rocking wall buildings had comparable displacements and peak floor accelerations. The displacements were mostly attributed to the rigid body base-rotation of the walls with only minor contribution from the elastic deformation of the wall panels.

ii) The rocking wall buildings had negligible residual displacements, which remained approximately constant with increasing earthquake intensity.

iii) The rocking wall buildings generally had higher moment and shear distributions along the height of the walls even though they were designed for a lower base moment and shear. This was attributed to the effects of higher modes, which could be mitigated through appropriate capacity design measures.

8.1.3 Parameters Influencing Floor Response Spectra in MDOF systems

Both elastic and inelastic floor response spectra were obtained from the time history analysis of the case study RC and rocking wall buildings at various earthquake intensities. From these floor spectra, three factors were identified as having a strong influence on spectral acceleration demands: non-structural damping, modal characteristics of the supporting building, and inelastic structural response. The following observations were made regarding the three parameters:

i) Low non-structural damping values were associated with higher acceleration demands. The influence of damping was found to be most significant at modal periods where peak spectral accelerations were also observed.

ii) The highest spectral acceleration demands for each mode occurred at the floor level with the highest modal coordinate for the mode under consideration.

iii) Inelastic structural response was observed to reduce spectral acceleration demands, particularly at modal periods. This reduction significantly reduced with increasing order of modes, with the third mode response remaining essentially elastic.

iv) Inelastic structural response was observed to cause a “plateau” of peak spectral accelerations at modal peaks due to period lengthening as the supporting structure goes into inelastic deformation. Period lengthening was observed to decrease with increasing order of modes.

8.1.4 Dynamic Interaction between Non-structural Elements and Supporting Buildings

One of the main objectives of the present study was to propose methodologies to estimate floor response spectra atop RC and rocking wall buildings that can be used to design non-structural elements (NSEs). An inherent assumption of the floor response spectrum (FRS) method to estimate acceleration demands on non-structural elements is that the NSE can be considered un-coupled from the supporting structure. Thus, the dynamic interaction between the NSE and the supporting structure is assumed to be negligible. In past research efforts, this assumption has been considered acceptable for mass-ratios of 1% or less (Singh and Ang, 1974; Sankaranarayanan, 2007; amongst others), but some have suggested 0.1% or less (Toro *et al.*, 1989).

Noting the large differences in the mass ratios at which dynamic interaction needs to be considered, a coupled NLTHA was conducted in which SDOF non-structural elements with mass ratios of 0.06% and 0.12% were modelled with the case-study buildings. The NSE accelerations from the coupled analysis were then compared to spectral acceleration demands from floor response spectra obtained from a decoupled NLTHA. From this comparison, the following observations were made:

i) For both mass ratios considered, the floor response spectra (obtained from the decoupled analyses) gave conservative acceleration demand estimates for a wide range of periods including NSE periods close to the higher mode periods of the supporting building.

ii) For both mass ratios considered, NSE accelerations from the coupled analysis were found to be higher than spectral acceleration values for NSEs with periods close to the fundamental period of the supporting building.

iii) A lower mass ratio was associated with higher accelerations for NSEs with periods close to the fundamental period of the supporting building.

iv) The effect of dynamic interaction was observed to diminish with increasing height of the supporting building.

In closing, the dynamic interaction of non-structural elements and supporting structures might be significant for mass ratios as low as 0.06%. Thus, a coupled analysis may be necessary to get an

accurate estimate of acceleration demands for non-structural elements with natural periods close to the fundamental period of the supporting structure.

8.1.5 Maximum Dynamic Amplification of Peak Floor Acceleration

Maximum dynamic amplification of peak floor acceleration occurs when a non-structural element is in resonance with the supporting structure. As such, the maximum dynamic amplification factor (DAF_{max}) is defined as the ratio between peak spectral acceleration and peak floor acceleration (PFA). The quantification of DAF_{max} was critical in the development of the three methodologies proposed for the estimation of floor response spectra. In all three procedures, the various modes of an MDOF system are transformed into equivalent SDOF systems. Subsequently, the peak spectral acceleration associated with a certain mode is determined by scaling the PFA contribution of the given mode by DAF_{max}.

For a better understanding of DAF_{max}, a study of floor spectra atop both elastic and inelastic SDOF systems was conducted through time history analysis. Through this study, the performance of two empirical formulations for DAF_{max} (Sullivan *et al.*, 2013; Welch, 2016) as well as the effects of inelastic structural response on DAF_{max} were investigated. The following observations were made from this study:

i) Non-structural damping was observed to have a strong influence on DAF_{max}, with lower damping values associated with higher dynamic amplification.

ii) The damping of the supporting structure was also observed to have an influence on DAF_{max}, but to a much smaller extent relative to non-structural damping. Again, lower damping values were associated with higher dynamic amplification.

iii) In general, inelastic structural response was associated with a decrease in DAF_{max} with the highest DAF_{max} observed during elastic structural response.

iv) A slight increase in DAF_{max} was observed at low levels of inelastic deformation (ductility slightly higher than one) relative to elastic response in SDOF systems with a flag-shaped hysteresis, which is representative of a base-rocking system. This might be attributed to numerical issues arising from the idealization of the flag-shaped hysteresis with sharp corners.

v) The DAF_{max} formulation proposed by Welch (2016), which was derived for elastic SDOF systems, was in very good agreement with the data set from the present study.

In closing, since increasing ductility demands were generally associated with lower DAF_{max} values, the DAF_{max} formulation proposed by Welch (2016) was adopted in this study for use in inelastic MDOF systems.

8.1.6 Methodologies to Estimate Floor Response Spectra atop RC and Rocking Wall Systems

One of the main objectives of the present study was to develop a procedure for the estimation of floor response spectra atop RC and rocking wall buildings responding non-linearly. In the end, three separate procedures were developed. The first two procedures assume that floor response spectra are being generated after the dynamic properties of the buildings are known. On the other hand, the third procedure assumes that floor response spectra are being generated in the early design phases of a building when the dynamic properties of the building are not known. This procedure was developed such that the design of non-structural elements, which can account for the majority of the total investment in a typical building (Taghavi and Miranda, 2003), could be considered early on in the building design process.

All three proposed procedures were developed based on the work of Calvi and Sullivan (2014) who proposed a simple procedure for the estimation of floor response spectra in MDOF buildings responding elastically. In this procedure, modal floor spectra are first generated by obtaining elastic PFA contributions from each mode using a traditional modal response spectrum method. The modal PFA contributions are then scaled by empirical dynamic amplification factors (DAF) to obtain elastic modal floor spectra. The individual modal floor spectra are then combined using modal superposition to generate floor response spectra at each floor level. Each of the proposed procedures in the present study extends the procedure proposed by of Calvi and Sullivan (2014) to RC and rocking wall buildings responding non-linearly. Thus, the focus in developing the procedures was on how to take into account the effect of inelastic deformation on spectral acceleration demands. The main findings from each of the procedures are presented below.

Method (a): Procedure that utilizes transitory inelastic modal characteristics

This procedure accounts for the inelastic deformation by obtaining the modal PFA contributions using transitory (instead of elastic) modal characteristics. Transitory modes can be obtained through an Eigen-value analysis of the building in which the location of inelastic mechanism (i.e. plastic hinge region or rocking joint) is defined using a linear spring with an assigned secant (instead of elastic) stiffness. The secant stiffness is related to the ductility of the structural system, so transitory modes can be determined at any level of inelastic deformation or ductility.

Once the transitory modes are obtained, the modal PFA contributions are computed using a traditional modal response spectrum method. In doing so, it was also proposed that the first mode contribution to the PFA be obtained from a design ground response spectrum scaled at the equivalent viscous damping of the building, which incorporates both elastic and hysteretic damping. The hysteretic damping, which is dependent upon the ductility and behavior of a structural system, accounts for the added damping resulting from inelastic deformation. The incorporation of hysteretic damping was only proposed for the first mode because it has been noted by Sullivan *et al.* (2008) and others that inelastic structural response mainly affects the first mode response.

The PFA and floor response spectra estimates from the current procedure improved with increasing earthquake intensity. This might be an indication that transitory inelastic modal characteristics are better suited for estimating structural response at high ductility demands.

Method (b): Procedure that utilizes empirical modal reduction factors

This procedure, which was adapted from Welch (2016), accounts for inelastic structural response by reducing the individual elastic modal floor response spectra with empirical modal reduction factors. The reduction factors are defined as the ratio between the spectral floor accelerations from linear and non-linear response at the modal period. The reduction factors R_i were quantified through a record-by-record regression analysis as a function of the expected ductility of the structural system μ. The regression analysis was conducted in the form of a simple power law $R_i = \mu^{\alpha_i}$ where α_i is the exponent governing the rate of reduction in mode i. From the analysis, reduction factors were obtained for the first three modes of the RC and rocking wall buildings. The observations made from the regression analysis are summarized as follows:

i) The reduction factors significantly reduced with increasing order of modes, with the first mode having the highest reduction factor. This supports the notion that inelastic deformation mainly affects the first mode response.

ii) The scatter in reduction factors increased with increasing ductility demand for all three modes. Thus, this procedure might be best suited for low to moderate ductility demands.

iii) For all three modes, the rocking walls had lower reduction factors relative to the RC walls. Thus, for the same increment in ductility, a lower reduction in spectral floor acceleration is expected in the rocking walls. This indicates that the RC wall buildings have a better energy dissipation capability relative to the rocking walls.

Method (c): Procedure that utilizes dynamics of distributed-mass systems

This procedure is different from the previous two procedures in that it assumes the modal characteristics of the building are not known when floor response spectra are being estimated. In this context, the main goal of this procedure is to estimate the acceleration demands on non-structural elements in the early design phases of a building, such as after the completion of a direct displacement-based design (DDBD).

The first step in the development of this procedure was to provide an effective means of estimating the modal characteristics of RC and rocking wall buildings. To this end, it was proposed that the structural walls be idealized as continuous distributed-mass systems to estimate their modal characteristics. More specifically, RC walls can be idealized as continuous cantilever beams, and rocking walls as continuous fully-pinned (at the foundation) beams. Based on these idealizations, the periods and mode shapes of the RC and rocking wall case study buildings were estimated and compared to modal analysis values. The following observations were made from the comparison of the modal characteristics:

i) Reasonable approximations of modal periods were obtained for both RC and rocking wall buildings. The approximations were significantly better for the RC wall buildings.

ii) There was a significant amount of error in the mode shape approximations for both RC and rocking wall buildings.

iii) The approximations for both periods and mode shapes significantly improved with decreasing order of modes and increasing buildings height (i.e. floor levels). The latter was expected since idealizing a lumped-mass system as a continuous system becomes more realistic as the number of DOF (i.e. floor levels) increases.

The second step in the development of the current procedure was to provide an effective means of taking into account the effect of inelastic deformation on spectral acceleration demands. To this end, it was proposed that the first mode PFA contributions be obtained from the equivalent lateral force distribution of the design base shear, which typically only takes into account the first mode response of the building. For the case-study buildings, this was very effective in providing reasonable estimates of peak spectral acceleration demands in the first mode region.

For higher modes, it was proposed that the modal PFA contributions be determined by a traditional modal response spectrum method using the approximate elastic modal properties. Assuming that the higher mode response remains elastic is potentially conservative, but overall reasonable, considering the minor reductions in spectral floor acceleration demands observed in higher modes during inelastic structural response. For the case-study buildings, this assumption led non-conservative estimates of peak spectral acceleration demands for the second and third mode regions, which was mainly attributed to the error in the mode shape approximations.

8.2 Limitations of the Present Study and Recommendations for Further Research

The mass ratio at which dynamic interaction of non-structural elements and supporting structures needs to be considered was investigated in the present study. Dynamic interaction was observed in non-structural elements with mass ratios as low as 0.06% and natural periods close to the fundamental period of the supporting structure. These results call into question the commonly accepted mass ratio threshold of 1%. However, only two mass ratios were considered in the present study. Thus, future research efforts should investigate dynamic interaction at a wide range of mass ratios.

The floor response spectra estimation procedures proposed in the present study were developed for RC and rocking wall buildings with one inelastic mechanism (i.e. plastic hinge or rocking joint) at the base of the walls. For tall RC wall buildings, however, a second plastic hinge could form,

particularly in the presence bar of curtailment along the height of an RC wall (Panagiotou and Restrepo, 2009). The formation of the second plastic hinge could reduce the effects of higher modes (Panagiotou and Restrepo, 2009; Wiebe, 2008). Thus, the proposed floor response spectra estimation procedures are expected to provide a conservative estimate for spectral acceleration demands, mainly in the higher mode regions, for RC walls with multiple plastic hinges. For rocking wall buildings, the introduction of multiple rocking joints could cause an increase in the floor acceleration response of the building as observed by Khanmohammadi and Heydari (2015) and Wiebe (2008). Therefore, the proposed procedures to estimate floor response spectra might provide non-conservative estimates for spectral acceleration demands for rocking walls with multiple rocking joints. Nevertheless, the present study did not address the applicability of the proposed procedures to RC and rocking wall buildings with multiple plastic hinges and rocking joints, and thus should be properly addressed in future studies.

In addition, the applicability of the proposed procedures to other common structural systems should be investigated in future studies. In doing so, future research efforts regarding the first procedure should focus on developing methodologies to estimate transitory modal characteristics in structural systems with more than one inelastic mechanism, such as moment frames or dual systems. In such systems, obtaining transitory modal characteristics requires the consideration of a number of different stiffness distributions in plastic hinge regions, which was not dealt with in the present study.

Regarding the last procedure proposed for the estimation of floor response spectra, the error in the mode shape approximations was identified as the main source of error in the estimation of spectral acceleration demands. Thus, future research efforts should focus on the development of correction factors for the mode shapes obtained by idealizing RC and rocking wall buildings as continuous distributed-mass systems.

REFERENCES

Amaris, A. D. (2002). *Dynamic amplification of seismic moments and shear forces in cantilever walls*. *Master's Dissertation*. European School of Advanced Studies in Reduction of Seismic Risk (ROSE School), Pavia, Italy.

American Society of Civil Engineers (ASCE). (2010). Minimum Design Loads for Buildings and Other Structures. *ASCE 7-10*. Reston, Virginia, USA: American Society of Civil Engineers.

ASTM International. (2016). ASTM A416/A416M-16 Standard Specification for Low-Relaxation, Seven-Wire Steel Strand for Prestressed Concrete. West Conshohocken, PA, USA: ASTM International.

ASTM International. (2016). ASTM A615/A615M-16 Standard Specification for Deformed and Plain Carbon-Steel Bars for Concrete Reinforcement. West Conshohocken, PA, USA: ASTM International.

ASTM International. (2016). ASTM A706/A706M-16 Standard Specification for Deformed and Plain Low-Alloy Steel Bars for Concrete Reinforcement. West Conshohocken, PA, USA: ASTM International.

Belleri, A., Schoettler, M. J., Restrepo, J. I., & Fleischman, R. B. (2014). Dynamic behavior of rocking and hybrid cantilever walls in a precast concrete building. *ACI Structural Journal*, *111*(3), 661.

Calvi, P. M., & Sullivan, T. J. (2014). Estimating floor spectra in multiple degree of freedom systems. *Earthquakes and Structures*, *6*(7), 17–38.

Carr, A. J. (2004). Ruaumoko 2D, Inelastic dynamic analysis. *Department of Civil Engineering, University of Canterbury, Christchurch*.

Cattanach, A., & Pampanin, S. (2008). 21st century precast: the detailing and manufacture of NZ's first multi-storey PRESSS-Building. In *NZ Concrete Industry Conference, Rotorua*.

Charleson, A. (2008). *Seismic Design for Architects: Outwitting the Quake*. Architectural Press.

Chopra, A. K. (2001). *Dynamics of Structures* (Second Edi). Upper Saddle River, NJ, USA: Prentice-Hall.

Christopoulos, C., Pampanin, S., & Nigel Priestley, M. J. (2003). Performance-based seismic response of frame structures including residual deformations Part I: Single-degree of freedom systems. *Journal of Earthquake Engineering*, *7*(1), 97–118.

Chun, K. R. (1972). Free vibration of a beam with one end spring-hinged and the other free. *Journal of Applied Mechanics*, *39*(4), 1154–1155.

Conley, J., Sritharan, S., & Priestley, M. J. N. (2002). Precast seismic structural systems PRESSS-3: The five-story precast test building, Vol. 3-1: Wall direction response. Report Number: SSRP-99/19. San Diego, CA.

European Committee for Standardization (CEN). (2004). Design of structures for earthquake resistance - Part 1 : General rules, seismic actions and rules for buildings. *Eurocode 8*. Brussels, Belgium: European Committee for Standardization.

Fathali, S., & Filiatrault, A. (2008). Effect of elastomeric snubber properties on seismic response of vibration-isolated mechanical equipment: An experimental study. *Earthquake Spectra*, *24*(2), 387–403.

Federal Emergency Management Agency (FEMA). (2012). Reducing the Risks of Nonstructural Earthquake Damage – A Practical Guide. *FEMA E-74*. Washington, DC, USA: Federal Emergency Management Agency.

Ferner, H., Wemyss, M., Baird, A., Beer, A., & Hunter, D. (2014). Seismic Performance of Non-structural Elements within Buildings. In *Proceedings of the 2014 Conference for the New Zealand Society for Earthquake Engineering*. Paper No. O69.

Filiatrault, A., & Sullivan, T. (2014). Performance-based seismic design of nonstructural building components: The next frontier of earthquake engineering. *Earthquake Engineering and Engineering Vibration*, *13*(1), 17–46. https://doi.org/10.1007/s11803-014-0238-9

Filiatrault, A., Uang, C.-M., Folz, B., Chrstopoulos, C., & Gatto, K. (2001). *Reconnaissance report of the February 28, 2001 Nisqually (Seattle-Olympia) earthquake*. *Structural Systems Research Project Report No. SSRP-2000/15*. La Jolla, CA.

Fintel, M. (1995). Performance of buildings with shear walls in earthquakes of the last thirty years. *PCI Journal*, *40*(3), 62–80.

Galusha, J. G. (1999). *Precast, post-tensioned concrete walls designed to rock*. *Master's Thesis*. University of Washington.

Gavridou, S. (2015). *Shake Table Testing and Analytical Modeling of a Full-Scale, Four-Story Unbonded Post-Tensioned Concrete Wall Building*. *Doctoral Dissertation*. University of California Los Angeles, Los Angeles, CA, USA.

Gidaris, I., Taflanidis, A. A., Lopez-Garcia, D., & Mavroeidis, G. P. (2016). Multi-objective risk-informed design of floor isolation systems. *Earthquake Engineering & Structural Dynamics*, *45*(8), 1293–1313.

Holden, T., Restrepo, J., & Mander, J. B. (2003). Seismic performance of precast reinforced and prestressed concrete walls. *Journal of Structural Engineering*, *129*(3), 286–296.

Jacobsen, L. S., & Ayre, R. S. (1958). *Engineering vibrations: with applications to structures and machinery*. New York, NY: McGraw-Hill.

Khanmohammadi, M., & Heydari, S. (2015). Seismic behavior improvement of reinforced concrete shear wall buildings using multiple rocking systems. *Engineering Structures*, *100*, 577–589.

Kurama, Y. C. (2000). Unbonded post-tensioned precast concrete walls with supplemental viscous damping. *ACI Structural Journal*, 97(4), 648–658.

Kurama, Y. C. (2001). Simplified Seismic Design Approach for Friction-Damped Unbonded Post-Tensioned Precast Concrete Walls. *ACI Structural Journal*, *98*(5), 705–716. https://doi.org/10.14359/10624

Kurama, Y. C. (2002). Hybrid post-tensioned precast concrete walls for use in seismic regions. *PCI Journal*, *47*(5), 36–59.

Marriott, D., Pampanin, S., Bull, D., & Palermo, A. (2008). Dynamic testing of precast, post-tensioned rocking wall systems with alternative dissipating solutions. *Bulletin of the New Zealand Society for Earthquake Engineering*, *41*(2), 90–103.

Marsantyo, R., Shimazu, T., & Araki, H. (2000). Dynamic response of nonstructural systems mounted on floors of buildings. In *Proceedings of the 12th World Conference on Earthquake Engineering*. Paper No. 1872. Auckland, New Zealand.

Menon, A., & Magenes, G. (2008). *Out-of-plane seismic response of unreinforced masonry: definition of seismic input*. *Research Report ROSE - 2008/04*. Pavia, Italy: IUSS Press.

Miranda, E., & Taghavi, S. (2005). Approximate Floor Acceleration Demands in Multistory Buildings. I: Formulation. *Journal of Structural Engineering*, *131*(2), 212–220. https://doi.org/10.1061/(ASCE)0733-9445(2005)131:2(212)

Mitchell, D., DeVall, R. H., Saatcioglu, M., Simpson, R., Tinawi, R., & Tremblay, R. (1995). Damage to concrete structures due to the 1994 Northridge earthquake. *Canadian Journal of Civil Engineering*, *22*(2), 361–377.

Montejo, L. A., & Kowalsky, M. J. (2007). CUMBIA—Set of codes for the analysis of reinforced concrete members. *CFL Technical Rep. No. IS-07*, *1*.

Nakaki, S. D., Stanton, J. F., & Sritharan, S. (1999). An overview of the PRESSS five-story precast test building. PCI Journal, 44(2), 26–39.

New Zealand Standard (NZS). (2004). Part 5 : Earthquake actions – New Zealand. *NZS 1170.5:2004*. Wellington, New Zealand: Standards New Zealand.

Palermo, A., Pampanin, S., & Carr, A. J. (2005). Efficiency of simplified alternative modelling approaches to predict the seismic response of precast concrete hybrid systems. In *2005 fib Symposium "Keep Concrete Attractive."* Budapest. Hungary.

Pampanin, S., Kam, W., Haverland, G., & Gardiner, S. (2011). Expectation meets reality: seismic performance of post-tensioned precast concrete southern cross endoscopy building during the 22nd Feb 2011 Christchurch earthquake. In *NZ Concrete Industry Conference, Rotorua*.

Panagiotou, M., & Restrepo, J. I. (2009). Dual-plastic hinge design concept for reducing higher-mode effects on high-rise cantilever wall buildings. Earthquake Engineering & Structural Dynamics, 38(12), 1359–1380.

Paquette, J., Bruneau, M., & Filiatrault, A. (2001). Out-of-Plane Seismic Evaluation and Retrofit of Turn-of-the-Century North American Masonry Walls. *Journal of Structural Engineering*, *127*(5), 561–569. https://doi.org/10.1061/(ASCE)0733-9445(2001)127:5(561)

Paulay, T., & Priestley, M. J. N. (1992). *Seismic design of reinforced concrete and masonry buildings*. John Wiley & Sons, Inc.

Pennucci, D., Calvi, G. M., & Sullivan, T. J. (2009). Displacement-Based Design of Precast Walls with Additional Dampers. *Journal of Earthquake Engineering*, *13*(S1), 40–65.

Pennucci, D., Sullivan, T. J., & Calvi, G. M. (2015). Inelastic Higher-Mode Response in Reinforced Concrete Wall Structures. *Earthquake Spectra*, *31*(3), 1493–1514. https://doi.org/10.1193/051213EQS123M

Pennucci, D., Sullivan, T. J., & Calvi, G. M. (2011). *Performance-based seismic design of tall RC wall buildings*. *Research Report ROSE - 2011/02*. Pavia, Italy: IUSS Press.

Perez, F. J., Pessiki, S., & Sause, R. (2004). Seismic design of unbonded post-tensioned precast concrete walls with vertical joint connectors. PCI Journal, 49(1), 58–79.

Pinkawa, M., Hoffmeister, B., & Feldmann, M. (2014). A critical review of current approaches on the determination of seismic force demands on nonstructural components. In *Proceedings of the 9th International Conference on Structural Dynamics, EURODYN 2014*. Porto, Portugal.

Priestley, M. J. N., & Grant, D. N. (2005). Viscous damping in seismic design and analysis. *Journal of Earthquake Engineering*, *9*(spec02), 229–255.

Priestley, M. J. N. (1991). Overview of PRESSS research program. *PCI Journal*, *36*(4), 50–57.

Priestley, M. J. N. (1996). The PRESSS program—current status and proposed plans for phase III. PCI Journal, 4(2), 22–40.

Priestley, M. J. N. (1998). Displacement-based approaches to rational limit states design of new structures. *Keynote Address, 11th European Conference on Earthquake Engineering.* Paris, France.

Priestley, M. J. N., Sritharan, S., Conley, J. R., & Pampanin, S. (1999). Preliminary results and conclusions from the PRESSS five-story precast concrete test building. *PCI Journal*, *44*(6), 42–67.

Priestley, M. J. N. (2002). Direct displacement-based design of precast/prestressed concrete buildings. PCI Journal, 47(6), 66–79.

Priestley, M. J. N., Calvi, G. M., & Kowalsky, M. J. (2007). *Displacement-Based Seismic Design of Structures*. Pavia, Italy: IUSS Press.

Qureshi, I. M., & Warnitchai, P. (2016). Computer modeling of dynamic behavior of rocking wall structures including the impact-related effects. *Advances in Structural Engineering*, *19*(8), 1245–1261. https://doi.org/10.1177/1369433216642057

Rahman, A. M., & Restrepo, J. I. (2000). *Earthquake Resistant Precast Concrete Buildings: Seismic Performance of Cantilever Walls Prestressed Using Unbonded Tendons*. Christchurch, New Zealand.

Rahman, M. A., & Sritharan, S. (2006). An evaluation of force-based design vs. direct displacement-based design of jointed precast post-tensioned wall systems. Earthquake Engineering and Engineering Vibration, 5(2), 285–296.

Restrepo, J. I., & Rahman, A. (2007). Seismic performance of self-centering structural walls incorporating energy dissipators. *Journal of Structural Engineering*, *133*(11), 1560–1570.

Rodriguez, M. E., Restrepo, J. I., & Carr, A. J. (2002). Earthquake-induced floor horizontal accelerations in buildings. *Earthquake Engineering & Structural Dynamics*, *31*(3), 693–718. https://doi.org/10.1002/eqe.149

Ryu, K. P., Reinhorn, A. M., & Filiatrault, A. (2012). Full scale dynamic testing of large area suspended ceiling system. In *Proceedings 15th World Conference on Earthquake Engineering* (Vol. 5474). Lisbon,Portugal.

Sankaranarayanan, R. (2007). *Seismic response of acceleration-sensitive nonstructural components mounted on moment-resisting frame structures*. *Doctoral Dissertation*. University of Maryland, College Park, Maryland, USA.

Schoettler, M. J., Belleri, A., Dichuan, Z., Restrepo, J. I., & Fleischman, R. B. (2009). Preliminary results of the shake-table testing for the development of a diaphragm seismic design methodology. *PCI Journal*, *54*(1), 100–124.

Sewell, R. T. (1986). *Study of Factors Influencing Floor Response Spectra in Nonlinear Multi-Degree-of-Freedom Structures*. John A. Blume Earthquake Engineering Center.

Singh, A. K., & Ang, A.-S. (1974). Stochastic prediction of maximum seismic response of light secondary systems. *Nuclear Engineering and Design*, *29*(2), 218–230.

Smyrou, E., Priestley, M. J. N., & Carr, A. J. (2011). Modelling of elastic damping in nonlinear time-history analyses of cantilever RC walls. *Bulletin of Earthquake Engineering*, *9*(5), 1559–1578.

Sritharan, S., Aaleti, S., Henry, R. S., Liu, K., & Tsai, K. (2015). Precast concrete wall with end columns (PreWEC) for earthquake resistant design. *Earthquake Engineering & Structural Dynamics*, *44*(12), 2075–2092.

Stanton, J., Pizano-Battle, V. and Pizano-Thomen, V. (2003). "Design of the Cala Building using PRESSS technology." *Concrete Structures in Seismic Regions: FIB 2003 Symposium.*

Sullivan, T. J., Priestley, M. J. N., & Calvi, G. M. (2008). Estimating the higher-mode response of ductile structures. *Journal of Earthquake Engineering*, *12*(3), 456–472.

Sullivan, T. J., Priestley, M. J. N., and Calvi, G. M. (2006). *Seismic design of frame-wall structures*. *Research Report ROSE - 2006/02*. Pavia, Italy: IUSS Press.

Sullivan, T. J., Calvi, P. M., & Nascimbene, R. (2013). Towards improved floor spectra estimates for seismic design. *Earthquakes and Structures*, *4*(1), 109–132.

Taghavi, S., & Miranda, E. (2003). *Response assessment of nonstructural building components*. Berkeley, CA, USA: PEER Report 2003/05.

Taghavi, S., & Miranda, E. (2008). Effect of interaction between primary and secondary systems on floor response spectra. In *Proceedings of the 14th World Conference on Earthquake Engineering*. Beijing, China.

Tian, Y., Filiatrault, A., & Mosqueda, G. (2015). Seismic response of pressurized fire sprinkler piping systems I: experimental study. *Journal of Earthquake Engineering*, *19*(4), 649–673.

Todd, D., Carino, N., Chung, R. M., Lew, H. S., Taylor, A. W., Walton, W. D., … Nimis, R. (1994). *1994 Northridge earthquake: performance of structures, lifelines, and fire protection systems*. *NIST Special Publication 862*. Gaithersburg, MD: US Department of Commerce, National Institute of Standards and Technology.

Toranzo-Dianderas, L. A. (2002). *The use of rocking walls in confined masonry structures: a performance-based approach*. *PhD Dissertation*. University of Canterbury, Christchurch, New Zealand.

Toro, G. R., McGuire, R. K., Cornell, C. A., Sewell Inc., Golden, CO (USA), R. T. (Risk E., & Stanford Univ., C. A. (USA)). (1989). *Linear and nonlinear response of structures and equipment to California and eastern United States earthquakes*. *EPRI-NP-5566*. Palo Alto, CA, USA.

Twigden, K. M., Watkins, J., Henry, R. S., & Sritharan, S. (2013). Dynamic test evaluation of numerical models for unbonded post-tensioned concrete walls. In *2013 NZSEE Annual Conference*. Wellington, New Zealand.

Uma, S. R., Zhao, J. X., & King, A. B. (2010). Seismic actions on acceleration sensitive non-structural components in ductile frames. *Bulletin of the New Zealand Society for Earthquake Engineering*, *43*(2), 110–125.

Villaverde, R. (1997). Seismic design of secondary structures: state of the art. *Journal of Structural Engineering*, *123*(8), 1011–1019.

Vukobratović, V. (2015). *The influence of nonlinear seismic response of structures on the floor acceleration spectra : doctoral dissertation = Vpliv nelinearnega potresnega odziva konstrukcij na etažne spektre pospeškov : doktorska disertacija*. *Doctoral Dissertation*. University of Ljubljana, Ljubljana, Slovenia.

Wanitkorkul, A., & Filiatrault, A. (2008). Influence of passive supplemental damping systems on structural and nonstructural seismic fragilities of a steel building. *Engineering Structures*, *30*(3), 675–682.

Welch, D. P. (2016). *Non-Structural Element Considerations for Contemporary Performance-Based Earthquake Engineering*. *Doctoral Dissertation*. University of Pavia, Pavia, Italy.

Wiebe, L. (2008). Mitigation of higher mode effects in self-centering walls by using multiple rocking sections. *Master's Dissertation*.

Wiebe, L., & Christopoulos, C. (2009). Mitigation of higher mode effects in base-rocking systems by using multiple rocking sections. *Journal of Earthquake Engineering*, *13*(S1), 83–108.

Wiebe, L., & Christopoulos, C. (2010). Characterizing acceleration spikes due to stiffness changes in nonlinear systems. *Earthquake Engineering & Structural Dynamics*, *39*(14), 1653–1670. https://doi.org/10.1002/eqe.1009

Wiebe, L., & Christopoulos, C. (2011). Using Bézier curves to model gradual stiffness transitions in nonlinear elements: Application to self-centering systems. *Earthquake Engineering & Structural Dynamics*, *40*(14), 1535–1552. https://doi.org/10.1002/eqe.1099

Wood, S. L., Wight, J. K., & Moehle, J. P. (1987). *The 1985 Chile earthquake: observations on earthquake-resistant construction in Viña del Mar*. University of Illinois Engineering Experiment Station. College of Engineering. University of Illinois at Urbana-Champaign.

APPENDIX A. MODAL CHARACTERISTICS OF CASE STUDY BUILDINGS

Section A.1 presents the elastic modal characteristics of the case-study buildings. Section A.2 presents the transitory modal characteristics of the case-study buildings at each intensity level considered. Section A.3 presents approximate elastic modal characteristics for the case study buildings idealized as continuous distributed-mass systems.

A.1 Elastic Modal Characteristics

Table A.1 Elastic modal characteristics of the 4-story RC wall building

Mode	**1**	**2**	**3**	**4**
Frequency, f_i (Hz)	0.741	4.613	12.490	21.400
Period, T_i (sec)	1.350	0.217	0.080	0.047
Damping Ratio, ξ_i (%)	1.987	5.000	5.000	5.000
Modal Participation Factor, Γ_i (-)	1.367	0.633	0.354	-0.188
Effective Modal Mass, $M_{e,i}$ (tons)	296.5	91.3	29.7	9.4
Fraction of Total Mass (%)	69.0%	22.0%	7.0%	2.0%
Floor Level	**Mode Shapes**			
	Φ_1	**Φ_2**	**Φ_3**	**Φ_4**
0	0.000	0.000	0.000	0.000
1	0.094	0.522	1.000	-0.994
2	0.330	1.000	0.290	1.000
3	0.649	0.513	-0.944	-0.654
4	1.000	-0.776	0.461	0.204

Table A.2 Elastic modal characteristics of the 8-story RC wall building

Mode	**1**	**2**	**3**	**4**	**5**	**6**
Frequency, f_i (Hz)	0.393	2.426	6.605	12.370	19.140	26.060
Period, T_i (sec)	2.543	0.412	0.151	0.081	0.052	0.038
Damping Ratio, ξ_i (%)	1.960	5.000	5.000	5.000	5.000	5.000
Modal Participation Factor, Γ_i (-)	1.458	-0.662	0.371	0.255	0.195	0.156
Effective Modal Mass, $M_{e,i}$ (tons)	1088.0	338.1	117.1	59.1	33.2	18.4
Fraction of Total Mass (%)	65.0%	21.0%	7.0%	3.0%	2.0%	1.0%
Floor Level	**Mode Shapes**					
	Φ_1	**Φ_2**	**Φ_3**	**Φ_4**	**Φ_5**	**Φ_6**
0	0.000	0.000	0.000	0.000	0.000	0.000
1	0.026	-0.180	0.466	0.786	1.000	1.000
2	0.096	-0.529	1.000	1.000	0.401	-0.393
3	0.202	-0.839	0.913	-0.082	-0.944	-0.547
4	0.335	-0.953	0.173	-0.994	-0.174	0.909
5	0.488	-0.789	-0.656	-0.439	0.991	-0.282
6	0.654	-0.352	-0.894	0.736	-0.014	-0.659
7	0.826	0.280	-0.286	0.730	-0.919	0.843
8	1.000	1.000	0.851	-0.685	0.505	-0.334

Table A.3 Elastic modal characteristics of the 12-story RC wall building

MODE	1	2	3	4	5	6
Frequency, f_i (Hz)	0.271	1.676	4.586	8.686	13.730	19.400
Period, T_i (sec)	3.686	0.597	0.218	0.115	0.073	0.052
Damping Ratio, ξ_i (%)	1.955	5.000	5.000	5.000	5.000	5.000
Modal Participation Factor, Γ_i (-)	1.493	-0.729	0.378	0.261	0.217	0.161
Effective Modal Mass, $M_{e,i}$ (tons)	1633.0	506.8	176.3	90.9	54.5	35.0
Fraction of Total Mass (%)	64.0%	19.9%	6.9%	3.6%	2.1%	1.4%
Floor Level	**Mode Shapes**					
	Φ_1	**Φ_2**	**Φ_3**	**Φ_4**	**Φ_5**	**Φ_6**
0	0.000	0.000	0.000	0.000	0.000	0.000
1	0.012	-0.083	0.249	0.467	0.641	0.895
2	0.045	-0.266	0.673	1.000	1.000	0.867
3	0.097	-0.488	0.985	0.981	0.371	-0.412
4	0.164	-0.690	1.000	0.325	-0.627	-0.971
5	0.245	-0.826	0.676	-0.536	-0.881	0.066
6	0.337	-0.862	0.121	-0.993	-0.112	1.000
7	0.437	-0.778	-0.458	-0.725	0.791	0.305
8	0.544	-0.576	-0.836	0.064	0.788	-0.889
9	0.655	-0.269	-0.855	0.783	-0.109	-0.644
10	0.769	0.117	-0.483	0.879	-0.843	0.621
11	0.884	0.549	0.190	0.210	-0.500	0.779
12	1.000	1.000	0.998	-0.896	0.712	-0.650

Table A.4 Elastic modal characteristics of the 4-story rocking wall building

Mode	**1**	**2**	**3**	**4**
Frequency, f_i (Hz)	1.258	9.923	25.920	40.530
Period, T_i (sec)	0.795	0.101	0.039	0.025
Damping Ratio, ξ_i (%)	1.000	5.000	5.000	5.000
Modal Participation Factor, Γ_i (-)	1.365	0.516	0.251	-0.105
Effective Modal Mass, $M_{e,i}$ (tons)	338.7	71.8	14.0	2.5
Fraction of Total Mass (%)	79.0%	17.0%	3.0%	1.0%
Floor Level	**Mode Shapes**			
	Φ_1	**Φ_2**	**Φ_3**	**Φ_4**
0	0.000	0.000	0.000	0.000
1	0.198	0.785	1.000	-0.707
2	0.444	1.000	-0.071	1.000
3	0.718	0.322	-0.890	-0.742
4	1.000	-0.905	0.515	0.249

Table A.5 Elastic modal characteristics of the 8-story rocking wall building

Mode	**1**	**2**	**3**	**4**	**5**	**6**
Frequency, f_i (Hz)	0.627	4.432	11.960	21.010	29.890	37.510
Period, T_i (sec)	1.594	0.226	0.084	0.048	0.033	0.027
Damping Ratio, ξ_i (%)	1.000	5.000	5.000	5.000	5.000	5.000
Modal Participation Factor, Γ_i (-)	1.450	-0.628	0.312	-0.189	0.130	0.084
Effective Modal Mass, $M_{e,i}$ (tons)	1227.0	302.1	80.0	32.0	14.2	6.3
Fraction of Total Mass (%)	74.0%	18.0%	5.0%	2.0%	0.0%	1.0%
Floor Level	**Mode Shapes**					
	Φ_1	**Φ_2**	**Φ_3**	**Φ_4**	**Φ_5**	**Φ_6**
0	0.000	0.000	0.000	0.000	0.000	0.000
1	0.079	-0.361	0.707	-0.960	1.000	0.940
2	0.179	-0.693	1.000	-0.694	-0.043	-0.742
3	0.296	-0.886	0.631	0.486	-0.973	-0.305
4	0.425	-0.869	-0.153	1.000	0.155	1.000
5	0.563	-0.622	-0.794	0.168	0.970	-0.537
6	0.707	-0.179	-0.816	-0.853	-0.227	-0.570
7	0.853	0.389	-0.148	-0.614	-0.866	0.953
8	1.000	1.000	0.854	0.714	0.542	-0.413

Table A.6 Elastic modal characteristics of the 12-story rocking wall building

Mode	1	2	3	4	5	6
Frequency, f_i (Hz)	0.439	3.062	8.407	15.230	22.560	29.720
Period, T_i (sec)	2.277	0.327	0.119	0.066	0.044	0.034
Damping Ratio, ξ_i (%)	1.000	5.000	5.000	5.000	5.000	5.000
Modal Participation Factor, Γ_i (-)	1.483	-0.690	0.324	0.213	0.145	0.110
Effective Modal Mass, $M_{e,i}$ (tons)	1833.0	465.3	130.2	56.6	29.0	16.3
Fraction of Total Mass (%)	72.0%	18.0%	5.0%	2.0%	1.0%	1.0%
Floor Level	**Mode Shapes**					
	Φ_1	**Φ_2**	**Φ_3**	**Φ_4**	**Φ_5**	**Φ_6**
0	0.000	0.000	0.000	0.000	0.000	0.000
1	0.048	-0.216	0.491	0.706	0.910	1.000
2	0.106	-0.441	0.875	1.000	0.887	0.480
3	0.174	-0.640	1.000	0.657	-0.073	-0.771
4	0.250	-0.778	0.812	-0.110	-0.941	-0.805
5	0.332	-0.835	0.367	-0.797	-0.779	0.426
6	0.420	-0.795	-0.186	-0.952	0.235	0.990
7	0.512	-0.656	-0.660	-0.477	1.000	-0.001
8	0.607	-0.428	-0.889	0.303	0.690	-0.998
9	0.704	-0.124	-0.783	0.853	-0.347	-0.449
10	0.802	0.230	-0.355	0.780	-0.957	0.762
11	0.901	0.612	0.289	0.083	-0.422	0.685
12	1.000	1.000	0.996	-0.871	0.795	-0.681

A.2 Transitory Modal Characteristics

Table A.7 Transitory modal characteristics of the 4-story RC wall building; Intensity 1 (PGA = 0.225 g)

Mode	1	2	3	4
Frequency, f_i (Hz)	0.497	3.700	10.880	20.220
Period, T_i (sec)	2.014	0.270	0.092	0.049
Damping Ratio, ξ_i (%)	1.987	5.000	5.000	5.000
Modal Participation Factor, Γ_i (-)	1.369	0.542	0.271	-0.117
Effective Modal Mass, $M_{e,i}$ (tons)	331.1	76.4	16.3	3.1
Fraction of Total Mass (%)	77.5%	17.9%	3.8%	0.7%
Floor Level	Mode Shapes			
	Φ_1	Φ_2	Φ_3	Φ_4
0	0.000	0.000	0.000	0.000
1	0.177	0.738	1.000	-0.746
2	0.421	1.000	-0.005	1.000
3	0.703	0.365	-0.901	-0.715
4	1.000	-0.881	0.500	0.233

Table A.8 Transitory modal characteristics of the 4-story RC wall building; Intensity 5 (PGA = 0.450 g)

Mode	1	2	3	4
Frequency, f_i (Hz)	0.362	3.470	10.620	20.080
Period, T_i (sec)	2.766	0.288	0.094	0.050
Damping Ratio, ξ_i (%)	1.987	5.000	5.000	5.000
Modal Participation Factor, Γ_i (-)	1.362	0.496	0.245	-0.106
Effective Modal Mass, $M_{e,i}$ (tons)	343.0	67.8	13.6	2.6
Fraction of Total Mass (%)	80.3%	15.9%	3.2%	0.6%
Floor Level	Mode Shapes			
	Φ_1	Φ_2	Φ_3	Φ_4
0	0.000	0.000	0.000	0.000
1	0.211	0.790	1.000	-0.715
2	0.458	1.000	-0.055	1.000
3	0.725	0.322	-0.910	-0.723
4	1.000	-0.934	0.517	0.237

Table A.9 Transitory modal characteristics of the 4-story RC wall building; Intensity 6 (PGA = 0.675 g)

Mode	**1**	**2**	**3**	**4**
Frequency, f_i (Hz)	0.304	3.403	10.550	20.040
Period, T_i (sec)	3.295	0.294	0.095	0.050
Damping Ratio, ξ_i (%)	1.987	5.000	5.000	5.000
Modal Participation Factor, Γ_i (-)	1.358	0.481	0.238	-0.103
Effective Modal Mass, $M_{e,i}$ (tons)	346.8	64.9	12.9	2.4
Fraction of Total Mass (%)	81.2%	15.2%	3.0%	0.6%
Floor Level	**Mode Shapes**			
	Φ_1	**Φ_2**	**Φ_3**	**Φ_4**
0	0.000	0.000	0.000	0.000
1	0.222	0.805	1.000	-0.707
2	0.470	1.000	-0.068	1.000
3	0.732	0.308	-0.913	-0.725
4	1.000	-0.953	0.522	0.238

Table A.10 Transitory modal characteristics of the 8-story RC wall building; Intensity 1 (PGA = 0.225 g)

Mode	1	2	3	4	5	6
Frequency, f_i (Hz)	0.301	2.044	5.860	11.380	18.090	25.170
Period, T_i (sec)	3.320	0.489	0.171	0.088	0.055	0.040
Damping Ratio, ξ_i (%)	1.960	5.000	5.000	5.000	5.000	5.000
Modal Participation Factor, Γ_i (-)	1.456	-0.645	0.331	-0.205	0.144	0.095
Effective Modal Mass, $M_{e,i}$ (tons)	1193.0	316.8	89.8	37.2	17.2	7.8
Fraction of Total Mass (%)	71.6%	19.0%	5.4%	2.2%	1.0%	0.5%
Floor Level	Mode Shapes					
	Φ_1	Φ_2	Φ_3	Φ_4	Φ_5	Φ_6
0	0.000	0.000	0.000	0.000	0.000	0.000
1	0.065	-0.320	0.658	-0.930	1.000	0.966
2	0.156	-0.655	1.000	-0.764	0.048	-0.681
3	0.270	-0.873	0.695	0.389	-0.970	-0.381
4	0.400	-0.887	-0.070	1.000	0.055	1.000
5	0.542	-0.662	-0.750	0.258	0.971	-0.447
6	0.692	-0.226	-0.837	-0.803	-0.131	-0.639
7	0.845	0.356	-0.201	-0.670	-0.887	0.929
8	1.000	1.000	0.858	0.706	0.519	-0.381

Table A.11 Transitory modal characteristics of the 8-story RC wall building; Intensity 5 (PGA = 0.450 g)

Mode	1	2	3	4	5	6
Frequency, f_i (Hz)	0.220	1.872	5.631	11.150	17.900	25.030
Period, T_i (sec)	4.537	0.534	0.178	0.090	0.056	0.040
Damping Ratio, ξ_i (%)	1.960	5.000	5.000	5.000	5.000	5.000
Modal Participation Factor, Γ_i (-)	1.444	-0.620	0.297	-0.185	0.128	0.085
Effective Modal Mass, $M_{e,i}$ (tons)	1255.0	281.2	74.7	30.4	13.9	6.3
Fraction of Total Mass (%)	75.4%	16.9%	4.5%	1.8%	0.8%	0.4%
Floor Level	Mode Shapes					
	Φ_1	Φ_2	Φ_3	Φ_4	Φ_5	Φ_6
0	0.000	0.000	0.000	0.000	0.000	0.000
1	0.092	-0.363	0.712	-0.945	1.000	0.937
2	0.199	-0.681	1.000	-0.697	-0.020	-0.718
3	0.318	-0.858	0.632	0.460	-0.985	-0.345
4	0.446	-0.832	-0.150	1.000	0.098	1.000
5	0.580	-0.589	-0.799	0.216	0.982	-0.470
6	0.718	-0.159	-0.841	-0.823	-0.155	-0.627
7	0.859	0.394	-0.180	-0.660	-0.897	0.932
8	1.000	1.000	0.887	0.717	0.531	-0.384

Table A.12 Transitory modal characteristics of the 8-story RC wall building; Intensity 6 (PGA = 0.675 g)

Mode	**1**	**2**	**3**	**4**	**5**	**6**
Frequency, f_i (Hz)	0.185	1.823	5.575	11.100	17.860	25.000
Period, T_i (sec)	5.402	0.549	0.179	0.090	0.056	0.040
Damping Ratio, ξ_i (%)	1.960	5.000	5.000	5.000	5.000	5.000
Modal Participation Factor, Γ_i (-)	1.439	-0.611	0.287	-0.180	0.125	0.083
Effective Modal Mass, $M_{e,i}$ (tons)	1276.0	267.8	70.6	28.8	13.2	6.0
Fraction of Total Mass (%)	76.6%	16.1%	4.2%	1.7%	0.8%	0.4%
Floor Level	**Mode Shapes**					
	Φ_1	**Φ_2**	**Φ_3**	**Φ_4**	**Φ_5**	**Φ_6**
0	0.000	0.000	0.000	0.000	0.000	0.000
1	0.101	-0.372	0.725	-0.947	1.000	0.931
2	0.214	-0.685	1.000	-0.680	-0.035	-0.726
3	0.334	-0.849	0.616	0.476	-0.989	-0.337
4	0.461	-0.813	-0.171	1.000	0.108	1.000
5	0.593	-0.565	-0.813	0.207	0.986	-0.474
6	0.727	-0.139	-0.844	-0.828	-0.161	-0.625
7	0.864	0.406	-0.175	-0.658	-0.900	0.933
8	1.000	1.000	0.897	0.719	0.534	-0.385

Table A.13 Transitory modal characteristics of the 12-story RC wall building; Intensity 1 (PGA = 0.225 g)

Mode	1	2	3	4	5	6
Frequency, f_i (Hz)	0.228	1.476	4.163	8.074	13.000	18.640
Period, T_i (sec)	4.385	0.678	0.240	0.124	0.077	0.054
Damping Ratio, ξ_i (%)	1.955	5.000	5.000	5.000	5.000	5.000
Modal Participation Factor, Γ_i (-)	1.492	-0.717	0.353	0.237	0.157	0.125
Effective Modal Mass, $M_{e,i}$ (tons)	1747.0	497.6	152.6	69.2	36.6	20.9
Fraction of Total Mass (%)	68.5%	19.5%	6.0%	2.7%	1.4%	0.8%
Floor Level	**Mode Shapes**					
	Φ_1	**Φ_2**	**Φ_3**	**Φ_4**	**Φ_5**	**Φ_6**
0	0.000	0.000	0.000	0.000	0.000	0.000
1	0.031	-0.167	0.413	0.636	0.898	0.980
2	0.078	-0.378	0.812	1.000	1.000	0.594
3	0.139	-0.586	1.000	0.759	0.079	-0.670
4	0.211	-0.749	0.881	0.035	-0.903	-0.870
5	0.292	-0.836	0.481	-0.698	-0.891	0.297
6	0.382	-0.825	-0.069	-0.955	0.098	1.000
7	0.478	-0.708	-0.577	-0.567	0.983	0.137
8	0.578	-0.490	-0.861	0.196	0.802	-0.943
9	0.682	-0.187	-0.808	0.802	-0.237	-0.557
10	0.787	0.179	-0.412	0.812	-0.973	0.671
11	0.893	0.583	0.238	0.153	-0.526	0.751
12	1.000	1.000	1.000	-0.876	0.826	-0.662

Table A.14 Transitory modal characteristics of the 12-story RC wall building; Intensity 5 (PGA = 0.450 g)

Mode	1	2	3	4	5	6
Frequency, f_i (Hz)	0.178	1.338	3.956	7.844	12.780	18.440
Period, T_i (sec)	5.629	0.747	0.253	0.128	0.078	0.054
Damping Ratio, ξ_i (%)	1.955	5.000	5.000	5.000	5.000	5.000
Modal Participation Factor, Γ_i (-)	1.481	-0.691	0.327	0.210	0.141	0.112
Effective Modal Mass, $M_{e,i}$ (tons)	1848.0	451.9	127.3	56.0	29.3	16.7
Fraction of Total Mass (%)	72.5%	17.7%	5.0%	2.2%	1.1%	0.7%
Floor Level	**Mode Shapes**					
	Φ_1	**Φ_2**	**Φ_3**	**Φ_4**	**Φ_5**	**Φ_6**
0	0.000	0.000	0.000	0.000	0.000	0.000
1	0.051	-0.213	0.471	0.694	0.919	0.987
2	0.112	-0.434	0.844	1.000	0.927	0.512
3	0.181	-0.627	0.971	0.679	-0.032	-0.735
4	0.257	-0.762	0.797	-0.075	-0.946	-0.838
5	0.339	-0.816	0.373	-0.774	-0.842	0.359
6	0.427	-0.777	-0.163	-0.964	0.167	1.000
7	0.518	-0.643	-0.630	-0.523	1.000	0.092
8	0.612	-0.419	-0.867	0.251	0.767	-0.961
9	0.708	-0.122	-0.781	0.835	-0.271	-0.536
10	0.805	0.228	-0.375	0.815	-0.974	0.688
11	0.902	0.608	0.262	0.137	-0.511	0.748
12	1.000	1.000	1.000	-0.900	0.828	-0.670

Table A.15 Transitory modal characteristics of the 12-story RC wall building; Intensity 6 (PGA = 0.675 g)

Mode	1	2	3	4	5	6
Frequency, f_i (Hz)	0.153	1.292	3.898	7.786	12.720	18.400
Period, T_i (sec)	6.559	0.774	0.257	0.128	0.079	0.054
Damping Ratio, ξ_i (%)	1.955	5.000	5.000	5.000	5.000	5.000
Modal Participation Factor, Γ_i (-)	1.474	-0.678	0.318	0.202	0.138	0.108
Effective Modal Mass, $M_{e,i}$ (tons)	1887.0	428.8	118.9	52.4	27.5	15.7
Fraction of Total Mass (%)	74.0%	16.8%	4.7%	2.1%	1.1%	0.6%
Floor Level	**Mode Shapes**					
	Φ_1	**Φ_2**	**Φ_3**	**Φ_4**	**Φ_5**	**Φ_6**
0	0.000	0.000	0.000	0.000	0.000	0.000
1	0.059	-0.225	0.484	0.709	0.919	0.987
2	0.126	-0.447	0.848	1.000	0.905	0.493
3	0.198	-0.635	0.958	0.659	-0.058	-0.750
4	0.277	-0.760	0.770	-0.104	-0.952	-0.830
5	0.359	-0.804	0.341	-0.796	-0.827	0.373
6	0.446	-0.757	-0.190	-0.968	0.183	1.000
7	0.535	-0.617	-0.645	-0.513	1.000	0.082
8	0.626	-0.393	-0.868	0.266	0.756	-0.966
9	0.718	-0.099	-0.773	0.846	-0.278	-0.532
10	0.812	0.245	-0.365	0.818	-0.971	0.693
11	0.906	0.617	0.268	0.133	-0.505	0.748
12	1.000	1.000	1.000	-0.909	0.826	-0.672

Table A.16 Transitory modal characteristics of the 4-story rocking wall building; Intensity 1 (PGA = 0.225 g)

Mode	1	2	3	4
Frequency, f_i (Hz)	0.516	9.325	25.530	40.420
Period, T_i (sec)	1.939	0.107	0.039	0.025
Damping Ratio, ξ_i (%)	1.000	5.000	5.000	5.000
Modal Participation Factor, Γ_i (-)	1.352	0.459	0.225	-0.096
Effective Modal Mass, $M_{e,i}$ (tons)	352.7	60.7	11.5	2.1
Fraction of Total Mass (%)	82.6%	14.2%	2.7%	0.5%
Floor Level	Mode Shapes			
	Φ_1	Φ_2	Φ_3	Φ_4
0	0.000	0.000	0.000	0.000
1	0.241	0.836	1.000	-0.684
2	0.491	1.000	-0.114	1.000
3	0.745	0.273	-0.904	-0.747
4	1.000	-0.975	0.532	0.251

Table A.17 Transitory modal characteristics of the 4-story rocking wall building; Intensity 5 (PGA = 0.450 g)

Mode	1	2	3	4
Frequency, f_i (Hz)	0.331	9.261	25.490	40.410
Period, T_i (sec)	3.018	0.108	0.039	0.025
Damping Ratio, ξ_i (%)	1.000	5.000	5.000	5.000
Modal Participation Factor, Γ_i (-)	1.350	0.452	0.222	-0.095
Effective Modal Mass, $M_{e,i}$ (tons)	354.3	59.4	11.3	2.1
Fraction of Total Mass (%)	83.0%	13.9%	2.6%	0.5%
Floor Level	Mode Shapes			
	Φ_1	Φ_2	Φ_3	Φ_4
0	0.000	0.000	0.000	0.000
1	0.246	0.841	1.000	-0.682
2	0.496	1.000	-0.118	1.000
3	0.748	0.267	-0.906	-0.747
4	1.000	-0.984	0.533	0.251

Table A.18 Transitory modal characteristics of the 4-story rocking wall building; Intensity 6 (PGA = 0.675 g)

Mode	**1**	**2**	**3**	**4**
Frequency, f_i (Hz)	0.274	9.248	25.480	40.410
Period, T_i (sec)	3.647	0.108	0.039	0.025
Damping Ratio, ξ_i (%)	1.000	5.000	5.000	5.000
Modal Participation Factor, Γ_i (-)	1.350	0.450	0.222	-0.095
Effective Modal Mass, $M_{e,i}$ (tons)	354.6	59.1	11.2	2.1
Fraction of Total Mass (%)	83.1%	13.8%	2.6%	0.5%
Floor Level	**Mode Shapes**			
	Φ_1	**Φ_2**	**Φ_3**	**Φ_4**
0	0.000	0.000	0.000	0.000
1	0.248	0.842	1.000	-0.681
2	0.497	1.000	-0.119	1.000
3	0.748	0.266	-0.906	-0.747
4	1.000	-0.986	0.534	0.252

Table A.19 Transitory modal characteristics of the 8-story rocking wall building; Intensity 1 (PGA = 0.225 g)

Mode	1	2	3	4	5	6
Frequency, f_i (Hz)	0.285	4.051	11.630	20.790	29.770	37.450
Period, T_i (sec)	3.504	0.247	0.086	0.048	0.034	0.027
Damping Ratio, ξ_i (%)	1.000	5.000	5.000	5.000	5.000	5.000
Modal Participation Factor, Γ_i (-)	1.429	-0.592	0.275	-0.173	0.119	0.078
Effective Modal Mass, $M_{e,i}$ (tons)	1303.0	250.2	64.9	26.5	12.1	5.4
Fraction of Total Mass (%)	78.3%	15.0%	3.9%	1.6%	0.7%	0.3%
Floor Level	Mode Shapes					
	Φ_1	Φ_2	Φ_3	Φ_4	Φ_5	Φ_6
0	0.000	0.000	0.000	0.000	0.000	0.000
1	0.115	-0.390	0.748	-0.960	1.000	0.923
2	0.235	-0.699	1.000	-0.644	-0.083	-0.761
3	0.358	-0.849	0.579	0.533	-0.988	-0.290
4	0.484	-0.795	-0.222	1.000	0.180	1.000
5	0.612	-0.535	-0.843	0.142	0.982	-0.547
6	0.741	-0.105	-0.830	-0.865	-0.242	-0.565
7	0.870	0.430	-0.134	-0.609	-0.878	0.956
8	1.000	1.000	0.890	0.722	0.553	-0.416

Table A.20 Transitory modal characteristics of the 8-story rocking wall building; Intensity 5 (PGA = 0.450 g)

Mode	1	2	3	4	5	6
Frequency, f_i (Hz)	0.194	4.005	11.590	20.770	29.760	37.440
Period, T_i (sec)	5.163	0.250	0.086	0.048	0.034	0.027
Damping Ratio, ξ_i (%)	1.000	5.000	5.000	5.000	5.000	5.000
Modal Participation Factor, Γ_i (-)	1.425	-0.586	0.270	-0.171	0.117	0.078
Effective Modal Mass, $M_{e,i}$ (tons)	1313.0	242.8	63.2	26.0	11.8	5.3
Fraction of Total Mass (%)	78.9%	14.6%	3.8%	1.6%	0.7%	0.3%
Floor Level	Mode Shapes					
	Φ_1	Φ_2	Φ_3	Φ_4	Φ_5	Φ_6
0	0.000	0.000	0.000	0.000	0.000	0.000
1	0.120	-0.392	0.753	-0.960	1.000	0.922
2	0.243	-0.698	1.000	-0.639	-0.087	-0.762
3	0.367	-0.843	0.574	0.538	-0.989	-0.288
4	0.493	-0.785	-0.230	1.000	0.182	1.000
5	0.619	-0.523	-0.849	0.139	0.983	-0.549
6	0.746	-0.096	-0.832	-0.866	-0.243	-0.565
7	0.873	0.435	-0.132	-0.608	-0.879	0.956
8	1.000	1.000	0.894	0.723	0.554	-0.416

Table A.21 Transitory modal characteristics of the 8-story rocking wall building; Intensity 6 (PGA = 0.675 g)

Mode	**1**	**2**	**3**	**4**	**5**	**6**
Frequency, f_i (Hz)	0.159	3.993	11.580	20.770	29.750	37.440
Period, T_i (sec)	6.276	0.250	0.086	0.048	0.034	0.027
Damping Ratio, ξ_i (%)	1.000	5.000	5.000	5.000	5.000	5.000
Modal Participation Factor, Γ_i (-)	1.424	-0.584	0.269	-0.170	0.117	0.078
Effective Modal Mass, $M_{e,i}$ (tons)	1316.0	240.7	62.8	25.8	11.8	5.3
Fraction of Total Mass (%)	79.0%	14.5%	3.8%	1.6%	0.7%	0.3%
Floor Level	**Mode Shapes**					
	Φ_1	**Φ_2**	**Φ_3**	**Φ_4**	**Φ_5**	**Φ_6**
0	0.000	0.000	0.000	0.000	0.000	0.000
1	0.122	-0.393	0.754	-0.960	1.000	0.921
2	0.245	-0.698	1.000	-0.637	-0.088	-0.763
3	0.370	-0.841	0.572	0.539	-0.990	-0.288
4	0.495	-0.782	-0.232	1.000	0.183	1.000
5	0.621	-0.520	-0.850	0.139	0.983	-0.549
6	0.747	-0.093	-0.832	-0.867	-0.244	-0.565
7	0.874	0.437	-0.132	-0.608	-0.879	0.956
8	1.000	1.000	0.895	0.723	0.554	-0.416

Table A.22 Transitory modal characteristics of the 12-story rocking wall building; Intensity 1 (PGA = 0.225 g)

Mode	1	2	3	4	5	6
Frequency, f_i (Hz)	0.229	2.789	8.141	15.040	22.430	29.630
Period, T_i (sec)	4.358	0.359	0.123	0.067	0.045	0.034
Damping Ratio, ξ_i (%)	1.000	5.000	5.000	5.000	5.000	5.000
Modal Participation Factor, Γ_i (-)	1.460	-0.650	0.296	0.191	0.136	-0.103
Effective Modal Mass, $M_{e,i}$ (tons)	1949.0	390.5	106.5	47.3	24.9	14.2
Fraction of Total Mass (%)	76.4%	15.3%	4.2%	1.9%	1.0%	0.6%
Floor Level	**Mode Shapes**					
	Φ_1	**Φ_2**	**Φ_3**	**Φ_4**	**Φ_5**	**Φ_6**
0	0.000	0.000	0.000	0.000	0.000	0.000
1	0.073	-0.245	0.518	0.736	0.904	-0.991
2	0.150	-0.472	0.880	1.000	0.844	-0.444
3	0.229	-0.652	0.965	0.613	-0.121	0.792
4	0.310	-0.764	0.744	-0.174	-0.953	0.790
5	0.393	-0.792	0.289	-0.848	-0.754	-0.446
6	0.478	-0.730	-0.252	-0.967	0.261	-0.985
7	0.563	-0.580	-0.696	-0.459	1.000	0.017
8	0.650	-0.351	-0.894	0.336	0.672	1.000
9	0.737	-0.058	-0.766	0.881	-0.358	0.440
10	0.825	0.278	-0.332	0.792	-0.952	-0.766
11	0.912	0.637	0.305	0.075	-0.414	-0.681
12	1.000	1.000	1.000	-0.897	0.793	0.682

Table A.23 Transitory modal characteristics of the 12-story rocking wall building; Intensity 5 (PGA = 0.450 g)

Mode	1	2	3	4	5	6
Frequency, f_i (Hz)	0.152	2.740	8.099	15.010	22.410	29.620
Period, T_i (sec)	6.599	0.365	0.124	0.067	0.045	0.034
Damping Ratio, ξ_i (%)	1.000	5.000	5.000	5.000	5.000	5.000
Modal Participation Factor, Γ_i (-)	1.453	-0.640	0.292	0.187	0.134	-0.102
Effective Modal Mass, $M_{e,i}$ (tons)	1972.0	374.0	102.6	46.0	24.3	13.9
Fraction of Total Mass (%)	77.3%	14.7%	4.0%	1.8%	1.0%	0.5%
Floor Level	**Mode Shapes**					
	Φ_1	**Φ_2**	**Φ_3**	**Φ_4**	**Φ_5**	**Φ_6**
0	0.000	0.000	0.000	0.000	0.000	0.000
1	0.079	-0.249	0.521	0.740	0.903	-0.990
2	0.159	-0.475	0.879	1.000	0.838	-0.439
3	0.241	-0.651	0.958	0.607	-0.128	0.795
4	0.323	-0.758	0.732	-0.184	-0.954	0.788
5	0.406	-0.782	0.276	-0.856	-0.751	-0.448
6	0.490	-0.717	-0.262	-0.970	0.265	-0.984
7	0.575	-0.565	-0.702	-0.456	1.000	0.020
8	0.659	-0.336	-0.894	0.341	0.669	1.000
9	0.744	-0.045	-0.763	0.886	-0.360	0.438
10	0.830	0.287	-0.329	0.794	-0.952	-0.766
11	0.915	0.642	0.307	0.074	-0.413	-0.681
12	1.000	1.000	1.000	-0.901	0.793	0.682

Table A.24 Transitory modal characteristics of the 12-story rocking wall building; Intensity 6 (PGA = 0.675 g)

Mode	1	2	3	4	5	6
Frequency, f_i (Hz)	0.122	2.728	8.089	15.000	22.410	29.620
Period, T_i (sec)	8.174	0.367	0.124	0.067	0.045	0.034
Damping Ratio, ξ_i (%)	1.000	5.000	5.000	5.000	5.000	5.000
Modal Participation Factor, Γ_i (-)	1.451	-0.638	0.290	0.187	0.134	-0.102
Effective Modal Mass, $M_{e,i}$ (tons)	1978.0	369.6	101.6	45.6	24.1	13.9
Fraction of Total Mass (%)	77.5%	14.5%	4.0%	1.8%	0.9%	0.5%
Floor Level	**Mode Shapes**					
	Φ_1	**Φ_2**	**Φ_3**	**Φ_4**	**Φ_5**	**Φ_6**
0	0.000	0.000	0.000	0.000	0.000	0.000
1	0.080	-0.250	0.522	0.741	0.903	-0.989
2	0.162	-0.475	0.879	1.000	0.836	-0.437
3	0.244	-0.651	0.956	0.605	-0.130	0.796
4	0.327	-0.757	0.729	-0.187	-0.955	0.787
5	0.410	-0.780	0.272	-0.858	-0.750	-0.449
6	0.494	-0.714	-0.264	-0.971	0.266	-0.983
7	0.578	-0.561	-0.703	-0.456	1.000	0.020
8	0.662	-0.332	-0.894	0.343	0.668	1.000
9	0.746	-0.042	-0.762	0.887	-0.360	0.438
10	0.831	0.290	-0.328	0.795	-0.951	-0.766
11	0.915	0.643	0.307	0.074	-0.413	-0.680
12	1.000	1.000	1.000	-0.902	0.793	0.682

A.3 Approximate Elastic Modal Characteristics from Continuous Distributed-mass Beams

Table A.25 Approximate elastic modal characteristics of the 4-story RC wall building idealized as a continuous cantilever beam

Mode	**1**	**2**	**3**	**4**
Frequency, f_i (Hz)	0.790	4.951	13.862	27.167
Period, T_i (sec)	1.266	0.202	0.072	0.037
Modal Participation Factor, Γ_i (-)	1.364	0.215	0.607	-0.140
Floor Level	**Mode Shapes**			
	Φ_1	**Φ_2**	**Φ_3**	**Φ_4**
0	0.000	0.000	0.000	0.000
1	0.097	0.417	0.724	0.685
2	0.340	0.714	0.020	-0.707
3	0.658	0.135	-0.581	0.621
4	1.000	-1.000	1.000	-1.000

Table A.26 Approximate elastic modal characteristics of the 8-story RC wall building idealized as a continuous cantilever beam

Mode	**1**	**2**	**3**	**4**	**5**	**6**
Frequency, f_i (Hz)	0.403	2.526	7.072	13.859	22.908	34.220
Period, T_i (sec)	2.481	0.396	0.141	0.072	0.044	0.029
Modal Participation Factor, Γ_i (-)	1.455	0.497	0.589	0.068	0.414	-0.057
Floor Level	**Mode Shapes**					
	Φ_1	**Φ_2**	**Φ_3**	**Φ_4**	**Φ_5**	**Φ_6**
0	0.000	0.000	0.000	0.000	0.000	0.000
1	0.026	0.138	0.325	0.519	0.673	0.751
2	0.097	0.417	0.724	0.685	0.285	-0.264
3	0.205	0.654	0.618	-0.130	-0.691	-0.392
4	0.340	0.714	0.020	-0.707	0.001	0.707
5	0.493	0.534	-0.558	-0.145	0.696	-0.394
6	0.658	0.135	-0.581	0.621	-0.256	-0.277
7	0.828	-0.407	0.050	0.266	-0.502	0.636
8	1.000	-1.000	1.000	-1.000	1.000	-1.000

Table A.27 Approximate elastic modal characteristics of the 12-story RC wall building idealized as a continuous cantilever beam

Mode	1	2	3	4	5	6
Frequency, f_i (Hz)	0.268	1.679	4.701	9.213	15.229	22.749
Period, T_i (sec)	3.733	0.596	0.213	0.109	0.066	0.044
Modal Participation Factor, Γ_i (-)	1.491	0.617	0.567	0.166	0.377	0.041
Floor Level	**Mode Shapes**					
	Φ_1	**Φ_2**	**Φ_3**	**Φ_4**	**Φ_5**	**Φ_6**
0	0.000	0.000	0.000	0.000	0.000	0.000
1	0.012	0.066	0.168	0.292	0.425	0.549
2	0.045	0.225	0.489	0.692	0.754	0.640
3	0.097	0.417	0.724	0.685	0.285	-0.264
4	0.166	0.590	0.722	0.195	-0.495	-0.681
5	0.247	0.698	0.454	-0.426	-0.652	0.093
6	0.340	0.714	0.020	-0.707	0.001	0.707
7	0.440	0.621	-0.406	-0.434	0.655	0.092
8	0.547	0.423	-0.644	0.171	0.505	-0.685
9	0.658	0.135	-0.581	0.621	-0.256	-0.277
10	0.771	-0.216	-0.218	0.532	-0.660	0.584
11	0.885	-0.603	0.353	-0.108	-0.117	0.312
12	1.000	-1.000	1.000	-1.000	1.000	-1.000

Table A.28 Approximate elastic modal characteristics of the 4-story rocking wall building idealized as a fully-pinned continuous cantilever beam

Mode	**1**	**2**	**3**	**4**
Frequency, f_i (Hz)	0.956	11.963	38.767	80.888
Period, T_i (sec)	1.046	0.084	0.026	0.012
Modal Participation Factor, Γ_i (-)	1.349	0.116	0.497	-0.273
Floor Level	**Mode Shapes**			
	Φ_1	**Φ_2**	**Φ_3**	**Φ_4**
0	0.000	0.000	0.000	0.000
1	0.250	0.566	0.696	0.393
2	0.500	0.585	-0.256	-0.656
3	0.750	-0.049	-0.503	0.655
4	1.000	-1.000	1.000	-1.000

Table A.29 Approximate elastic modal characteristics of the 8-story rocking wall building idealized as a fully-pinned continuous cantilever beam

Mode	**1**	**2**	**3**	**4**	**5**	**6**
Frequency, f_i (Hz)	0.500	4.609	14.935	31.162	53.288	81.315
Period, T_i (sec)	2.002	0.217	0.067	0.032	0.019	0.012
Modal Participation Factor, Γ_i (-)	1.421	0.392	0.485	-0.022	0.328	-0.140
Floor Level	**Mode Shapes**					
	Φ_1	**Φ_2**	**Φ_3**	**Φ_4**	**Φ_5**	**Φ_6**
0	0.000	0.000	0.000	0.000	0.000	0.000
1	0.125	0.323	0.548	0.677	0.704	0.624
2	0.250	0.566	0.696	0.393	-0.138	-0.588
3	0.375	0.663	0.339	-0.449	-0.677	-0.069
4	0.500	0.585	-0.256	-0.656	0.271	0.653
5	0.625	0.335	-0.641	0.058	0.627	-0.548
6	0.750	-0.049	-0.503	0.655	-0.375	-0.146
7	0.875	-0.511	0.137	0.194	-0.452	0.613
8	1.000	-1.000	1.000	-1.000	1.000	-1.000

Table A.30 Approximate elastic modal characteristics of the 12-story rocking wall building idealized as a fully-pinned continuous cantilever beam

Mode	1	2	3	4	5	6
Frequency, f_i (Hz)	0.329	3.004	9.735	20.312	34.735	53.003
Period, T_i (sec)	3.040	0.333	0.103	0.049	0.029	0.019
Modal Participation Factor, Γ_i (-)	1.448	0.505	0.464	0.081	0.300	-0.029
Floor Level	Mode Shapes					
	Φ_1	Φ_2	Φ_3	Φ_4	Φ_5	Φ_6
0	0.000	0.000	0.000	0.000	0.000	0.000
1	0.083	0.221	0.393	0.532	0.634	0.694
2	0.167	0.417	0.655	0.701	0.561	0.271
3	0.250	0.566	0.696	0.393	-0.138	-0.588
4	0.333	0.649	0.505	-0.184	-0.683	-0.500
5	0.417	0.657	0.146	-0.635	-0.466	0.393
6	0.500	0.585	-0.256	-0.656	0.271	0.653
7	0.583	0.436	-0.562	-0.234	0.707	-0.138
8	0.667	0.219	-0.660	0.337	0.359	-0.709
9	0.750	-0.049	-0.503	0.655	-0.375	-0.146
10	0.833	-0.352	-0.117	0.470	-0.647	0.621
11	0.917	-0.673	0.415	-0.167	-0.063	0.266
12	1.000	-1.000	1.000	-1.000	1.000	-1.000

Table A.31 Approximate elastic modal characteristics of the 4-story rocking wall building idealized as a spring-hinged continuous cantilever beam

Mode	1	2	3	4
Frequency, f_i (Hz)	0.956	12.354	39.197	81.323
Period, T_i (sec)	1.046	0.081	0.026	0.012
Modal Participation Factor, Γ_i (-)	1.356	0.136	0.504	-0.266
Floor Level	Mode Shapes			
	Φ_1	Φ_2	Φ_3	Φ_4
0	0.000	0.000	0.000	0.000
1	0.229	0.564	0.704	0.406
2	0.479	0.603	-0.243	-0.660
3	0.738	-0.031	-0.507	0.654
4	1.000	-1.000	1.000	-1.000

Table A.32 Approximate elastic modal characteristics of the 8-story rocking wall building idealized as a spring-hinged continuous cantilever beam

Mode	**1**	**2**	**3**	**4**	**5**	**6**
Frequency, f_i (Hz)	0.500	4.899	15.263	31.506	53.637	81.668
Period, T_i (sec)	2.002	0.204	0.066	0.032	0.019	0.012
Modal Participation Factor, Γ_i (-)	1.438	0.430	0.501	-0.011	0.334	-0.134
Floor Level	**Mode Shapes**					
	Φ_1	**Φ_2**	**Φ_3**	**Φ_4**	**Φ_5**	**Φ_6**
0	0.000	0.000	0.000	0.000	0.000	0.000
1	0.100	0.308	0.538	0.676	0.711	0.636
2	0.212	0.561	0.712	0.419	-0.115	-0.577
3	0.333	0.680	0.372	-0.429	-0.681	-0.084
4	0.461	0.618	-0.230	-0.662	0.257	0.657
5	0.593	0.374	-0.636	0.045	0.631	-0.541
6	0.728	-0.016	-0.511	0.652	-0.369	-0.151
7	0.864	-0.493	0.129	0.198	-0.454	0.613
8	1.000	-1.000	1.000	-1.000	1.000	-1.000

Table A.33 Approximate elastic modal characteristics of the 12-story rocking wall building idealized as a spring-hinged continuous cantilever beam

Mode	**1**	**2**	**3**	**4**	**5**	**6**
Frequency, f_i (Hz)	0.329	3.198	9.954	20.536	34.962	53.233
Period, T_i (sec)	3.040	0.313	0.100	0.049	0.029	0.019
Modal Participation Factor, Γ_i (-)	1.468	0.545	0.483	0.093	0.307	-0.023
Floor Level	**Mode Shapes**					
	Φ_1	**Φ_2**	**Φ_3**	**Φ_4**	**Φ_5**	**Φ_6**
0	0.000	0.000	0.000	0.000	0.000	0.000
1	0.065	0.206	0.381	0.524	0.631	0.695
2	0.136	0.403	0.652	0.712	0.580	0.292
3	0.212	0.561	0.712	0.420	-0.114	-0.577
4	0.291	0.659	0.535	-0.156	-0.677	-0.512
5	0.374	0.681	0.180	-0.624	-0.479	0.380
6	0.460	0.619	-0.229	-0.663	0.257	0.658
7	0.548	0.475	-0.548	-0.250	0.707	-0.128
8	0.637	0.259	-0.660	0.326	0.368	-0.709
9	0.727	-0.015	-0.511	0.653	-0.369	-0.152
10	0.818	-0.328	-0.127	0.475	-0.648	0.620
11	0.909	-0.661	0.409	-0.163	-0.066	0.268
12	1.000	-1.000	1.000	-1.000	1.000	-1.000

APPENDIX B. ADDITIONAL FLOOR RESPONSE SPECTRA RESULTS

This appendix presents additional information for Section 5.3, which discussed the main observations that were made from floor spectra obtained from the time history analysis of the case study buildings. Sections B.1 and B.2 provide information regarding the influence of non-structural damping and inelastic structural response, respectively, on spectral acceleration demands. Section B.3 provides comparisons between mean NSE accelerations from coupled NLTHA and mean floor spectra from uncoupled NLTHA

B.1 Influence of Non-structural Damping on Spectral Acceleration Demands

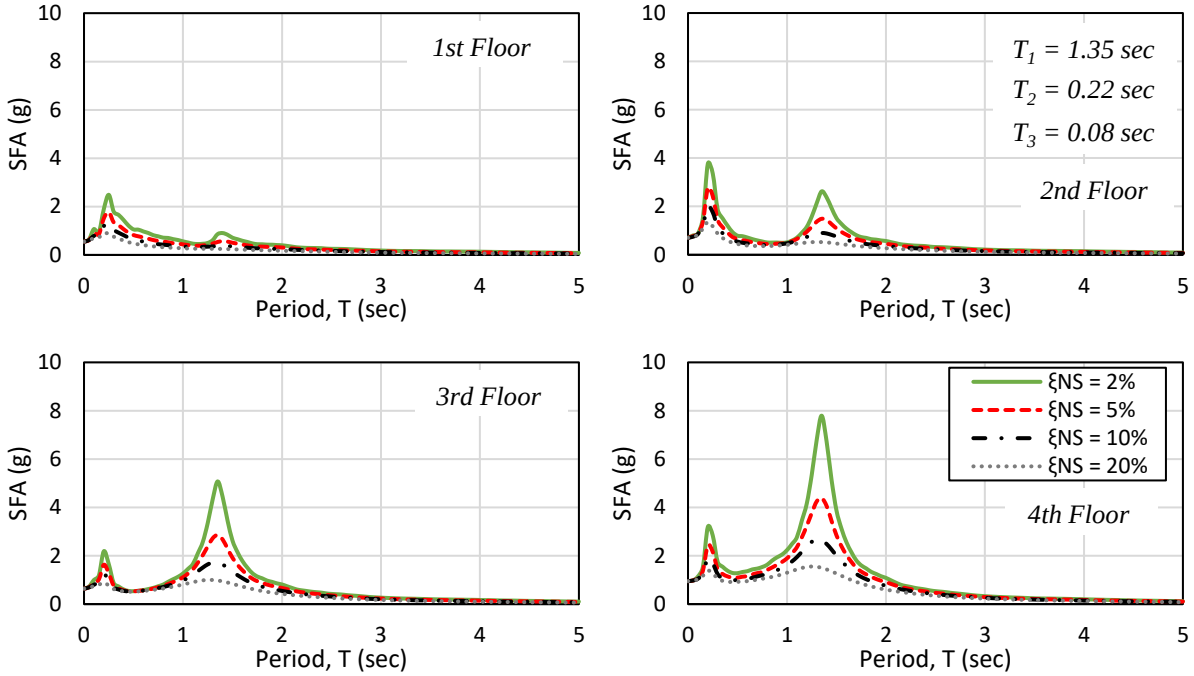

Figure B.1 Mean floor response spectra atop 4-story RC wall building for fully elastic structural response at Intensity 5 (PGA = 0.450 g)

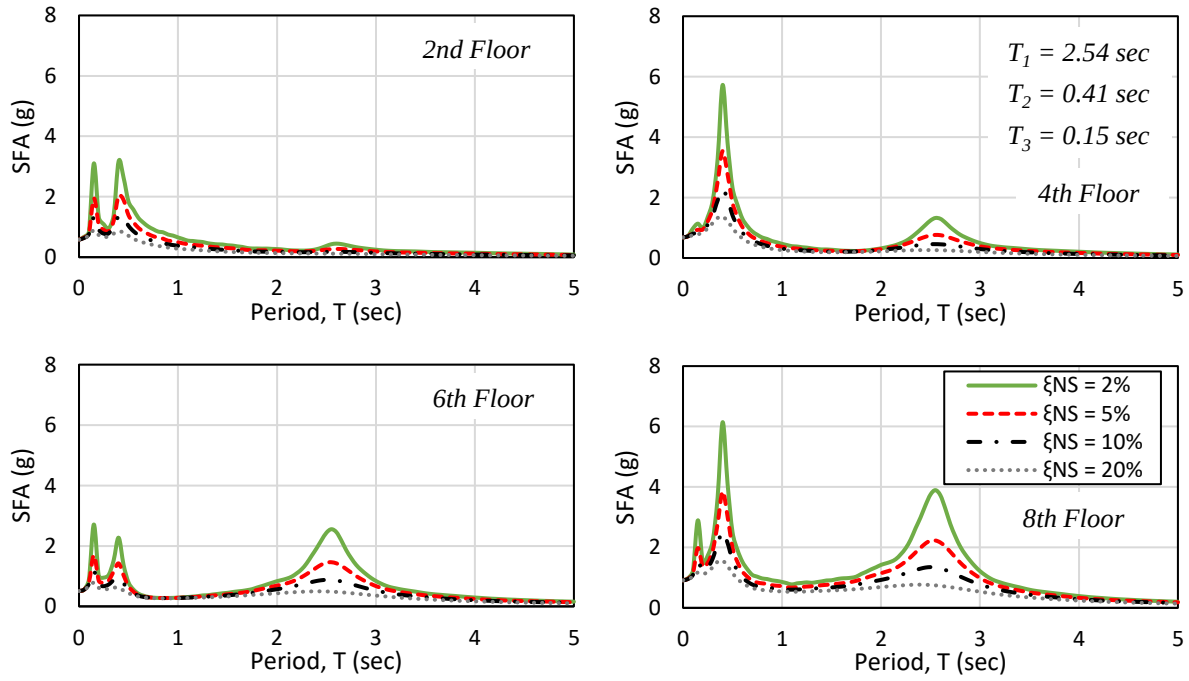

Figure B.2 Mean floor response spectra atop 8-story RC wall building for fully elastic structural response at Intensity 5 (PGA = 0.450 g)

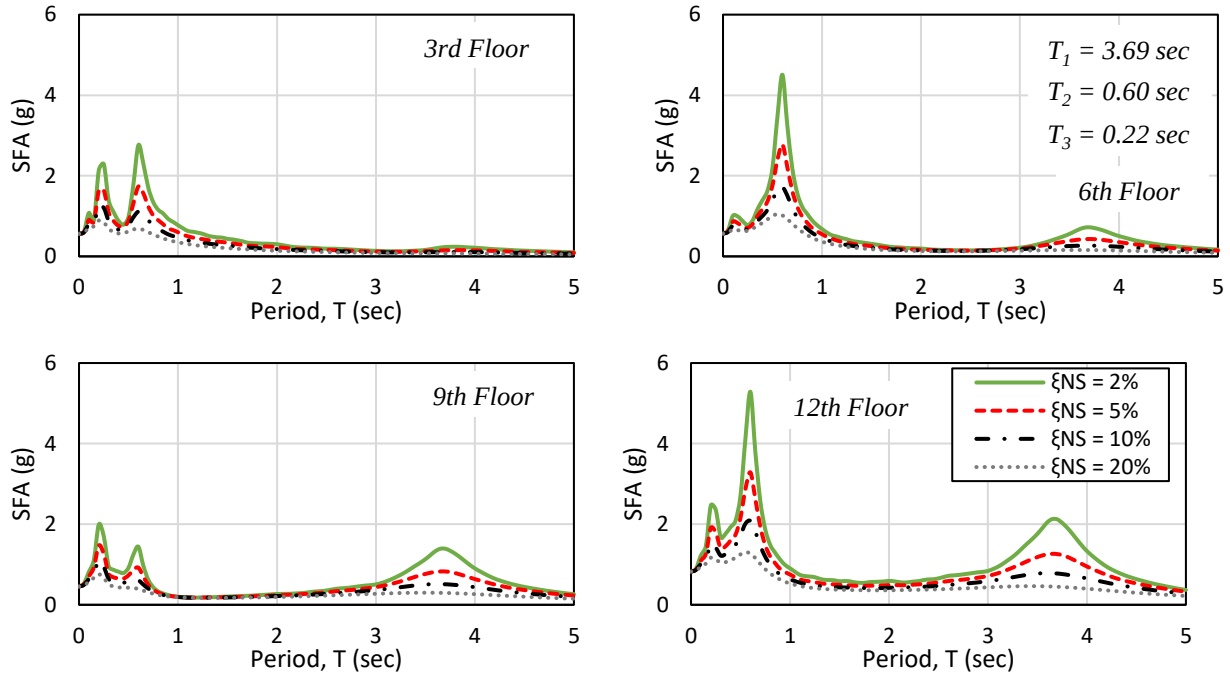

Figure B.3 Mean floor response spectra atop 12-story RC wall building for fully elastic structural response at Intensity 5 (PGA = 0.450 g)

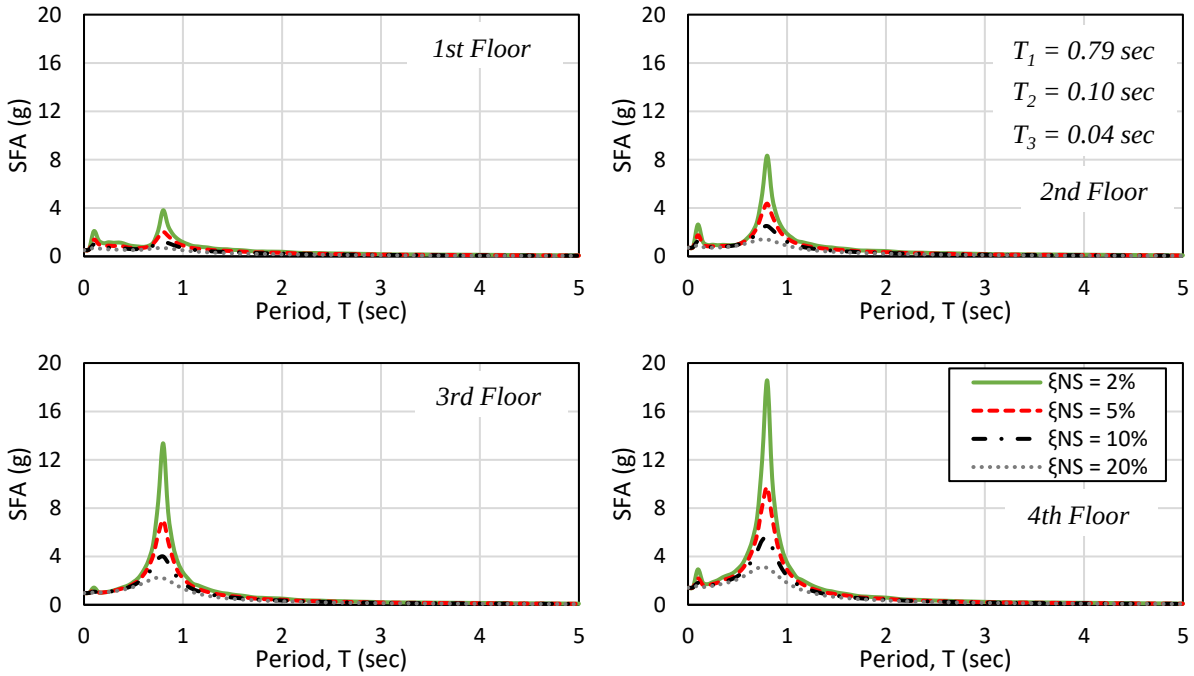

Figure B.4 Mean floor response spectra atop 4-story rocking wall building for fully elastic structural response at Intensity 5 (PGA = 0.450 g)

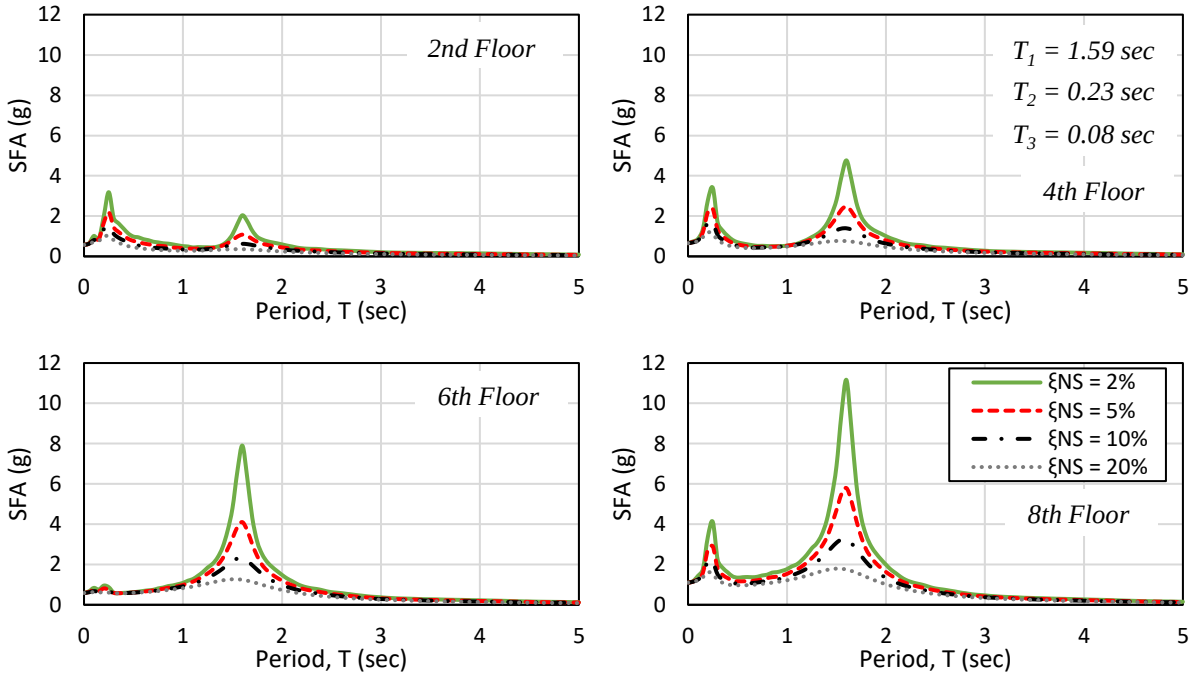

Figure B.5 Mean floor response spectra atop 8-story rocking wall building for fully elastic structural response at Intensity 5 (PGA = 0.450 g)

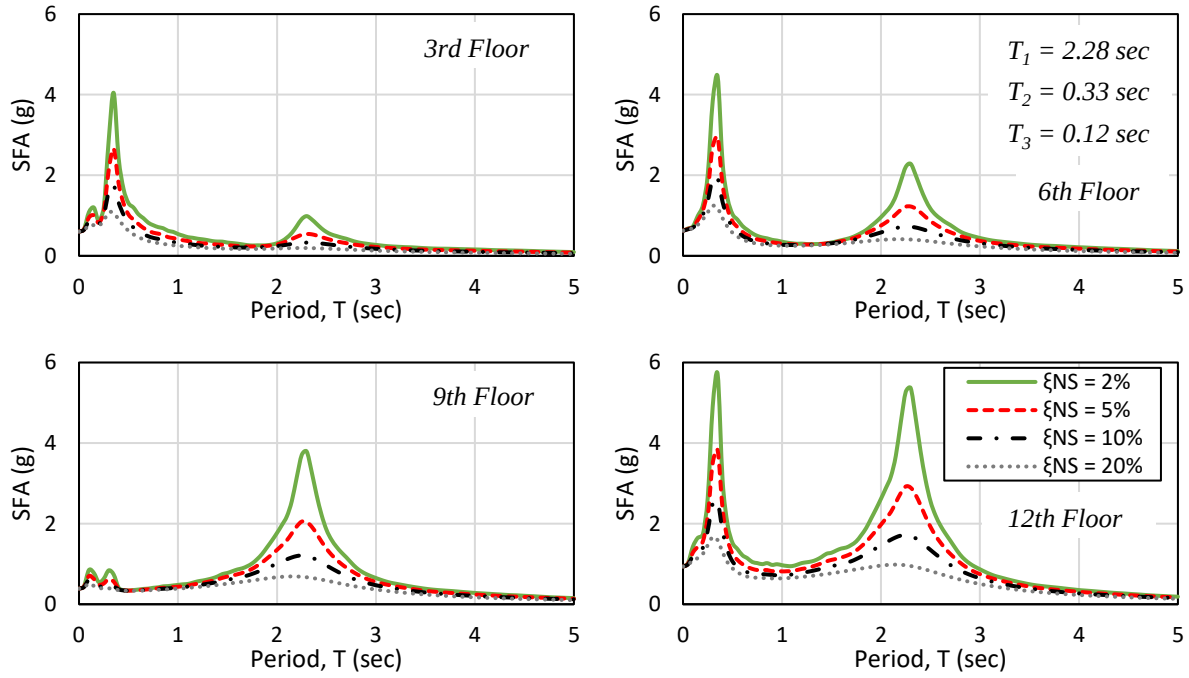

Figure B.6 Mean floor response spectra atop 12-story rocking wall building for fully elastic structural response at Intensity 5 (PGA = 0.450 g)

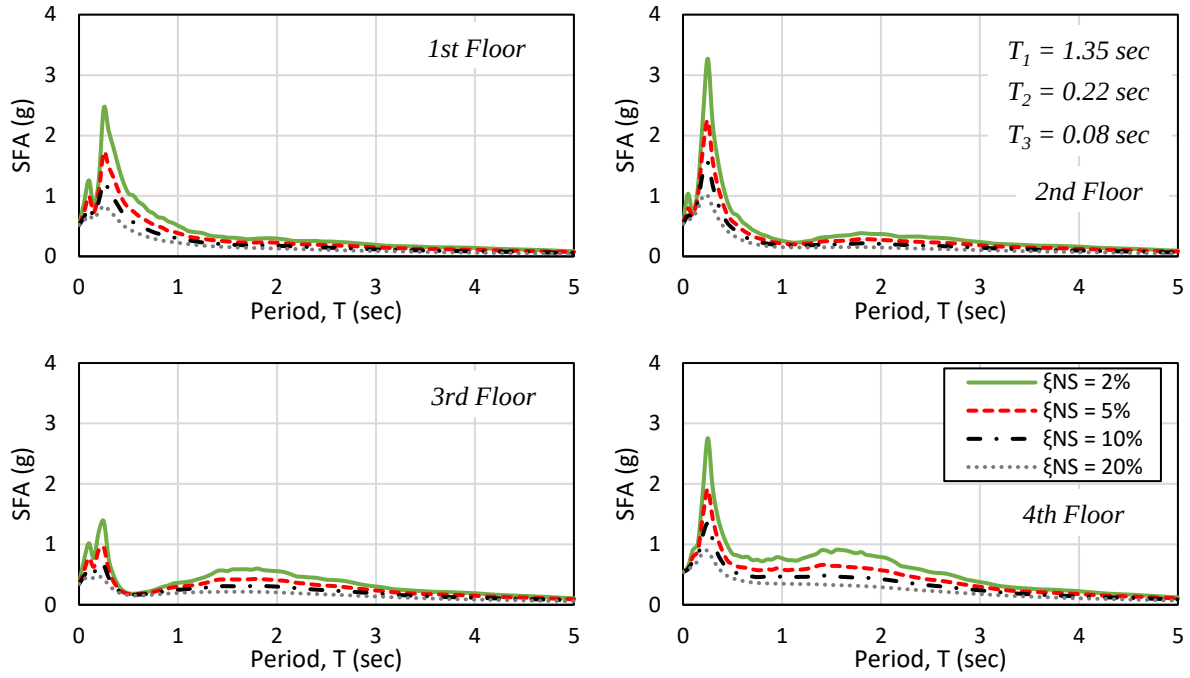

Figure B.7 Mean floor response spectra atop 4-story RC wall building for inelastic structural response at Intensity 5 (PGA = 0.450 g)

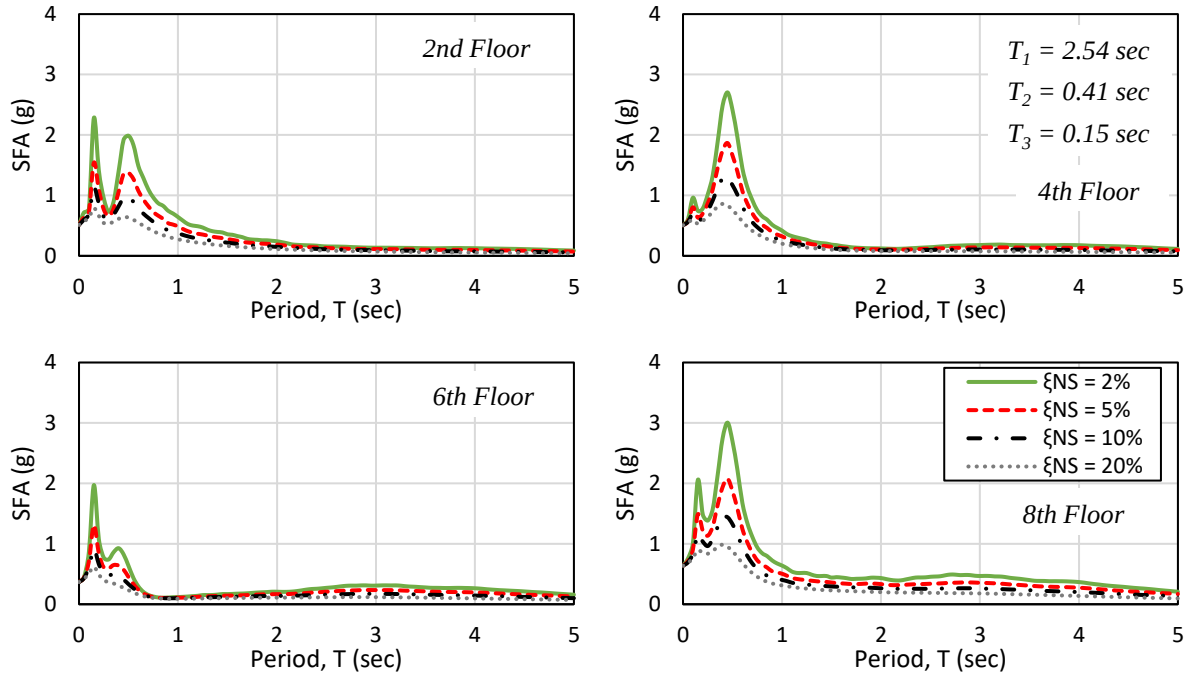

Figure B.8 Mean floor response spectra atop 8-story RC wall building for inelastic structural response at Intensity 5 (PGA = 0.450 g)

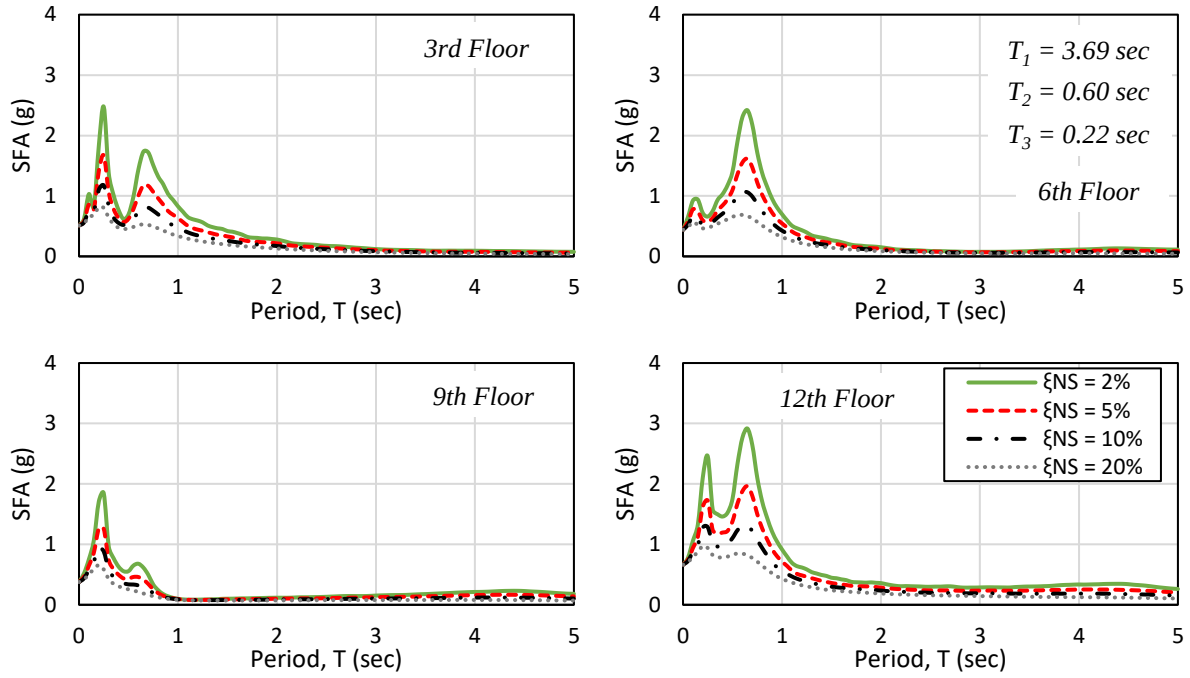

Figure B.9 Mean floor response spectra atop 12-story RC wall building for inelastic structural response at Intensity 5 (PGA = 0.450 g)

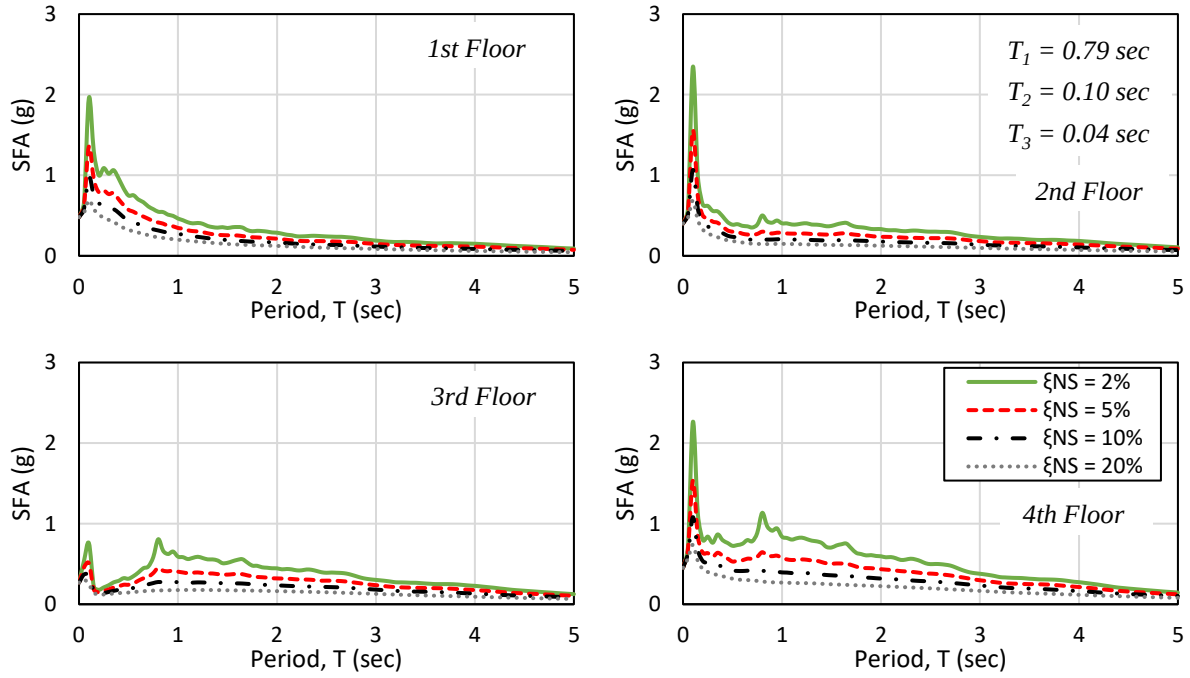

Figure B.10 Mean floor response spectra atop 4-story rocking wall building for inelastic structural response at Intensity 5 (PGA = 0.450 g)

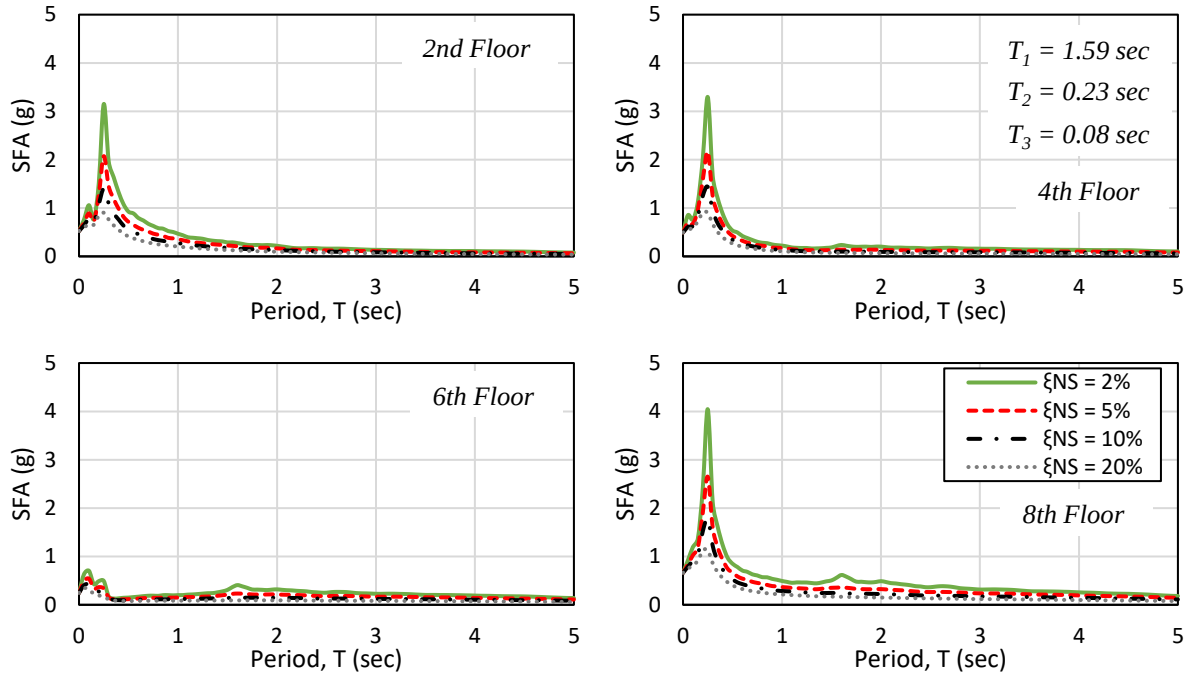

Figure B.11 Mean floor response spectra atop 8-story rocking wall building for inelastic structural response at Intensity 5 (PGA = 0.450 g)

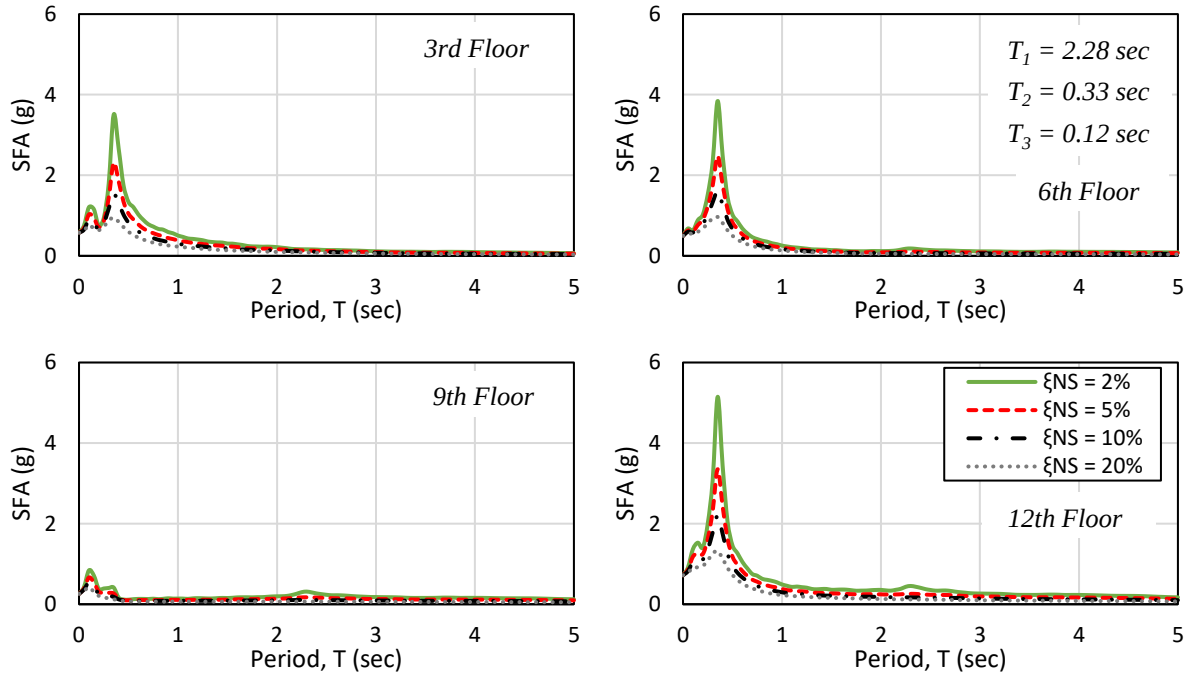

Figure B.12 Mean floor response spectra atop 12-story rocking wall building for inelastic structural response at Intensity 5 (PGA = 0.450 g)

B.2 Influence of Inelastic Structural Response on Spectral Acceleration Demands

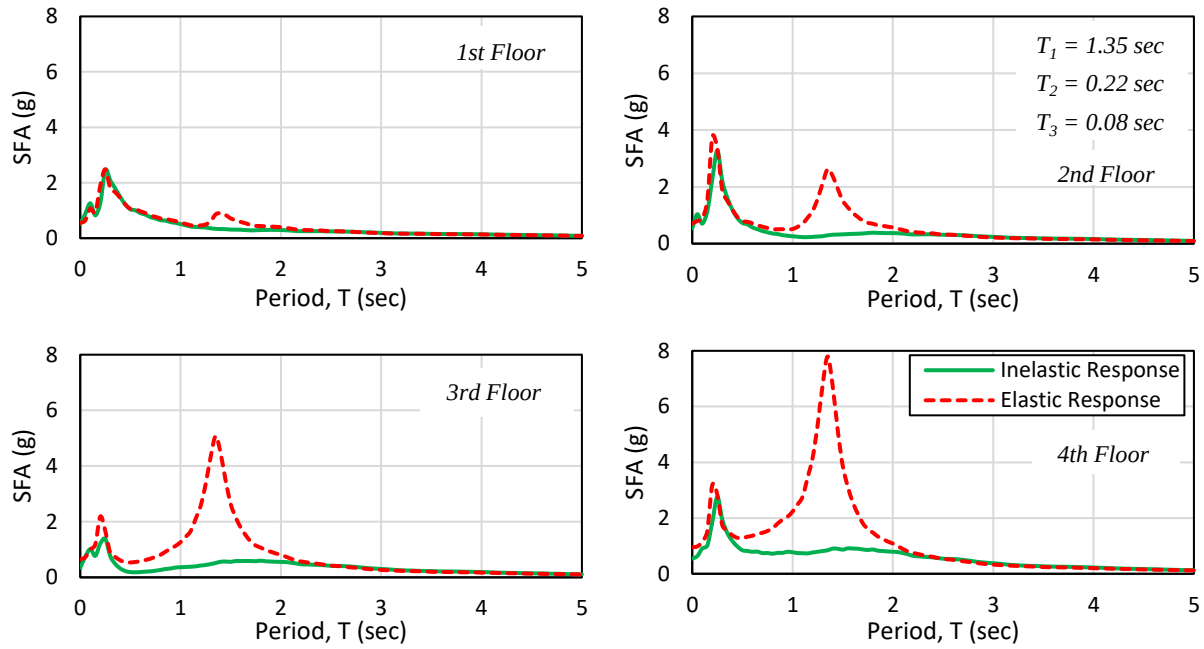

Figure B.13 Mean floor response spectra atop 4-story RC wall for fully elastic and inelastic structural response at Intensity 5 (PGA = 0.450 g); ξ_{NS} = 2%

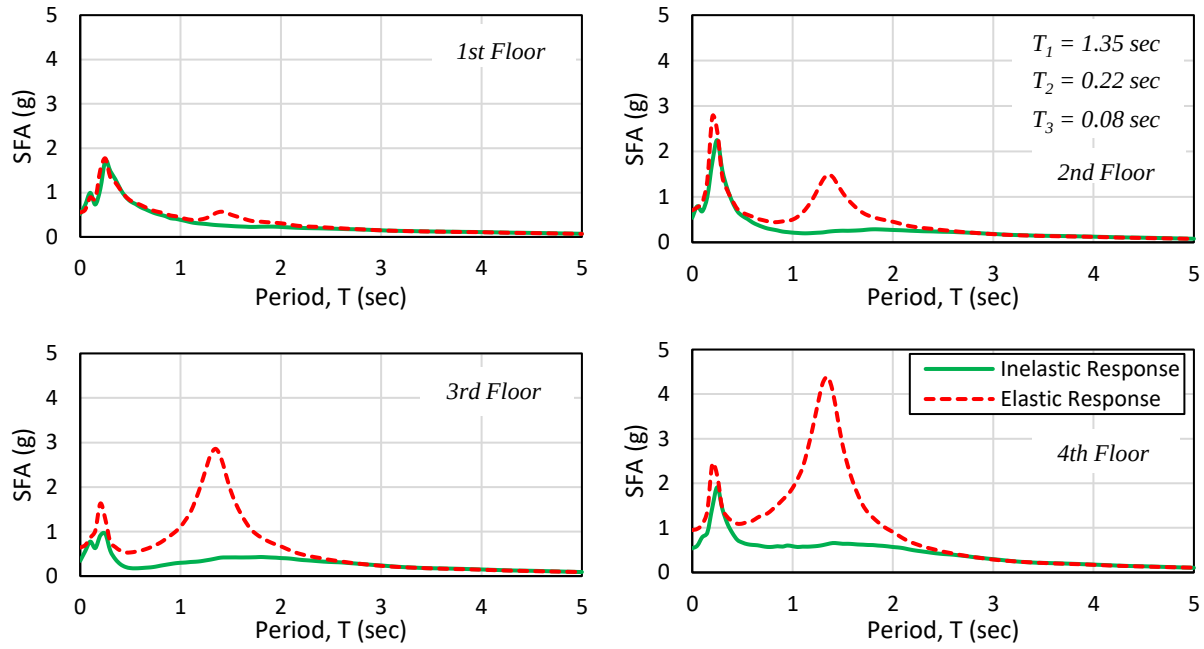

Figure B.14 Mean floor response spectra atop 4-story RC wall for fully elastic and inelastic structural response at Intensity 5 (PGA = 0.450 g); ξ_{NS} = 5%

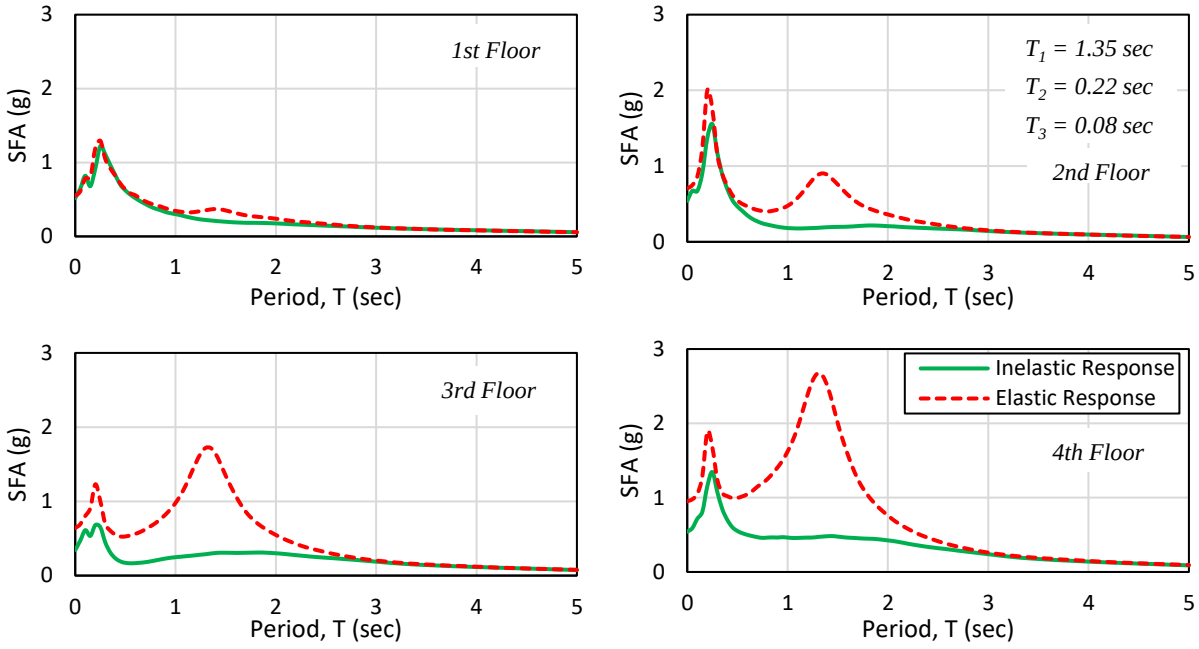

Figure B.15 Mean floor response spectra atop 4-story RC wall for fully elastic and inelastic structural response at Intensity 5 (PGA = 0.450 g); ξ_{NS} = 10%

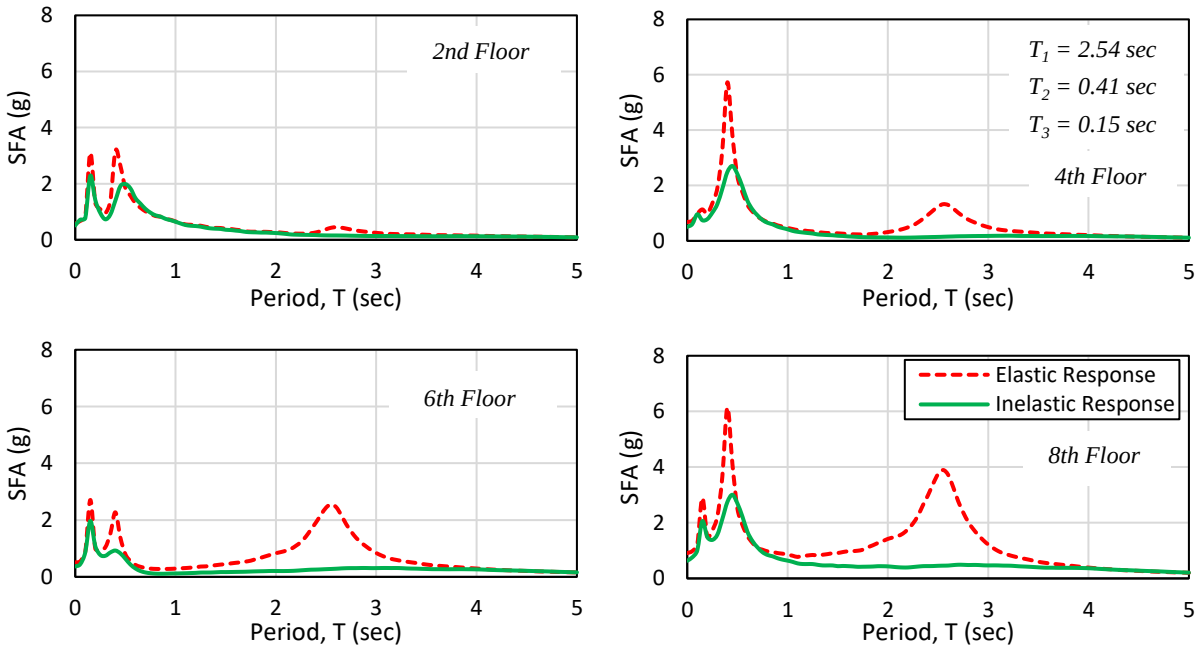

Figure B.16 Mean floor response spectra atop 8-story RC wall for fully elastic and inelastic structural response at Intensity 5 (PGA = 0.450 g); ξ_{NS} = 2%

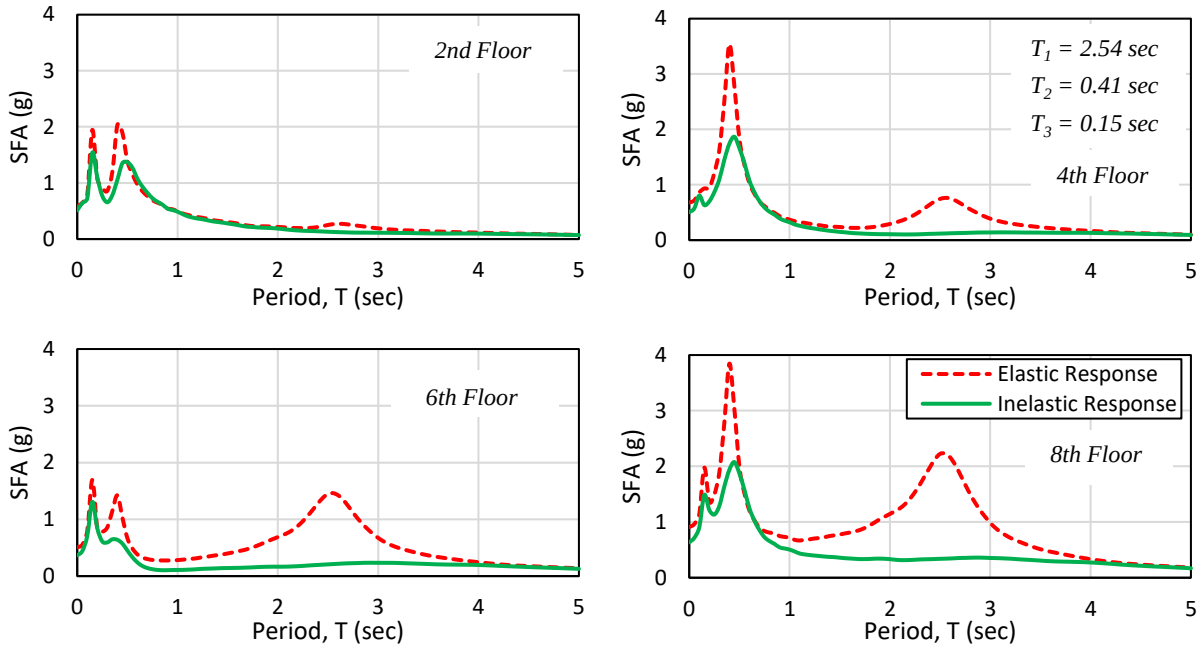

Figure B.17 Mean floor response spectra atop 8-story RC wall for fully elastic and inelastic structural response at Intensity 5 (PGA = 0.450 g); ξ_{NS} = 5%

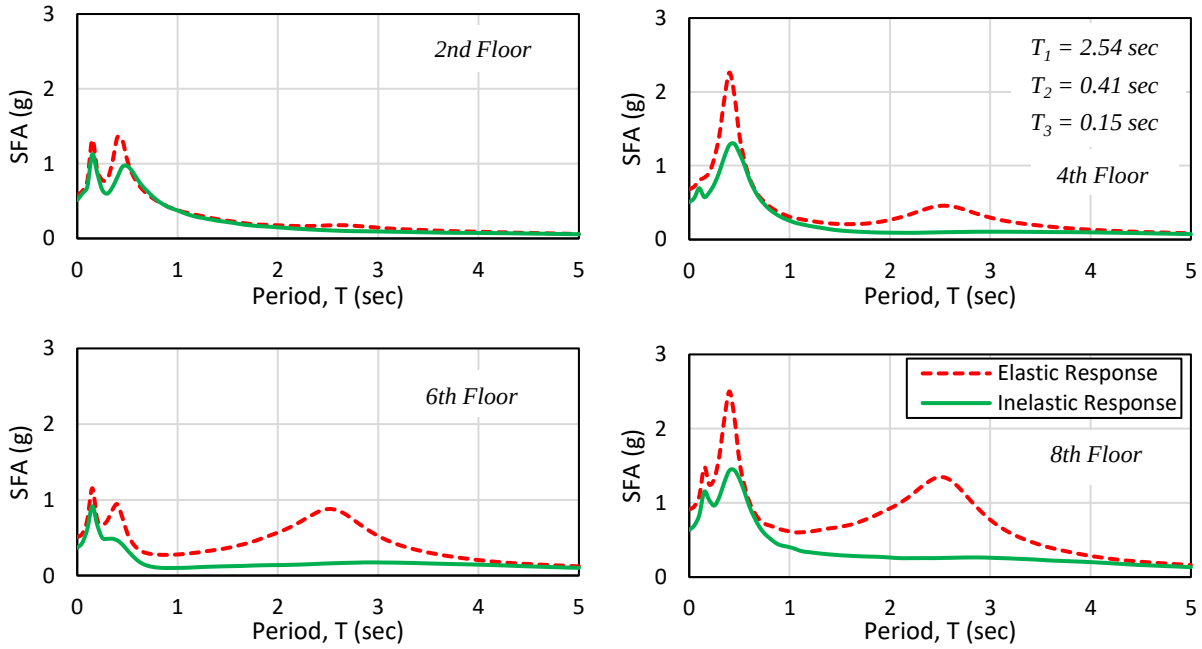

Figure B.18 Mean floor response spectra atop 8-story RC wall for fully elastic and inelastic structural response at Intensity 5 (PGA = 0.450 g); ξ_{NS} = 10%

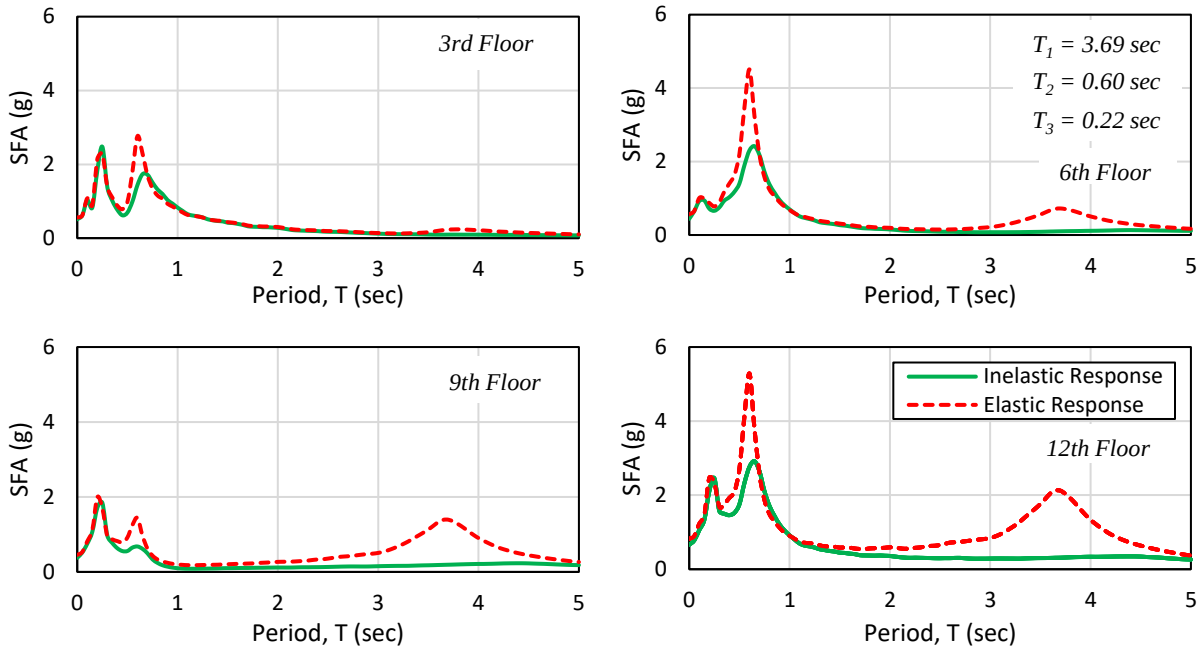

Figure B.19 Mean floor response spectra atop 12-story RC wall for fully elastic and inelastic structural response at Intensity 5 (PGA = 0.450 g); ξ_{NS} = 2%

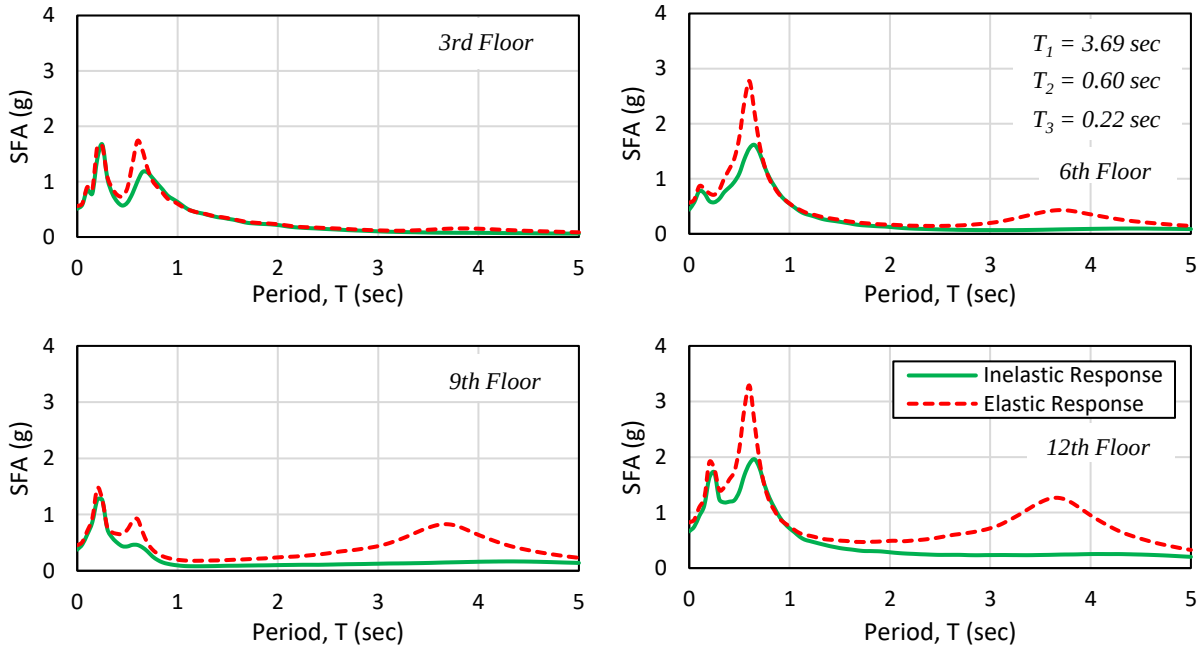

Figure B.20 Mean floor response spectra atop 12-story RC wall for fully elastic and inelastic structural response at Intensity 5 (PGA = 0.450 g); ξ_{NS} = 5%

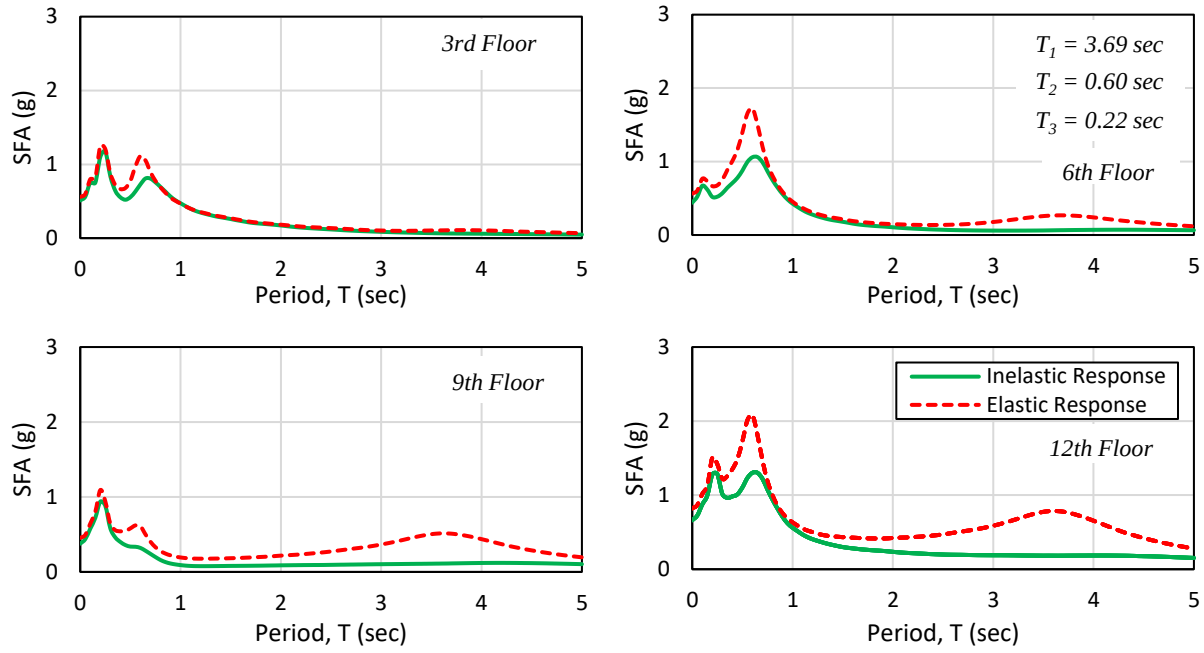

Figure B.21 Mean floor response spectra atop 12-story RC wall for fully elastic and inelastic structural response at Intensity 5 (PGA = 0.450 g); ξ_{NS} = 10%

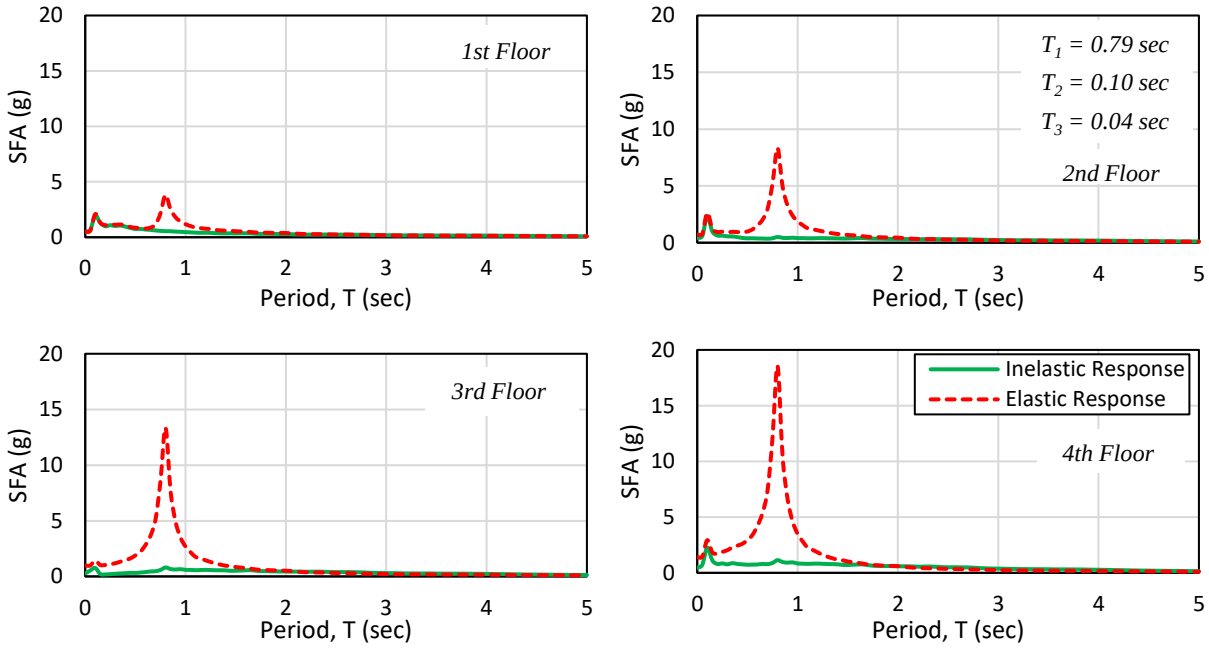

Figure B.22 Mean floor response spectra atop 4-story rocking wall for fully elastic and inelastic structural response at Intensity 5 (PGA = 0.450 g); ξ_{NS} = 2%

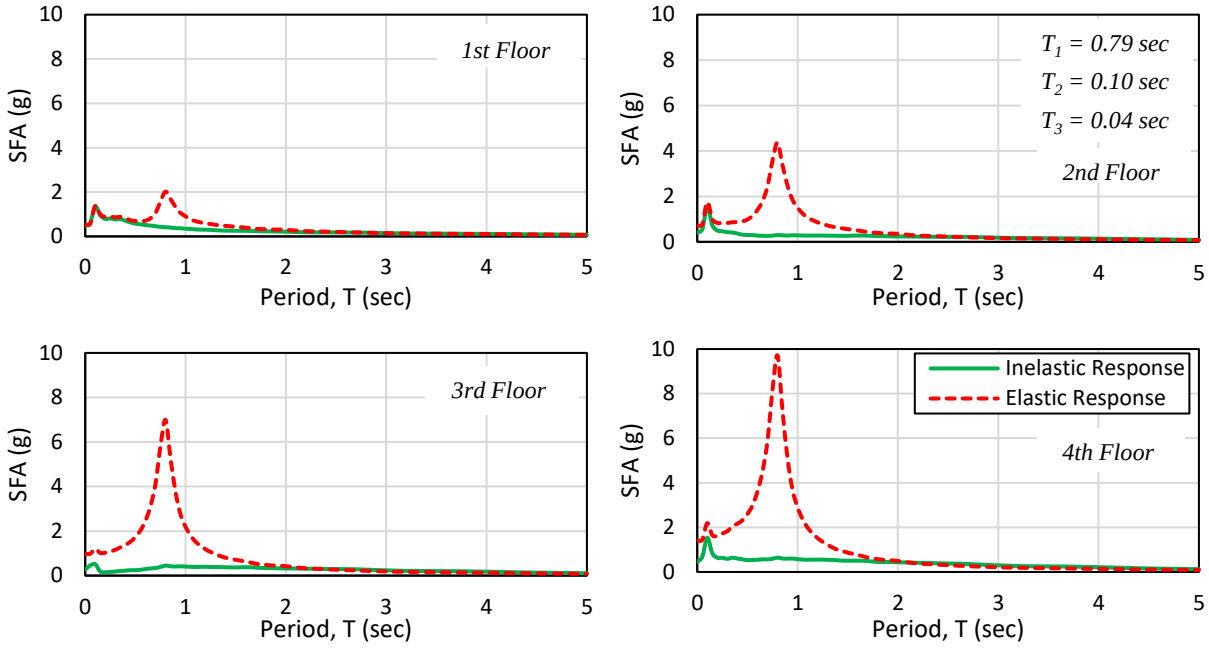

Figure B.23 Mean floor response spectra atop 4-story rocking wall for fully elastic and inelastic structural response at Intensity 5 (PGA = 0.450 g); ξ_{NS} = 5%

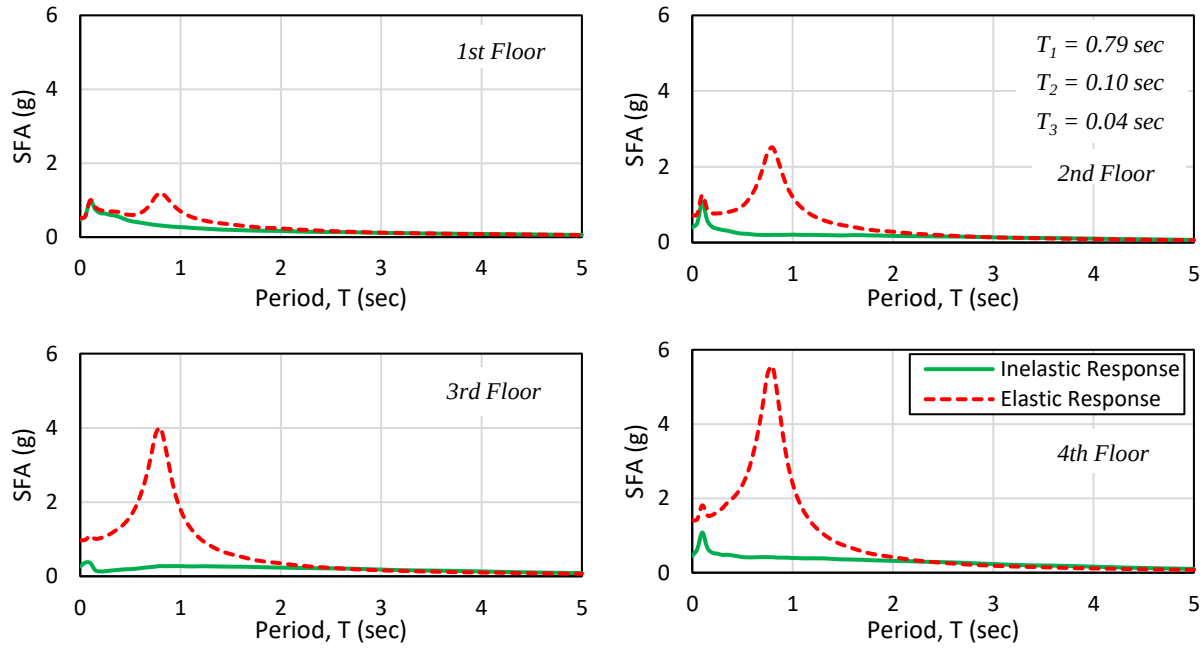

Figure B.24 Mean floor response spectra atop 4-story rocking wall for fully elastic and inelastic structural response at Intensity 5 (PGA = 0.450 g); ξ_{NS} = 10%

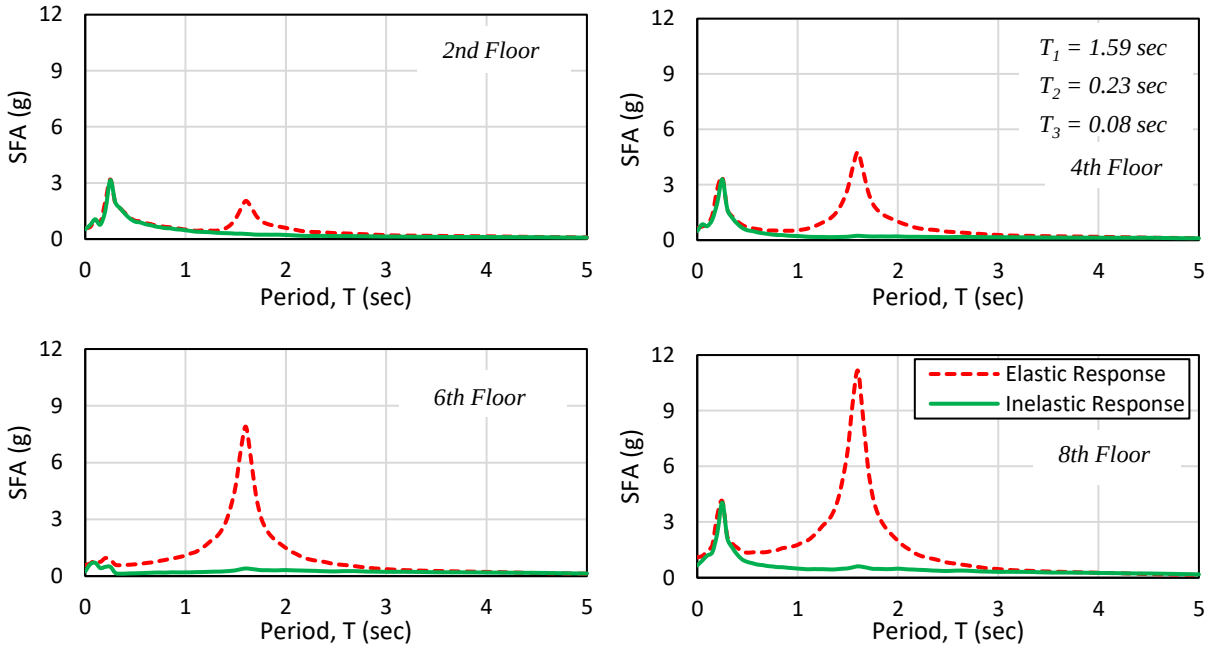

Figure B.25 Mean floor response spectra atop 8-story rocking wall for fully elastic and inelastic structural response at Intensity 5 (PGA = 0.450 g); ξ_{NS} = 2%

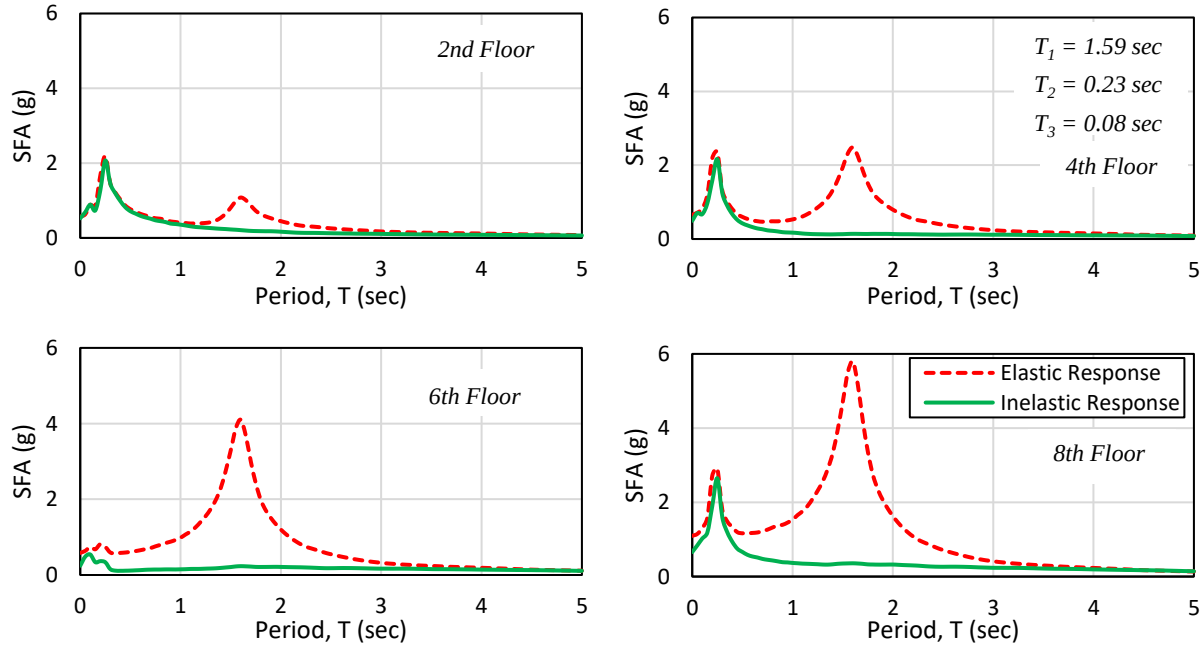

Figure B.26 Mean floor response spectra atop 8-story rocking wall for fully elastic and inelastic structural response at Intensity 5 (PGA = 0.450 g); ξ_{NS} = 5%

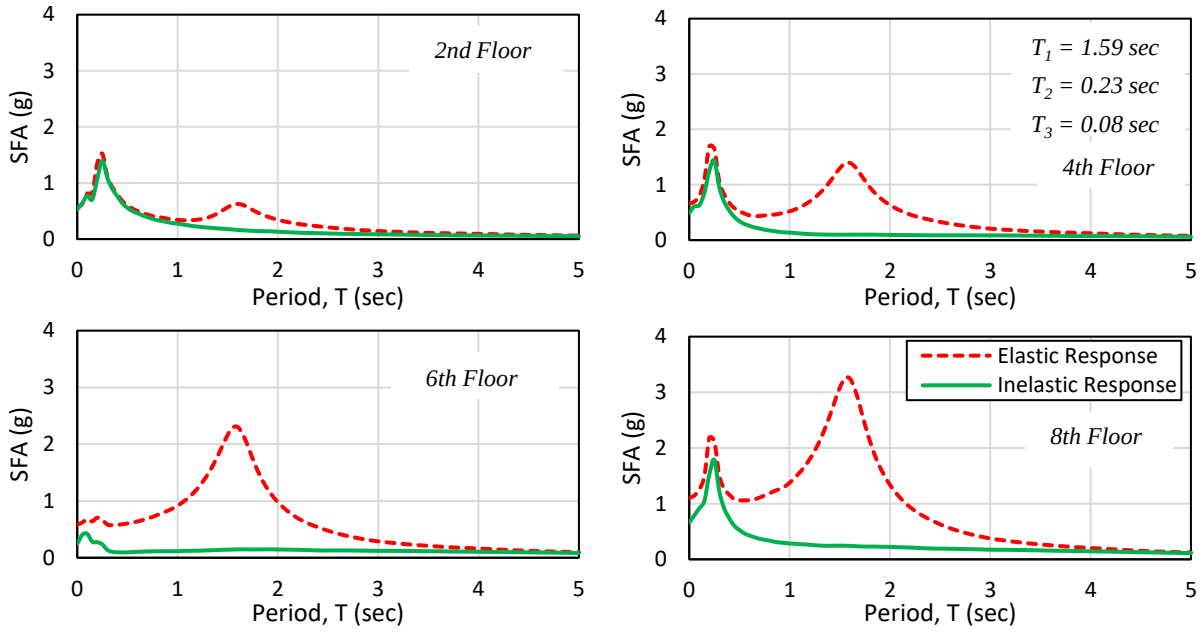

Figure B.27 Mean floor response spectra atop 8-story rocking wall for fully elastic and inelastic structural response at Intensity 5 (PGA = 0.450 g); ξ_{NS} = 10%

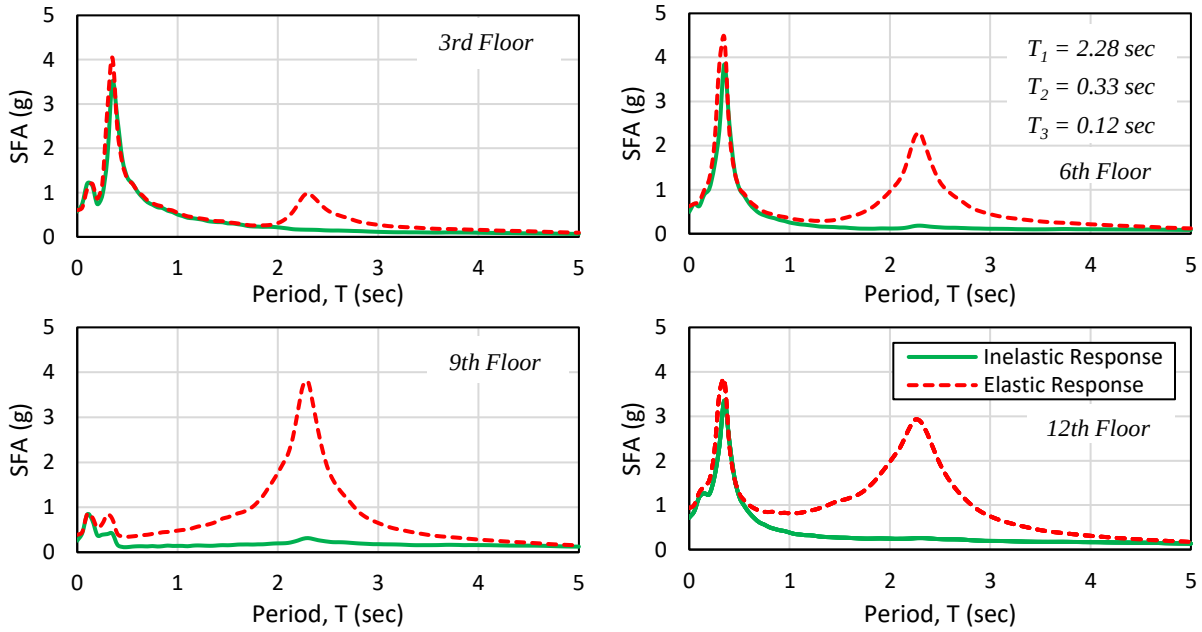

Figure B.28 Mean floor response spectra atop 12-story rocking wall for fully elastic and inelastic structural response at Intensity 5 (PGA = 0.450 g); ξ_{NS} = 2%

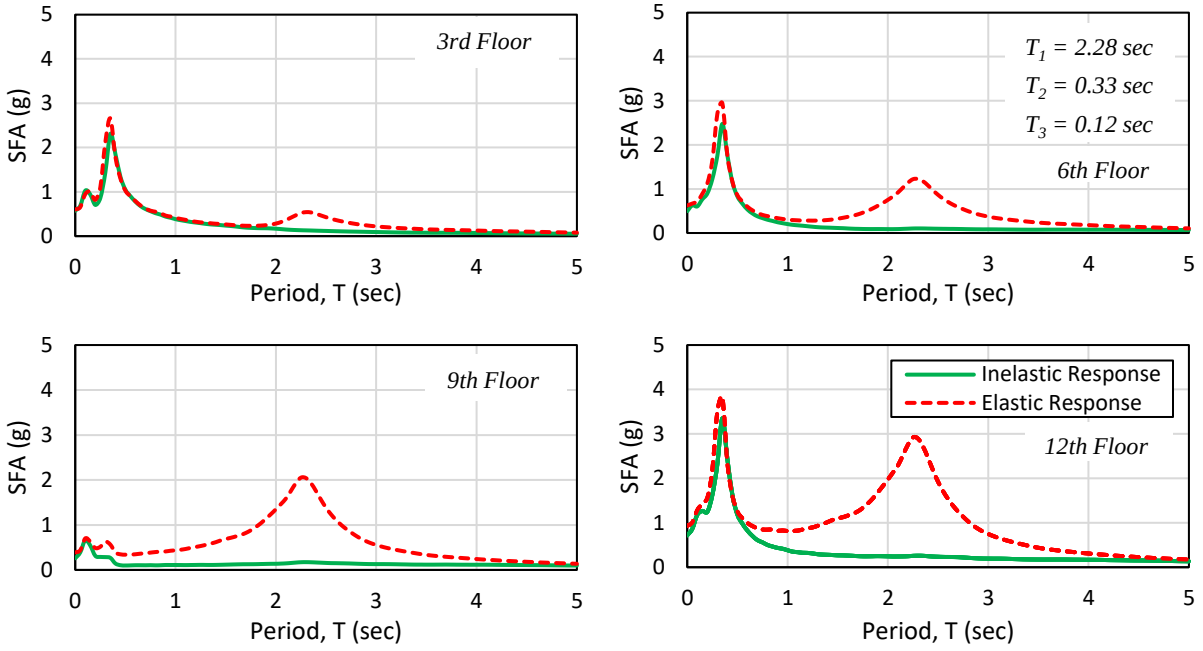

Figure B.29 Mean floor response spectra atop 12-story rocking wall for fully elastic and inelastic structural response at Intensity 5 (PGA = 0.450 g); ξ_{NS} = 5%

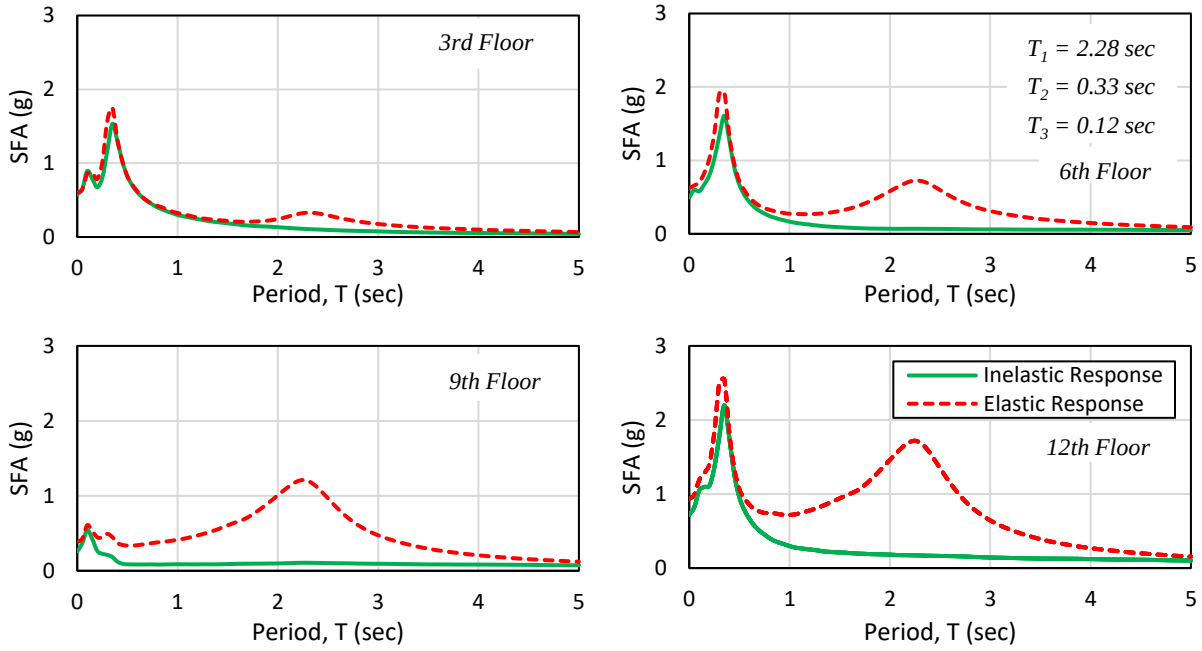

Figure B.30 Mean floor response spectra atop 12-story rocking wall for fully elastic and inelastic structural response at Intensity 5 (PGA = 0.450 g); ξ_{NS} = 10%

B.3 Comparisons between Mean NSE Accelerations from Coupled NLTHA and Mean Floor Response Spectra from Uncoupled NLTHA

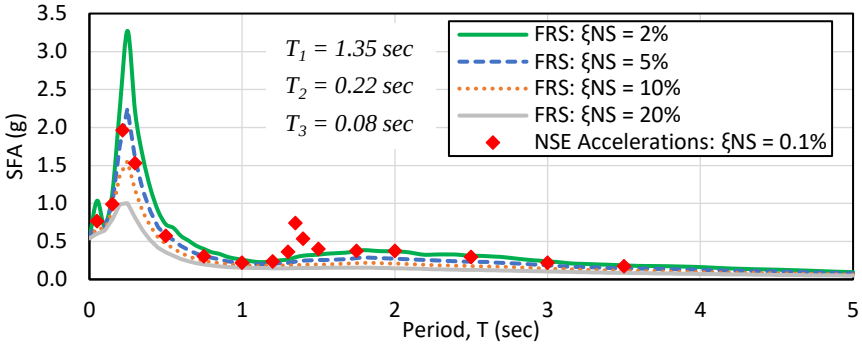

Figure B.31 Comparison between mean NSE accelerations from coupled analysis (MR=0.12%; ξ_{NS} = 0.1%) and mean FRS at various levels of ξ_{NS} from decoupled analysis; mid-height level of 4-story RC wall, inelastic structural response at Intensity 5 (PGA = 0.450 g)

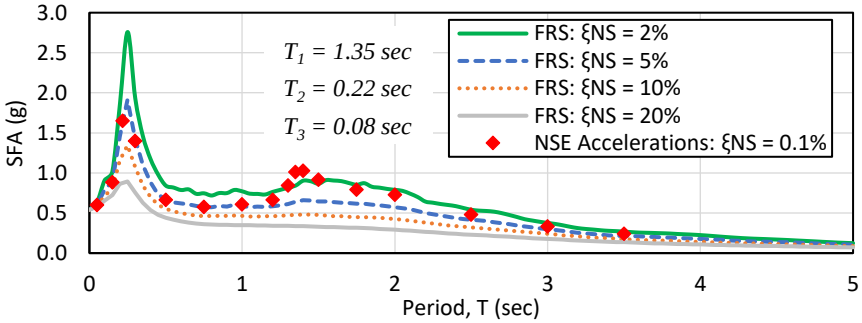

Figure B.32 Comparison between mean NSE accelerations from coupled analysis (MR=0.12%; ξ_{NS} = 0.1%) and mean FRS at various levels of ξ_{NS} from decoupled analysis; roof level of 4-story RC wall, inelastic structural response at Intensity 5 (PGA = 0.450 g)

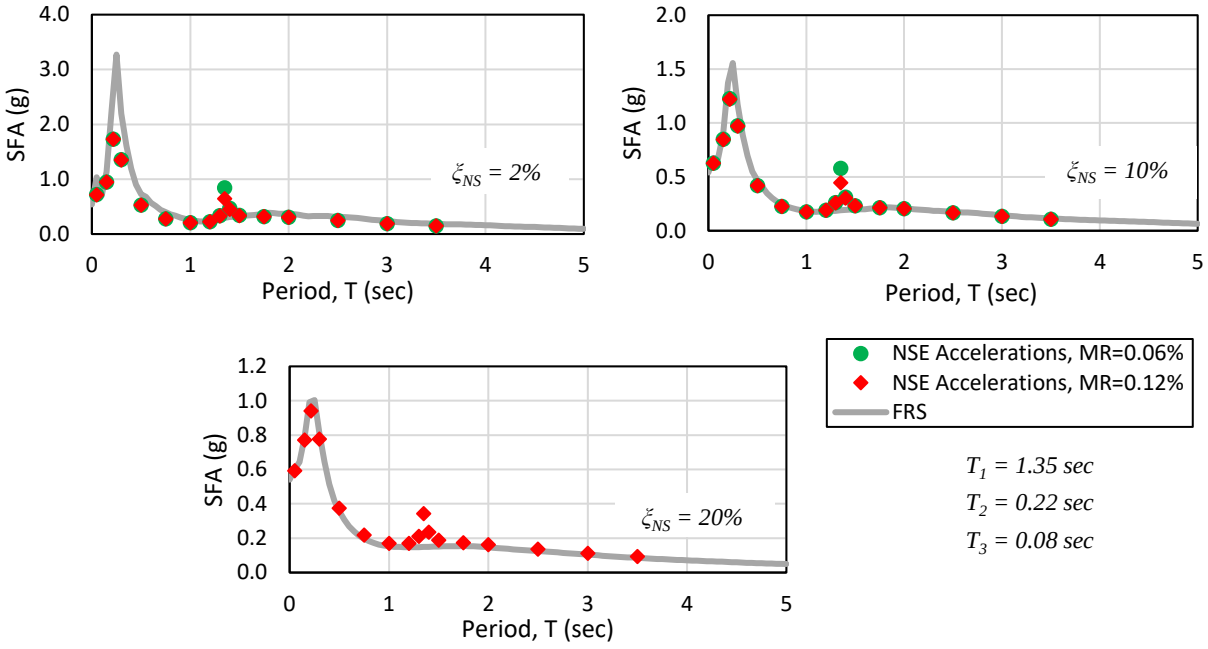

Figure B.33 Comparison between mean NSE accelerations from coupled analysis and mean FRS from decoupled analysis for mid-height level of 4-story RC wall; inelastic structural response at Intensity 5 (PGA = 0.450 g)

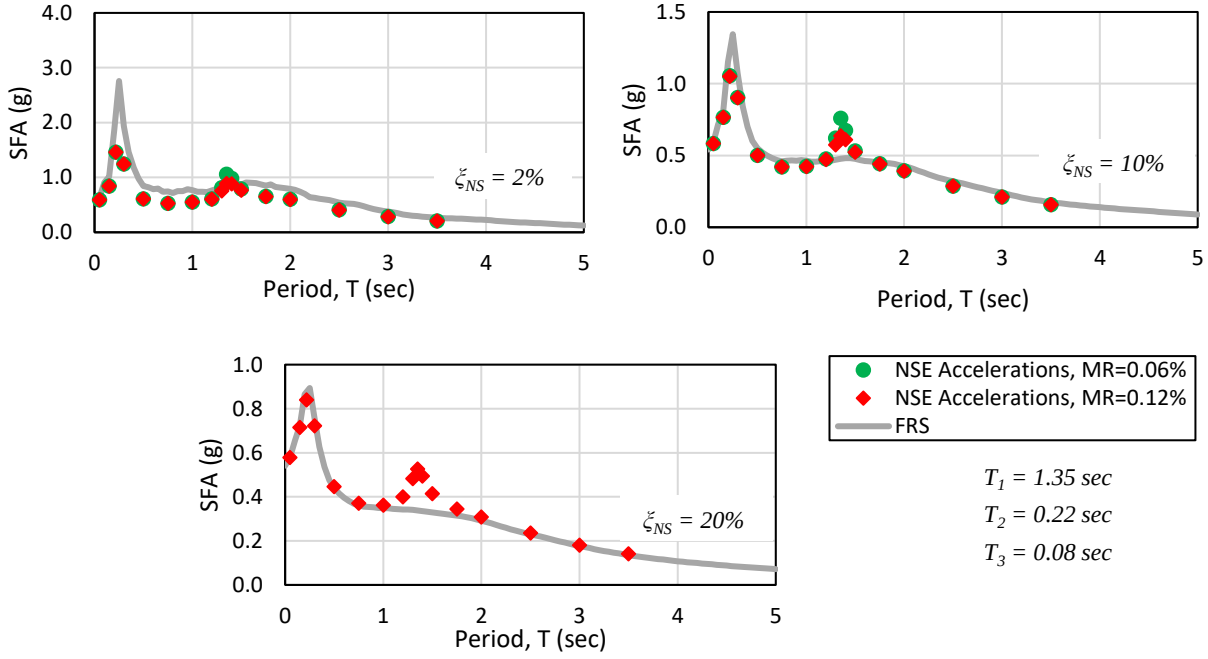

Figure B.34 Comparison between mean NSE accelerations from coupled analysis and mean FRS from decoupled analysis for roof level of 4-story RC wall; inelastic structural response at Intensity 5 (PGA = 0.450 g)

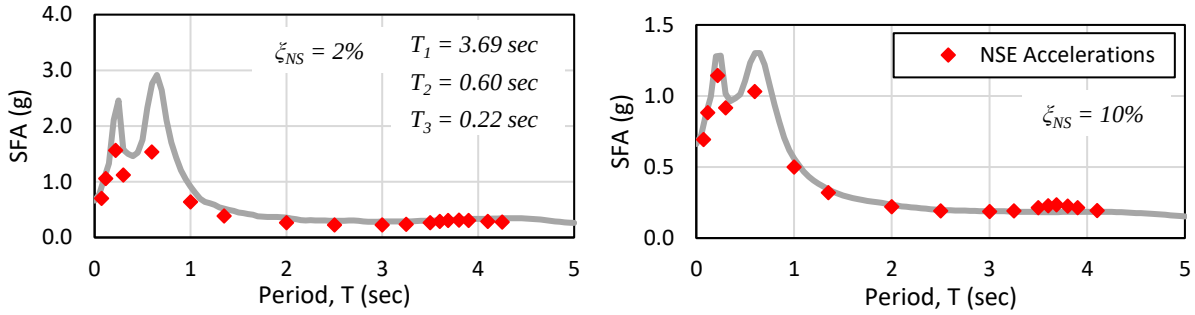

Figure B.35 Comparison between mean NSE accelerations from coupled analysis (MR = 0.12%) and mean FRS from decoupled analysis roof level of 12-story RC wall; inelastic structural response at Intensity 5 (PGA = 0.450 g)

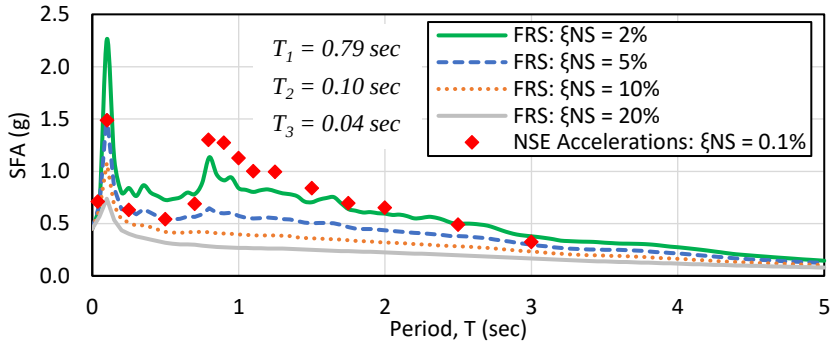

Figure B.36 Comparison between mean NSE accelerations from coupled analysis (MR=0.12%; ξ_{NS} = 0.1%) and mean FRS at various levels of ξ_{NS} from decoupled analysis; roof level of 4-story rocking wall, inelastic structural response at Intensity 5 (PGA = 0.450 g)

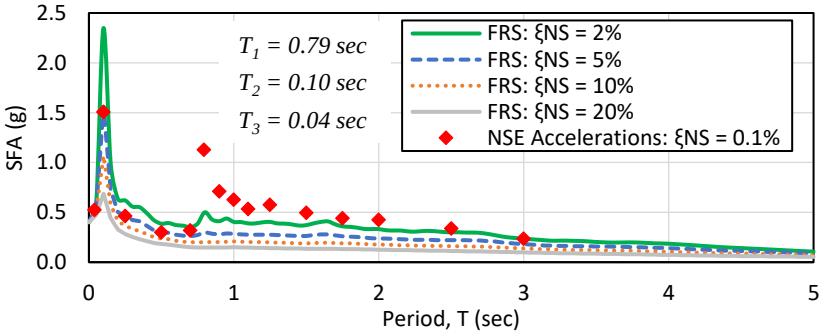

Figure B.37 Comparison between mean NSE accelerations from coupled analysis (MR=0.12%; ξ_{NS} = 0.1%) and mean FRS at various levels of ξ_{NS} from decoupled analysis; mid-height level of 4-story rocking wall, inelastic structural response at Intensity 5 (PGA = 0.450 g)

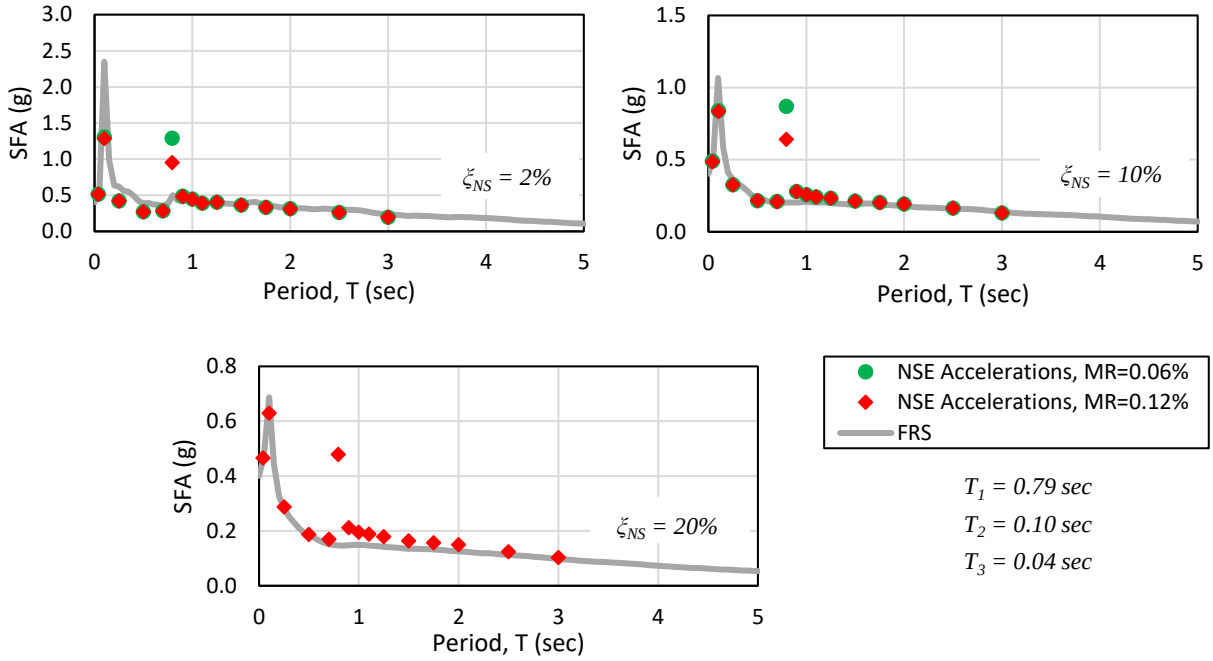

Figure B.38 Comparison between mean NSE accelerations from coupled analysis and mean FRS from decoupled analysis for mid-height level of 4-story rocking wall; inelastic structural response at Intensity 5 (PGA = 0.450 g)

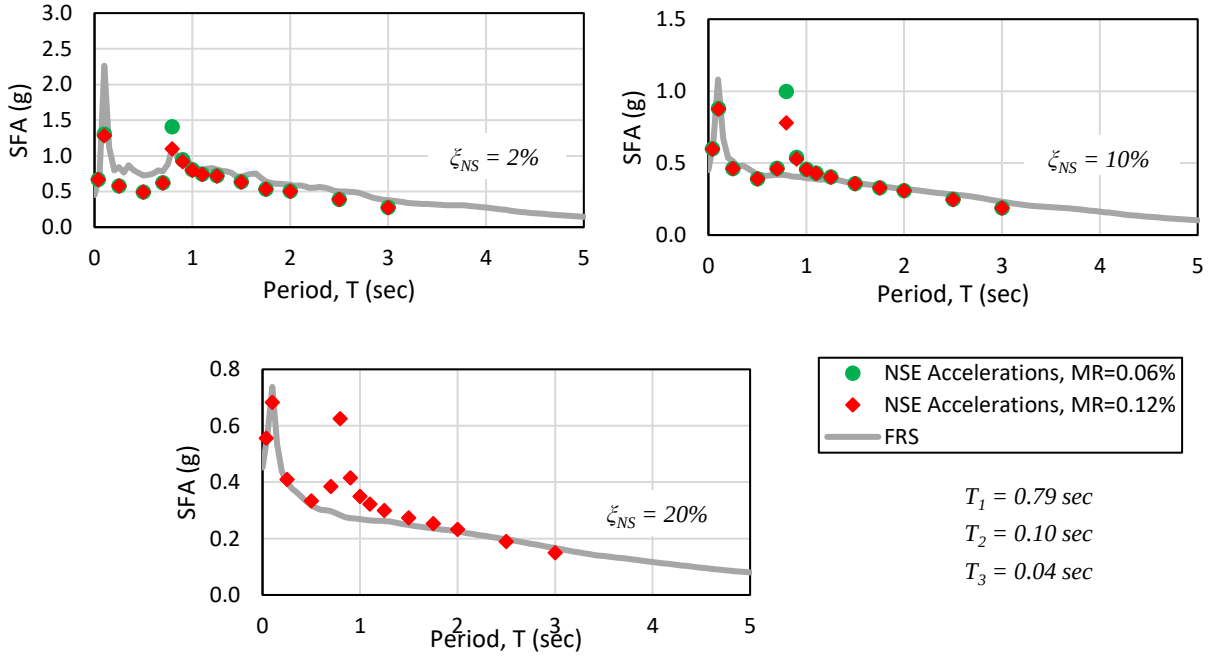

Figure B.39 Comparison between mean NSE accelerations from coupled analysis and mean FRS from decoupled analysis for roof level of 4-story rocking wall; inelastic structural response at Intensity 5 (PGA = 0.450 g)

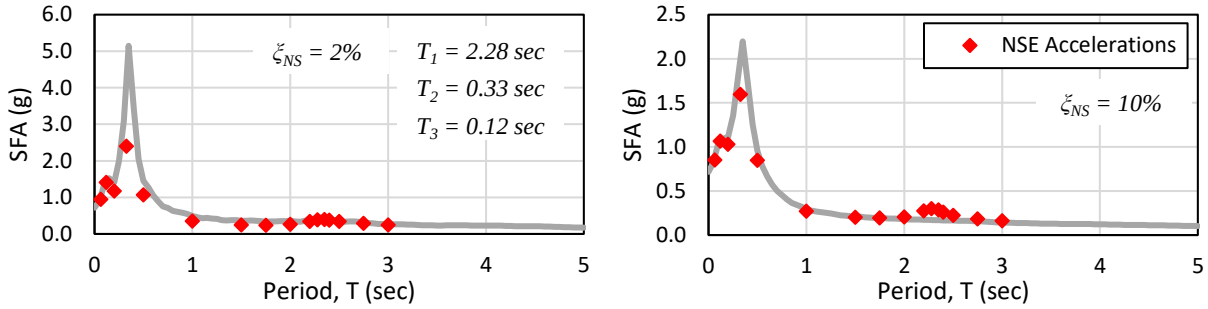

Figure B.40 Comparison between mean NSE accelerations from coupled analysis (MR = 0.12%) and mean FRS from decoupled analysis roof level of 12-story rocking wall; inelastic structural response at Intensity 5 (PGA = 0.450 g)

APPENDIX C. ADDITIONAL FLOOR RESPONSE SPECTRA ESTIMATES FOR THE PROPOSED METHODOLOGIES

This appendix presents additional information for Chapter 7, in which three procedures were proposed to estimate floor response spectra in RC and rocking wall buildings responding non-linearly. Section C.1 presents comparisons between mean floor spectra obtained from NLTHA and floor spectra estimates using the procedure that utilizes transitory inelastic modal characteristics. Section C.2 presents comparisons between mean floor spectra obtained from NLTHA and floor spectra estimates using the procedure that utilizes modal reduction factors. Section C.3 presents comparisons between mean floor spectra obtained from NLTHA and floor spectra estimates using the procedure that utilizes dynamics of distributed-mass systems.

C.1 Procedure that Utilizes Transitory Inelastic Modal Characteristics

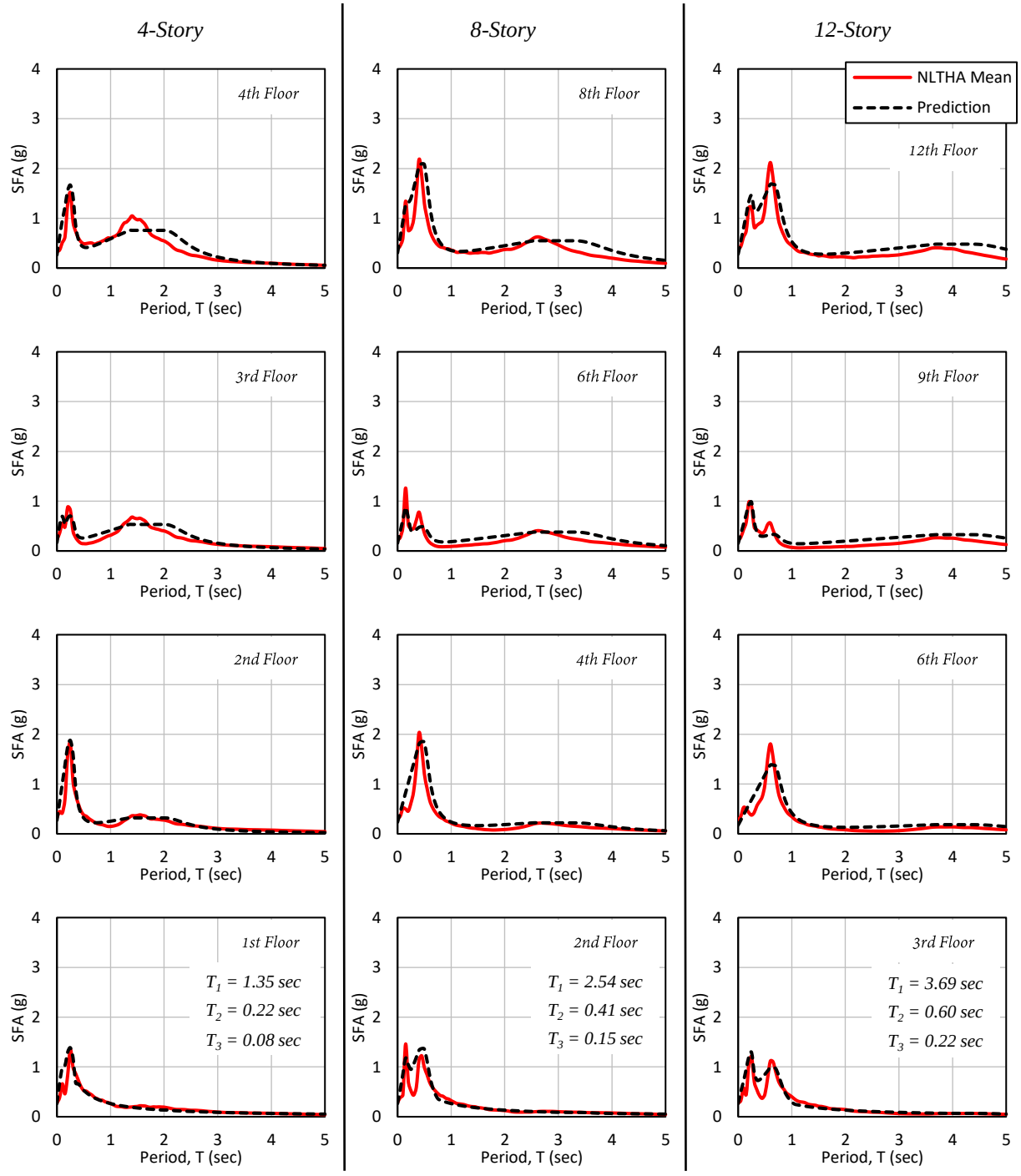

Figure 0.1 Comparison between mean floor spectra from NLTHA and estimates using transitory modal properties; RC wall buildings, Intensity 1 (PGA = 0.225g), ξ_{NS} = 2%

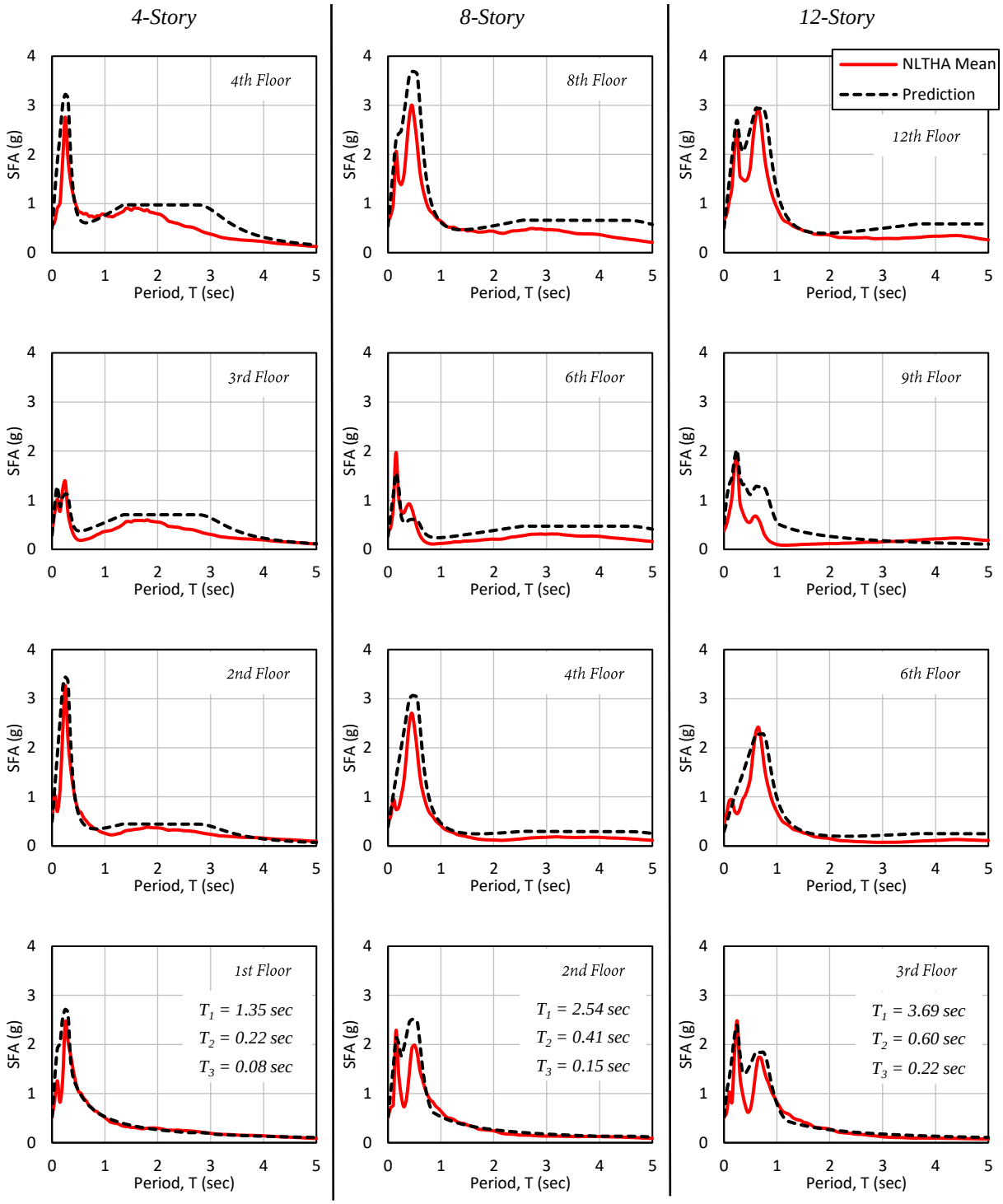

Figure 0.2 Comparison between mean floor spectra from NLTHA and estimates using transitory modal properties; RC wall buildings, Intensity 5 (PGA = 0.450g), ξ_{NS} = 2%

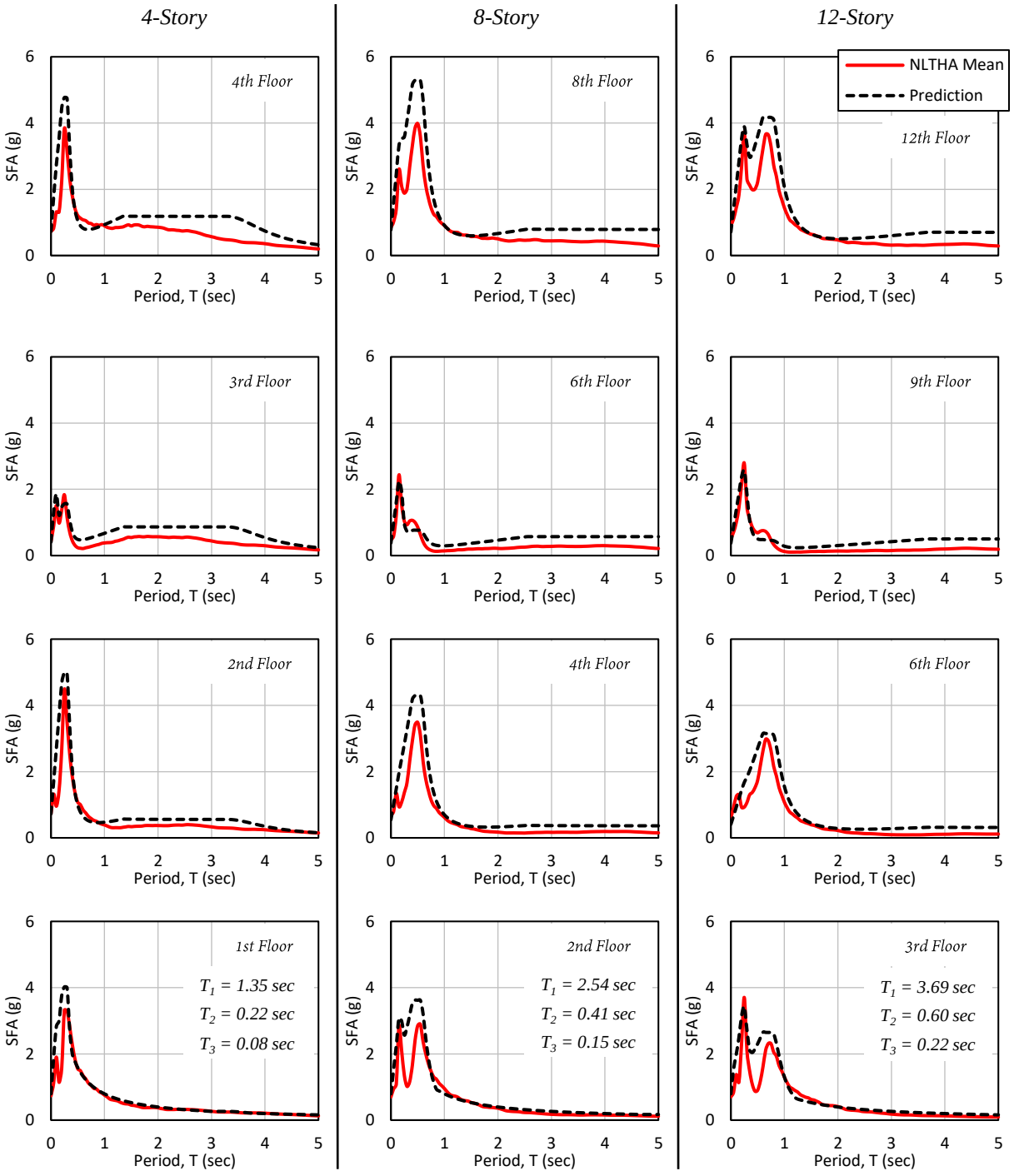

Figure 0.3 Comparison between mean floor spectra from NLTHA and estimates using transitory modal properties; RC wall buildings, Intensity 6 (PGA = 0.675g), ξ_{NS} = 2%

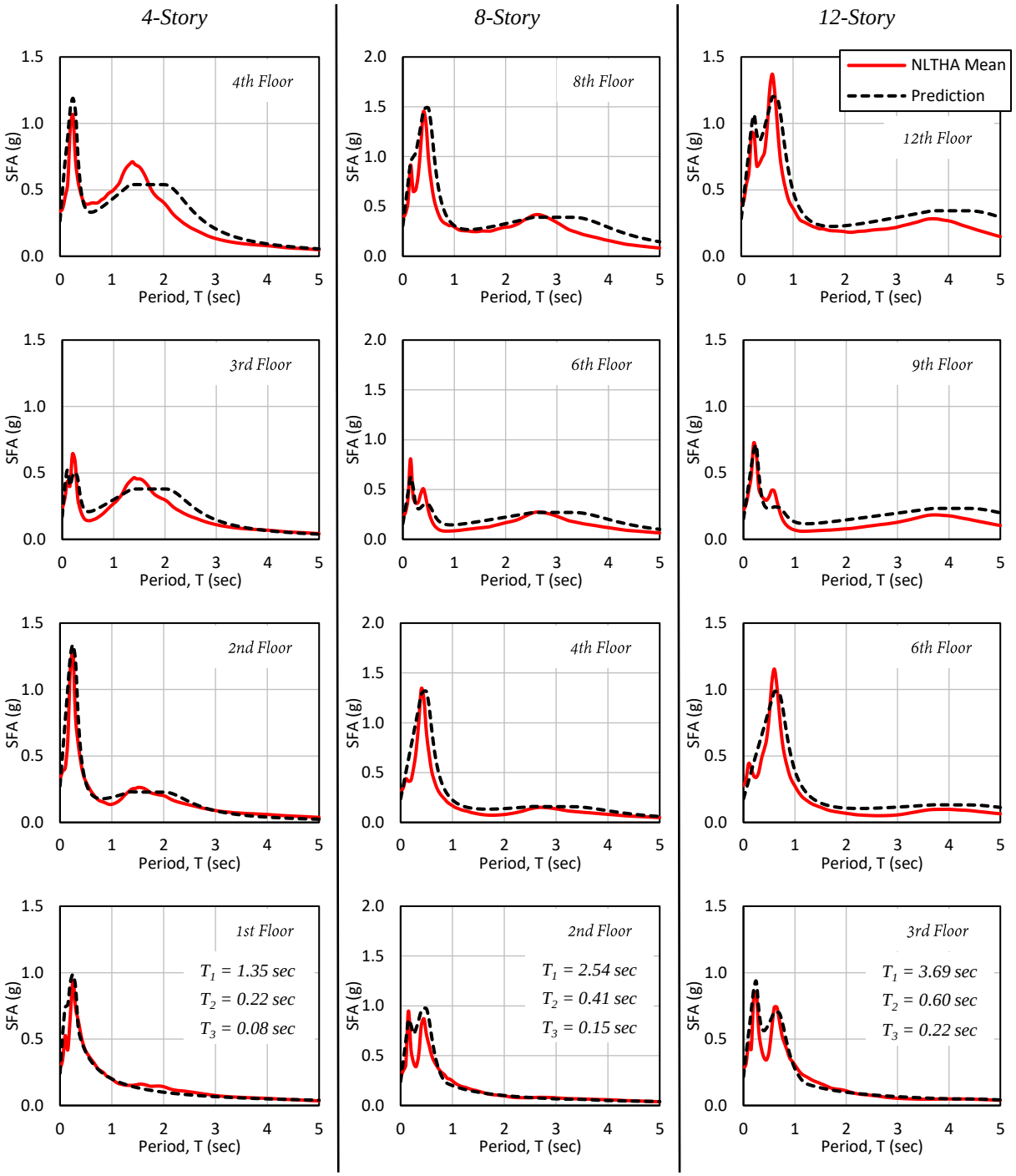

Figure 0.4 Comparison between mean floor spectra from NLTHA and estimates using transitory modal properties; RC wall buildings, Intensity 1 (PGA = 0.225g), ξ_{NS} = 5%

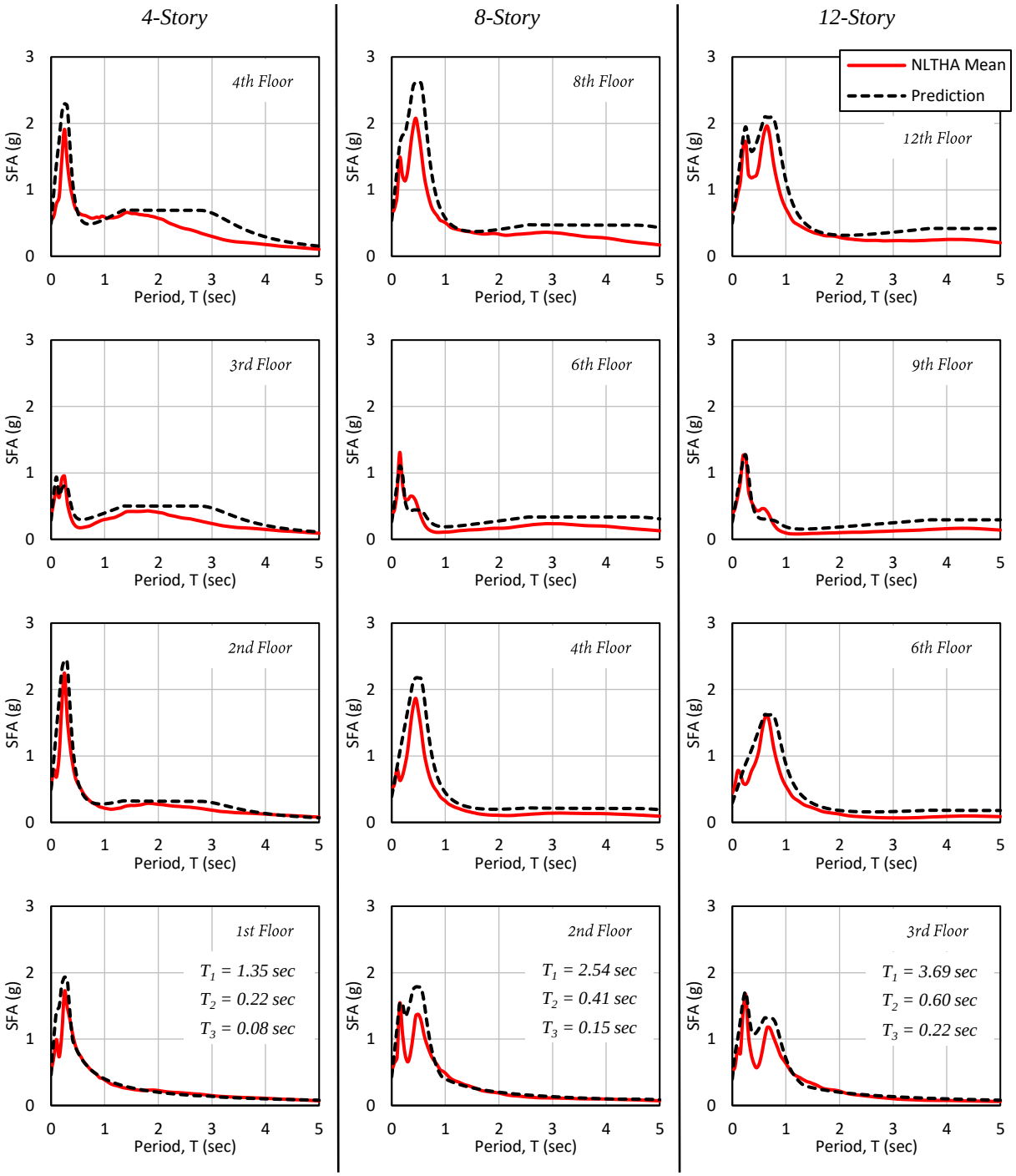

Figure 0.5 Comparison between mean floor spectra from NLTHA and estimates using transitory modal properties; RC wall buildings, Intensity 5 (PGA = 0.450g), ξ_{NS} = 5%

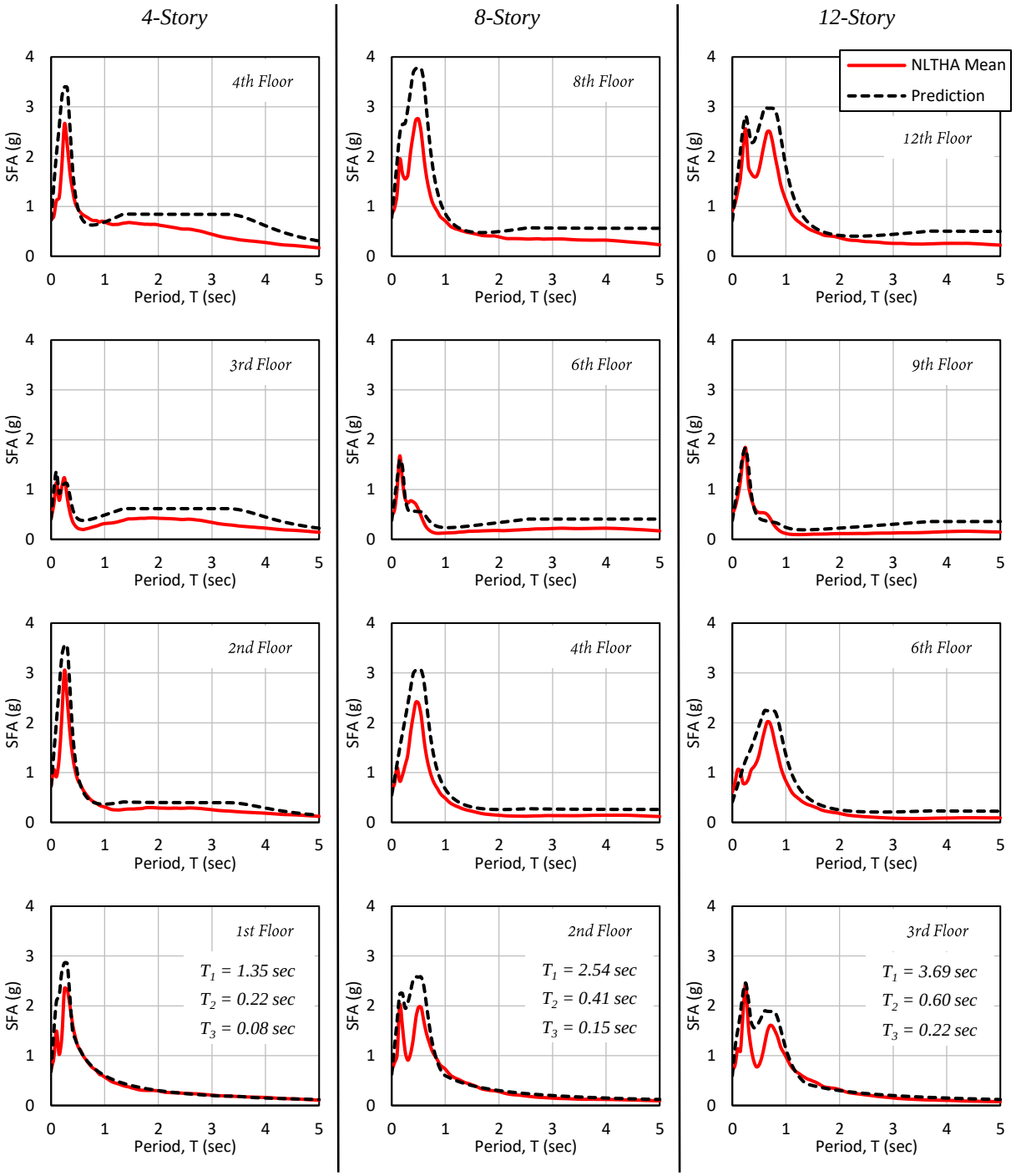

Figure 0.6 Comparison between mean floor spectra from NLTHA and estimates using transitory modal properties; RC wall buildings, Intensity 6 (PGA = 0.675g), ξ_{NS} = 5%

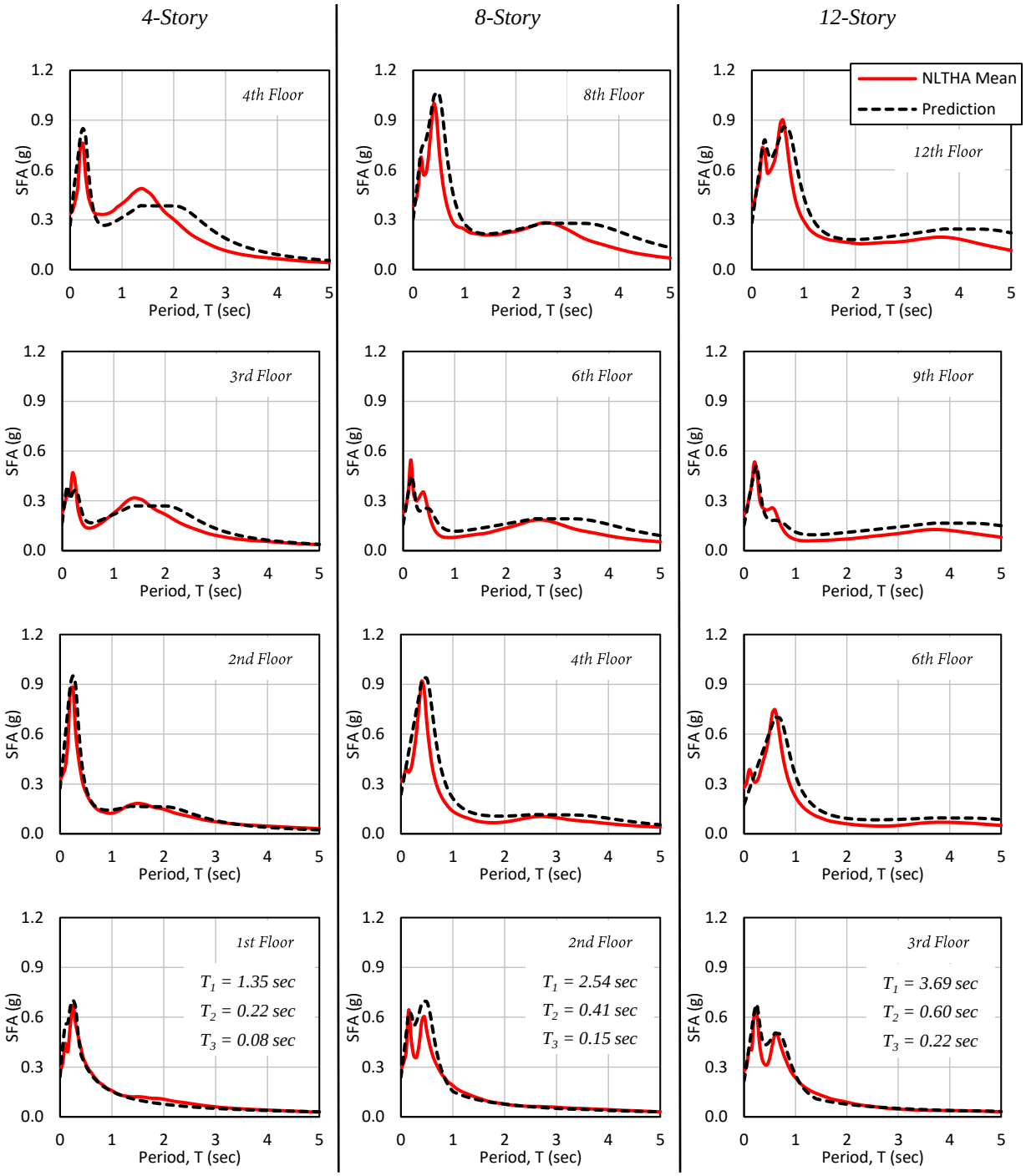

Figure 0.7 Comparison between mean floor spectra from NLTHA and estimates using transitory modal properties; RC wall buildings, Intensity 1 (PGA = 0.225g), ξ_{NS} = 10%

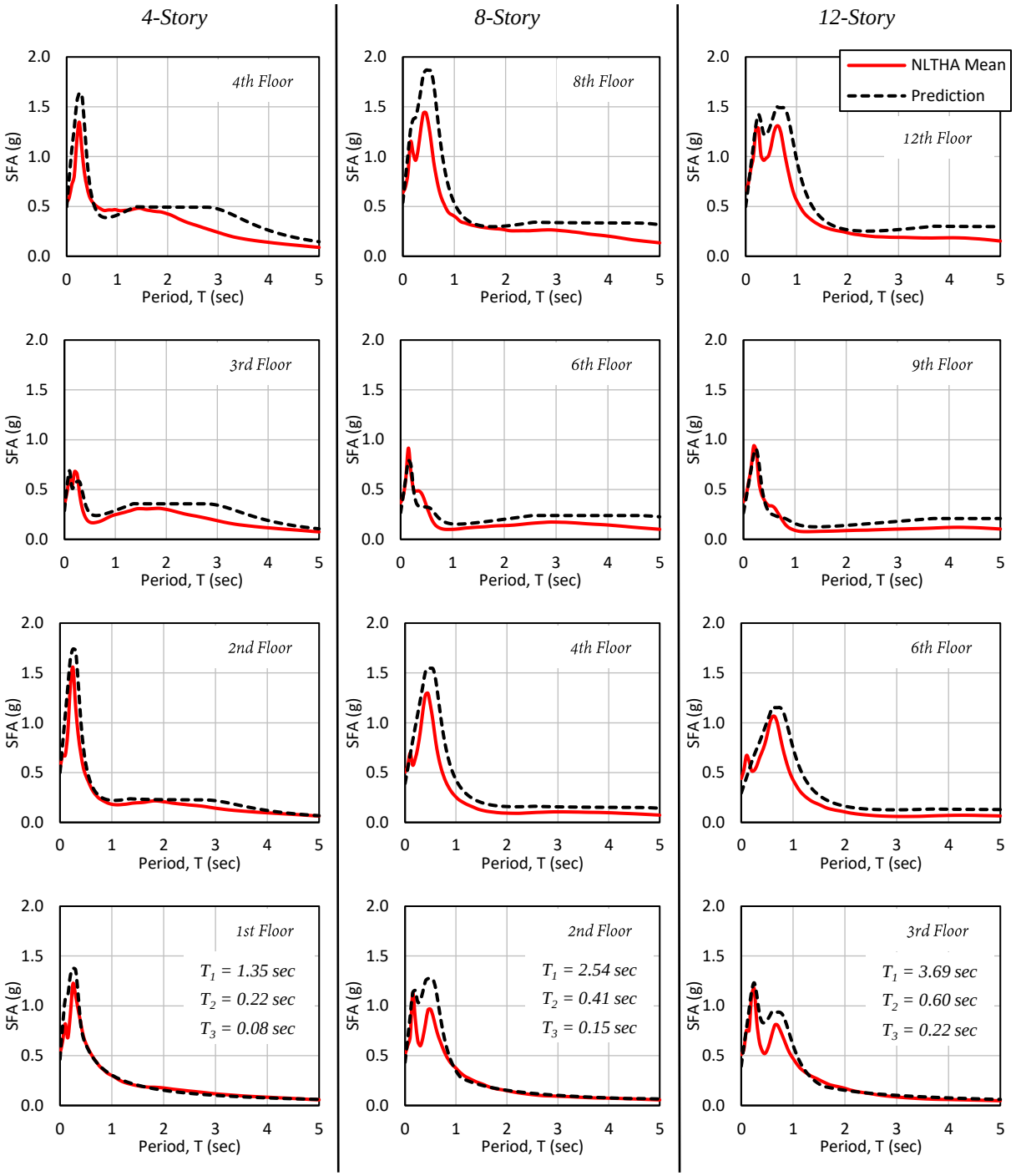

Figure 0.8 Comparison between mean floor spectra from NLTHA and estimates using transitory modal properties; RC wall buildings, Intensity 5 (PGA = 0.450g), ξ_{NS} = 10%

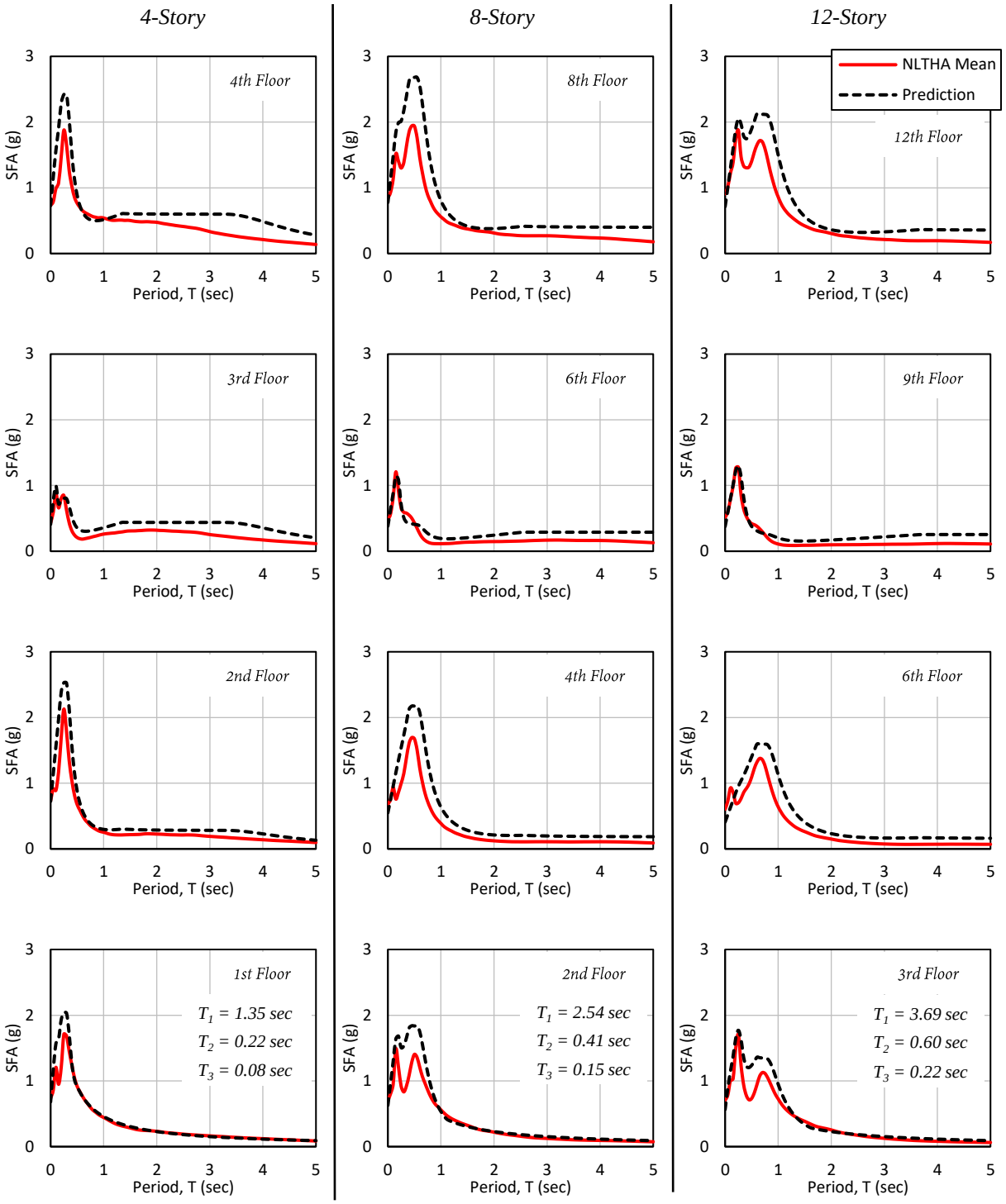

Figure 0.9 Comparison between mean floor spectra from NLTHA and estimates using transitory modal properties; RC wall buildings, Intensity 6 (PGA = 0.675g), ξ_{NS} = 10%

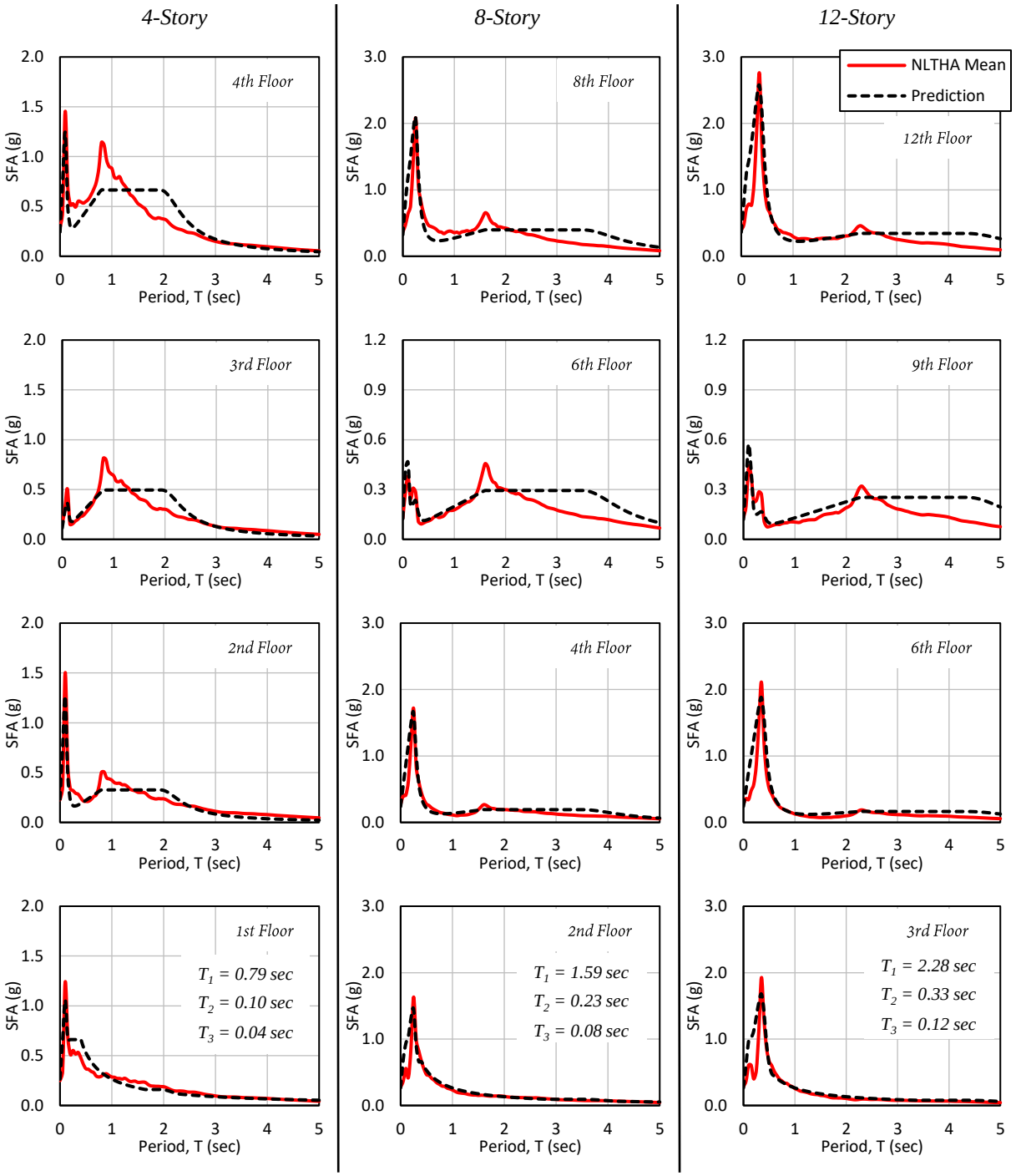

Figure 0.10 Comparison between mean floor spectra from NLTHA and estimates using transitory modal properties; rocking wall buildings, Intensity 1 (PGA = 0.225g), ξ_{NS} = 2%

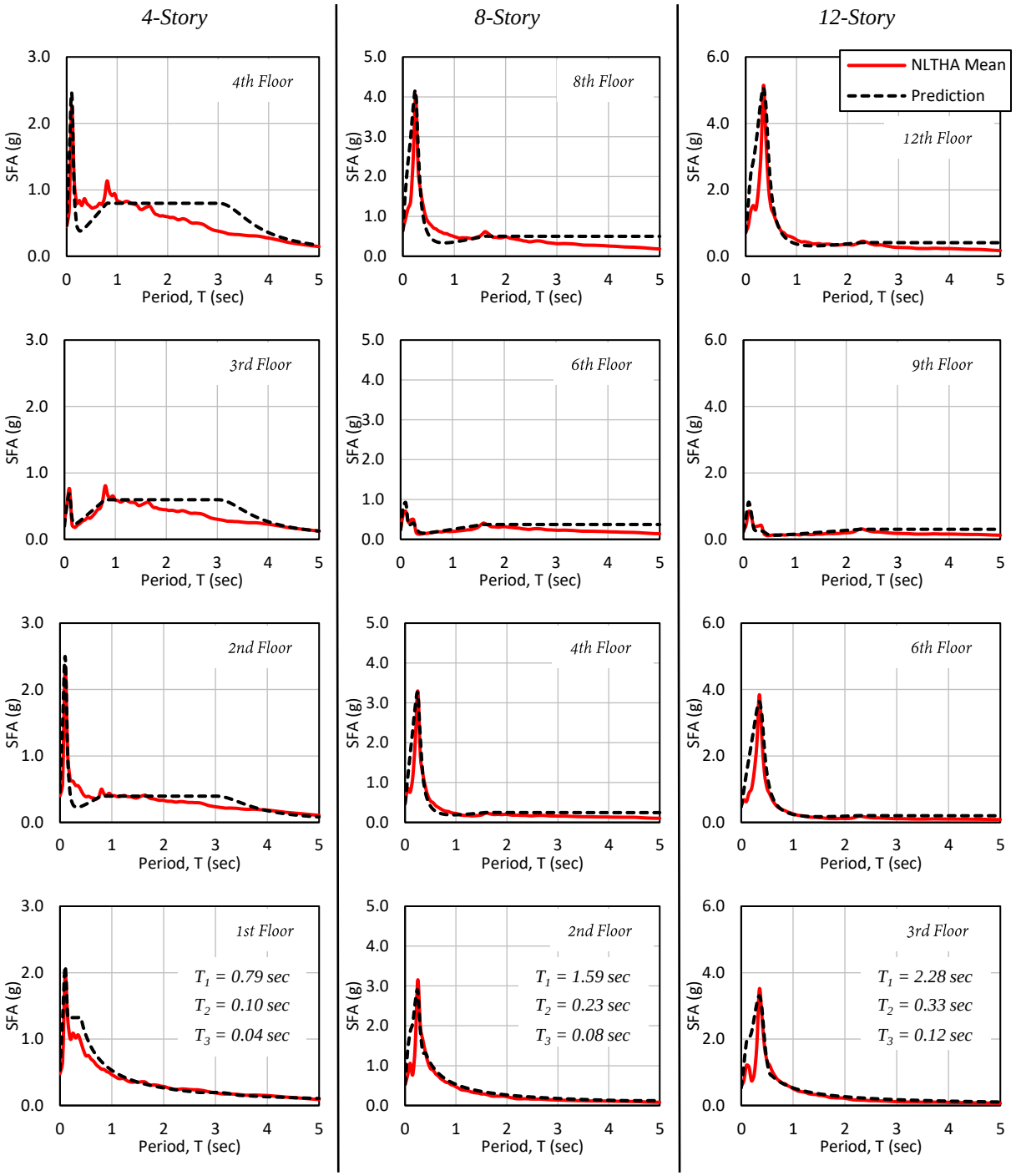

Figure 0.11 Comparison between mean floor spectra from NLTHA and estimates using transitory modal properties; rocking wall buildings, Intensity 5 (PGA = 0.450g), ξ_{NS} = 2%

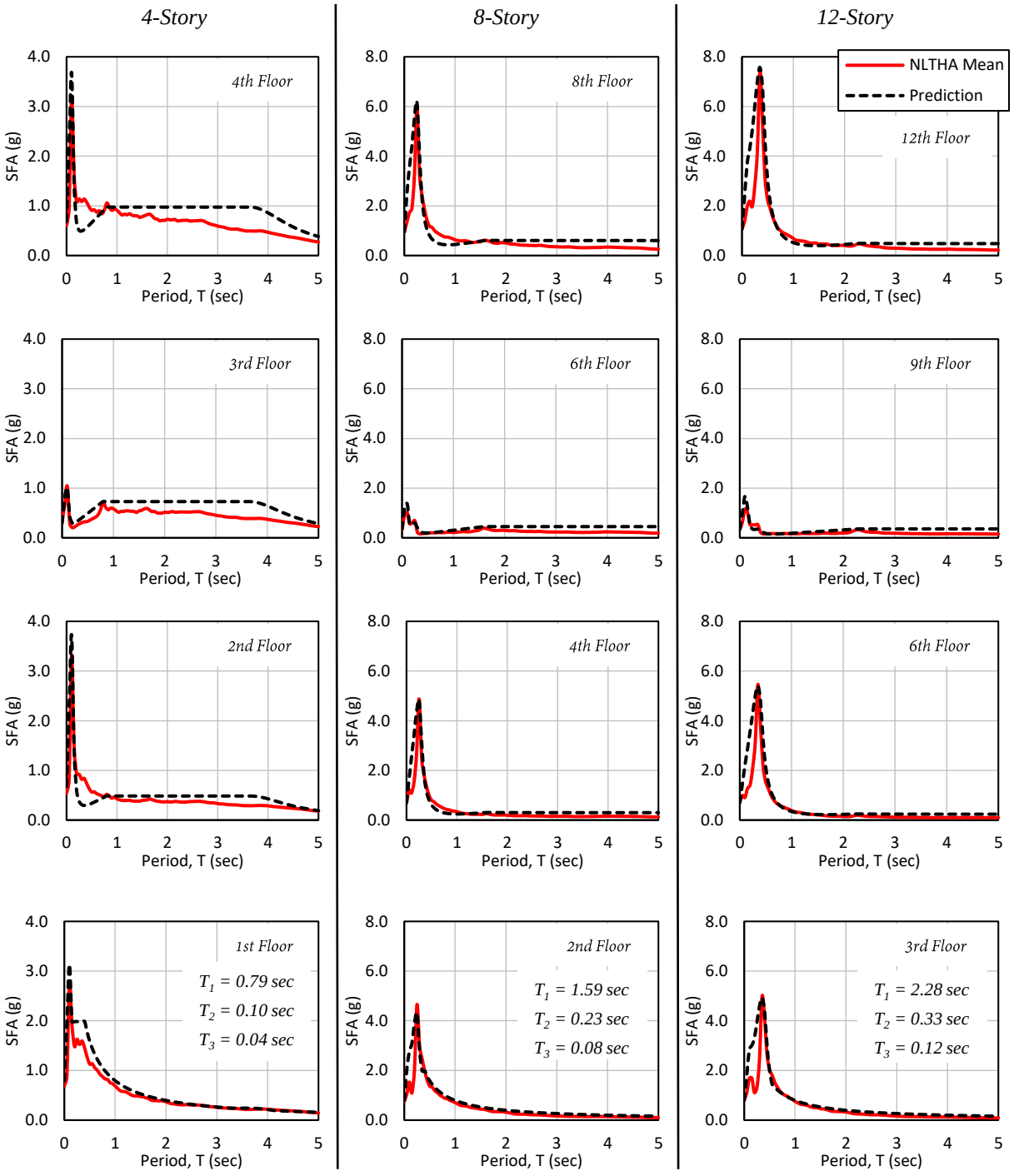

Figure 0.12 Comparison between mean floor spectra from NLTHA and estimates using transitory modal properties; rocking wall buildings, Intensity 6 (PGA = 0.675g), ξ_{NS} = 2%

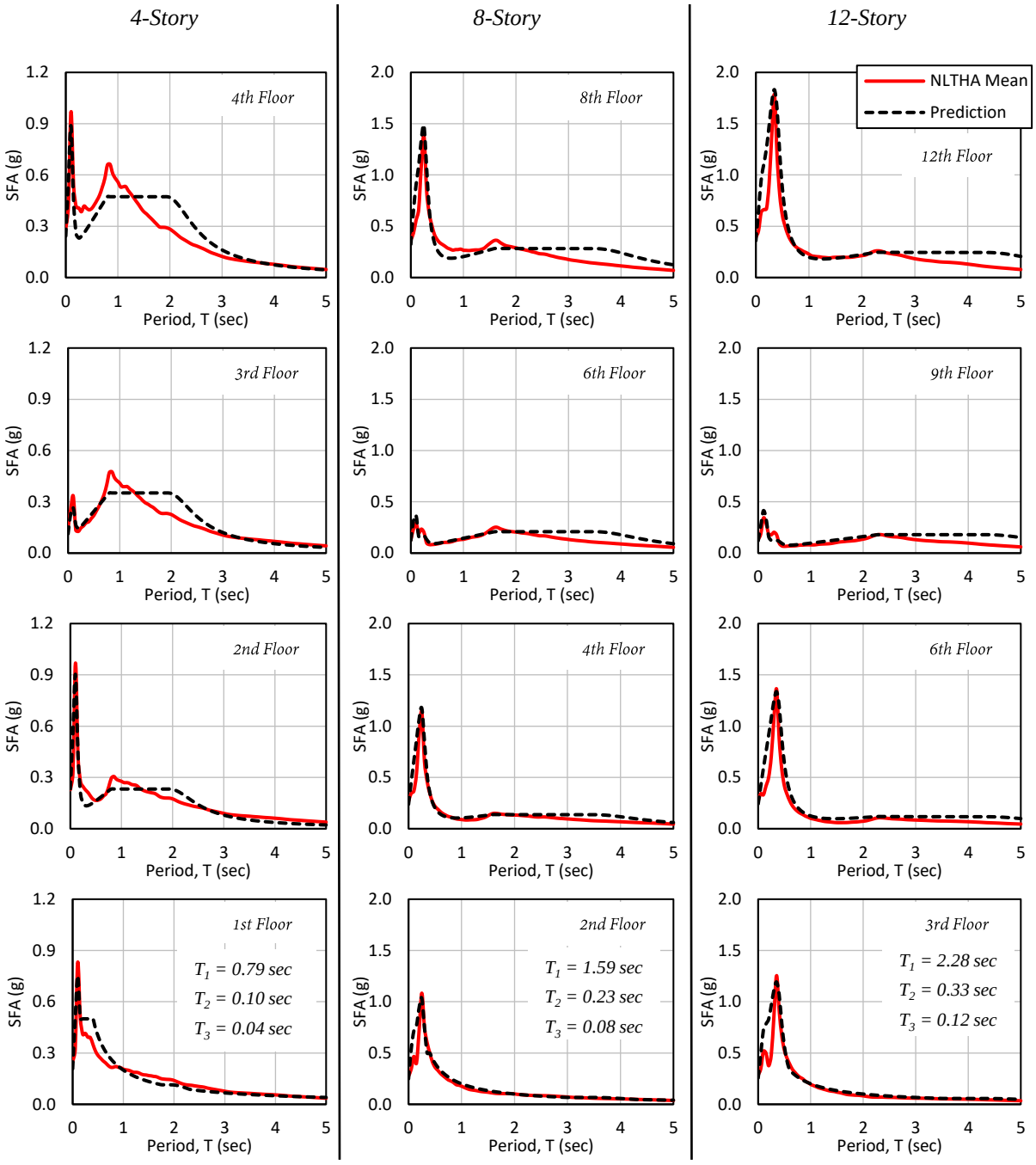

Figure 0.13 Comparison between mean floor spectra from NLTHA and estimates using transitory modal properties; rocking wall buildings, Intensity 1 (PGA = 0.225g), ξ_{NS} = 5%

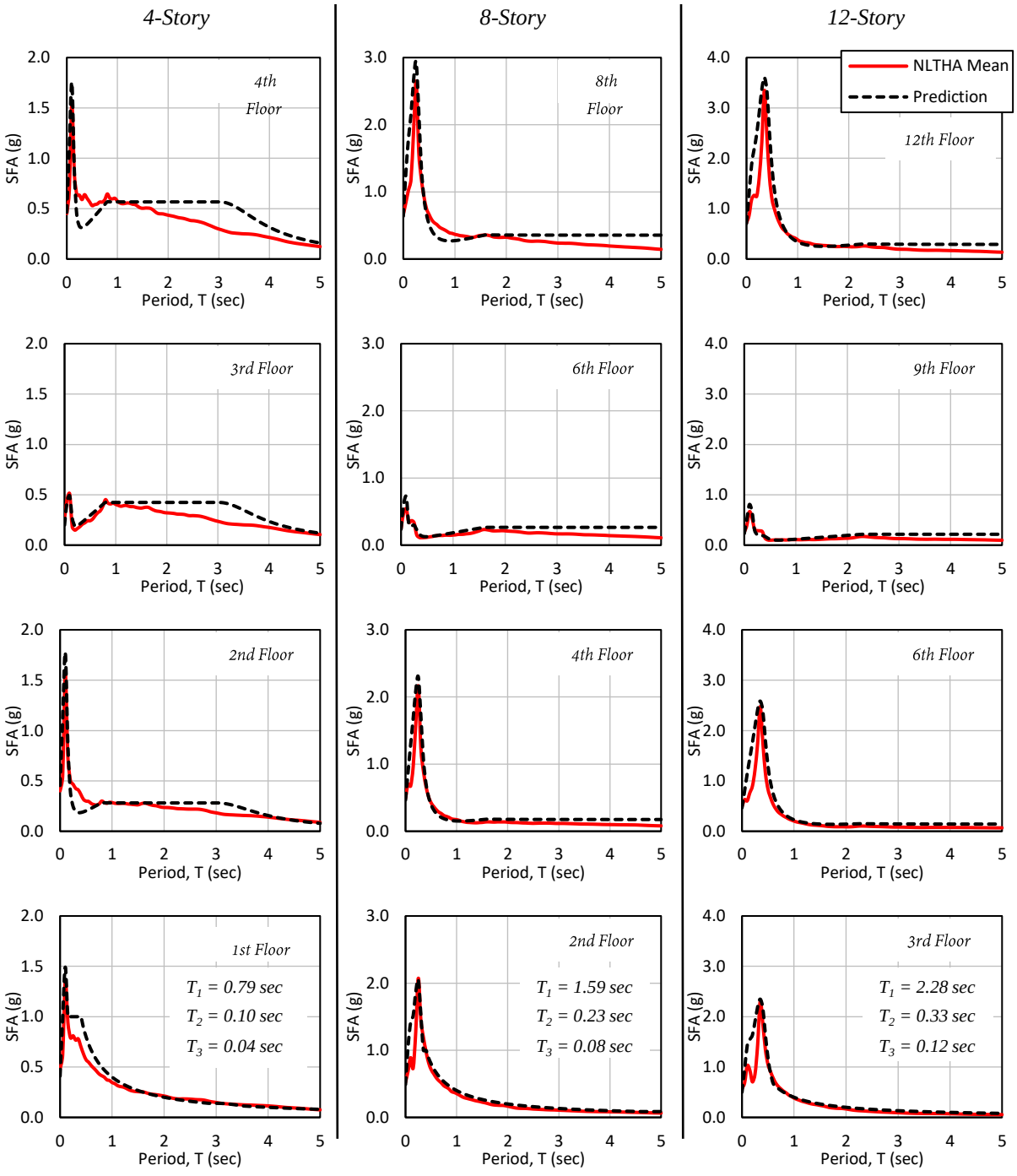

Figure 0.14 Comparison between mean floor spectra from NLTHA and estimates using transitory modal properties; rocking wall buildings, Intensity 5 (PGA = 0.450g), ξ_{NS} = 5%

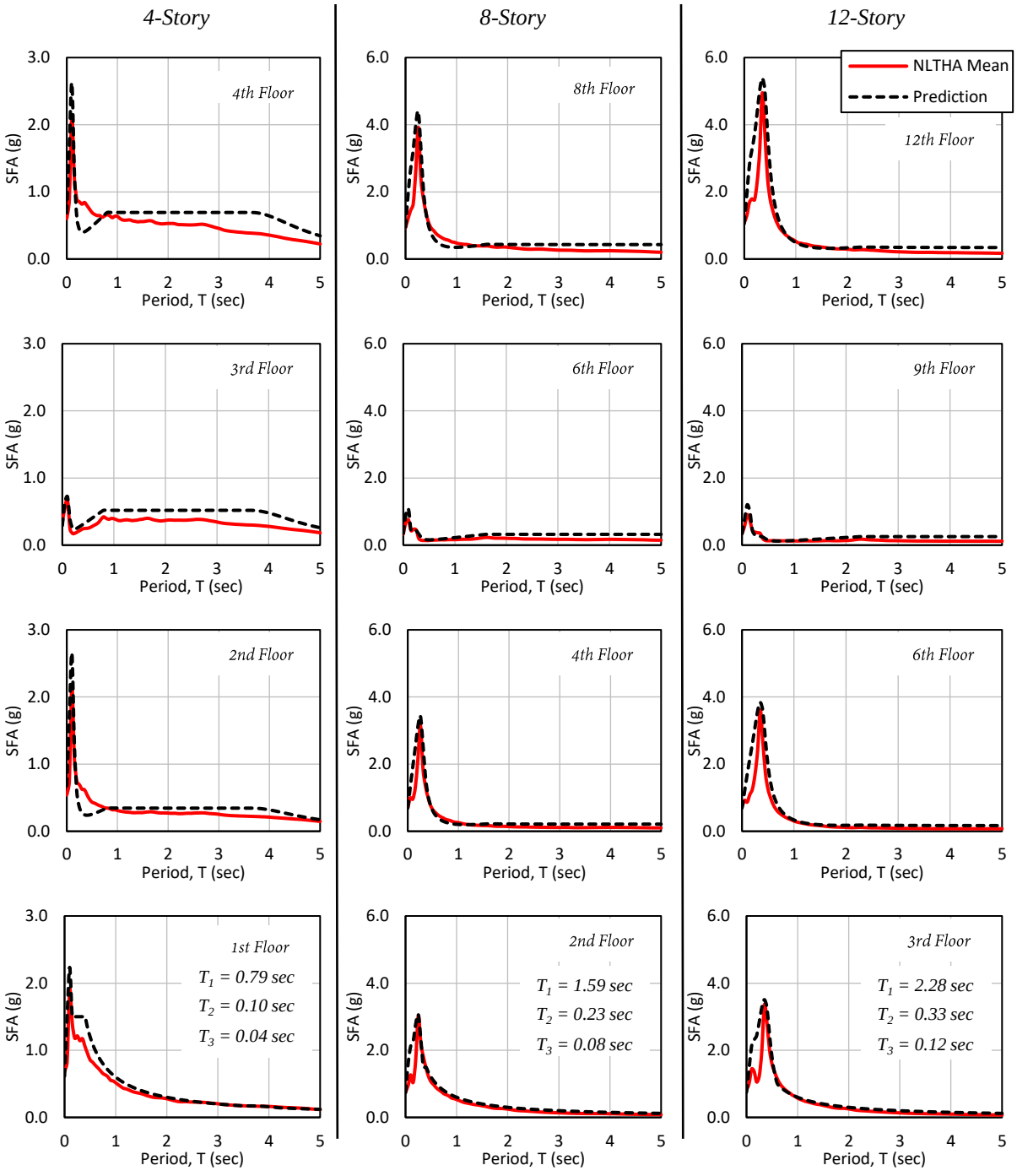

Figure 0.15 Comparison between mean floor spectra from NLTHA and estimates using transitory modal properties; rocking wall buildings, Intensity 6 (PGA = 0.675g), ξ_{NS} = 5%

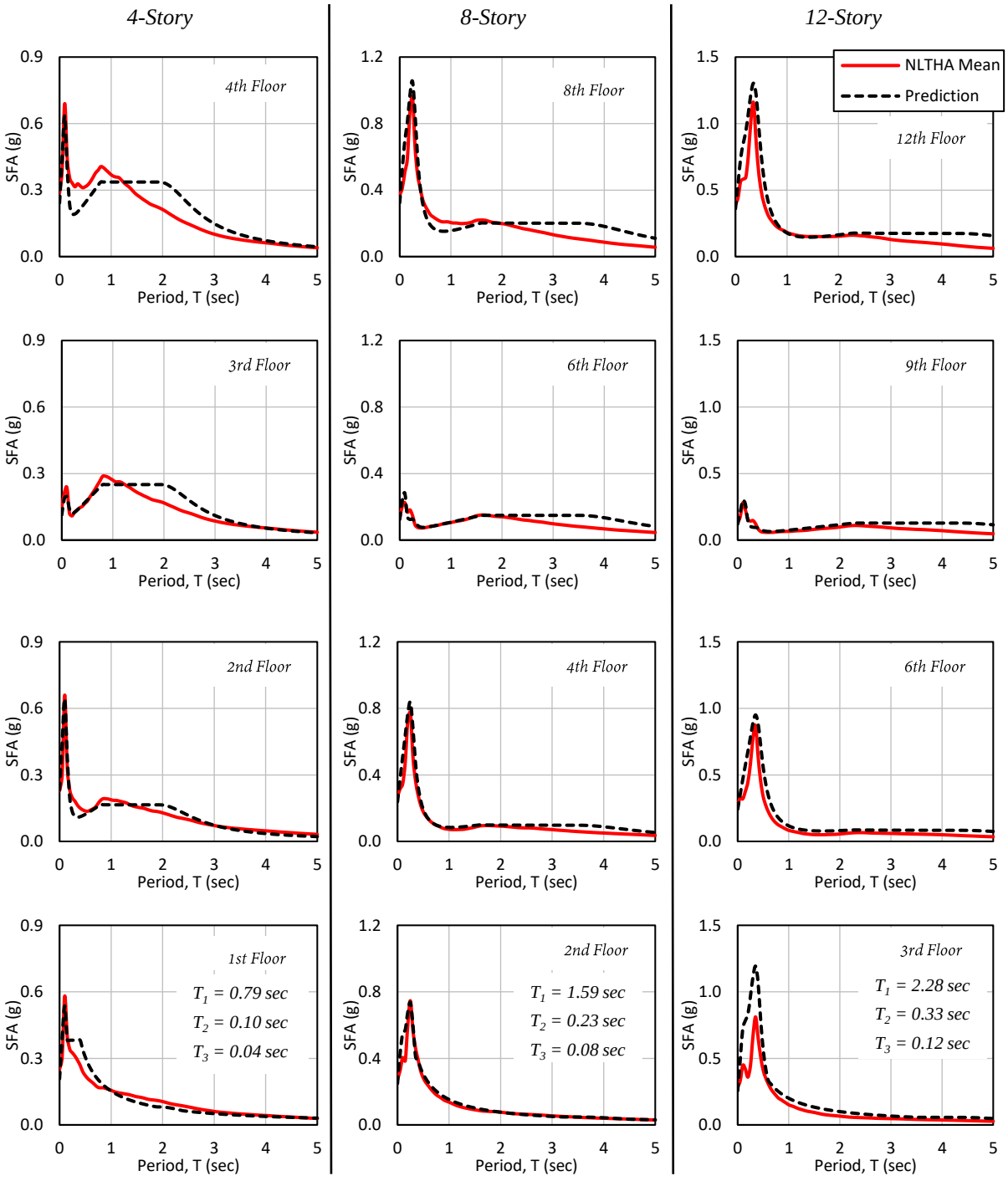

Figure 0.16 Comparison between mean floor spectra from NLTHA and estimates using transitory modal properties; rocking wall buildings, Intensity 1 (PGA = 0.225g), ξ_{NS} = 10%

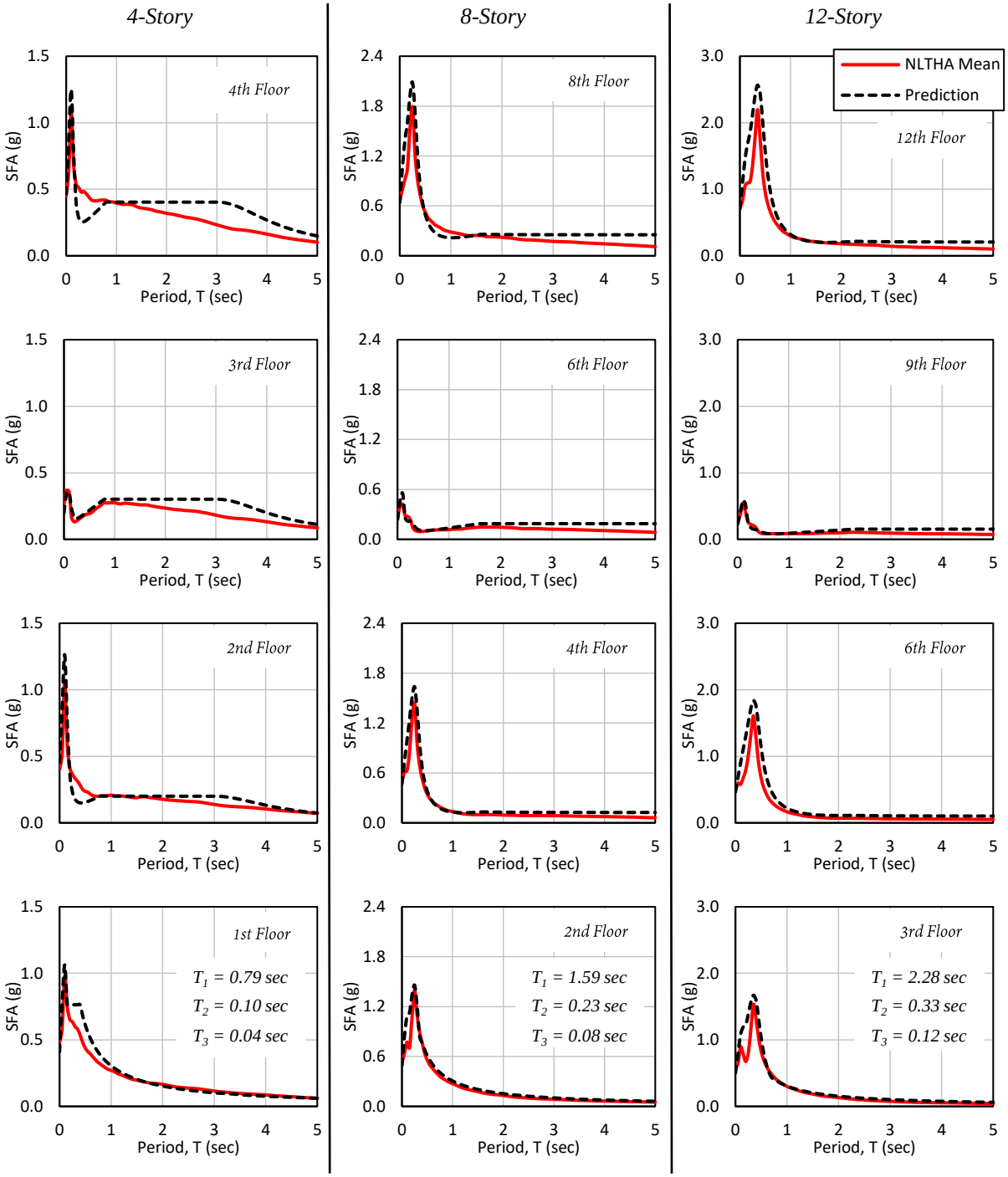

Figure 0.17 Comparison between mean floor spectra from NLTHA and estimates using transitory modal properties; rocking wall buildings, Intensity 5 (PGA = 0.450g), ξ_{NS} = 10%

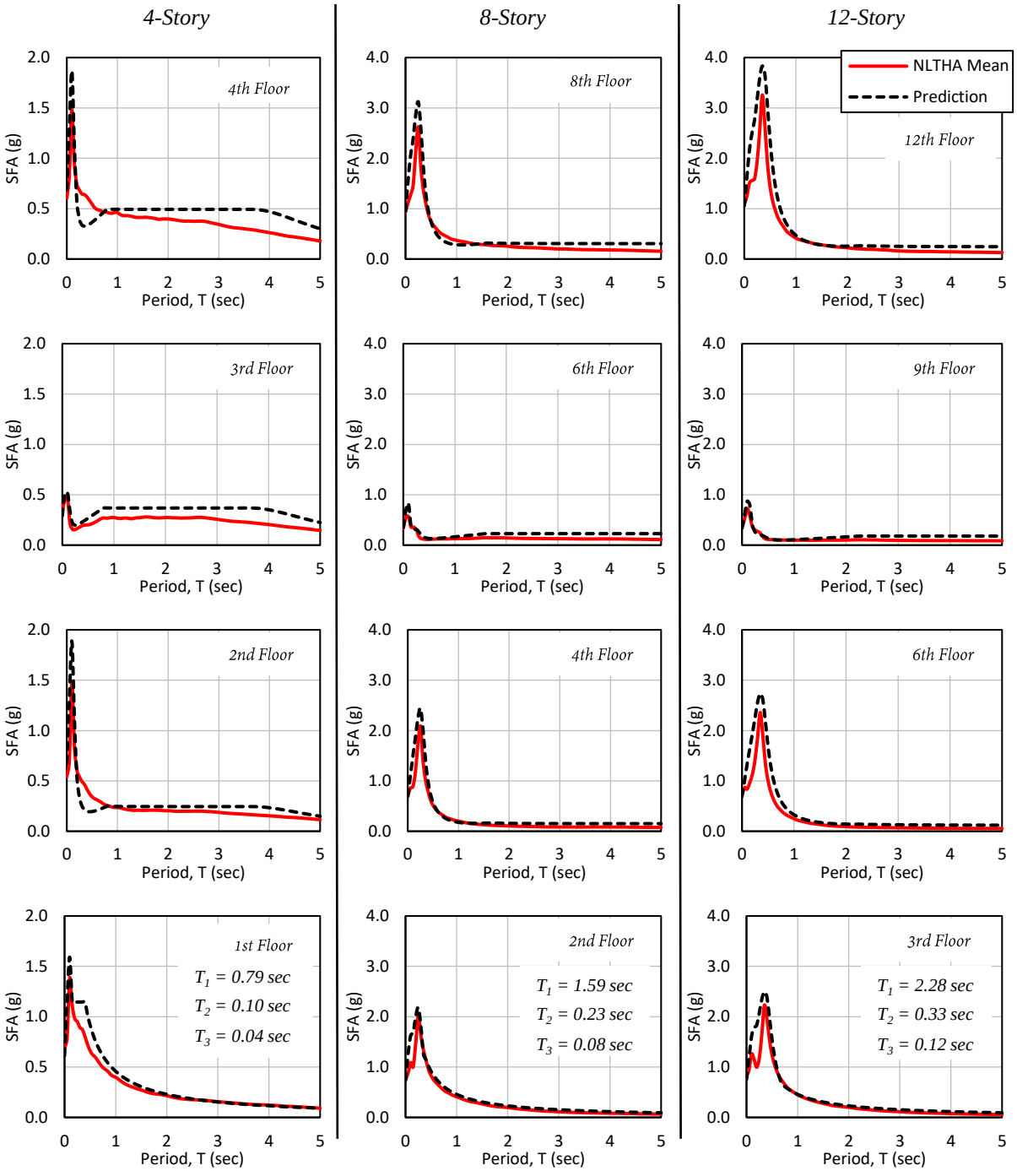

Figure 0.18 Comparison between mean floor spectra from NLTHA and estimates using transitory modal properties; rocking wall buildings, Intensity 6 (PGA = 0.675g), ξ_{NS} = 10%

C.2 Procedure that Utilizes Modal Reduction Factors

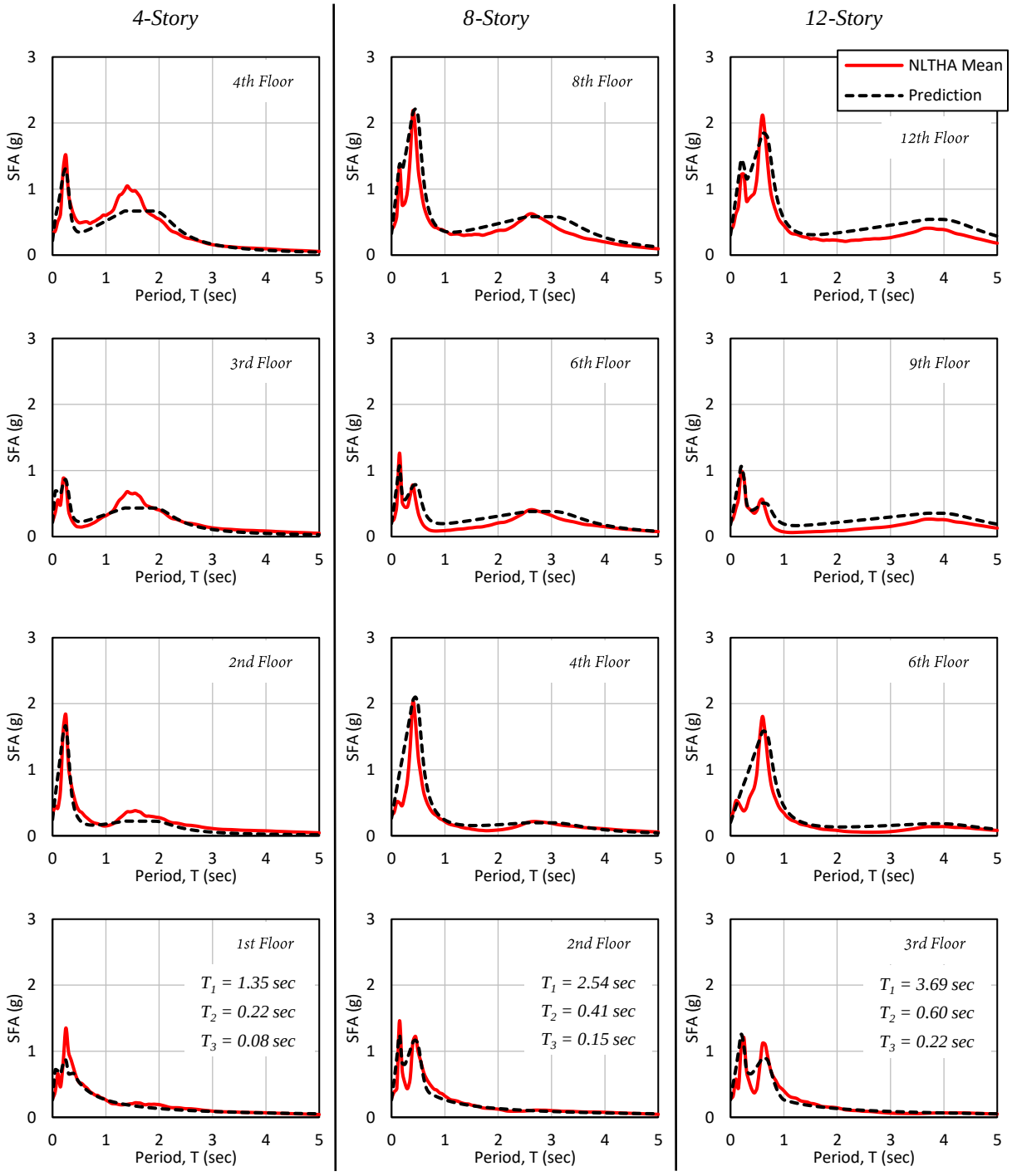

Figure 0.19 Comparison between mean floor spectra from NLTHA and estimates using modal reduction factors; RC wall buildings, Intensity 1 (PGA = 0.225 g), ξ_{NS} = 2%

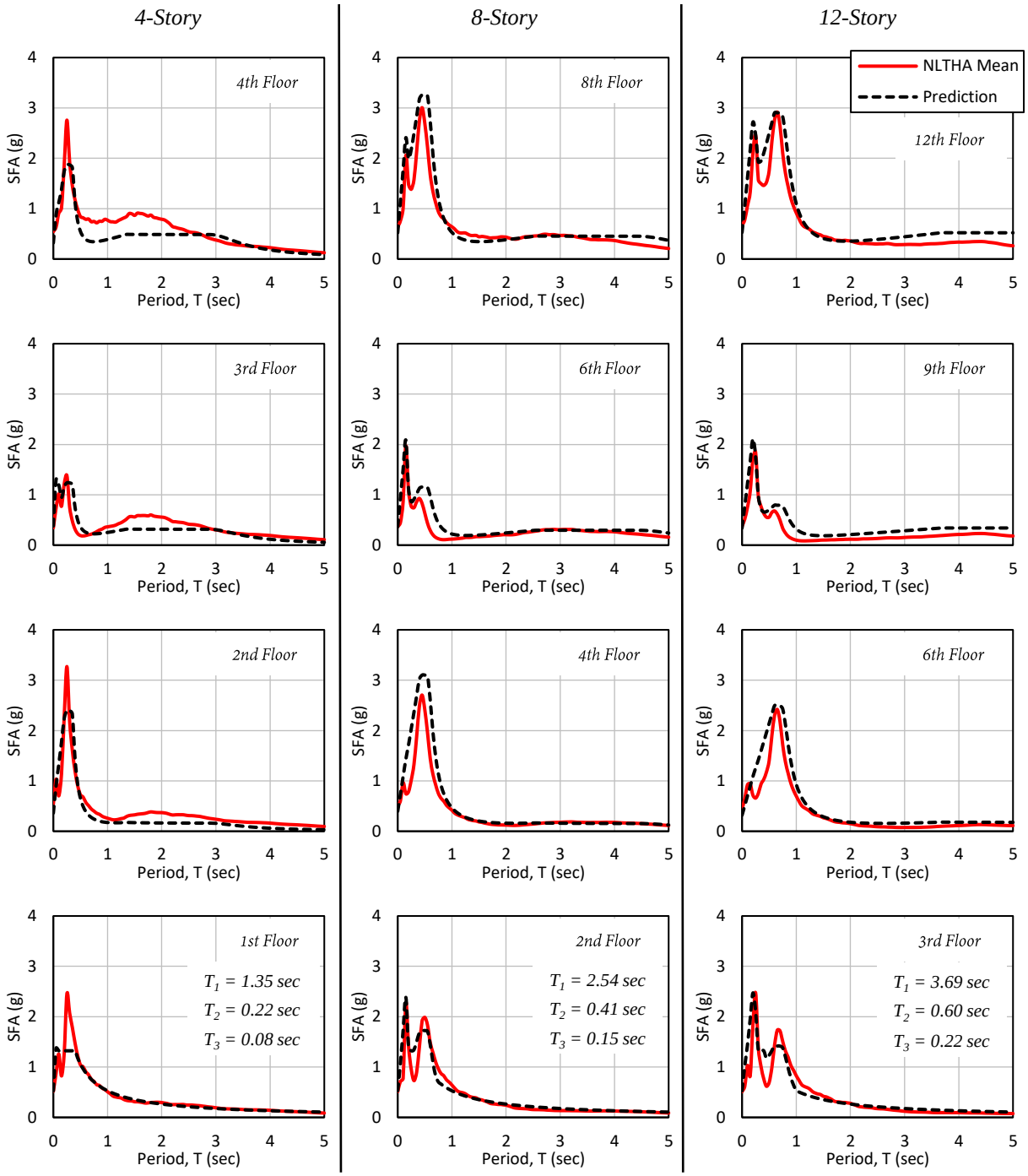

Figure 0.20 Comparison between mean floor spectra from NLTHA and estimates using modal reduction factors; RC wall buildings, Intensity 5 (PGA = 0.450 g), ξ_{NS} = 2%

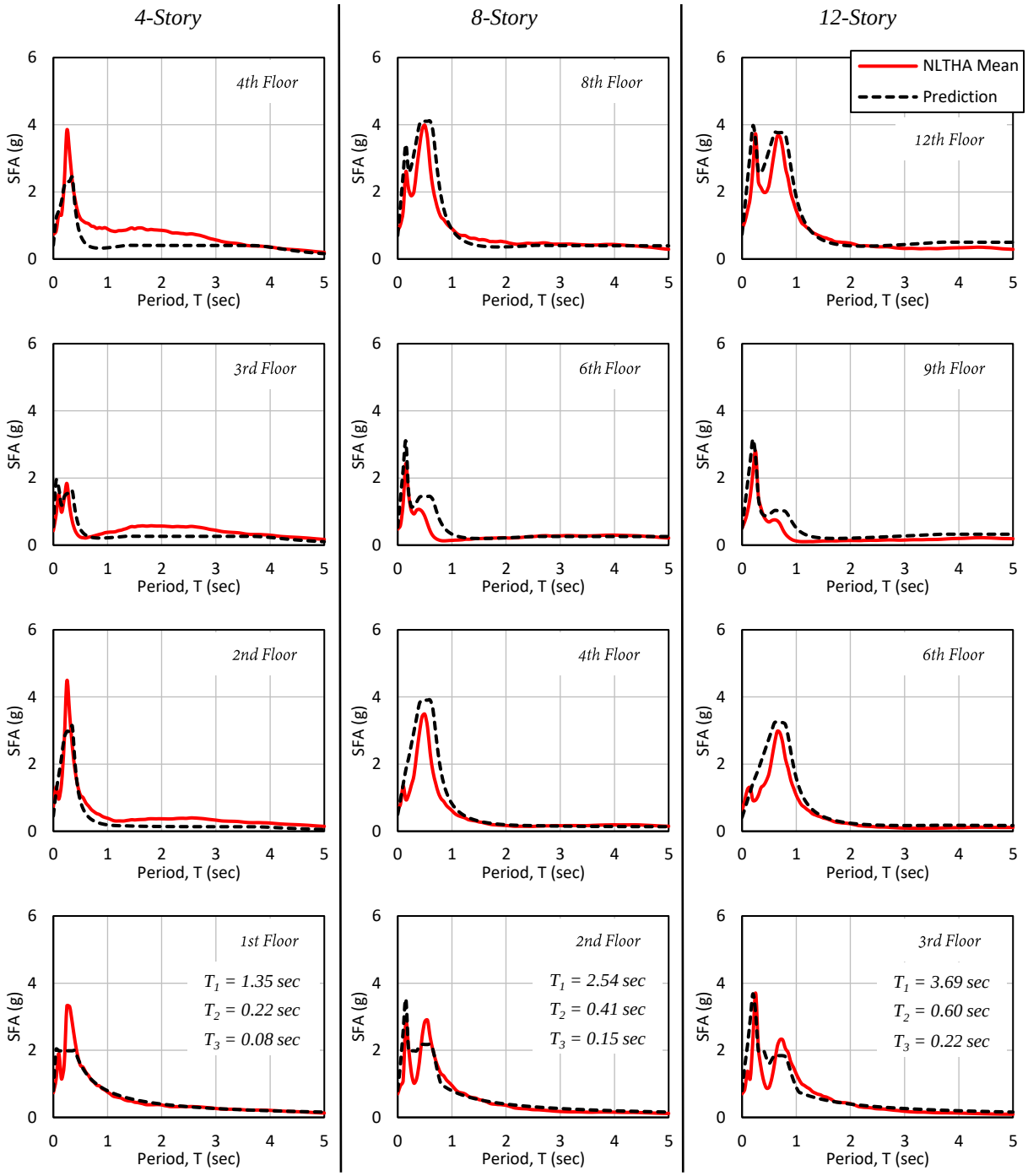

Figure 0.21 Comparison between mean floor spectra from NLTHA and estimates using modal reduction factors; RC wall buildings, Intensity 6 (PGA = 0.675 g), ξ_{NS} = 2%

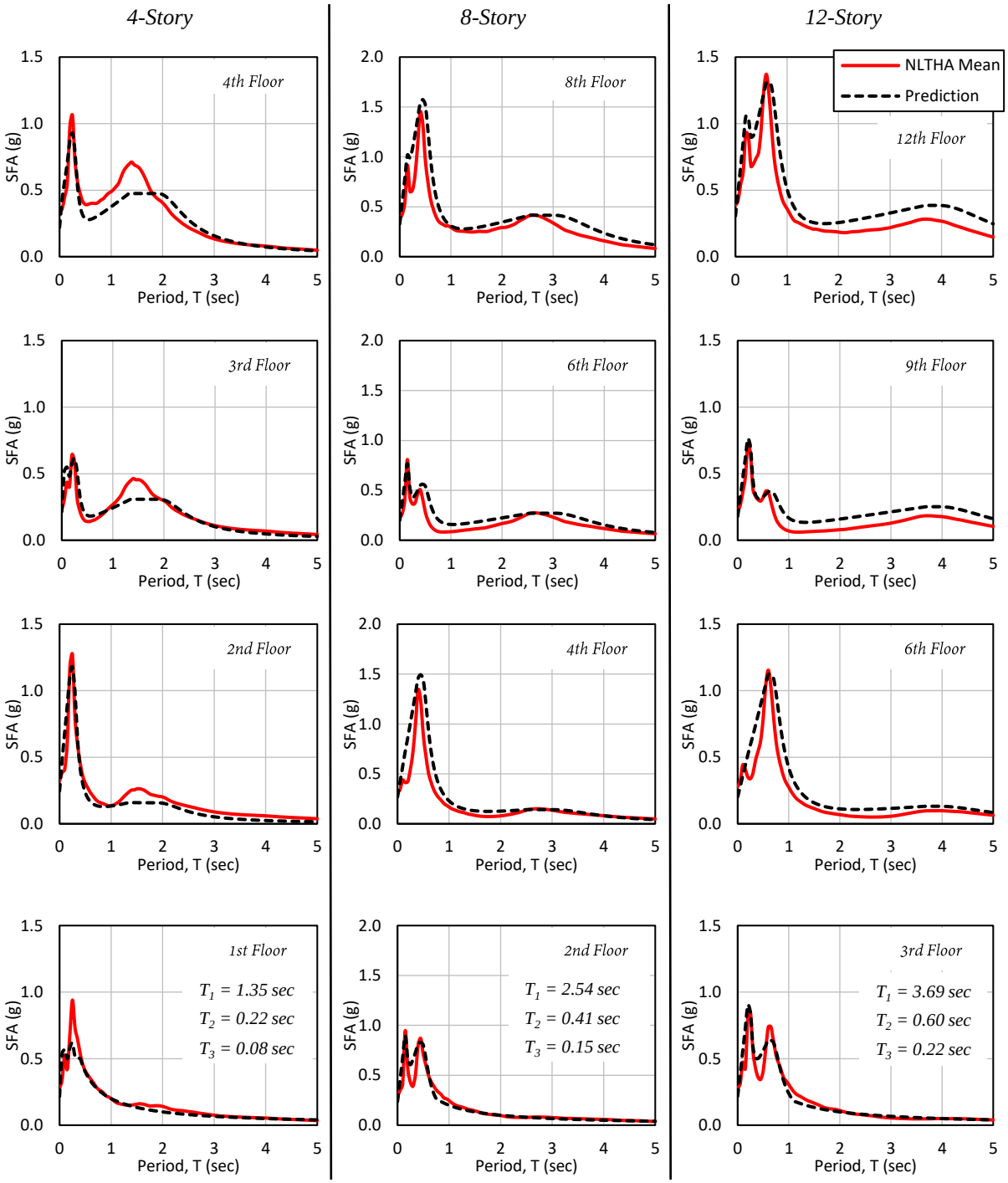

Figure 0.22 Comparison between mean floor spectra from NLTHA and estimates using modal reduction factors; RC wall buildings, Intensity 1 (PGA = 0.225 g), ξ_{NS} = 5%

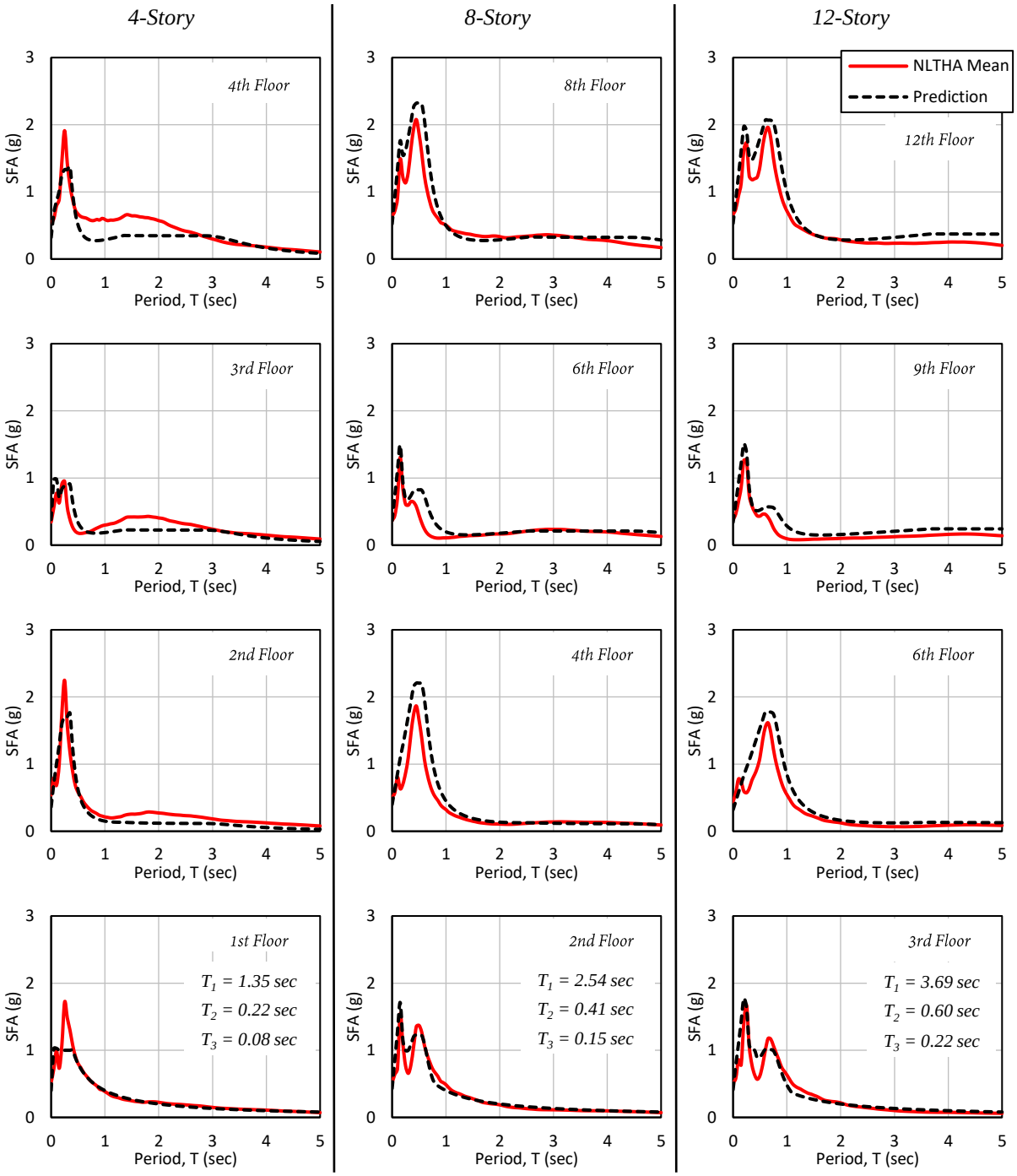

Figure 0.23 Comparison between mean floor spectra from NLTHA and estimates using modal reduction factors; RC wall buildings, Intensity 5 (PGA = 0.450 g), ξ_{NS} = 5%

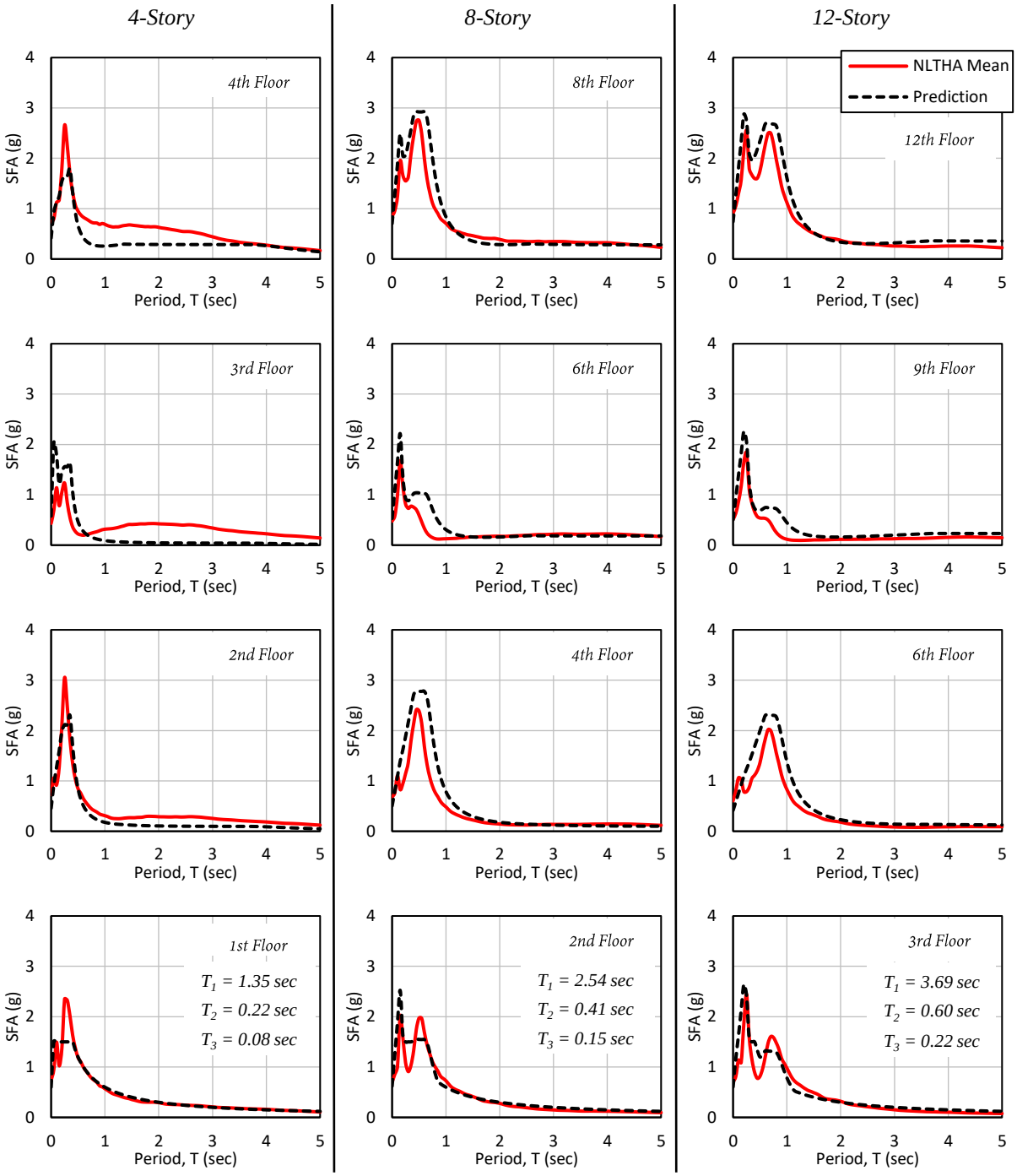

Figure 0.24 Comparison between mean floor spectra from NLTHA and estimates using modal reduction factors; RC wall buildings, Intensity 6 (PGA = 0.675 g), ξ_{NS} = 5%

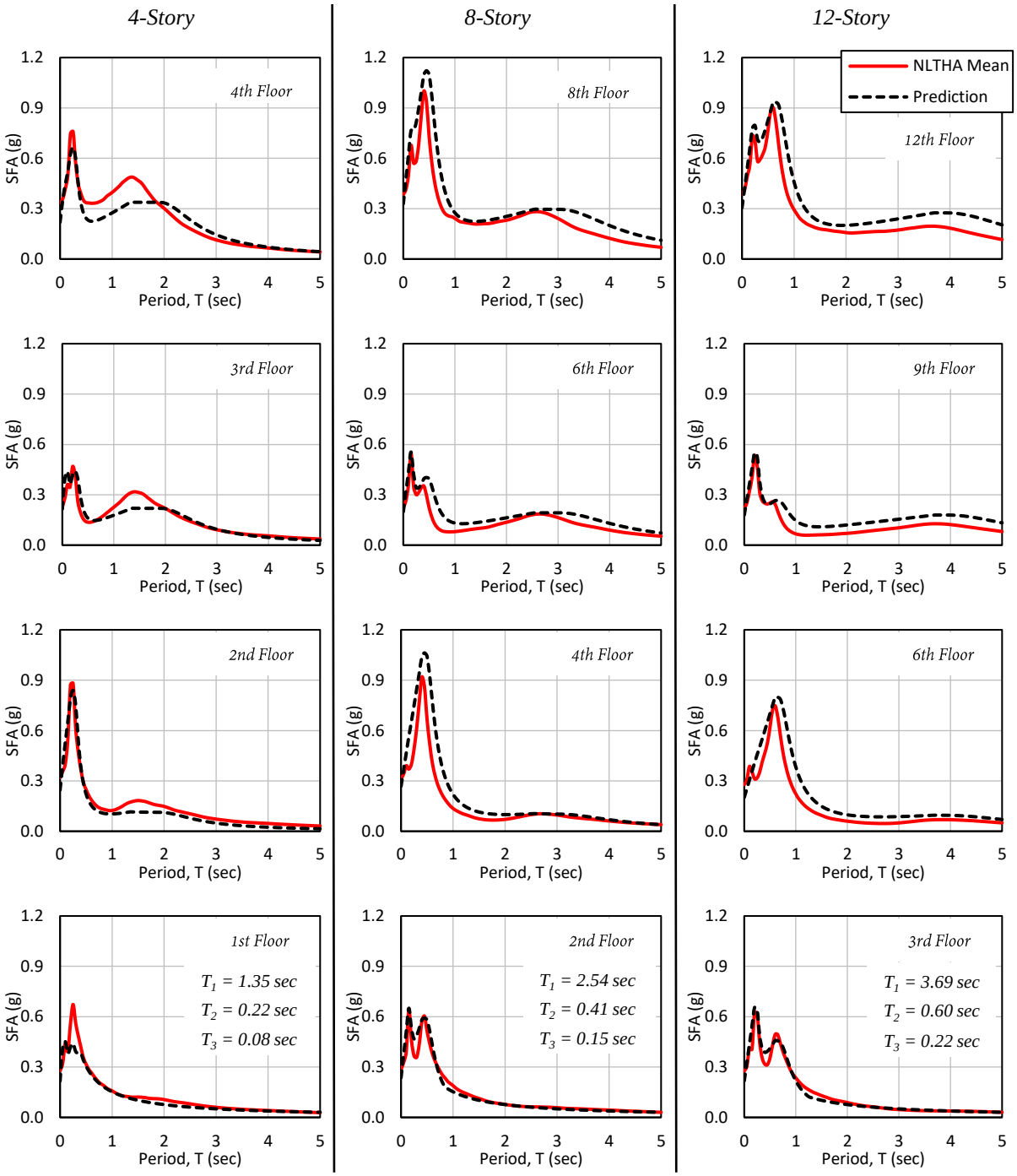

Figure 0.25 Comparison between mean floor spectra from NLTHA and estimates using modal reduction factors; RC wall buildings, Intensity 1 (PGA = 0.225 g), ξ_{NS} = 10%

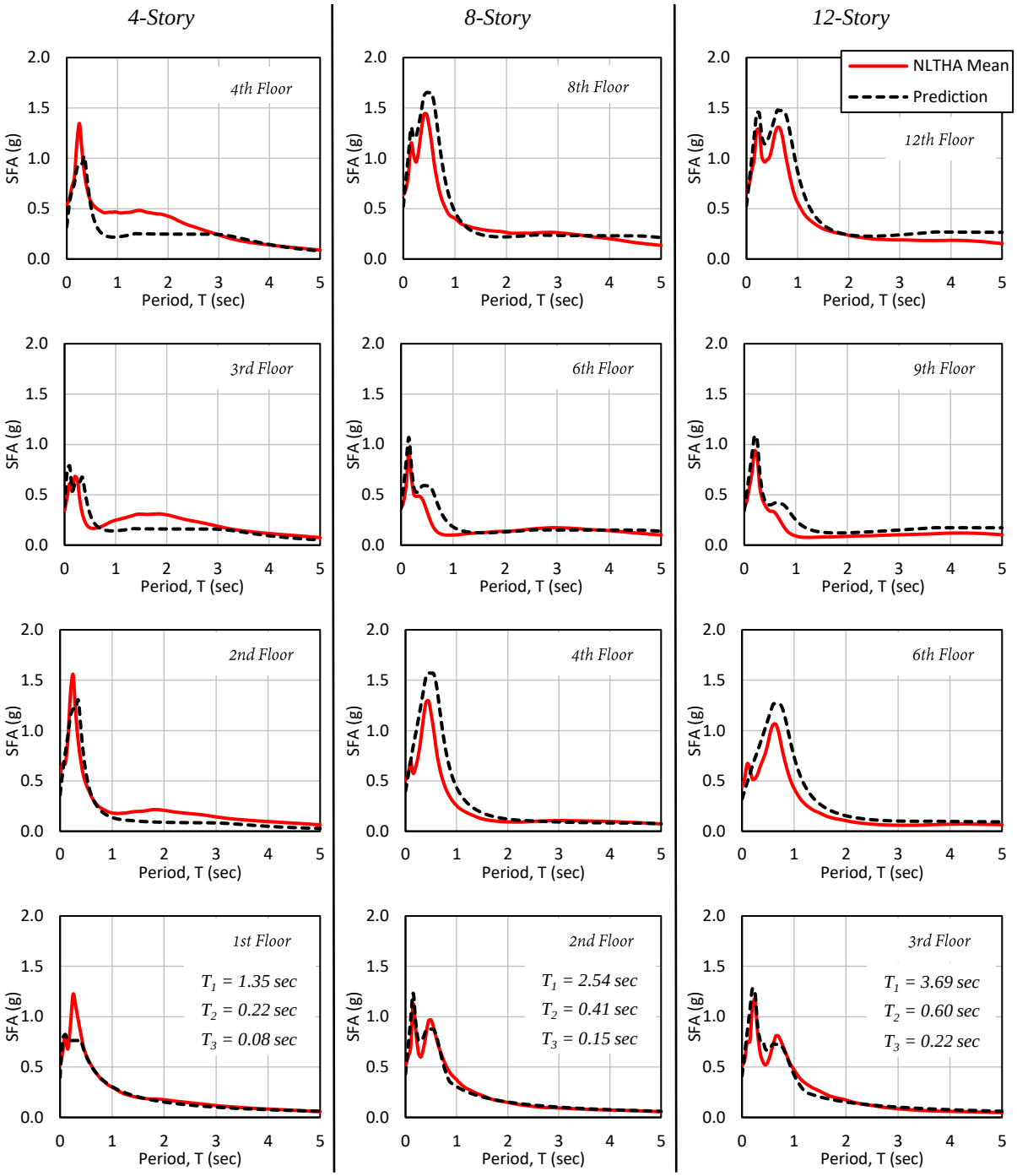

Figure 0.26 Comparison between mean floor spectra from NLTHA and estimates using modal reduction factors; RC wall buildings, Intensity 5 (PGA = 0.450 g), ξ_{NS} = 10%

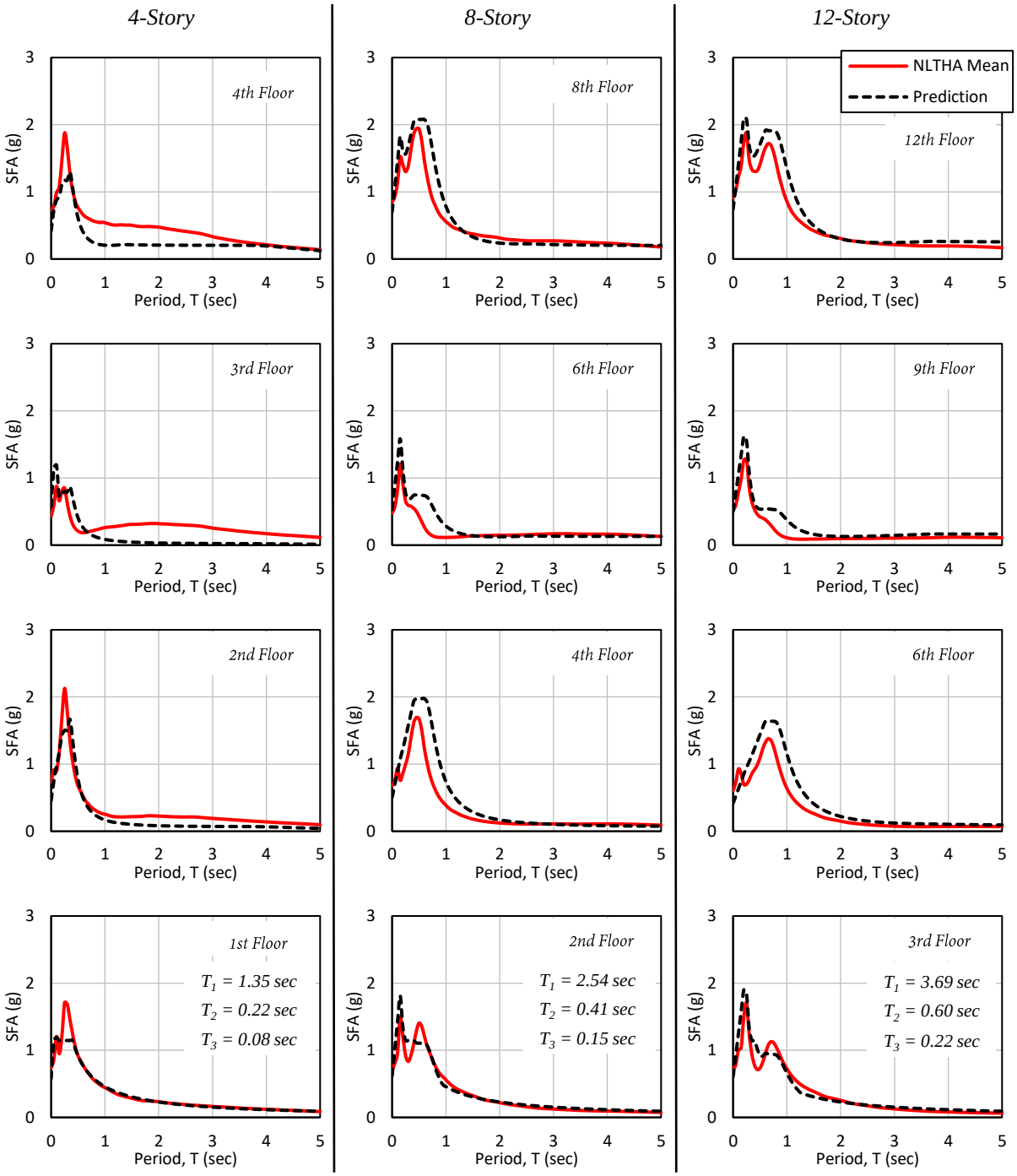

Figure 0.27 Comparison between mean floor spectra from NLTHA and estimates using modal reduction factors; RC wall buildings, Intensity 6 (PGA = 0.675 g), ξ_{NS} = 10%

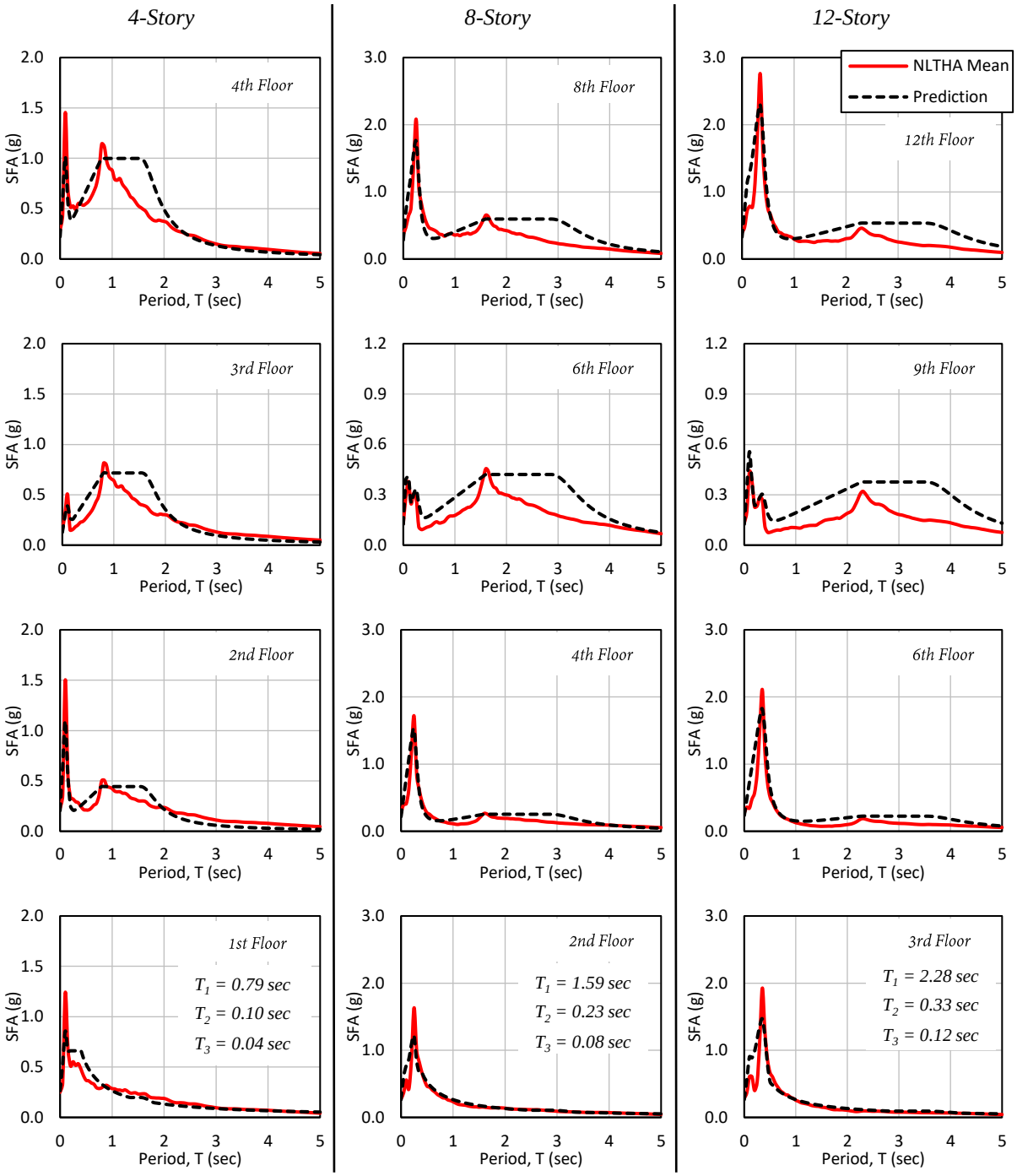

Figure 0.28 Comparison between mean floor spectra from NLTHA and estimates using modal reduction factors; rocking wall buildings, Intensity 1 (PGA = 0.225 g), ξ_{NS} = 2%

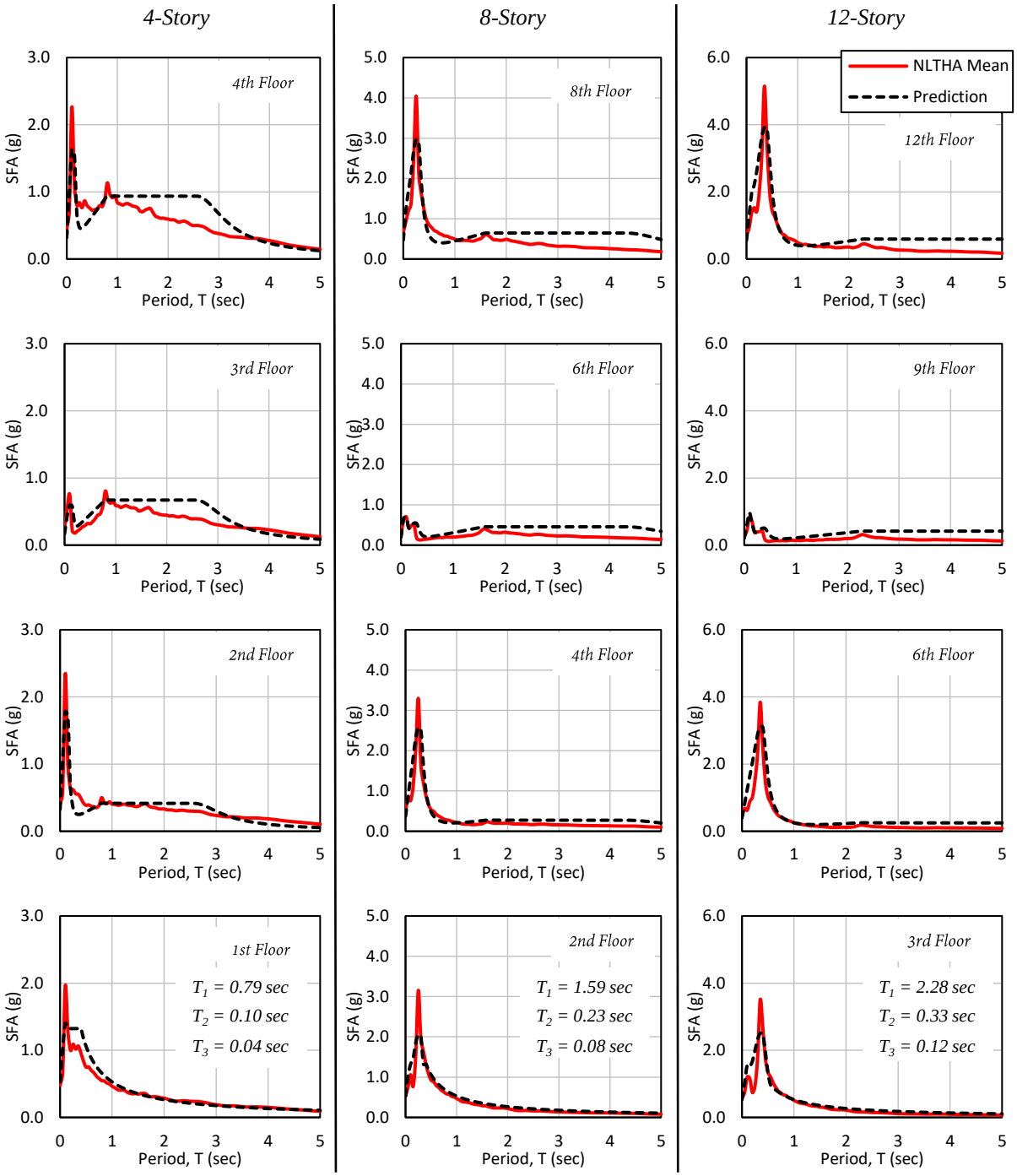

Figure 0.29 Comparison between mean floor spectra from NLTHA and estimates using modal reduction factors; rocking wall buildings, Intensity 5 (PGA = 0.450 g), ξ_{NS} = 2%

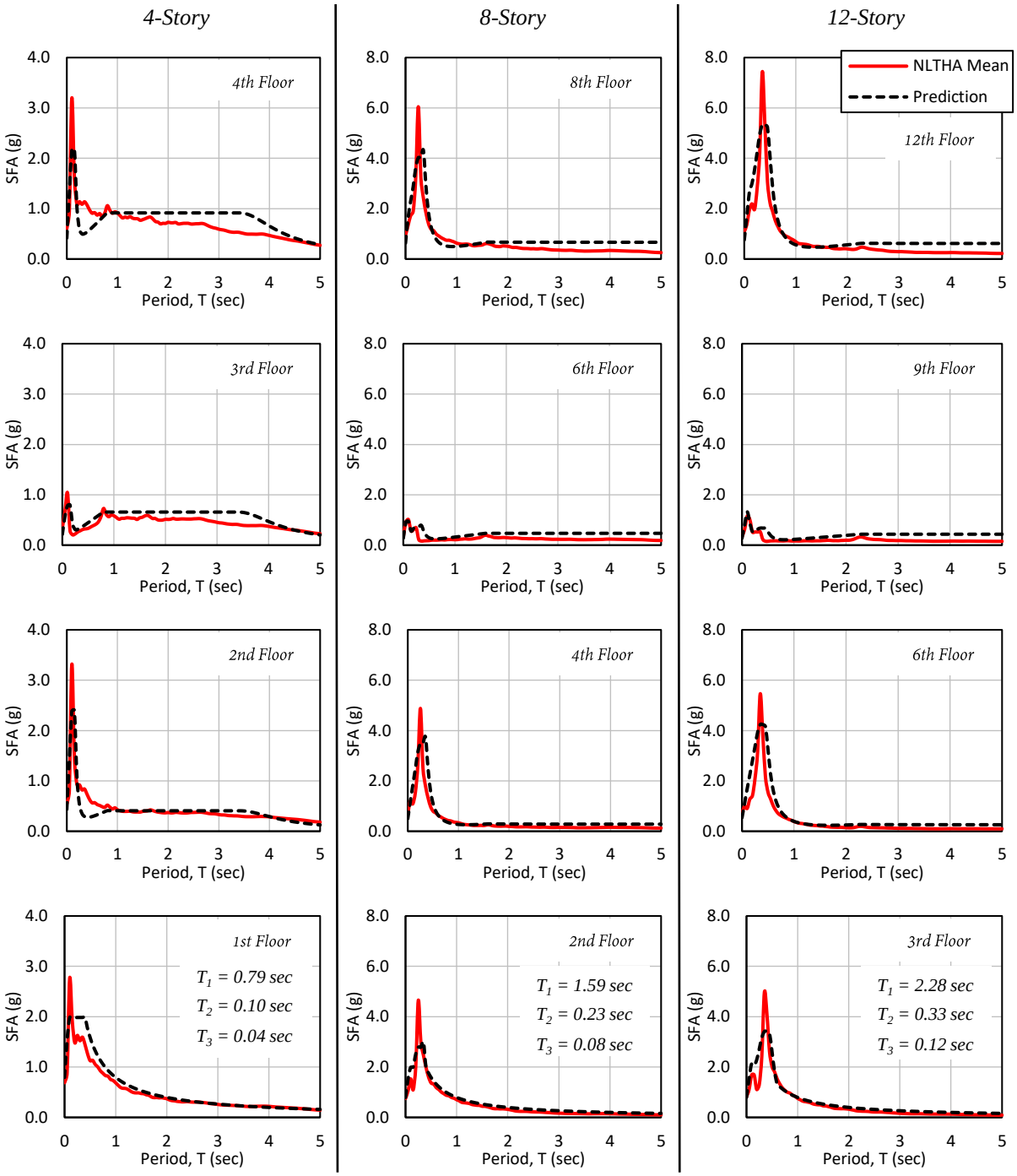

Figure 0.30 Comparison between mean floor spectra from NLTHA and estimates using modal reduction factors; rocking wall buildings, Intensity 6 (PGA = 0.675 g), ξ_{NS} = 2%

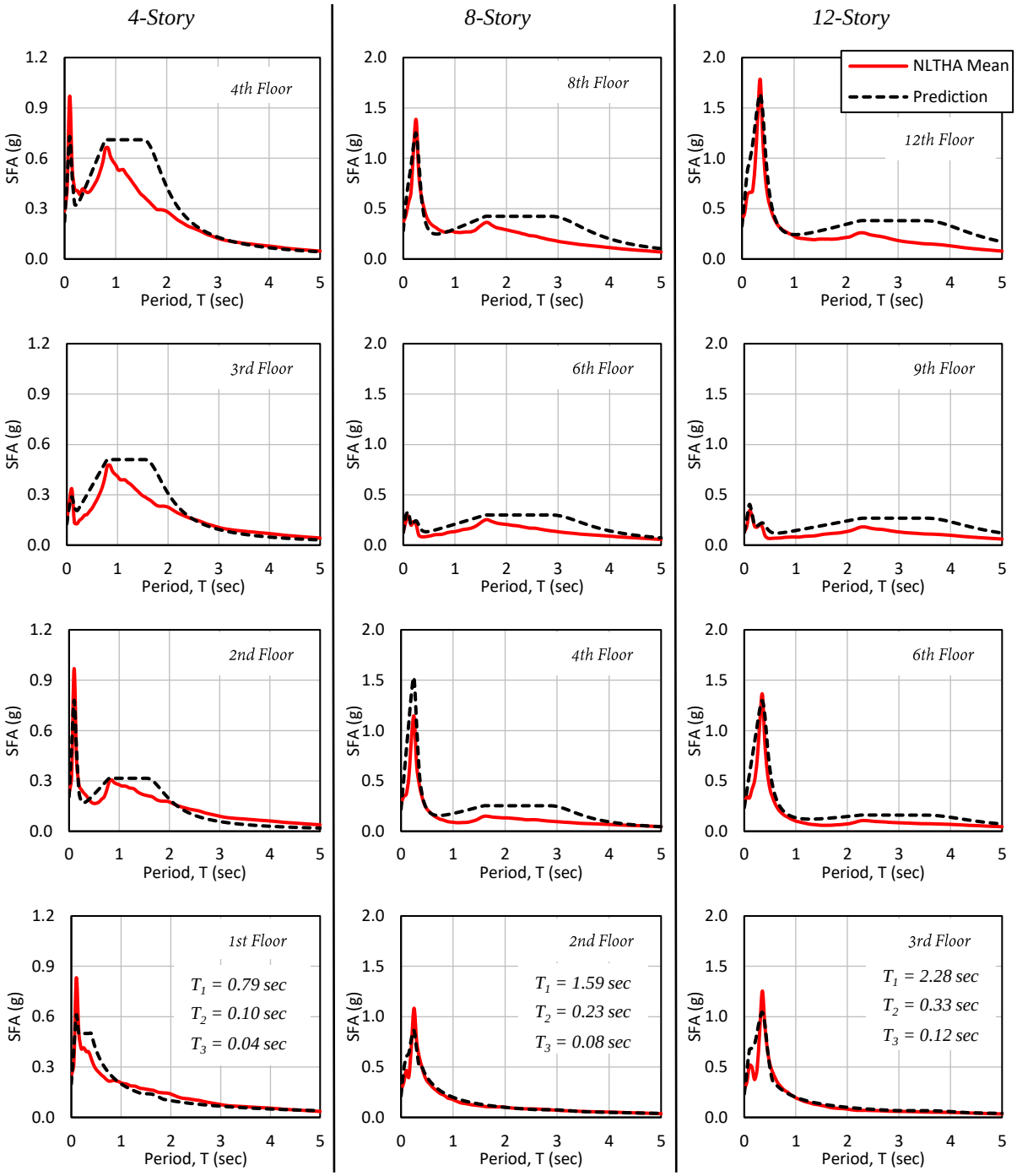

Figure 0.31 Comparison between mean floor spectra from NLTHA and estimates using modal reduction factors; rocking wall buildings, Intensity 1 (PGA = 0.225 g), ξ_{NS} = 5%

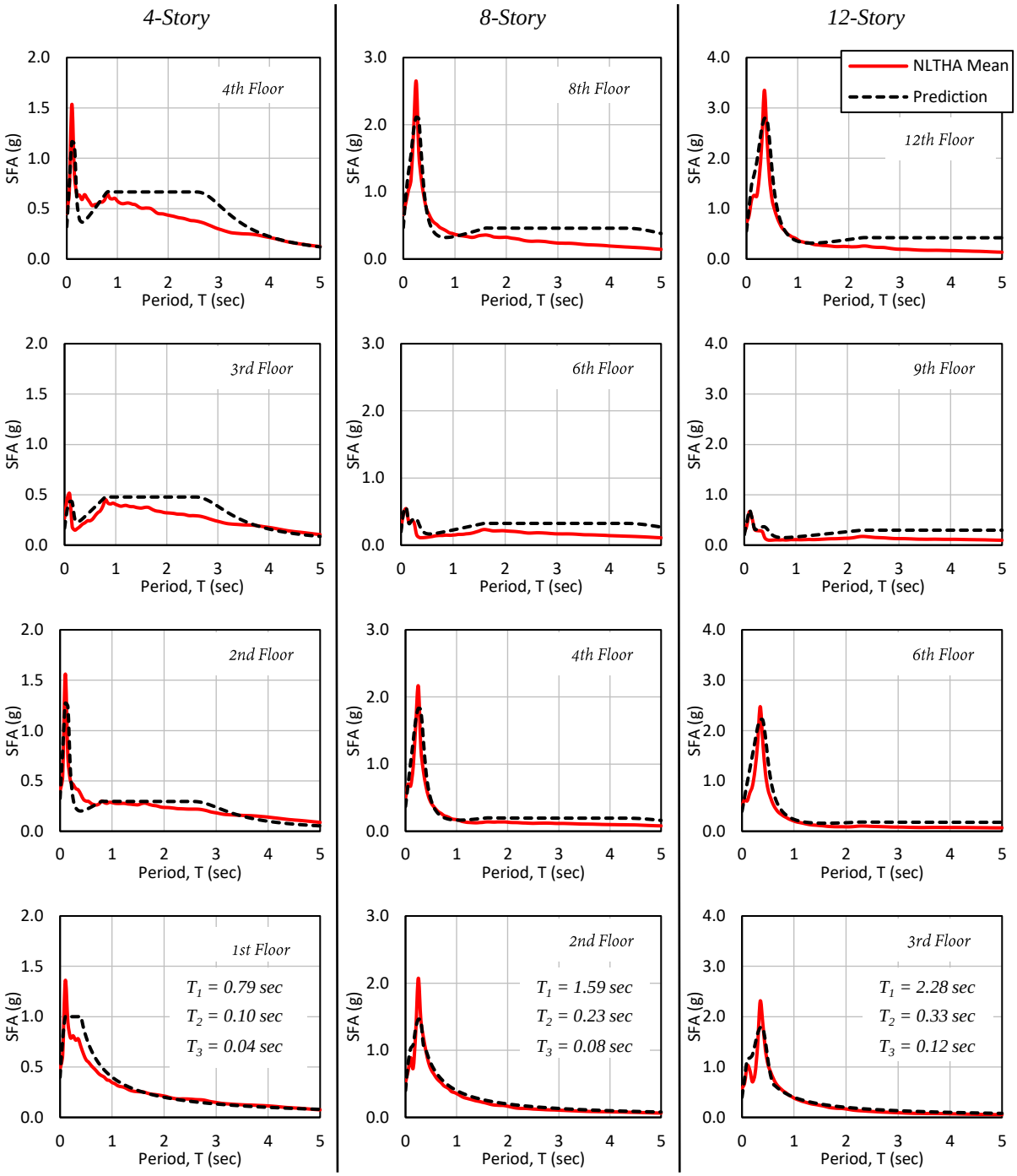

Figure 0.32 Comparison between mean floor spectra from NLTHA and estimates using modal reduction factors; rocking wall buildings, Intensity 5 (PGA = 0.450 g), ξ_{NS} = 5%

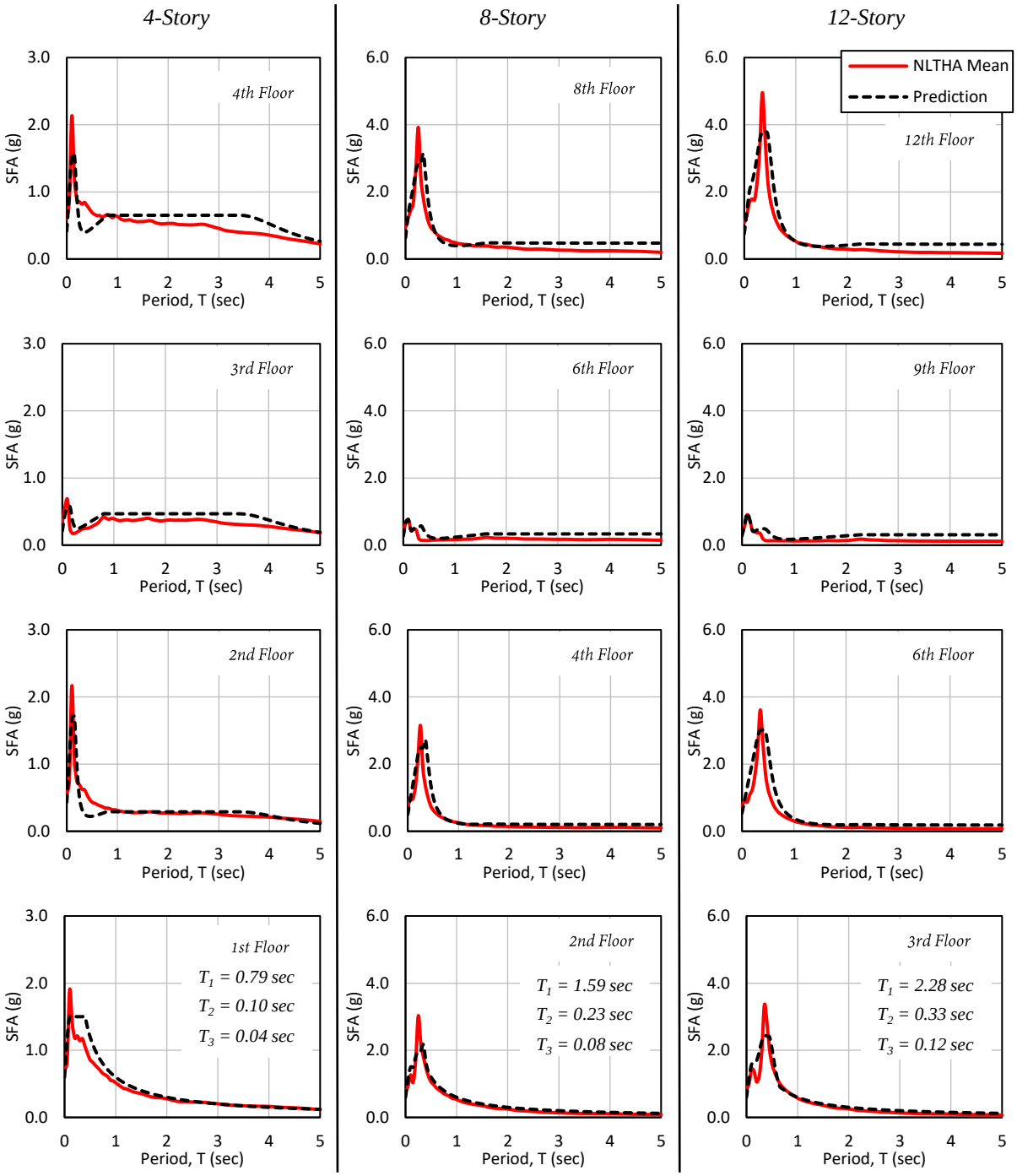

Figure 0.33 Comparison between mean floor spectra from NLTHA and estimates using modal reduction factors; rocking wall buildings, Intensity 6 (PGA = 0.675 g), ξ_{NS} = 5%

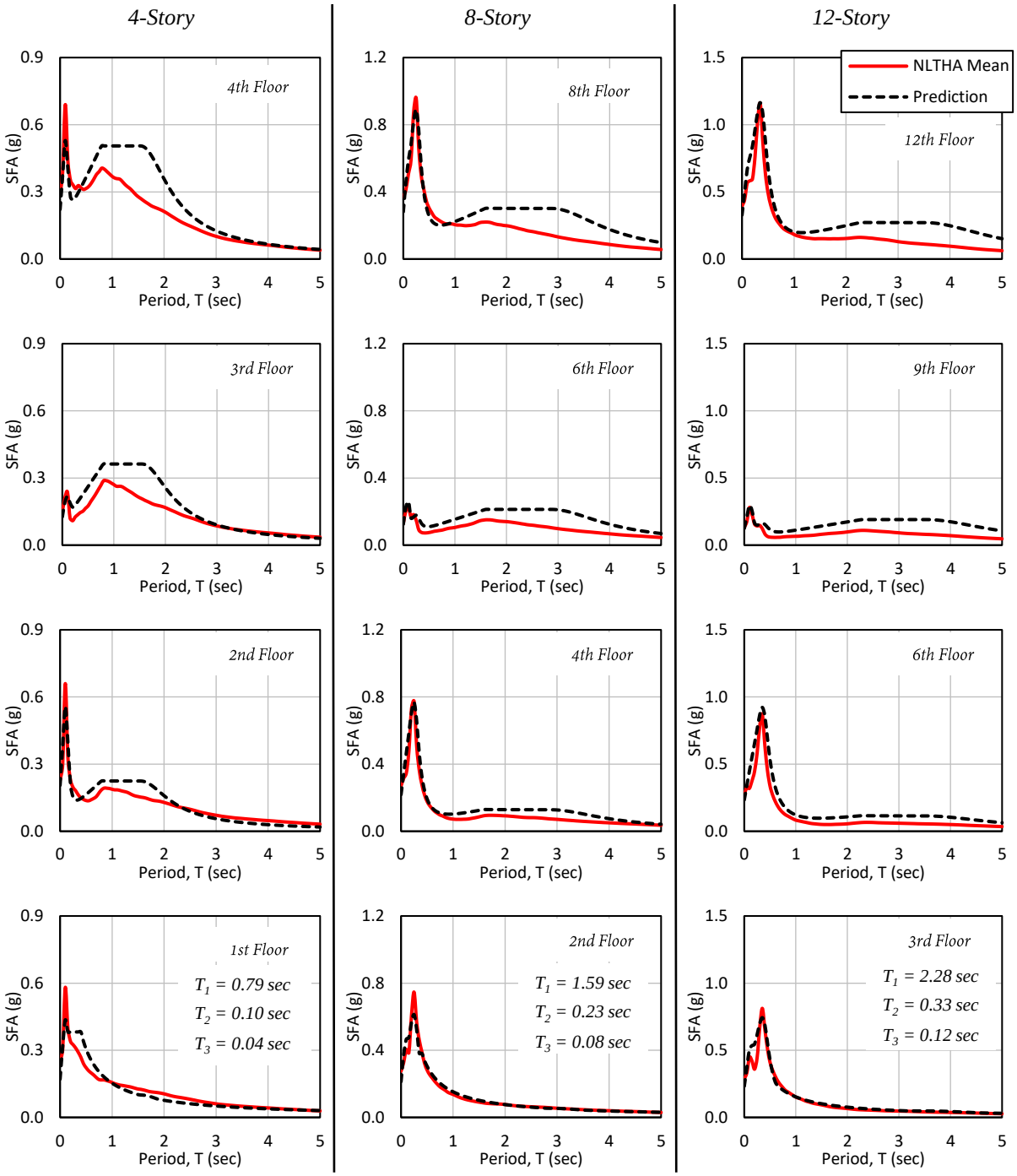

Figure 0.34 Comparison between mean floor spectra from NLTHA and estimates using modal reduction factors; rocking wall buildings, Intensity 1 (PGA = 0.225 g), ξ_{NS} = 10%

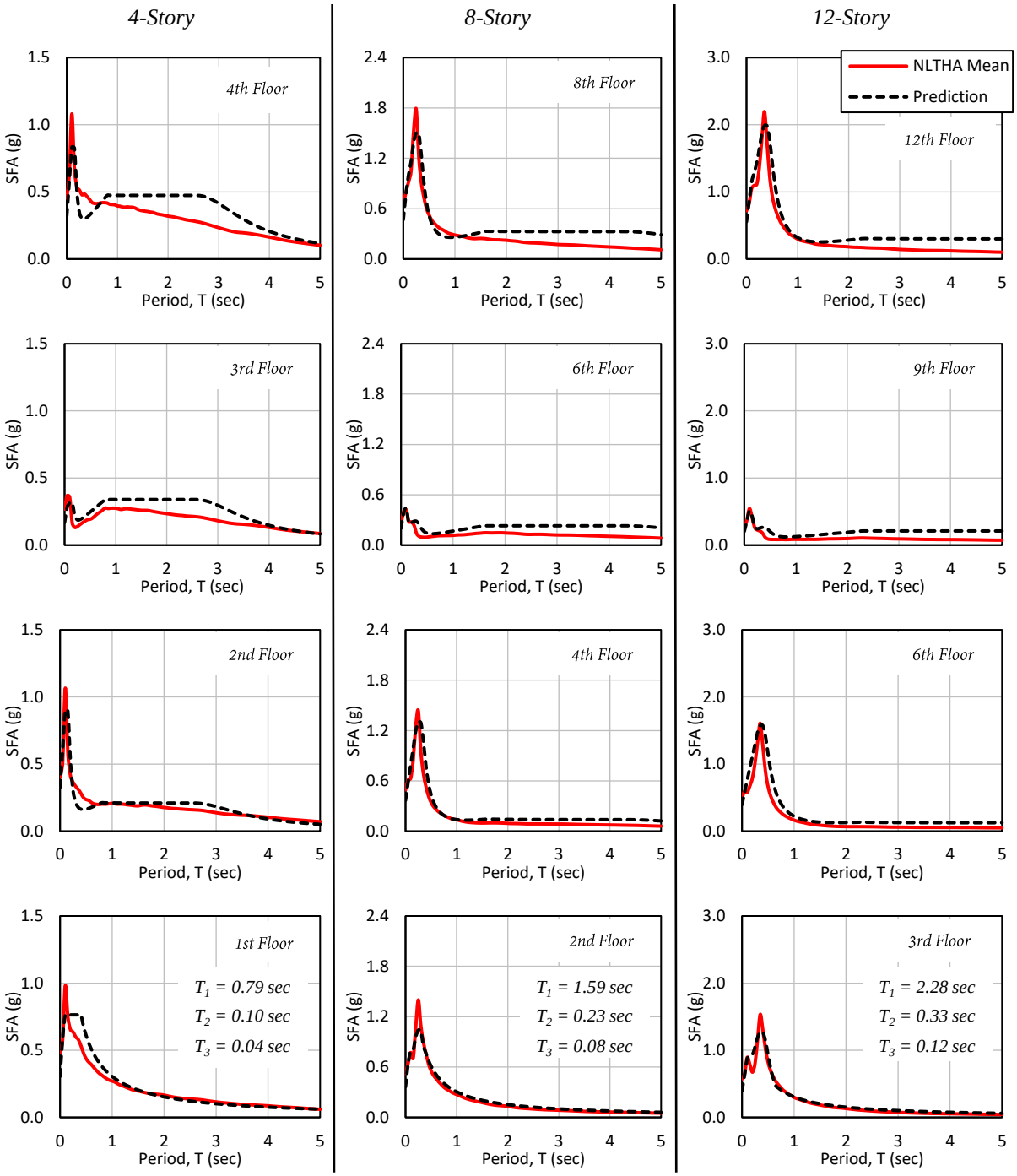

Figure 0.35 Comparison between mean floor spectra from NLTHA and estimates using modal reduction factors; rocking wall buildings, Intensity 5 (PGA = 0.450 g), ξ_{NS} = 10%

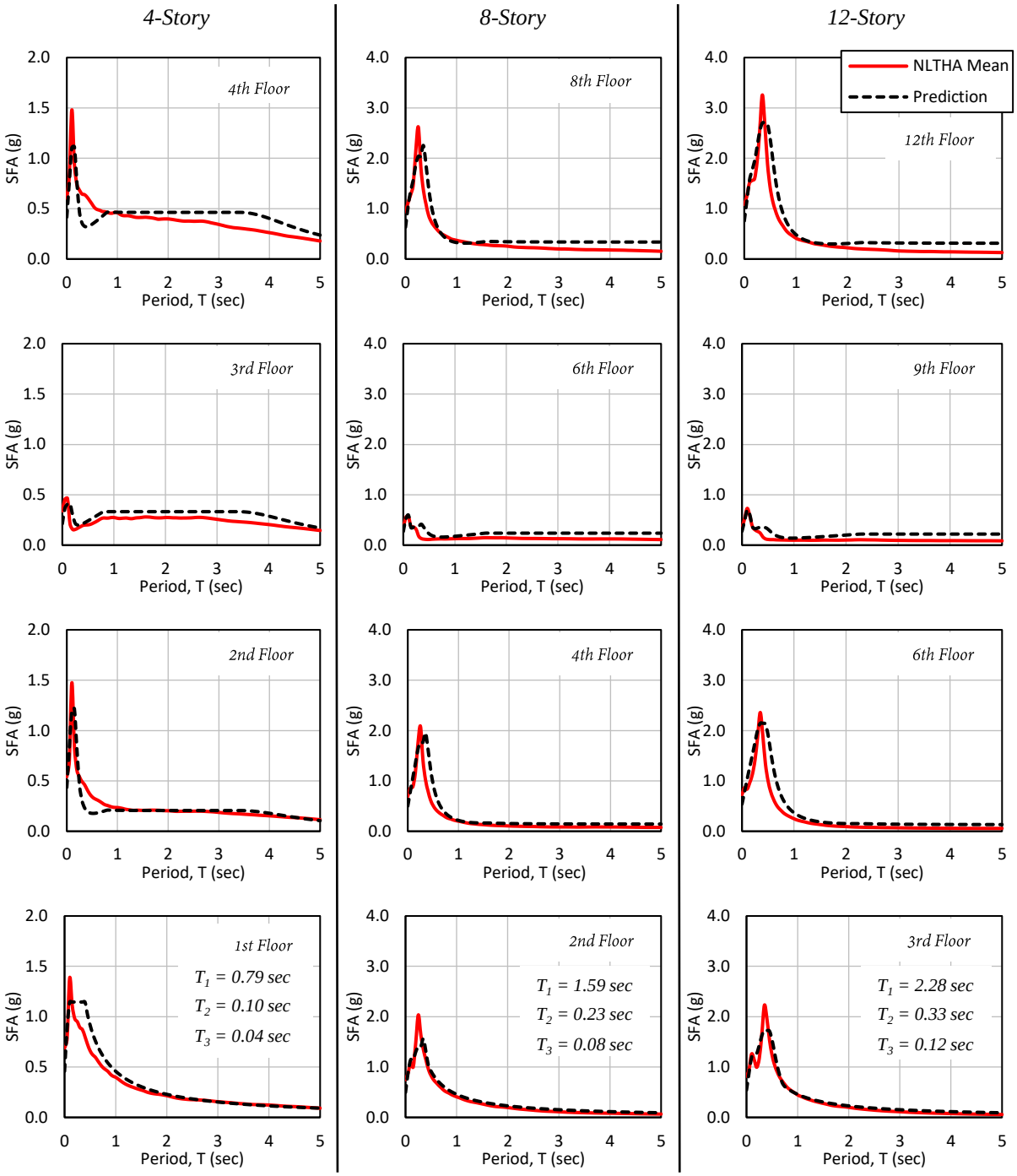

Figure 0.36 Comparison between mean floor spectra from NLTHA and estimates using modal reduction factors; rocking wall buildings, Intensity 6 (PGA = 0.675 g), ξ_{NS} = 10%

C.3 Procedure that Utilizes Dynamics of Distributed-mass Systems

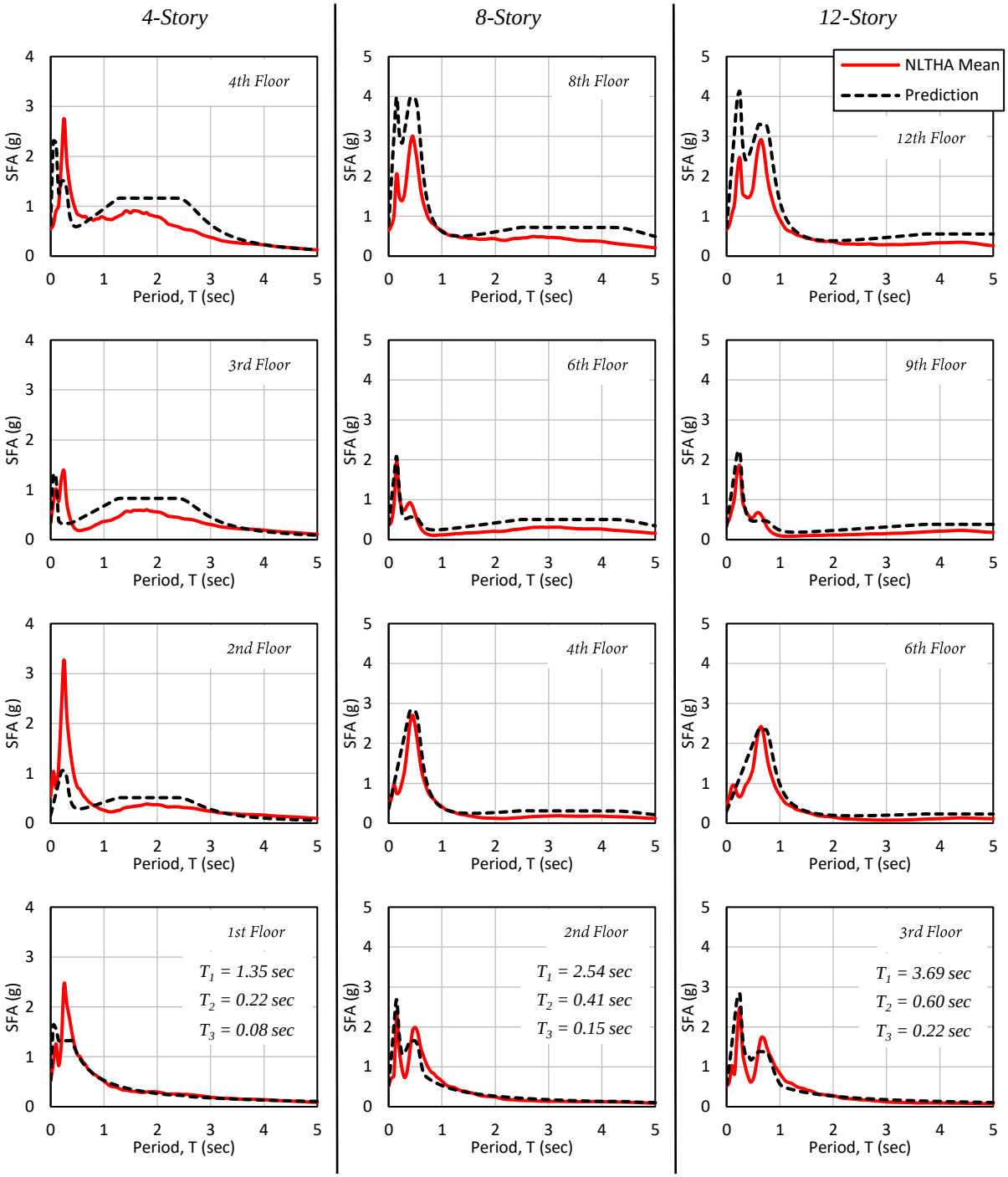

Figure 0.37 Comparison between mean floor spectra from NLTHA and estimates using closed-form modal properties of a continuous cantilever beam; RC wall buildings, Intensity 5 (PGA = 0.450 g), ξ_{NS} = 2%

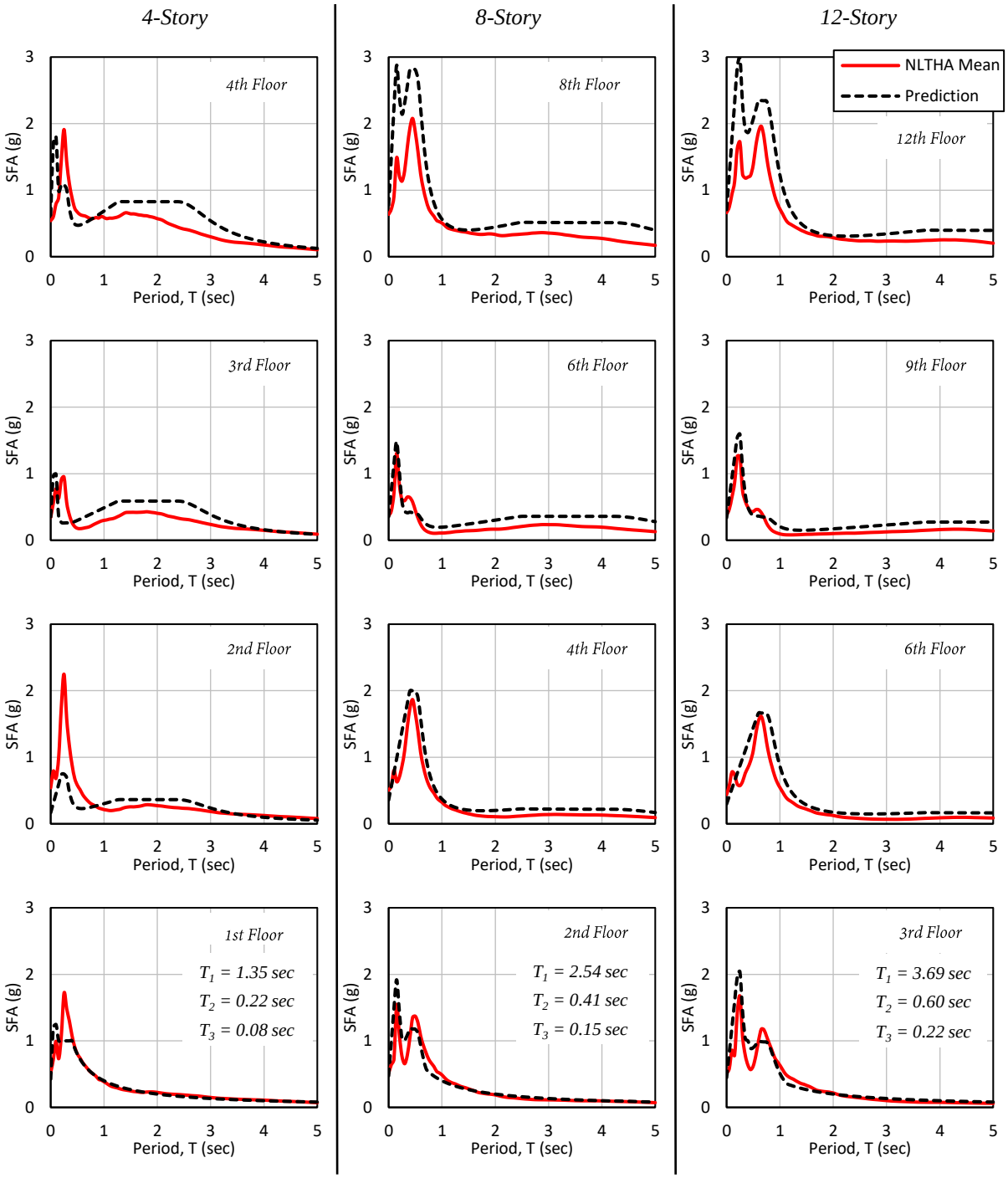

Figure 0.38 Comparison between mean floor spectra from NLTHA and estimates using closed-form modal properties of a continuous cantilever beam; RC wall buildings, Intensity 5 (PGA = 0.450 g), ξ_{NS} = 5%

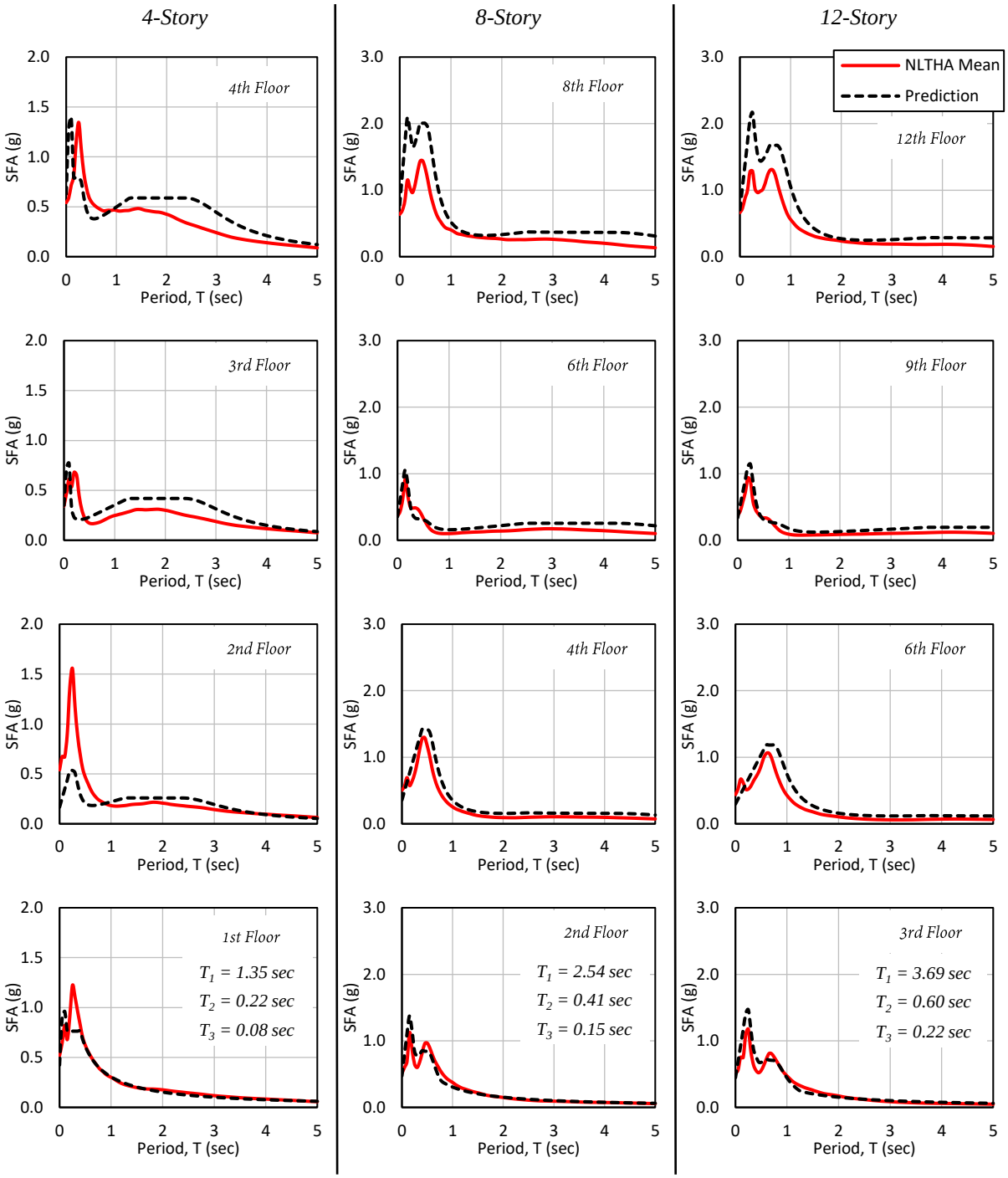

Figure 0.39 Comparison between mean floor spectra from NLTHA and estimates using closed-form modal properties of a continuous cantilever beam; RC wall buildings, Intensity 5 (PGA = 0.450 g), ξ_{NS} = 10%

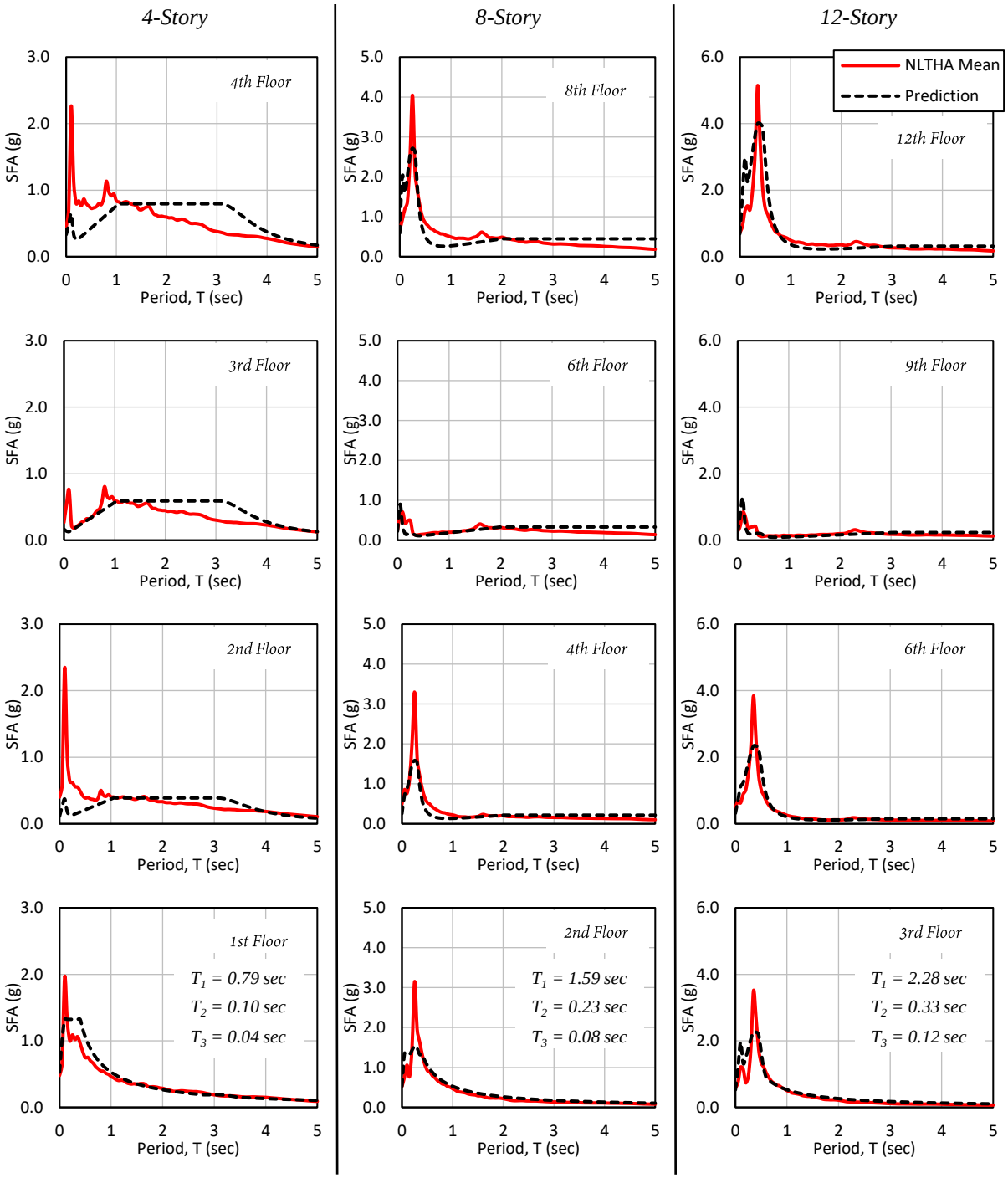

Figure 0.40 Comparison between mean floor spectra from NLTHA and estimates using closed-form modal properties of a fully-pinned continuous cantilever beam; rocking wall buildings, Intensity 5 (PGA = 0.450 g), ξ_{NS} = 2%

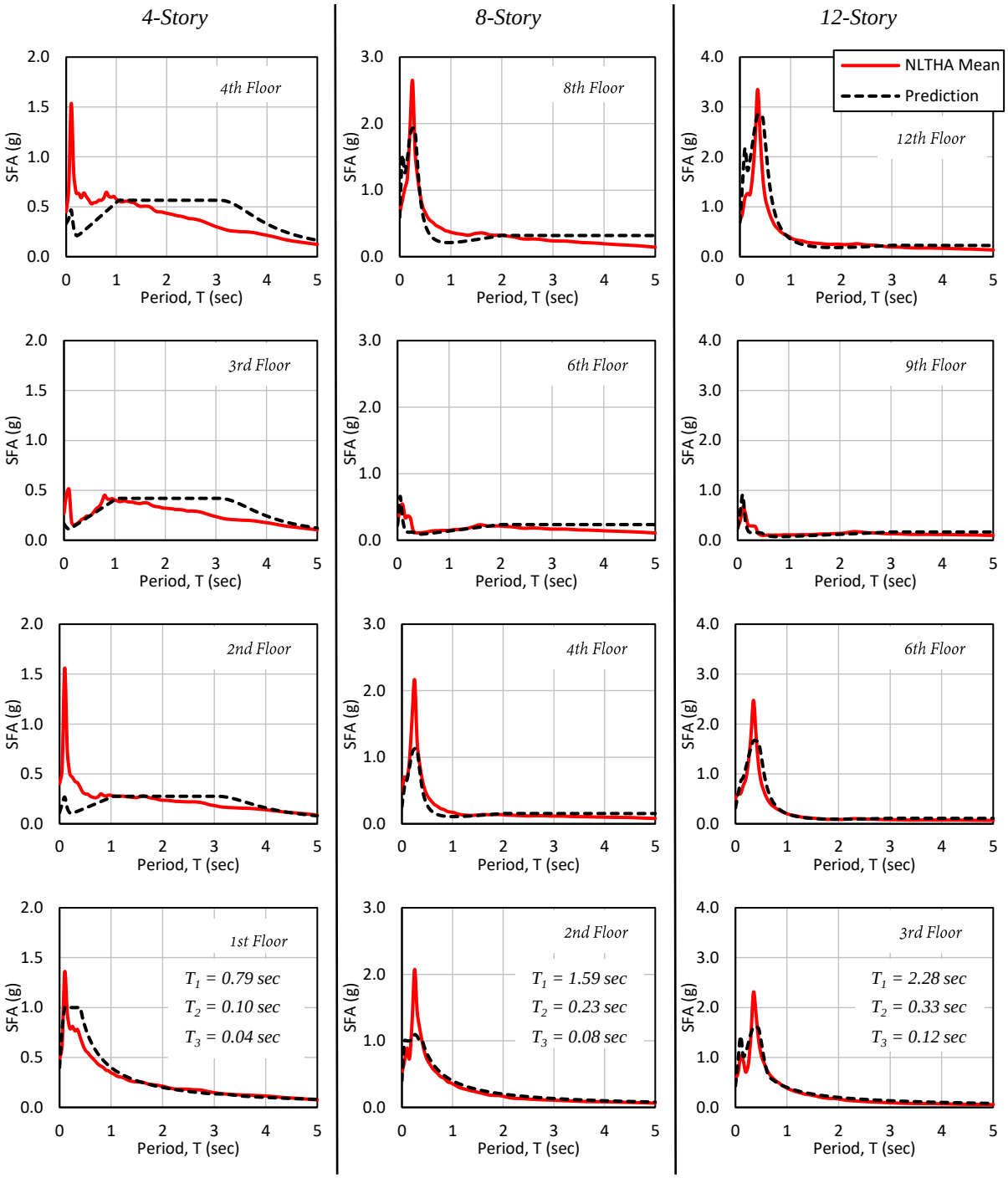

Figure 0.41 Comparison between mean floor spectra from NLTHA and estimates using closed-form modal properties of a fully-pinned continuous cantilever beam; rocking wall buildings, Intensity 5 (PGA = 0.450 g), ξ_{NS} = 5%

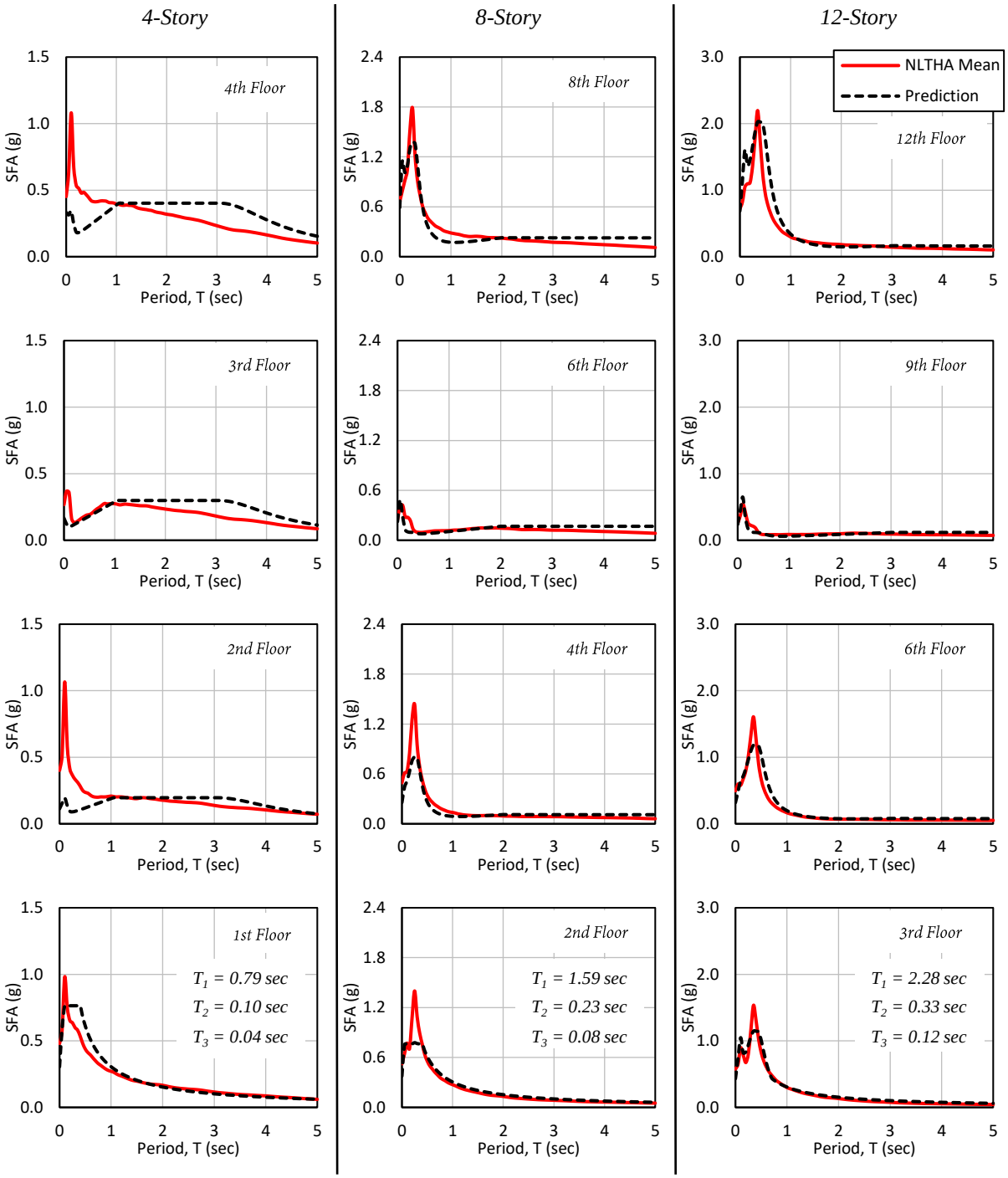

Figure 0.42 Comparison between mean floor spectra from NLTHA and estimates using closed-form modal properties of a fully-pinned continuous cantilever beam; rocking wall buildings, Intensity 5 (PGA = 0.450 g), ξ_{NS} = 10%